Enriched Finite Element Methods: Advances & Applications

Sundararajan Natarajan

Supervisors: Prof. Stéphane PA Bordas
Dr. Pierre Kerfriden

A thesis submitted to the graduate school
in fulfilment of the requirements for the degree of
Doctor of Philosophy

June 20, 2011

Institute of Mechanics and Advanced Materials
Theoretical and Computational Mechanics

Cardiff, Wales, U.K.

Summary

ENRICHED FINITE ELEMENT METHODS: ADVANCES & APPLICATIONS

This thesis presents advances and applications of the eXtended Finite Element Method (XFEM). The novelty of the XFEM is the enrichment of the primary variables in the elements intersected by the discontinuity surface by appropriate functions. The enrichment scheme carries the local behaviour of the problem and the main advantage is that the method does not require the mesh to conform to the internal boundaries. But this flexibility comes with associated difficulties: (1) Blending problem; (2) Numerical integration of enrichment functions and (3) sub-optimal rate of convergence.

This thesis addresses the difficulty in the numerical integration of the enrichment functions in the XFEM by proposing two new numerical integration schemes. The first method relies on conformal mapping, where the regions intersected by the discontinuity surface are mapped onto a unit disk. The second method relies on strain smoothing applied to discontinuous finite element approximations. By writing the strain field as a non-local weighted average of the compatible strain field, integration on the interior of the finite elements is transformed into boundary integration, so that no sub-division into integration cells is required.

The accuracy and the efficiency of both the methods are studied numerically with problems involving strong and weak discontinuities. The XFEM is applied to study the crack inclusion interaction in a particle reinforced composite material. The influence of the crack length, the number of inclusions and the geometry of the inclusions on the crack tip stress field is numerically studied. Linear natural frequencies of cracked functionally graded material plates are studied within the framework of the XFEM. The effect of the plate aspect ratio, the crack length, the crack orientation, the gradient index and the influence of cracks is numerically studied.

LaTeX-ed Friday, October 14, 2011; 10:55am

Declaration

DECLARATION

This work has not previously been accepted in substance for any degree and is not concurrently submitted in candidature for any degree.

Signed..... (candidate) **Date**.....

STATEMENT 1

This thesis is being submitted in partial fulfillment of the requirements for the degree of **PhD**.

Signed..... (candidate) **Date**.....

STATEMENT 2

This thesis is the result of my own independent work/investigation, except where otherwise stated. Other sources are acknowledged by explicit references.

Signed..... (candidate) **Date**.....

STATEMENT 3

I hereby give consent for my thesis, if accepted, to be available for photocopying and for inter-library loan, and for the title and summary to be made available to outside organisations.

Signed..... (candidate) **Date**.....

Acknowledgements

I cannot thank my supervisor Prof. Stéphane Bordas enough for his assistance, guidance, friendship and support over the past four years. Conversations, discussions and explanations during lunch/bus journey have been of tremendous help to guide me through all my work and my life. Apart from ensuring that I was working on my core research topic, he also gave me the freedom to explore different research areas and the opportunity to work on a variety of projects. Working with him has resulted in fruitful collaborations with different groups of people, esp., Prof. Timon Rabczuk, Dr. Pedro M Baiz, Dr. Zayong Guo, Prof. Uday Banerjee, Prof. Sonia Garcia. He has been patient throughout this endeavour, allowed me to make mistakes and corrected me when I went too far off course. I could not have asked for more from him. I thank him for having been a wonderful mentor. I am very thankful to Dr. Pierre Kerfriden for everything. My thanks go to Prof. Bhushan L Karihaloo for his comments during review meetings and constant encouragement. I extend my thanks to Dr. D Roy Mahapatra for all the discussions on research and on other topics, have been invaluable through these past four years.

I wish to acknowledge the staff of the School of Engineering for providing me with office space and all the facilities. In particular to staff of the Research Office, School of Engineering: Aderyn Reid, Julie Cleaver, Jeanette Whyte, Hannah Cook, Chris Lee and Fiona Pac-Soo, for their kind words and constant assistance with travel, office supplies and institute procedures.

I am also grateful to the Overseas Research Student Awards Scheme (ORSAS), James Watt Engineering Scholarship, University of Glasgow and School of Engineering Scholarship, Cardiff University that have supported me financially during my work at University of Glasgow and at Cardiff University.

I owe a special note of thanks to Dr. Ganapathi who has consistently provided me with encouragement. I would also like to extend my thanks for Prof. PSS Srinivasan and A Nagamani for their trust in me and support. I would like to thank my colleagues and friends, especially Ahmad Akbari R, Dr. Robert Simpson, Dr. Octavio Andrés González-Estrada, Oliver Goury, Lian Haojie, Chang Kye Lee and Jubel for making this whole experience and stay in Cardiff an enjoyable and memorable one. I also wish to thank Lisa Cahill for allowing me to be a part of her work on cracks in orthotropic materials and to Dr. Robert Simpson for his comments on Chapter 2. A special thanks to Lian Haojie for helping me with the compilation of the enrichment functions. I extend my thanks to Dr. Ravindra Duddu for helping me with level set formulation and Hari, Mike Winifred, Pattabhi and Renjith for helping me with various technical details.

I would like to give some special thanks to my friends: Abhishek (Nigam, Mishra), Bala, Deepak Chachra, Ghanesh, Guru, Hire, Jyotis, Kamesh, (G, U, K) Karthik, Kaushal, Manish, Mrinal, Nikhil, Prakash, Puneet, Raamaa, Sasi, Sanjay, Sandeep, Senthil, Soumik, Subbu, Vivek for consistent and perpetual support during hard times and good times. I extend my thanks to my mentors Baskaran, Jassie, JS, Murali at General Electric, India for their support and guidance. I extend my thanks to my elder brothers Saravana & Sriram and my elder sisters Ganga, Chandra, Sai Lakshmi and Bhuvaneshwari for their support, guidance

and timely advice. A special thanks to my young friends and philosophers: Ayush, Pranav, Mahathi, Aswin, Kavya, Aravind, Shruthi, Arunima, Sid, Anu, Bhavana for their love and affection.

Obviously without my parents, I would not be sitting in front of the computer, typing these acknowledgements. I owe my parents, Natarajan and Geetha Natarajan much of what I have become. I am thankful for my sister Parvathi @ Uma's abundant love and affection. My thanks extend to Bugs, Nirmal, Mr. and Mrs. Chandrasekaran for their support, trust and encouragement.

Words are not enough to thank my wife Ramya who has always stood by me and supported me on numerous occasions. I thank her for bearing my little availability (mentally as well) and grumbling. And a very special thanks to my son Vaibhav for teaching me to be patient :). I admire his abundant source of energy and constant thirst to learn and do new things. And especially the attitude of performing tasks without the fear of failure and repeating them until success is attained. I owe a debt of gratitude for all the hours stolen from them.

Finally, I would like to thank the supreme creator for giving me the strength to swim through different hurdles.

Dedication

ॐ गणेशाय नमः

सर्वधर्मान् परित्यज्य मामेकम् शरनम् व्रज ।
अह्म् त्वा सर्वपापेभ्यो मोक्षयिष्यामि मा शुचः॥

Relinquish all dharmas and just surrender unto 'ME'. I shall deliver you from all sinful reaction.

Bhagavad-Gita, Chapter 18

सर्वम् क्रष्नार्पनम्

List of Abbreviations

Greek Letters

$\boldsymbol{\sigma}$	Stress tensor, $\mathrm{N/m^2}$
$\boldsymbol{\varepsilon}$	Strain tensor
ψ	Absolute value function
χ	Cut-off function
λ	Lagrange multipliers
(ξ, η)	Natural coordinates
β_x, β_y	Plate section rotations
$\overline{\Omega}$	Non-dimensionalized natural frequency
ω	Natural frequency
$\boldsymbol{\delta}$	Vector of degrees of freedom associated to the displacement field in a finite element discretization
υ	Transverse shear correction factors
Ω	Structural domain, open subset of $\mathbb{R}^2$
ϕ	Level set function
θ	Crack orientation
ϱ	Generic enrichment function
ϑ	Generic enrichment function to capture strong discontinuity
Φ	Smoothing function
Ψ	Generic function to capture weak discontinuities
Ξ	Generic asymptotic function
Υ	Level set function to represent the crack tips

Latin Letters

H	Heaviside function
N	Finite element shape functions
Φ_I, Φ_{II}	Asymptotic fields obtained from Williams' series expansion
$\mathbf{w}$	Pre-computed enrichment functions
A	Cross-sectional area
f	Conformal map
X, Y	Open sets
D	Open unit disk
z	Complex number
A_C	Area of the subcell
K_I, K_{II}	Mode I and II stress intensity factors
L, W	Length and Width of the plate
R	Ramp function
$2a$	Length of the crack
T, U	Kinetic and potential energy
H_x, V_y	Horizontal and vertical distance between the crack surfaces
u_o, v_o, w_o	Mid-plane displacements at a point (x, y, z)
$\mathbf{N}^{st}, \mathbf{M}^{st}$	Membrane and bending stress resultants

$a(\cdot,\cdot)$	Bilinear form
$\ell(\cdot)$	Linear form
nc	Number of subcells
n_c	Number of inclusions
$\mathbf{q}$	Standard nodal variables
$\mathbf{a}$	Enriched nodal variables associated to strong discontinuity
B_α	Isotropic or orthotropic near-tip asymptotic fields
$\mathbf{b}^\alpha$	Enriched nodal variables associated to asymptotic fields
$\mathbf{c}$	Enriched nodal variables associated to material interface enrichment
G_ℓ, F_ℓ	Near-tip asymptotic fields for Reissner-Mindlin plates
$\mathcal{N}^{\mathrm{c}}$	Set of nodes enriched with Heaviside function
$\mathcal{N}^{\mathrm{f}}$	Set of nodes enriched with near-tip asymptotic fields
$\mathcal{N}^{\mathrm{int}}$	Set of nodes enriched with absolute value function
$\mathcal{N}^{\mathrm{fem}}$	Set of all nodes in finite element mesh
(r,θ)	Crack tip polar coordinates
$\mathbf{x}$	Co-ordinates in Cartesian co-ordinate system

Subscripts and Superscripts

p	Subscript index used to represent the membrane strain
b	Subscript index used to represent the bending strain
s	Subscript index used to represent the shear strain
st	Superscript index used to represent the stress resultants
I, J, K, L	Subscript index used to represent nodes in the finite element mesh
ex	Superscript index used to represent exact solution
e, be, b	Subscript index to represent the extensional, bending-extensional and bending coefficients
$,i$	Subscript index to represent partial differentiation with respect to the variable of index i
h	Superscript index used to represent the discrete quantities, e.g $\mathbf{u}^h$
m, c	Subscript index for metal and ceramics

Various constants

$\mathbf{D}$	Fourth order elastic tensor, $\mathrm{N/m^2}$
E	Young's modulus, $\mathrm{N/m^2}$
T	Temperature, K
$\mathbf{A}_e, \mathbf{D_b}$	Extensional and bending stiffness coefficients, $\mathrm{N/m^2}$
$\mathbf{B}_{be}$	Extensional-bending coupling stiffness coefficients, $\mathrm{N/m^2}$
ν	Poisson's ratio
K	Bulk modulus, $\mathrm{N/m^2}$
G	Shear modulus, $\mathrm{N/m^2}$
ρ	Density, $\mathrm{Kg/m^3}$
κ	Thermal conductivity, W/mK
α	Thermal expansion coefficient, 1/K
n	Gradient index

V	Volume fraction

Spaces

$\mathbb{C}$	Complex plane
L^2	Lebesgue space
H^1	Hilbert space
$\mathcal{U}, \mathcal{V}$	Space of trial (unknowns) and test functions
U	Non-empty simply connected open subset of complex plane
$\mathbf{u}^h, \mathbf{v}^h$	Discrete space of trial (unknowns) and test functions

Global matrices

$\mathbf{K}$	Stiffness matrix
$\mathbf{u}$	Vector of unknown coefficients
$\tilde{\mathbf{K}}$	Smoothed stiffness matrix
$\mathbf{f}$	Force vector
$\mathbf{M}$	Mass matrix
$\mathbf{n}$	Unit outward normal vector
$\mathbf{F}$	Continuously differentiable vector field

Operators

∇_s	Symmetric gradient operator
$\mathbf{B}$	Gradient operator
$\tilde{\mathbf{B}}$	Smoothed gradient operator

Acronyms

FMM	Fast Marching Method
FSDT	First order Shear Deformation Theory
FS-FEM	Face-based Smoothed Finite Element Method
GFEM	Generalized Finite Element Method
HA-XFEM	Hybrid Analytic eXtended Finite Element Method
HCE	Hybrid Crack Element
LEFM	Linear Elastic Fracture Mechanics
LSM	Level Set Method
MITC4	Mixed Interpolated Tensorial Components
CS-FEM	Cell-based Smoothed Finite Element Method
MLPG	Meshless Local Petrov Galerkin
NS-FEM	Node-based Smoothed Finite Element Method
PUFEM	Partition of Unity Finite Element Method
PUM	Partition of Unity Method
RB-XFEM	Reduced Basis eXtended Finite Element Method
SCCM	Schwarz Christoffel Conformal Mapping
SC	Schwarz Christoffel

SFEM	Smoothed Finite Element Method
SIF	Stress Intensity Factor
DEM	Discrete Element Method
SmXFEM	Smoothed eXtended Finite Element Method
TSDT	Third order Shear Deformation Theory
XFEM	eXtended Finite Element Method
α-FEM	α Finite Element Method
SCNI	Stabilized conformal nodal integration
EFGM	Element free Galerkin method
E-FEM	Elemental enrichment Finite Element Method
ERR	Energy Release Rate
ES-FEM	Edge-based Smoothed Finite Element Method
FDM	Finite Difference Method
FEM	Finite Element Method
FETI	Finite Element Tearing and Interconnecting
FGM	Functionally Graded Material

Contents

1 Introduction

This thesis deals with problems in linear elastic fracture mechanics (LEFM) and problems with internal geometries or moving boundaries. The thesis presents advances and applications of the partition of unity method (PUM), in particular, the extended finite element method (XFEM).

Chapter 2 introduces the basics of PUM, with particular focus on the XFEM. A detailed discussion on some of the difficulties associated with the XFEM are discussed. The thesis is motivated by one such difficulty, i.e., numerical integration over the elements intersected by the discontinuity surface.

Chapter 3 presents two new numerical integration techniques to numerically integrate over enriched elements in the XFEM. The first method relies on conformal mapping for arbitrary polygons that can be used for the elements intersected by a discontinuity surface in 2D. In case of elements intersected by a discontinuity surface, each part of the element is conformally mapped onto a unit disk. Cubature rule on this unit disk is used to obtain the integration points. The proposed method (*is applicable to 2D cases only*) eliminates the need for a two level isoparametric mapping. The second method is based on the strain smoothing method (SSM). The SSM was originally proposed for meshless methods and later extended to the finite element method (FEM). The resulting method was coined as the Smoothed Finite Element Method (SFEM). In Chapter 3, Section 3.2.2, SSM is combined to the XFEM, to construct the Smoothed eXtended Finite Element Method (SmXFEM). The smoothing allows to transform the volume integration into surface integration in the case of 3D and surface integration into contour integration in the case of 2D by the divergence theorem, so that the computation of the stiffness matrix

- is done by boundary integration, along the smoothing cells' boundary,
- does not require the computation of derivatives of the shape functions (spatial differentiation is replaced by multiplication by the normal to the cells' boundary),

- does not require any iso-parametric mapping.

The accuracy, the efficiency and the robustness of the proposed methods are illustrated with numerical examples involving weak and strong discontinuities in Chapter 4. The results are compared with the conventional XFEM and with analytical solutions wherever available. The crack inclusion interactions in an elastic medium are numerically studied. Both the inclusion and the crack are modelled within the XFEM framework by appropriate enrichment functions. A structured mesh is used for the current study and the influence of crack length, number of inclusions on the crack tip stress field is numerically studied. The interaction integral for non-homogeneous materials is used to compute the stress intensity factors ahead of the crack tip. The accuracy and the flexibility of the XFEM to study crack inclusion interactions is demonstrated by various numerical examples.

In Chapter 5, the linear free flexural vibration of cracked functionally graded material plates is studied using the XFEM. A 4-noded quadrilateral plate bending element based on field and edge consistency, with 20 degrees of freedom per element is used for this study. The natural frequencies and mode shapes of simply supported and clamped, square and rectangular plates are computed as a function of the gradient index, the crack length, the crack orientation and the crack location. The effect of thickness and the influence of multiple cracks is also studied.

Finally, Chapter 6 contains the conclusions of this work, as well as suggestions and remarks about future work.

2

Partition of Unity Methods

Partial differential equations (PDEs) play an important role in a wide range of disciplines. They emerge as the governing equations of problems arising in different fields of Science, Engineering, Economy and Finance. Closed form or analytical solutions to these equations are not obtainable for most problems. Hence, scientists and engineers have developed numerical methods, such as the finite difference method (FDM) [119], the finite element method (FEM) [12, 166], meshless methods [68, 85], spectral methods [29], boundary element methods [130], discrete element methods [106], Lattice Boltzmann methods [140] etc.,

A popular and widely used approach to the solution of PDEs is the FEM. FEM based computational mechanics plays a prominent role in all fields of science and engineering. FEM does not operate on the differential equations; instead, the continuous boundary and initial value problems are reformulated into equivalent variational forms. The FEM requires the domain to be subdivided into non-overlapping regions, called the elements. In FEM, individual elements are connected together by a topological map, called a mesh and local polynomial representation is used for the fields within the element. The solution obtained is a function of the quality of mesh and the fundamental requirement is that the mesh has to conform to the geometry (see Figure 2.1). The main advantage of the FEM is that it can handle complex boundaries without much difficulty. Despite its popularity, FEM suffers from certain drawbacks. This is illustrated in Table 2.1 along with some solution methodologies that have been proposed to overcome the limitations of the FEM. Note that some solution methodologies aim at addressing more than one limitation of the FEM, for example, meshfree methods [68, 85] and the recently proposed Smoothed Finite Element Method (SFEM) [28, 87, 110].

It has been noted that the FEM with piecewise polynomials are inefficient to deal with singularities or high gradients in the domain. One strategy is to enrich the FEM approximation basis with additional functions [136]. Some of the proposed techniques can be combined with enrichment techniques to solve problems involving high gradients or singularities.

The idea of enriching the finite element (FE) approximation basis will be revisited in Chapter 3 Section 3.2.2 in the context of strain smoothing as applied to the enriched FEM. This thesis focusses on enrichment techniques for finite elements. Also, enrichment techniques are available in meshfree methods [27, 109, 123], but these will not be discussed in this study. The term 'enrichment' in this thesis implies augmenting or supplementing a basis of piecewise polynomial 'finite elements' by appropriate functions chosen to accurately represent the local behaviour.

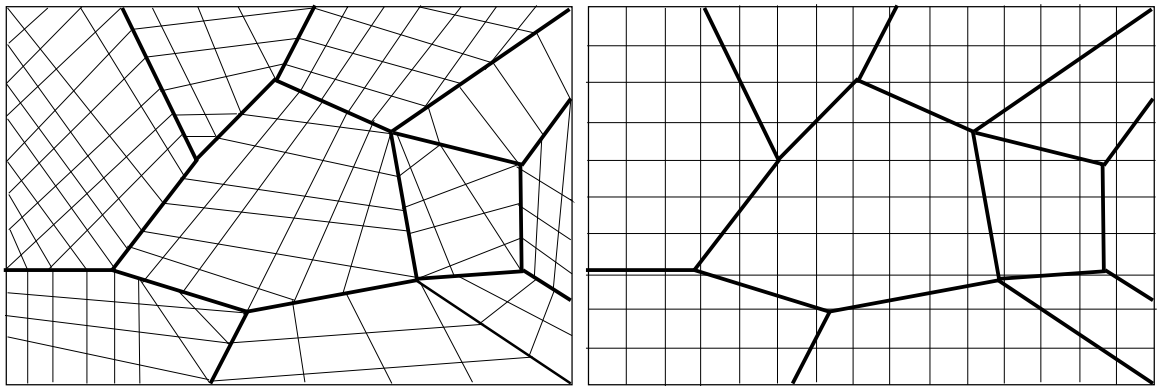

(a) FEM (b) XFEM/GFEM/PUFEM

Figure 2.1: Domain with internal boundaries: (a) conventional FEM discretization, the mesh conforms to the internal boundaries and (b) XFEM/GFEM/PUFEM approach, the mesh is independent of the internal boundaries.

This chapter is organized as follows. The governing equations for 2D elasticity problem and corresponding variational form is given in the next section. Section 2.2 presents the basics of the FEM. A brief summary of different enrichment techniques proposed since 1970 is discussed in Section 2.3. Section 2.4 gives an overview of the eXtended Finite Element Method (XFEM). The flexibility provided with the XFEM comes with associated difficulties. A brief discussion is presented on some of these difficulties. Simple numerical examples involving weak discontinuities are presented in Section 2.5, followed by a summary in the last section.

2.1 Governing equations and Variational form

The governing equilibrium equations for a 2D elasticity problem with internal boundary, Γ_c defined in the domain Ω and bounded by Γ is

$$\nabla_s^{\mathrm{T}}\boldsymbol{\sigma} + \mathbf{b} = \mathbf{0} \quad \text{in} \quad \Omega \tag{2.1}$$

where $\nabla_s(\cdot)$ is the symmetric part of the gradient operator, $\mathbf{0}$ is a null vector, $\boldsymbol{\sigma}$ is the stress

Table 2.1: Drawbacks of the FEM and solution methodologies.

Area of concern	Finite Element Method	Solution Methodologies
Element shape	Mapping and co-ordinate transformation is involved in the FEM and hence the element cannot take arbitrary shape. A necessary condition for a 4-noded isoparametric element is that no interior angle is greater than 180° and the positivity of the Jacobian should be ensured.	• SFEM [28, 87, 110] • Meshfree methods [68, 85, 123] • Polygonal FEM [43, 141, 142] • Voronoi cell FEM [62, 63]
Large deformation	Large deformation may result in severe mesh distortion leading to drastic deterioration in the accuracy.	• SFEM [88] • Meshfree methods [68, 85, 123]
High gradients or cracks or discontinuities	Requires a very fine discretization leading to increased computational time.	• Meshfree methods [36, 76, 86] • Special elements & mesh overlay techniques [16, 52, 54, 107] • Enrichment techniques [10, 15, 22, 136, 138] • Wavelet FEM [37, 122, 147]
Interpolation fields	FEM interpolation fields are primarily $\mathcal{C}^o$ functions. Higher order interpolation fields are difficult to construct. For example, gradient elasticity, plate theories	• Meshfree methods [5, 18, 89] • Iso-geometric analysis [73] • Spectral methods [29, 120]
Geometry representation	Piecewise polynomials are normally used to represent the geometry	• Iso-geometric analysis [73] • Implicit representation [101]

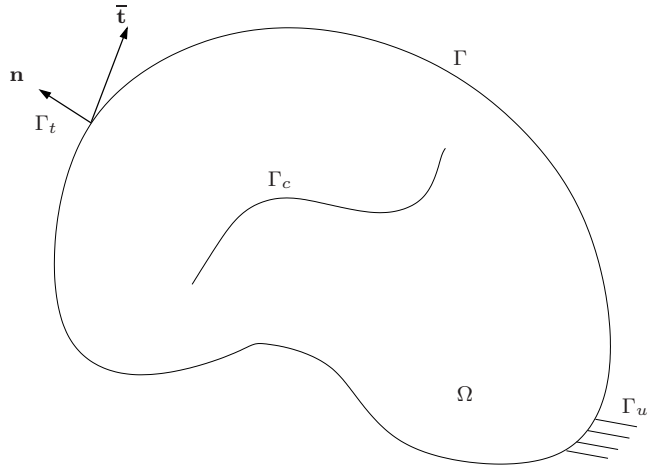

Figure 2.2: Two-dimensional elastic body with a crack.

tensor and $\mathbf{b}$ is the body force. The boundary conditions for this problem are:

$$\begin{aligned} \boldsymbol{\sigma} \cdot \mathbf{n} &= \overline{\mathbf{t}} \quad \text{on} \quad \Gamma_t \\ \mathbf{u} &= \overline{\mathbf{u}} \quad \text{on} \quad \Gamma_u \\ \boldsymbol{\sigma} \cdot \mathbf{n} &= \overline{\mathbf{t}} \quad \text{on} \quad \Gamma_c \end{aligned} \tag{2.2}$$

where $\overline{\mathbf{u}} = (\overline{u}_x, \overline{u}_y)^{\mathrm{T}}$ is the prescribed displacement vector on the essential boundary Γ_u; $\overline{\mathbf{t}} = (\overline{t}_x, \overline{t}_y)^{\mathrm{T}}$ is the prescribed traction vector on the natural boundary Γ_t and $\mathbf{n}$ is the outward normal vector. In this study, it is assumed that the displacements remain small and the strain-displacement relation is given by:

$$\boldsymbol{\varepsilon} = \nabla_s \mathbf{u} \tag{2.3}$$

The constitutive relation is given by:

$$\boldsymbol{\sigma} = \mathbf{D} : \boldsymbol{\varepsilon} \tag{2.4}$$

where $\mathbf{D}$ is a fourth order elasticity tensor. Equation (2.1) is called the 'strong form' and computational solutions of Equation (2.1) rely on a process called 'discretization' that converts the problem into system of algebraic equations. The first step in transforming Equation (2.1) into a discrete problem is to reformulate Equation (2.1) into a suitable variational equation. This is done by multiplying Equation (2.1) with a test function. Let us define,

$$\begin{aligned} \mathcal{U} &= \left\{ \mathbf{u} \in H^1(\Omega) \quad \text{such that} \quad \mathbf{u}|_{\Gamma_u} = \overline{\mathbf{u}} \right\} \\ \mathcal{V} &= \left\{ \mathbf{v} \in H^1(\Omega) \quad \text{such that} \quad \mathbf{v}|_{\Gamma_u} = \mathbf{0} \right\} \end{aligned} \tag{2.5}$$

The space $\mathcal{U}$ in which we seek the solution is referred to as the 'trial' space and the space $\mathcal{V}$ is called the 'test' space. Let us define a bilinear form $a(\cdot,\cdot)$ and a linear form $\ell(\cdot)$,

$$\begin{aligned} a(\mathbf{u},\mathbf{v}) \colon &= \int_\Omega \boldsymbol{\sigma}(\mathbf{u}) \colon \boldsymbol{\varepsilon}(\mathbf{v}) \, \mathrm{d}\Omega \\ \ell(\mathbf{v}) &= \int_{\Gamma_t} \mathbf{v} \cdot \overline{\mathbf{t}} \, \mathrm{d}\Gamma \end{aligned} \tag{2.6}$$

where $H^1(\Omega)$ is a Hilbert space[a] with weak derivatives up to order 1. The weak formulation of the static problem is then given by:

$$\text{find} \quad \mathbf{u} \in \mathcal{U} \quad \text{such that} \quad \forall \mathbf{v} \in \mathcal{V} \quad a(\mathbf{u},\mathbf{v}) = \ell(\mathbf{v}) \tag{2.9}$$

2.2 Galerkin Finite Element Method

In the variational weak form given by Equation (2.9), $\mathcal{U}$ and $\mathcal{V}$ are infinite dimensional subspaces of the Hilbert space H. To get an approximate solution, a finite dimensional subspace, i.e.,$\mathcal{U}^h \subset \mathcal{U}$ and $\mathcal{V}^h \subset \mathcal{V}$ is chosen. The weak formulation of the static form is then given by:

$$\text{find} \quad \mathbf{u}^h \in \mathcal{U}^h \quad \text{such that} \quad \forall \mathbf{v}^h \in \mathcal{V}^h \quad a(\mathbf{u}^h,\mathbf{v}^h) = \ell(\mathbf{v}^h) \tag{2.10}$$

where h is a discretizaton parameter. The above discretization is called the 'Galerkin' equation. The key property of the Galerkin approach is that error ($e_n = \mathbf{u} - \mathbf{u}^h$, the difference between the solution of original problem given by Equation (2.9) and the solution of

[a]The function space $L^2(\Omega)$ with the inner product

$$(u,v)_{L^2(\Omega)} = \int_\Omega uv \, \mathrm{d}\Omega \; u, v \in L^2(\Omega) \tag{2.7}$$

and with associated norm $||u||_{L^2(\Omega)} = \sqrt{(u,u)}_{L^2(\Omega)}$, where $L^2(\Omega)$ consists of functions that are square integrable:

$$L^2(\Omega) = \left\{ f \colon \int_\Omega f^2 \, \mathrm{d}\Omega < \infty \right\} \tag{2.8}$$

.

Galerkin equation given by Equation (2.10)) is orthogonal to the chosen subspaces. FEMs are distinguished by the manner in which the approximation subspaces $\mathcal{U}^h$ and $\mathcal{V}^h$ are chosen. In a Bubnov-Galerkin or Ritz-Galerkin method, both the approximation subspaces are chosen from the same finite-dimensional subspaces, while in Petrov-Galerkin method, they are chosen from different subspaces. Let,

$$\begin{aligned} \mathbf{u}^h &= N_i u^i \\ \mathbf{v}^h &= N_i v^i, \quad i = 1, 2, \cdots, M \end{aligned} \tag{2.11}$$

where u_i, v_i are the unknown coefficients, M is the total number of functions and N_i are the shape functions that span the subspaces. In FEM, it is a space of piecewise polynomial functions. Substituting Equation (2.11) into Equation (2.10), for arbitrary $\mathbf{v}^h$, we get the following discretized form:

$$\sum_{j=1}^{M} v_j \left(\sum_{i=1}^{M} K_{ij} u_i - f_j \right) = 0 \tag{2.12}$$

where

$$\begin{aligned} K_{ij} &= a(N_i, N_j) \\ f_j &= \langle \ell, N_j \rangle \end{aligned} \tag{2.13}$$

where $\langle \cdot, \cdot \rangle$ is an inner product vector space[b]. In matrix form,

$$\mathbf{K}\mathbf{u} = \mathbf{f} \tag{2.15}$$

where $\mathbf{u}$ is the vector containing the unknown coefficients, $\mathbf{K}$ is called the stiffness matrix and $\mathbf{f}$ is called the force vector.

2.3 Enrichment Techniques: Journey through time

Despite its robustness and versatility, FEM's efficiency to model cracks or discontinuities or large gradients has always been considered an area for improvement, since early 1970's [136,

[b]The inner product space of two functions is:

$$\langle f, g \rangle := \int_a^b f(t) g(t) \, \mathrm{d}t \tag{2.14}$$

155]. This is because 'finite element' methods using piecewise polynomials as approximating functions are inefficient to model such features. A modification (augmentation, enrichment) of the finite element spaces will improve the behaviour. As we will see in this section, the concept of 'enrichment' dates back to 1970's and an intensive research over the past 3 - 4 decades has led to some of the robust methods available to model cracks or discontinuities or large gradients, for example XFEM/Generalized FEM (GFEM)/ (Partition of Unity FEM (PUFEM) [10, 15, 138], hp-cloud [60] to name a few. Earlier work on enrichment [22, 56, 136] aimed at improving the approximation of singular solutions. Enriched methods can be broadly classified into three categories: (i) local enrichment; (ii) global enrichment and (iii) mesh-overlay techniques.

Table 2.2: Different enrichment techniques.

Local enrichment	Global enrichment	Mesh-over lay techniques
• Generalized isoparametric element [4, 22, 30, 117, 149]	• Higher-order Rayleigh Ritz [55, 56]	• Global-local FEM [100]
• Enrichment with cut-off function [136]	• Whiteman and Akin [158]	• Hybrid-element approach [148]
• Quarter point elements [11]	• PUM [9, 10, 92, 93]	• Spectral overlay techniques [17, 53]
• FEM for localized problems [115]		• s- FEM [52]
• Embedded localization [16]		
• XFEM [15]		
• GFEM [138]		
• Discrete enrichment method [57]		
• Hansbo and Hansbo [69]		
• Elemental enrichment (E-FEM) [114]		

2.3.1 Global enrichment strategies

One strategy to improve the performance of the finite elements using picewise polynomials to represent the singularities or high gradients or problems with oscillatory solutions is to enrich the FE approximation basis globally as done in the work of Fix *et al.,* [56], Fix [55], Wait and Mitchell [155], Whiteman and Akin [158] and Babuška *et al.,* [10]. Fix *et al.,* [56] and Fix [55] augmented FE approximation basis with singular functions to approximate accurately the eigenfunctions near re-entrant corners (for example, L-shaped problem). Their study showed that the convergence rate of the Rayleigh-Ritz approximations using piecewise functions without singular functions is much slower than when the approximation basis is augmented with the singular functions. Wait and Mitchell [155] and Whiteman and Akin [158] proposed to add singular functions to approximate the displacement field near the singularity. The addition of singular functions destroyed the band structure of the stiffness matrix and led to an ill-conditioned system when the basis functions are nearly linearly dependent. The work of Babuška *et al.,* [10] and Melenk and Babuška [93] proposed special FEs to solve problems with non-smooth coefficients and highly oscillatory solutions. The method was referred to as PUMFEM or the partition of unity method (PUM). Melenk [92] showed for Helmholtz's equation that if these functions (i.e., enrichment functions) have the same oscillatory behaviour as the solution, the convergence of the FEM is improved. This work involved using harmonic polynomials for Laplace and Helmholtz's equations. The PUM was referred to as the GFEM in [138].

2.3.2 Local enrichment techniques

Although, global enrichment serves the purpose of enhancing the performance of the finite elements for problems with non-smooth coefficients, the addition of enrichment functions has following difficulties:

- Increases the conditioning number[c] of the stiffness matrix.
- Destroys the band structure of the matrix and leads to increased storage requirements.
- The number of additional unknowns is proportional to the mesh parameter, h.

More importantly, regions of high gradients or cracks or discontinuities are local phenomenon and therefore it is sufficient to enrich the FE approximation basis in the vicinity of regions of interest. The term 'local' refers to the space in the vicinity of such features. Local enrichment can be used to capture strong discontinuities and singularities, which will be discussed next.

[c]The condition number associated with the linear equation $Ax = b$ gives a bound on how inaccurate the solution x is for small perturbations in b.

Strong discontinuities

Ortiz *et al.,* [115] proposed a method to model strain localization using isoparametric elements, which involved augmenting the FE approximation basis with localized deformation modes in the regions where localization is detected. The method was applied to study strain localization in both nearly incompressible and compressible solids. The additional degrees of freedom (dofs) due to the localized deformation modes are eliminated at the element level by static condensation. Note that these localized modes do not form partition of unity. By modifying the strain field, Belytschko *et al.,* [16] proposed a method to model localization zones. The jumps in strain are obtained by imposing traction continuity. Both these approaches use bifurcation analysis to detect the onset of localization. One of the distinct differences between these two methods is that the width of the localization band is smaller than the mesh parameter, h, in case of the method proposed by Belytschko *et al.,* [16], whereas the localization band width is of the same size as the mesh parameter in the method by Ortiz *et al.,* [115]. A very fine mesh is required to resolve the localization band in case of the method by Ortiz *et al.,* [115].

By using overlapping elements, Hansbo and Hansbo [69] suggested a method to model strong and weak discontinuities. In their method, when a discontinuity surface cuts an element e, another element, $\overline{e}$ is superimposed and the standard FE displacement field is replaced by

$$\mathbf{u}^h(\mathbf{x}) = \sum_{I\in e} N_I^e(\mathbf{x})H(\mathbf{x})\mathbf{q}_I^e + \sum_{J\in\overline{e}} N_J^{\overline{e}}(\mathbf{x})(1-H(\mathbf{x}))\mathbf{q}_J^{\overline{e}} \tag{2.16}$$

where N_I are the standard FE shape functions, H is a step function and $\mathbf{q}_I$ and $\mathbf{q}_J$ are the nodal variables associated with node I and node J, respectively. Areias and Belytschko [1] showed that Hansbo and Hansbo's approximation basis is a linear combination of the XFEM basis. In their method, the crack kinematics is obtained by overlapping elements and this does not introduce any additional dofs, see Figure 2.3. This has some advantages with respect to the implementation of the method in existing FE codes.

In the discontinuous enrichment method (DEM) [57], the FE approximation space is enriched within each element by additional non-conforming functions. This method also does not introduce additional dofs. The dofs associated with the enrichment functions are condensed on the element level prior to assembly. Lagrange multipliers are used to enforce the continuity across element boundaries and to apply Dirichlet boundary conditions.

In the embedded element method (EFEM) [91, 113], the enrichment is at the element level and is based on assumed enhanced strain. The additional dofs are condensed at element level leading to a global stiffness matrix with the bandwidth same as that of the FEM. Piecewise constant and linear crack opening can be modelled using EFEM. Oliver *et al.,* [114]

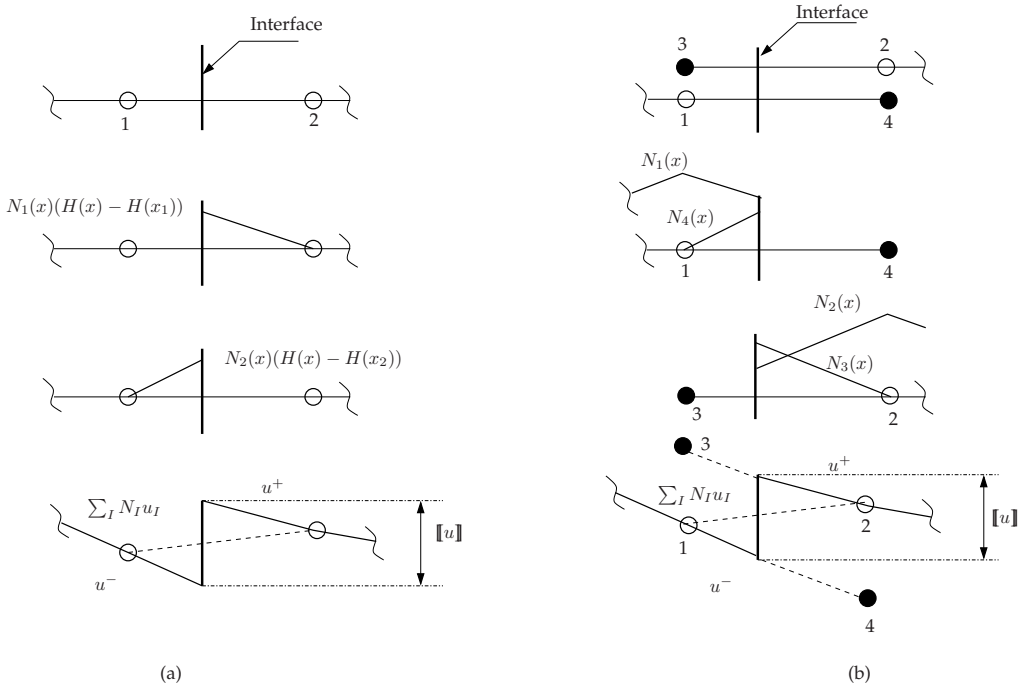

Figure 2.3: The representation of the discontinuity: (a) Std. XFEM and (b) Hansbo and Hansbo method to model discontinuities. 'Open' circles denote real nodes and 'filled' circles are called the phantom nodes.

presented a comparison between the XFEM and EFEM. Their study claimed the following:

- the convergence rates of both methods are similar;
- when implemented on same the element type, both methods yield identical results;
- the computational cost of XFEM was slightly greater than that of the EFEM;
- for relatively coarse meshes, EFEM obtained more accurate results when compared to that of the XFEM.

Singularities

Singularities can be captured by locally enriching the approximation space with singular functions [15, 22, 30, 117, 149] or by using quarter-point elements [11]. In case of the quarter-point elements, the singularity is captured by moving the element's mid-side node to the position one quarter of the way from the crack tip. This was considered to be a major milestone in applying FEM for LEFM, although sophisticated methods such as addition of singular functions were developed during the same period.
In order to improve the approximation of singular functions, Strang and Fix in their well known book [136], proposed to add singular functions to approximate the displacement

field near the singularity. The singular functions are defined locally near each singularity. The transition from the singular zone to the smooth zone is handled by a cut-off function that has polynomial coefficients. The polynomial coefficients are chosen as to merge the coefficient $r^{1/\tilde{\alpha}}, \tilde{\alpha} > 1$ smoothly into zero. Benzley [22] developed an arbitrary quadrilateral element with a singular corner node by 'enriching' a bilinear quadrilateral element with singular terms. According to Benzley, the displacement approximation is written as:

$$\mathbf{u} = \sum_{I=1}^{4} N_I \mathbf{q}_I + R\left\{ K_I \left(Q_{1k} - \sum_{I=1}^{4} N_I \overline{Q}_{1Ik} \right) + K_{II} \left(Q_{2k} - \sum_{I=1}^{4} N_I \overline{Q}_{2Ik} \right) \right\} \tag{2.17}$$

where K_I, K_{II} intensities of singular terms, $Q_{\ell k}, \ell, k = 1, 2$ are the specific singular functions, $\overline{Q}_{\ell Ik}$ is the value of singular function evaluated at node I, N_I are the standard FE shape functions and R is a ramp function that equals 1 on enriched elements and on the boundaries adjacent to 'enriched' elements and equals 0 on boundaries adjacent to standard element. Tracey [149] and Atluri *et al.,* [4] proposed a new element that has inverse square root singularity near the crack. The main advantage of this element is that the SIF can be computed more accurately.

Based on the seminal work of Babuška *et al.,* [10], Babuška and Melenk [9], Belytschko's group in 1999 [15] selected one of the enrichment functions as discontinuous function, thereby leading to a method able to model crack propagation and strong discontinuities in general with minimal remeshing. The resulting method, known as the XFEM is classified as one of the partition of unity methods (PUMs). A detailed discussion on XFEM is given in Section 2.4.

The main idea of the GFEM [138] is to combine the classical FEM and the PUM, so as to retain the best properties of the FEM. The GFEM can be interpreted as an FEM augmented with non-polynomial shape functions with compact support.

The main difference between the enrichment methods used in 1970's and the PUMs is that earlier methods still required the mesh to conform to internal boundaries, while the current methods can handle internal geometries without a conforming mesh (see Figure 2.1). The salient features of the XFEM/EFEM/GFEM/DEM are:

- the ability to include arbitrary a *priori* (includes experimentally determined and numerically determined enrichments) knowledge about the local behaviour of the solution in the approximation space;
- the finite element mesh need not conform to internal boundaries.

2.3.3 Mesh overlay methods

Mote [100] introduced the idea of 'global-local' finite element. In this method, a *priori* known shape functions are added to enrich the local finite element method. The formulation also includes singular elements in fracture mechanics. Tong *et al.,* [148] used a hybrid-element concept and complex variables to develop a super-element to be used in combination with the standard FE for problems in fracture mechanics. Belytschko *et al.,* [16] proposed the spectral overlay method for problems with high gradients. This is accomplished by superimposing the spectral approximation over the finite element mesh in regions where high gradients are indicated by the solution. Based on this work, Fish [52] proposed s-version of the FEM. This method consists of overlaying the FE mesh with a patch of higher-order hierarchical elements in the regions of high gradients.
Hughes [71] and Hughes *et al.,* [72] introduced the variational multiscale method (VMM) to solve problems involving multiscale phenomena. The idea is to decompose the displacement field into two parts: a coarse scale and a fine scale contribution. The fine-scale contribution incorporates the local behaviour, which is determined analytically. Hettich *et al.,* [70] combined XFEM with multiscale approach to model failure of composites using a two scale approach. Based on this work, Mergheim [96] applied VMM to solve propagation of cracks at finite strains. Both scales are discretized with finite elements.

2.4 eXtended Finite Element Method

XFEM is classified as one of the PUMs. A partition of unity in a domain Ω is a set of functions N_I such that

$$\sum_{I \in \mathcal{N}^{\text{fem}}} N_I(\mathbf{x}) = 1, \quad \mathbf{x} \in \Omega \tag{2.18}$$

where $\mathcal{N}^{\text{fem}}$ is the set of nodes in the FE mesh. Using this property, any function φ can be reproduced by a product of the PU shape functions with φ. Let $\mathbf{u}^h \subset \mathcal{U}$, the XFEM approximation can be decomposed into the standard part $\mathbf{u}^h_{\text{fem}}$ and into an enriched part $\mathbf{u}^h_{\text{enr}}$ as:

$$\begin{aligned} \mathbf{u}^h(\mathbf{x}) &= \mathbf{u}^h_{\text{fem}}(\mathbf{x}) + \mathbf{u}^h_{\text{enr}}(\mathbf{x}) \\ &= \sum_{I \in \mathcal{N}^{\text{fem}}} N_I(\mathbf{x})\mathbf{q}_I + \sum_{J \in \mathcal{N}^{\text{enr}}} N^{\dagger}_J(\mathbf{x})\varrho(\mathbf{x})\tilde{\mathbf{a}}_J \end{aligned} \tag{2.19}$$

where $\mathcal{N}^{\text{fem}}$ is the set of all the nodes in the FE mesh, $\mathcal{N}^{\text{enr}}$ is the set of nodes that are enriched with the enrichment function ϱ. The enrichment function ϱ carries with it the nature of

the solution or the information about the underlying physics of the problem, for example, $\varrho = H$, is used to capture strong discontinuities, where H is the Heaviside function. These are discussed in detail in the following sections. N_I and $N_J^\dagger$ are the standard finite element shape functions (not necessarily identical), $\mathbf{q}_I$ and $\tilde{\mathbf{a}}_J$ are the standard and the enriched nodal variables associated with node I and node J, respectively. In this study, N_I and $N_J^\dagger$ are assumed to be identical, unless otherwise mentioned.

The displacement approximation given by Equation (2.19) is called 'extrinsic' global enrichment (i.e., FE approximation basis is augmented with additional functions and all the nodes in the FE mesh are enriched with ϱ). This does not satisfy the Kronecker-δ property (i.e., $N_I(\mathbf{x}_J) = \delta_{IJ}$) which renders the imposition of essential boundary conditions and the interpretation of results difficult, expect for the phantom node method [124, 134]. In most cases, the region of interest is localized, for example, cracks or material interfaces and hence the enrichment could be restricted closer to the region of interest. This type of enrichment is called 'local enrichment'. Moreover, a global enrichment is computationally demanding because the number of degrees of freedom is proportional to the number of nodes and the number of enrichment functions and the resulting system matrix is not banded. A 'shifted enrichment' is used to retain the Kronecker-δ property, given by:

$$\begin{aligned} \mathbf{u}^h(\mathbf{x}) &= \mathbf{u}^h_{\text{fem}}(\mathbf{x}) + \mathbf{u}^h_{\text{enr}}(\mathbf{x}) \\ &= \sum_{I \in \mathcal{N}^{\text{fem}}} N_I(\mathbf{x})\mathbf{q}_I + \sum_{J \in \mathcal{N}^{\text{enr}}} N_J(\mathbf{x}) \left[\varrho(\mathbf{x}) - \varrho(\mathbf{x}_J)\right] \tilde{\mathbf{a}}_J \end{aligned} \tag{2.20}$$

where $\varrho(\mathbf{x}_J)$ is the value of the enrichment function evaluated at node J. Figure 2.4 illustrates the result of this shifting for 1D when $\varrho(x) = |\phi(x)| = |x - x_b|$, where x_b is the location of the interface from the left end. See § 2.4.4 for different enrichment functions proposed in the literature to capture strong and weak discontinuities arising in different problems in mechanics.

Substitute Equation (2.20) into Equation (2.10) to get:

$$\begin{bmatrix} \mathbf{K}_{uu} & \mathbf{K}_{ua} \\ \mathbf{K}_{au} & \mathbf{K}_{aa} \end{bmatrix} \begin{Bmatrix} \mathbf{q} \\ \mathbf{a} \end{Bmatrix} = \begin{Bmatrix} \mathbf{f}_q \\ \mathbf{f}_a \end{Bmatrix} \tag{2.21}$$

where $\mathbf{K}_{uu}, \mathbf{K}_{aa}$ and $\mathbf{K}_{ua}$ are the stiffness matrix associated with the standard FE approximation, the enriched approximation and the coupling between the standard FE approximation and the enriched approximation, respectively. The modification of the displacement approximation does not introduce a new form of the discretized finite element equilibrium equations, but leads to an enlarged problem to solve. In this study, extrinsic and local enrichment with mesh based shape functions is considered and is referred to as the

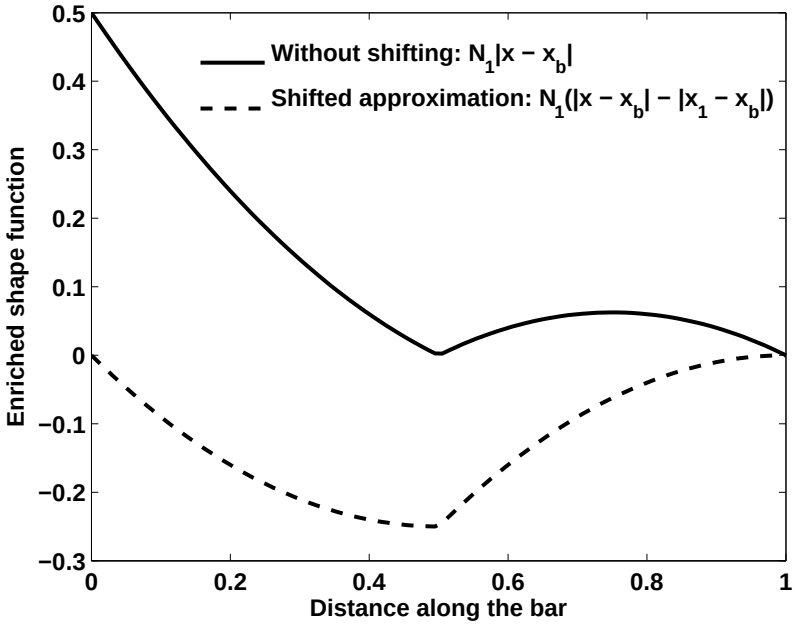

(a) Enrichment function for node 1

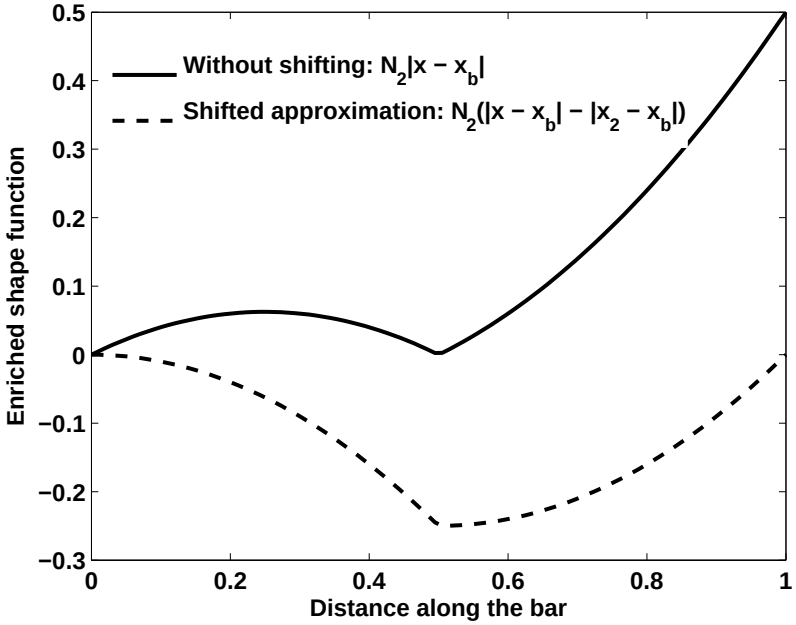

(b) Enrichment function for node 2

Figure 2.4: Enrichment function along the length of the bar. Note that the enrichment function without shifting does not go to zero at the nodes. This poses additional difficulty in imposing essential boundary conditions.

'conventional XFEM' or the 'Standard XFEM (Std. XFEM)'. This thesis focusses on modelling the material interfaces and cracks in a body independent of the underlying mesh. A generic form for the displacement approximation in case of the weak discontinuity is given by [19, 99, 146]:

$$\mathbf{u}^h(\mathbf{x}) = \sum_{I\in\mathcal{N}^{\text{fem}}} N_I(\mathbf{x})\mathbf{q}_I + \sum_{L\in\mathcal{N}^{\text{int}}} N_L(\mathbf{x})\Psi(\mathbf{x})\mathbf{c}_L \tag{2.22}$$

where $\mathcal{N}^{\text{int}}$ is the set of nodes whose support is cut by the material interface, Ψ is the enrichment function chosen such that its derivative is discontinuous. Some common types of enrichment functions used in the literature are discussed in Section 2.4.4. For the case of linear elastic fracture mechanics (LEFM), two sets of functions are used: a jump function to capture the displacement jump across the crack faces and asymptotic branch functions that span the two-dimensional asymptotic crack tip fields (3D methods have been proposed in [42] and applied to real life damage tolerance assessment [24, 160]). The enriched approximation for LEFM takes the form [15, 25, 26]:

$$\mathbf{u}^h(\mathbf{x}) = \sum_{I\in\mathcal{N}^{\text{fem}}} N_I(\mathbf{x})\mathbf{q}_I + \sum_{J\in\mathcal{N}^{\text{c}}} N_J(\mathbf{x})\vartheta(\mathbf{x})\mathbf{a}_J + \sum_{K\in\mathcal{N}^{\text{f}}} N_K(\mathbf{x}) \sum_{\alpha=1}^{n} \Xi_\alpha(r,\theta)\mathbf{b}_K^\alpha, \tag{2.23}$$

where $\mathcal{N}^{\text{c}}$ is the set of nodes whose shape function support is cut by the crack interior ('circled' nodes in Figure 2.5) and $\mathcal{N}^{\text{f}}$ is the set of nodes whose shape function support is cut by the crack tip ('squared' nodes in Figure 2.5). ϑ and Ξ_α are the enrichment functions chosen to capture the displacement jump across the crack surface and the singularity at the crack tip (see Section 2.4.4 for details) and n is the total number of asymptotic functions. $\mathbf{a}_J$ and $\mathbf{b}_K^\alpha$ are the nodal degrees of freedom corresponding to functions ϑ and Ξ_α, respectively. n is the total number of near-tip asymptotic functions and (r,θ) are the local crack tip coordinates. Equation (2.23) is a generic form of the displacement approximation to capture the displacement jump across the crack faces and to represent the singular field. In the literature, Ξ_α is denoted as B_α in case of the 2D continuum (see Section 2.4.4) and is denoted as G_ℓ and F_ℓ in case of the plate theory (see Section 5.4).
In Equations (2.22) and (2.23), the displacement field is global, but the support of the enriched functions are local because they are multiplied by the nodal shape functions. The local enrichment strategy introduces the following four types of elements apart from the standard elements:

- *Split elements* are elements completely cut by the crack. Their nodes are enriched with the discontinuous function ϑ.
- *Tip elements* either contain the tip, or are within a fixed distance independent of the mesh size, r_{enr} of the tip, if geometrical enrichment is used [21], where r_{enr} is the

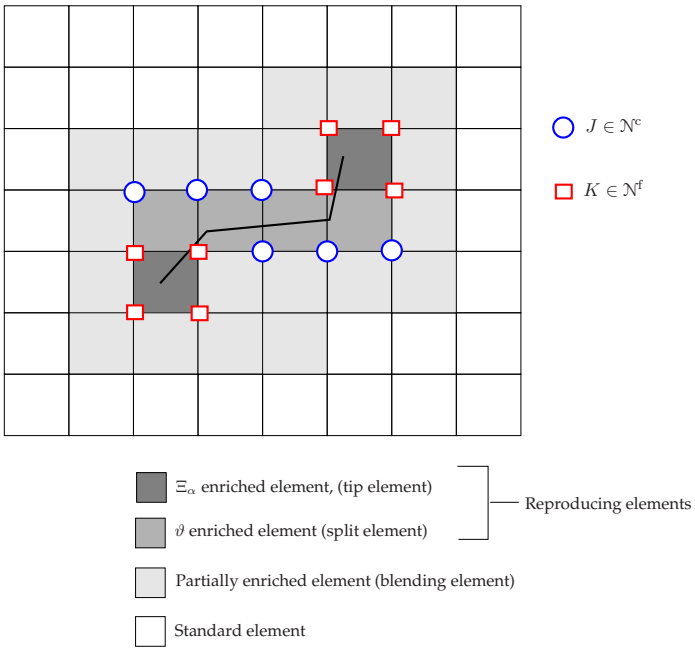

Figure 2.5: A typical FE mesh with an arbitrary crack. 'Circled' nodes are enriched with ϑ and 'squared' nodes are enriched with near-tip asymptotic fields. 'Reproducing elements' are the elements whose all the nodes are enriched.

radius of the domain centered at the crack tip. All nodes belonging to a tip element are enriched with the near-tip asymptotic fields.

- *Tip-blending elements* are elements neighbouring tip elements. They are such that some of their nodes are enriched with the near-tip and others are not enriched at all.
- *Split-blending elements* are elements neighbouring split elements. They are such that some of their nodes are enriched with the strongly or weakly discontinuous function and others are not enriched at all.

The necessary steps involved in the implementation of the XFEM are:

1. **Representation of the interface** The interface or discontinuity can be represented explicitly by line segments or implicitly by using the level set method (LSM) [116, 131].
2. **Selection of enriched nodes** In case of the local enrichment, only a subset of the nodes closer to the region of interest is enriched. The nodes to be enriched can be selected by using an area criterion or from the nodal values of the level set function. See Section 2.4.2.
3. **Choice of enrichment functions** Depending on the physics of the problem, different enrichment functions can be used. See Section 2.4.4.

4. **Integration** A consequence of adding custom tailored enrichment functions to the FE approximation basis, which are not necessarily smooth polynomial functions (for example, $\sqrt{r}$ in case of the LEFM) is that special care has to be taken in numerically integrating over the elements that are intersected by the discontinuity surface. The standard Gauß quadrature cannot be applied in elements enriched by discontinuous terms, because Gauß quadrature implicitly assumes a polynomial approximation. See Section 2.4.3

2.4.1 Interface or discontinuity representation

Introduced by Osher and Sethian, LSM has been used to represent interfaces and cracks in the XFEM framework [39, 46, 47, 49, 135, 145]. A brief discussion on the LSM is given in Appendix E.

Remark: It is not necessary that the interface should be represented by level sets. In the literature, cracks have been represented by polygons in 2D [15, 98] and by a set of connected planes in 3D [45, 144].
Sukumar *et al.,* [145] used the level set approach to model voids and inclusions in the XFEM. The geometric interface (for example, the boundary of a hole or inclusion) is represented by the zero level curve $\phi \equiv \phi(\mathbf{x}, t) = 0$. The interface is located from the value of the level set information stored at the nodes. The standard FE shape functions can be used to interpolate ϕ at any point $\mathbf{x}$ in the domain as[d]:

$$\phi(\mathbf{x}) = \sum_{I=1}^{n} N_I(\mathbf{x})\phi_I \tag{2.24}$$

where the summation is over all the nodes in the connectivity of the element that contains $\mathbf{x}$ and ϕ_I are the nodal values of the level set function.
Example: For circular inclusions, the level set function is given by:

$$\phi_I = \min_{\substack{\mathbf{x}_c^i \in \Omega_C^i \\ i=1,2,\cdots n_c}} \left\{ ||\mathbf{x}_I - \mathbf{x}_c^i|| - r_c^i \right\} \tag{2.25}$$

where $\mathbf{x}_c^i$ and r_c^i are the center and the radius of the i^{th} inclusion, ϕ_I is the value of the level set at node I and n_c is the total number of inclusions. Figure 2.6 shows the level set function for a a circle and a complex shaped inclusion. For complex shaped inclusion shown in Figure 2.6, r_c^i in Equation (2.25) is replaced by:

$$r_c^i(\theta) = r_o^i + a^i \cos(b^i \theta) \tag{2.26}$$

[d] A finite difference approximation of higher order can also be used to increase the resolution of the boundary representation

where r_o is the reference radius, a^i and b^i are parameters that control the amplitude and period of oscillations for i^{th} inclusion.

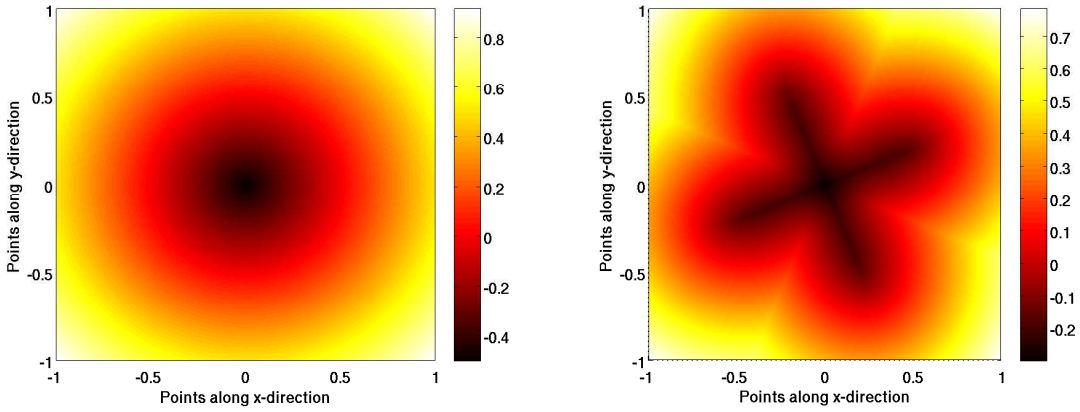

(a) Circular inclusion (b) Complex shape

Figure 2.6: Level set information for different shapes.

Stolarska *et al.,* [135] used level sets to represent the crack as the zero level set of a function. In this case, two mutually orthogonal level sets are required to represent the crack. For cracks that are entirely in the interior of the domain, two level set functions, χ_1 and χ_2, one for each crack tip is used. Sukumar *et al.,* [146] combined the XFEM and the fast marching method[e] [42, 131] to model three-dimensional fatigue cracks. The level set function that represents the crack tip is defined by:

$$\chi_i(\mathbf{x}) = (\mathbf{x} - \mathbf{x}_i) \cdot \mathbf{n} \tag{2.27}$$

where $\mathbf{n}$ is the unit vector tangent to the crack at its tip and $\mathbf{x}_i$ is the location of the i^{th} crack tip. The level set Υ used to represent the crack surface is a signed distance function[f].

2.4.2 Selection of enriched nodes

Interface represented by line segments

When the crack surface or interface is represented by line segments, the following approaches can be used to select the nodes for enrichment.

Strong or weak discontinuity In order to select the nodes to enrich with function ϑ to represent the displacement jump across the crack surface or with function Ψ to represent

[e]The fast marching method was introduced by Sethian [131] as a numerical method for solving boundary value problems that describe the evolution of a closed curve as a function of time t with speed $V(x)$.

[f]A signed distance function of a set S determines how close a given point $\mathbf{x}$ is to the boundary of S, with that function having positive values at points $\mathbf{x}$ inside S and negative values outside of S.

the weak discontinuity, an area criterion is used. Let the area above the crack be denoted by A_w^{ab} and the area below the crack be given by A_w^{be} and $A_w = A_w^{ab} + A_w^{be}$, where A_w is the area of the nodal support (see Figure 2.7). If either of the two ratios, A_w^{ab}/A_w or A_w^{be}/A_w is below a prescribed tolerance, the node is removed from the set $\mathcal{N}^c$ [143].

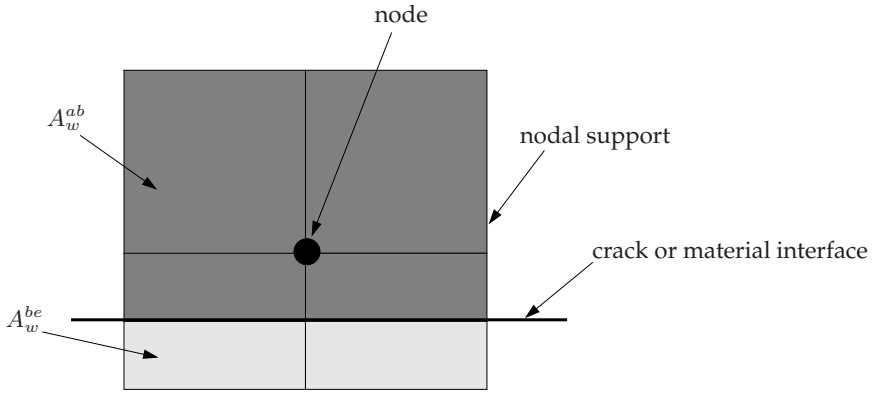

Figure 2.7: Area criterion for selection of $\vartheta(\mathbf{x})$ or $\Psi(\mathbf{x})$ enriched nodes.

Crack tip enriched nodes In the conventional XFEM, all the nodes of the tip-elements (see Figure 2.5) are enriched with near-tip asymptotic fields. Consequently, the support of the enriched functions vanishes as h goes to zero. In the literature alternate strategies have been proposed, which will be discussed in the next section.

Interface represented by level sets

When the crack surface is represented as a zero level set, the nodes chosen for enrichment can be determined from the nodal values of Υ and χ. For a bilinear quadrilateral element, let χ_{min} and χ_{max} be the minimum and maximum nodal values of χ on the nodes of the element. If $\chi_{min}\chi_{max} \leq 0$ and $\Upsilon_{min}\Upsilon_{max} \leq 0$, then the tip lies within the element and all the nodes of the element are enriched with near-tip asymptotic fields. Similarly, let ψ_{min} and ψ_{max} be the minimum and maximum nodal values of Υ on the nodes of an element. If $\chi < 0$ and $\Upsilon_{min}\Upsilon_{max} \leq 0$, then the crack cuts through the element and the nodes of the element are enriched with the Heaviside function. Figure 2.8 shows the normal level set Υ and the tangent level set χ for an edge cracked domain.

2.4.3 Integration

One potential solution for numerical integration is to partition the elements into subcells (triangles for example) aligned to the discontinuous surface in which the integrands are

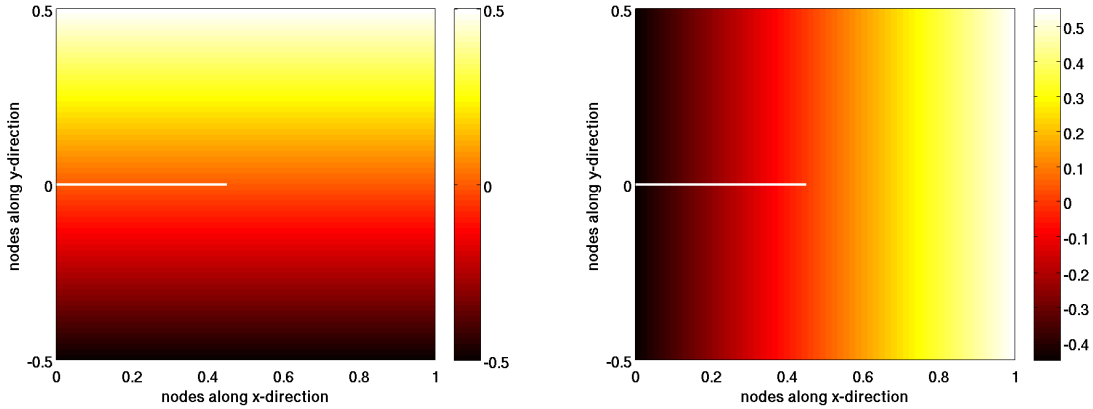

(a) Υ (b) χ

Figure 2.8: (a) Signed distance function Υ for the description of the crack surface and (b) second level set function χ to define the crack tip.

continuous and differentiable [15, 26]. Figure 2.9 shows a possible sub-triangulation commonly used in the XFEM. The purpose of sub-dividing into triangles is solely for the purpose of numerical integration and does not introduce new degrees of freedom.
Although the generation of quadrature subcells does not alter the approximation properties, it inherently introduces a 'mesh' requirement. The steps involved in this approach are:

- Split the element into subcells with the subcells aligned to the discontinuity surface. Usually the subcells are triangular
- Numerical integration is performed with the integration points from triangular quadrature.

The subcells must be aligned to the crack or to the interface and this is costly and less accurate if the discontinuity is curved [38]. Figures 2.10 and 2.11 illustrates necessary steps to determine the co-ordinates of the Gauß points over the enriched elements.

2.4.4 Enrichment schemes and applications of the XFEM

In this section, the common types of enrichment functions used in the XFEM in the context of solid mechanics are discussed. Tables 2.3 - 2.5 gives a summary of different enrichment functions proposed in the literature for different classes of problems.

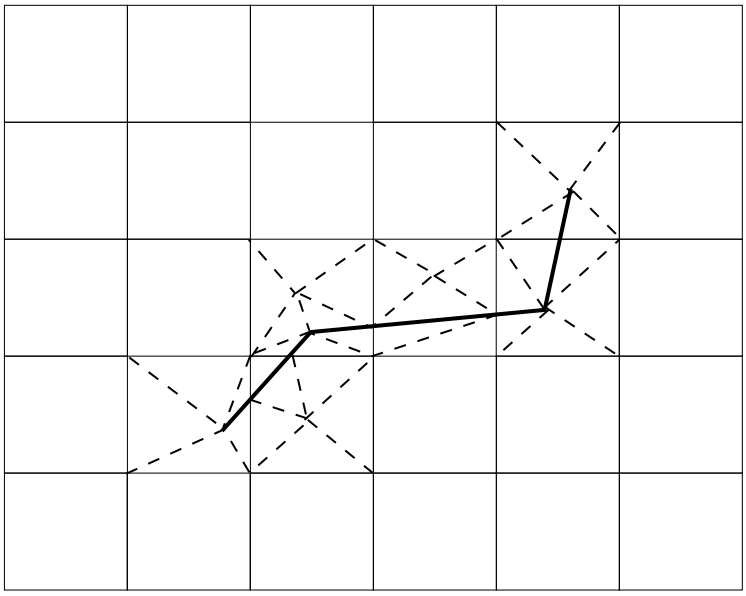

Figure 2.9: Sub-triangles used in numerical integration. Solid line represents the line of discontinuity and 'dashed' lines denotes the boundaries of the sub-cells.

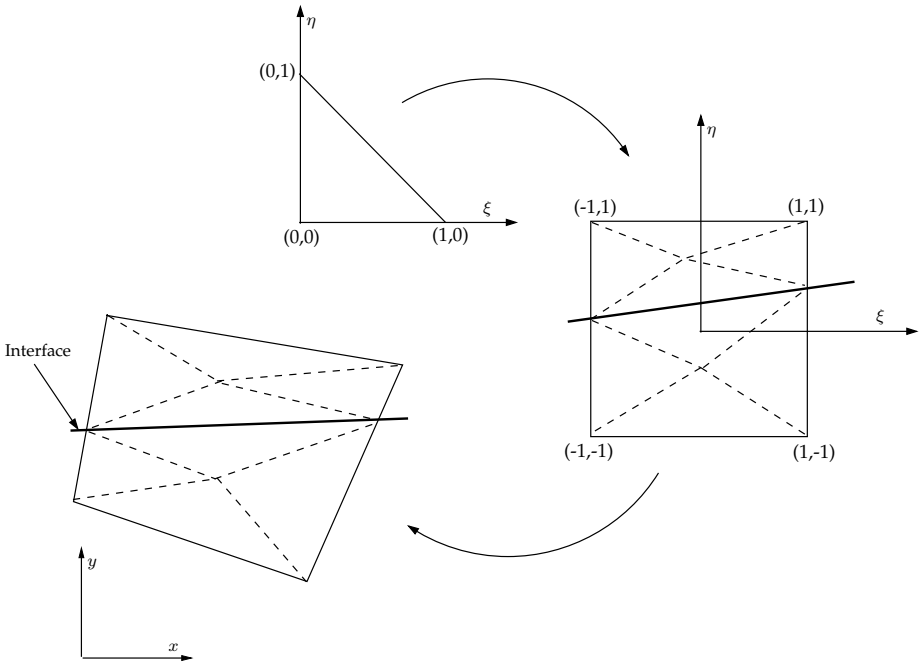

Figure 2.10: Physical element containing the crack tip is sub-divided into subcells (triangular subcells in this case). A quadrature rule on a standard triangular domain is used for the purpose of integration.

Table 2.3: Examples of choice of enrichment functions for fracture mechanics.

Kind of problem	**Displacement**	**Strain**	**Enrichment**
Crack body	Discontinuous	-	Heaviside: $\psi(\mathbf{x}) = \text{sign}(\phi(\mathbf{x}))$
Isotropic materials	Discontinuous for $\theta = \pm\pi$, $\sqrt{r}$ order	High gradient, $\frac{1}{\sqrt{r}}$ order	$\sqrt{r}\sin\frac{\theta}{2}$, $\sqrt{r}\cos\frac{\theta}{2}$, $\sqrt{r}\sin\frac{\theta}{2}\sin\theta$, $\sqrt{r}\cos\frac{\theta}{2}\sin\theta$.
Orthotropic materials [2]	Discontinuous	High gradient	$\sqrt{r}\cos(\frac{\theta_1}{2})\sqrt{g_1(\theta)}$, $\sqrt{r}\cos(\frac{\theta_2}{2})\sqrt{g_2(\theta)}$, $\sqrt{r}\sin(\frac{\theta_1}{2})\sqrt{g_1(\theta)}$, $\sqrt{r}\cos(\frac{\theta_2}{2})\sqrt{g_2(\theta)}$.
Cohesive crack [97]	Discontinuous	High gradient	$r\sin(\frac{\theta}{2})$, $r^{\frac{3}{2}}\sin(\frac{\theta}{2})$, $r^2\sin(\frac{\theta}{2})$.
Mindlin-Reissner plate [44]	Discontinuous	High gradient	Transverse displacements, $\sqrt{r}\sin(\frac{\theta}{2}), r^{3/2}\sin(\frac{\theta}{2})$, $r^{\frac{3}{2}}\cos(\frac{\theta}{2}), r^{\frac{3}{2}}\sin(\frac{3\theta}{2}), r^{\frac{3}{2}}\cos(\frac{3\theta}{2})$; Rotation displacements $\sqrt{r}\sin(\frac{\theta}{2})$, $\sqrt{r}\cos(\frac{\theta}{2})$, $\sqrt{r}\sin(\frac{\theta}{2})\sin\theta$, $\sqrt{r}\cos(\frac{\theta}{2})$,$\sqrt{r}\cos(\frac{\theta}{2}\sin\theta)$.
Kirchhoff-Love plate [80]	Discontinuous	High gradient	$r^{\frac{3}{2}}\sin(\frac{3\theta}{2})$, $r^{\frac{3}{2}}\cos(\frac{\theta}{2})$, $r^{\frac{3}{2}}\sin(\frac{3\theta}{2})$, $r^{\frac{3}{2}}\cos(\frac{\theta}{2})$.
Incompressible materials[84]	Discontinuous	High gradient	$\frac{1}{\sqrt{r}}\sin(\frac{\theta}{2})$, $\frac{1}{\sqrt{r}}\cos(\frac{\theta}{2})$.
Plastic materials [50]	Discontinuous	High gradient	$r^{\frac{1}{n+1}}\sin(\frac{\theta}{2})$, $r^{\frac{1}{n+1}}\cos(\frac{\theta}{2})$, $r^{\frac{1}{n+1}}\sin(\frac{\theta}{2})\sin(\theta)$, $r^{\frac{1}{n+1}}\cos(\frac{\theta}{2})\sin(\theta)$, $r^{\frac{1}{n+1}}\sin(\frac{\theta}{2})\sin(3\theta)$, $r^{\frac{1}{n+1}}\cos(\frac{\theta}{2})\sin(3\theta)$.
Thermo-elastic material [48]	Discontinuous	High gradient	Temprature field : $T = -\frac{K_T}{k}\sqrt{\frac{2r}{\pi}}\cos(\frac{\theta}{2})$; Flux : $\mathbf{q} = \frac{K_T}{\sqrt{2\pi r}}\begin{pmatrix}\cos(\frac{\theta}{2})\\ \sin(\frac{\theta}{2})\end{pmatrix}$.

Table 2.4: Examples of choice of enrichment functions for fracture mechanics.

Kind of problem	**Displacement**	**Strain**	**Enrichment**
Crack aligned to the interface of a material interface [74]	Discontinuous	High gradient	$\sqrt{r}\cos(\epsilon \log r)\mathrm{e}^{-\epsilon\theta}\sin\frac{\theta}{2}$, $\sqrt{r}\cos(\epsilon \log r)\mathrm{e}^{\epsilon\theta}\sin\frac{\theta}{2}\sin\theta$, $\sqrt{r}\cos(\epsilon \log r)\mathrm{e}^{-\epsilon\theta}\cos\frac{\theta}{2}$, $\sqrt{r}\cos(\epsilon \log r)\mathrm{e}^{\epsilon\theta}\cos\frac{\theta}{2}\sin\theta$, $\sqrt{r}\cos(\epsilon \log r)\mathrm{e}^{\epsilon\theta}\sin\frac{\theta}{2}$, $\sqrt{r}\sin(\epsilon \log r)\mathrm{e}^{\epsilon\theta}\sin\frac{\theta}{2}\sin\theta$, $\sqrt{r}\cos(\epsilon \log r)\mathrm{e}^{\epsilon\theta}\cos\frac{\theta}{2}$, $\sqrt{r}\sin(\epsilon \log r)\mathrm{e}^{\epsilon\theta}\cos\frac{\theta}{2}\sin\theta$, $\sqrt{r}\sin(\epsilon \log r)\mathrm{e}^{-\epsilon\theta}\sin\frac{\theta}{2}$, $\sqrt{r}\cos(\epsilon \log r)\mathrm{e}^{-\epsilon\theta}\sin\frac{\theta}{2}\sin\theta$, $\sqrt{r}\sin(\epsilon \log r)\mathrm{e}^{\epsilon\theta}\sin\frac{\theta}{2}$, $\sqrt{r}\sin(\epsilon \log r)\mathrm{e}^{\epsilon\theta}\sin\frac{\theta}{2}\sin\theta$.
Piezoelastic materials [14, 157]	Discontinuous	High gradient	$\sqrt{r}f_1(\theta)$, $\sqrt{r}f_2(\theta)$, $\sqrt{r}f_3(\theta)$, $\sqrt{r}f_4(\theta)$, $\sqrt{r}f_5(\theta)$, $\sqrt{r}f_6(\theta)$.
Magnetoelectroelastic materials [129]	Discontinuous	High gradient	$\sqrt{r}\rho_1\cos(\frac{\theta_1}{2})$, $\sqrt{r}\rho_2\cos(\frac{\theta_2}{2})$, $\sqrt{r}\rho_3\cos(\frac{\theta_3}{2})$, $\sqrt{r}\rho_4\cos(\frac{\theta_4}{2})$, $\sqrt{r}\rho_1\cos(\frac{\theta_1}{2})$, $\sqrt{r}\rho_2\cos(\frac{\theta_2}{2})$, $\sqrt{r}\rho_3\cos(\frac{\theta_3}{2})$, $\sqrt{r}\rho_4\cos(\frac{\theta_4}{2})$.
Complex cracks [77]	Discontinuous	High gradient	$\Delta H(\xi) = 0$
Hydraulic fracture [81]	Discontinuous	High gradient	$r^\lambda\cos(\lambda\theta)$, $r^\lambda\sin(\lambda\theta)$, $r^\lambda\sin(\theta)\sin(\lambda\theta)$, $r^\lambda\sin(\theta)\cos(\lambda\theta)$.
Crack tip in polycrystals [94]	Discontinuous	High gradient	$\Re[r(\mathbf{x})\Psi(\Theta(\mathbf{x}))]$

Table 2.5: Examples of choice of enrichment functions for other applications.

Kind of problem	**Displacement**	**Strain**	**Enrichment**
Bi-material	Continuous	Discontinuous	Ramp: $\psi(\mathbf{x}) = \lvert\phi(\mathbf{x})\rvert$
Dislocations [64, 65, 152]	Discontinuous	Discontinuous	For the edge component: $\frac{\mathbf{b}^\alpha \cdot \mathbf{e}_t}{2\pi}[(\tan^{-1}(\frac{y'}{x'}) + \frac{x'y'}{2(1-\nu)(x'^2+y'^2)})]\mathbf{e}_t$, $\frac{\mathbf{b}^\alpha \cdot \mathbf{r}_t}{2\pi}[-(\frac{1-2\nu}{4(1-\nu)}\ln(x'^2+y'^2) + \frac{x'^2-y'^2}{4(1-\nu)(x'^2+y'^2)})]\mathbf{e}_n$; For the screw component: $\frac{\mathbf{b}^\alpha \cdot (\mathbf{e}_t \times \mathbf{e}_n)}{2\pi}\tan^{-1}(\frac{y'}{x'})(\mathbf{e}_t \times \mathbf{e}_n)$.
Topology optimization [20]	Continuous	Discontinuous	Ramp: $\psi(\mathbf{x}) = \lvert\phi(\mathbf{x})\rvert$
Stokes flow [81]	-	-	Velocity field: $u_1 = \frac{1}{r^2}[(R^2-r^2)\cos^2\theta + r^2\ln(r/R) + (1/2)(r^2-R^2)]$, $v_1 = \frac{1}{r^2}[(R^2-r^2)\sin\theta\cos\theta]$, $u_2 = \frac{1}{r^2}[2(R^4-r^4)\cos^2\theta + 3r^4 - 2R^2r^2 - R^4]$, $v_2 = \frac{1}{r^2}[2(R^4-r^4)\sin\theta\cos\theta]$, $u_3 = \frac{1}{r^2}[(r^2-R^2)\sin\theta\cos\theta]$, $v_3 = \frac{1}{r^2}[(R^2-r^2)\cos^2\theta - r^2\ln(r/R + (1/2)(r^2-R^2))]$, $u_4 = \frac{1}{r^2}[2(r^4-R^4)\sin\theta\cos\theta]$, $v_4 = \frac{1}{r^2}[2(r^4-R^4)\cos^2\theta - r^4 + 2R^2r^2 - R^4]$; Pressure field: $p_1 = -\frac{2\cos\theta}{r}$, $p_2 = 8r\cos\theta$, $p_3 = \frac{2\sin\theta}{r}$, $p_4 = -8r\sin\theta$.
Solidification [40]	-	-	Ramp: $\psi(\mathbf{x}) = \lvert\phi(\mathbf{x})\rvert$.
Fluid-structure interaction [61]	Continuous	Discontinuous	Heaviside: $\psi(\mathbf{x}) = \text{sign}(\phi(\mathbf{x}))$.

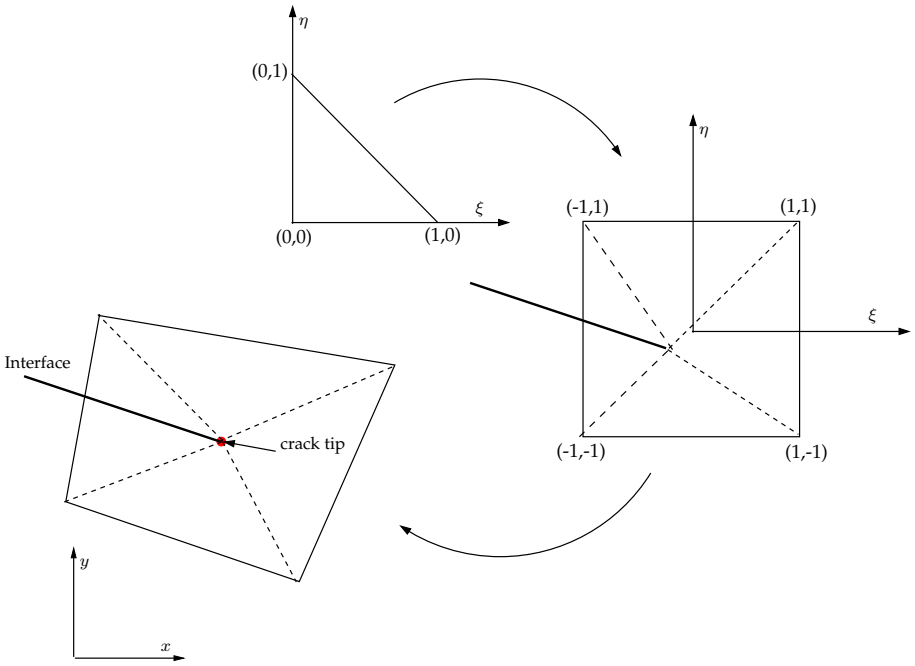

Figure 2.11: Physical element containing the crack tip is sub-divided into subcells (triangular subcells in this case). A quadrature rule on a standard triangular domain is used for the purpose of integration.

Weak discontinuities

For weak discontinuities, two types of enrichment functions are used in the literature. One choice for the enrichment function is the absolute value of the level-set function (c.f. Section § 2.4.1) [19, 146][g]

$$\psi_{\text{abs}}(\mathbf{x}) = |\phi(\mathbf{x})| \tag{2.28}$$

The other choice was proposed by Moës *et al.,* [99] as:

$$\psi(\mathbf{x}) = \sum_{I \in \mathcal{N}^c} |\phi_I| N_I(\mathbf{x}) - |\sum_{I \in \mathcal{N}^c} \phi_I N_I(\mathbf{x})| \tag{2.29}$$

The main advantage of the above enrichment function is that this enrichment function is non-zero only in the elements that are intersected by the discontinuity surface. Figure 2.12 shows the two choices of enrichment functions in the 1D case. For two- and three- dimensional problems, the enrichment function proposed by Moës *et al.,* [99] is a ridge centered on the interface and has zero value on the elements which are not crossed by the interface.

[g] A level set of a real-valued function f of n variables is a set of the form $\{(x_1, x_2, \cdots, x_n) | f(x_1, x_2, \cdots, x_n) = c\}$, where c is a constant.

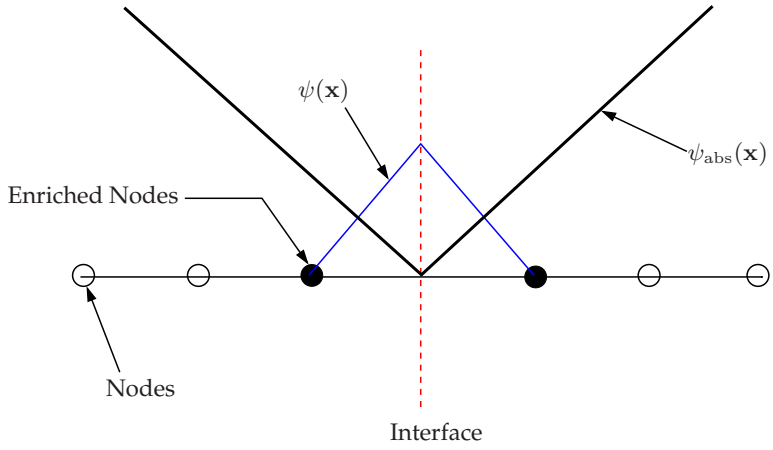

Figure 2.12: Weak discontinuity: different choices of enrichment functions

Strong discontinuities and Singularity: Isotropic materials

Strong discontinuity To model a strong discontinuity, the enrichment function ϑ in Equation (2.23) is chosen to be the Heaviside function H:

$$\vartheta(\mathbf{x}) = H(\mathbf{x}) = \begin{cases} +1 & \mathbf{x} \text{ above the crack face} \\ 0 & \mathbf{x} \text{ below the crack face} \end{cases} \tag{2.30}$$

The other choice of enrichment function is the sign of the level-set function ϕ:

$$\vartheta(\mathbf{x}) = \text{sign}(\phi(\mathbf{x})) = \begin{cases} +1 & \mathbf{x} \text{ above the crack face} \\ -1 & \mathbf{x} \text{ below the crack face} \end{cases} \tag{2.31}$$

These enrichment functions have been proposed in [15, 98]. Iarve [75] proposed a modification to the Heaviside function that eliminates the need to sub-triangulate for the purpose of numerical integration (see Section § 2.4.5). Figure 2.13 shows the plot of the Heaviside function for a straight and a kinked crack.

Singular fields For isotropic materials, the near-tip function, Ξ_α in Equation (2.23) is denoted by $\{B_\alpha\}_{1\leq\alpha\leq4}$ and is given by:

$$\{B_\alpha\}_{1\leq\alpha\leq4}(r,\theta) = \sqrt{r}\left\{\sin\frac{\theta}{2}, \cos\frac{\theta}{2}, \sin\theta\sin\frac{\theta}{2}, \sin\theta\cos\frac{\theta}{2}\right\}. \tag{2.32}$$

where (r,θ) are the crack tip polar coordinates. Figure 2.14 shows the near-tip asymptotic fields. Note that the first function in Equation (2.32) is discontinuous across the crack surface.

Remark: The above set of enrichment functions predict global displacements accurately, but

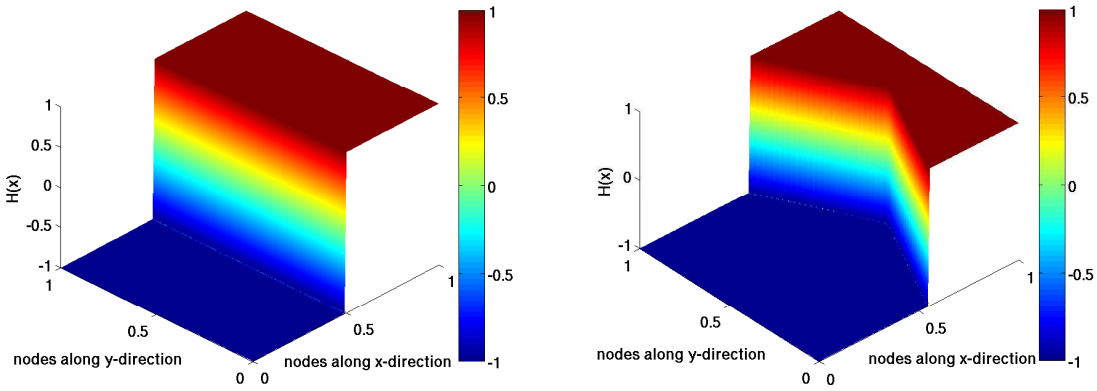

(a) Straight crack (b) Kinked crack

Figure 2.13: Heaviside function to capture strong discontinuities.

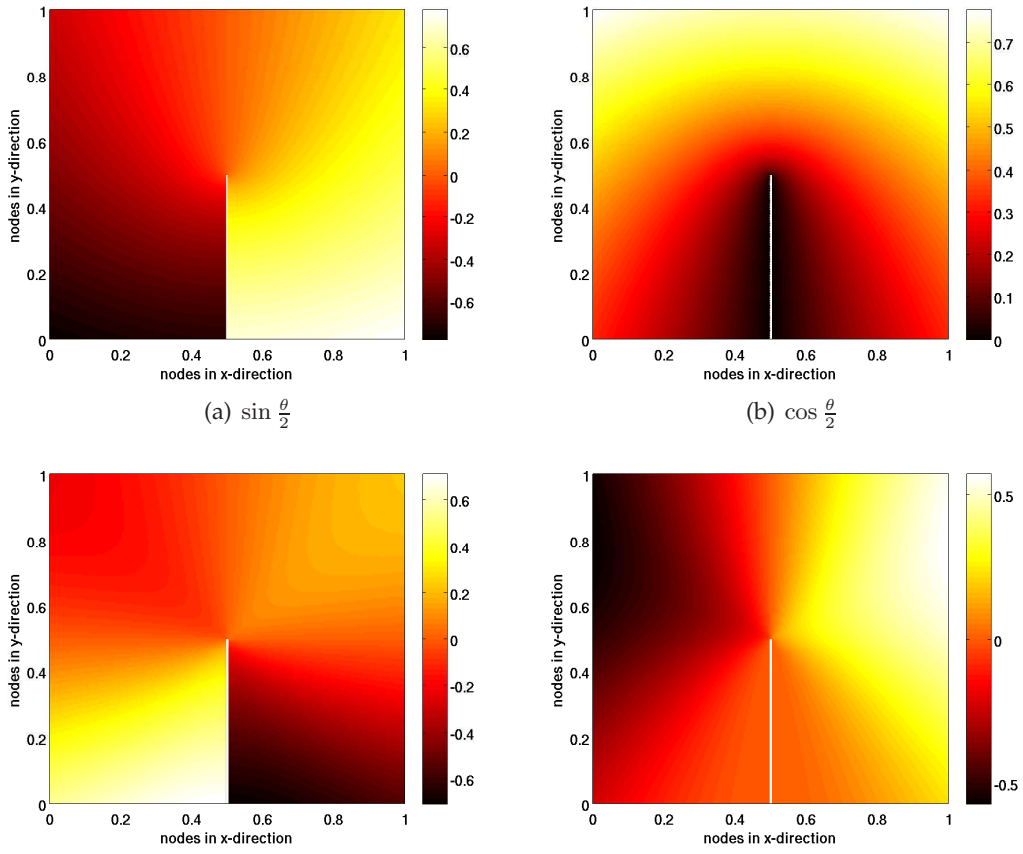

(a) $\sin\frac{\theta}{2}$ (b) $\cos\frac{\theta}{2}$

(c) $\sin\theta\sin\frac{\theta}{2}$ (d) $\sin\theta\cos\frac{\theta}{2}$

Figure 2.14: Near tip asymptotic fields. Note that the function $\sin\frac{\theta}{2}$ is discontinuous across the crack surface. The white line denotes the discontinuity line. The crack tip is located at (0.5,0.5).

requires a fine discretization to capture the displacements in the vicinity of the crack tip. Xiao and Karihaloo [162, 164] proposed an alternate approach to enrich the FE approximation with not only the first term but also the higher order terms of the linear elastic crack tip asymptotic field. Apart from improving the local behaviour in the vicinity of the crack tip, the approach also can determine the stress intensity factors directly without extra post-processing.

Orthotropic materials

For orthotropic materials, the asymptotic functions given by Equation (2.32) have to be modified because the material property is a function of material orientation. Asadpoure and Mohammadi [2, 3] proposed special near-tip functions for orthotropic materials as:

$$\{B_\alpha\}_{1\leq\alpha\leq4}(r,\theta) = \sqrt{r}\left\{\cos\frac{\theta_1}{2}\sqrt{g_1(\theta)}, \cos\frac{\theta_2}{2}\sqrt{g_2(\theta)}, \sin\frac{\theta_1}{2}\sqrt{g_1(\theta)}, \sin\frac{\theta_2}{2}\sqrt{g_2(\theta)}\right\} \quad (2.33)$$

where (r,θ) are the crack tip polar coordinates. The functions $g_i(i=1,2)$ and $\theta_i(i=1,2)$ are given by:

$$\begin{aligned} g_j(\theta) &= \left(\cos^2\theta + \frac{\sin^2\theta}{e_j^2}\right), \quad j=1,2 \\ \theta_j &= \arctan\left(\frac{\tan\theta}{e_j}\right). \quad j=1,2 \end{aligned} \quad (2.34)$$

where $e_j(j=1,2)$ are related to material constants, which depend on the orientation of the material [2]. Figure 2.15 shows the near-tip asymptotic fields in case of orthotropic material with material orientation, $\theta = 45^\circ$. The PUM has been extended to study matrix failures and debonding in thin fibre composites [125, 132].

Cohesive cracks

In cohesive cracks, the stresses and the strains are no longer singular and the step enrichment alone is suitable for the entire crack. Due to this, the XFEM approximation cannot treat crack tips or fronts that lie within the element and thus the crack is virtually extended to the next element edge. Wells and Sluys [156] used the step function as an enrichment function to treat cohesive cracks. Moës and Belytschko [97] used one of the following enrichment functions for two dimensional cohesive crack tips:

$$\{B_\alpha\}(r,\theta) = \left\{r\sin\frac{\theta}{2}, \sqrt[3]{r}\sin\frac{\theta}{2}, r^2\sin\frac{\theta}{2}\right\} \quad (2.35)$$

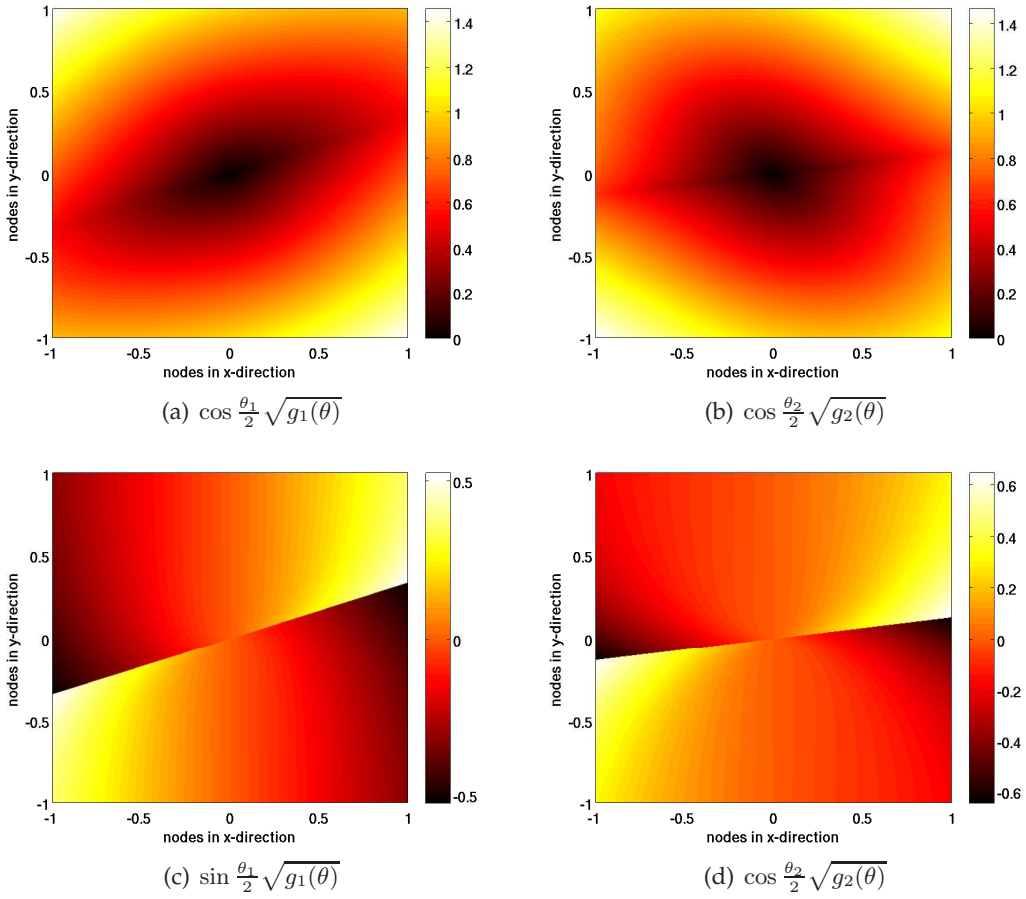

(a) $\cos\frac{\theta_1}{2}\sqrt{g_1(\theta)}$ (b) $\cos\frac{\theta_2}{2}\sqrt{g_2(\theta)}$

(c) $\sin\frac{\theta_1}{2}\sqrt{g_1(\theta)}$ (d) $\cos\frac{\theta_2}{2}\sqrt{g_2(\theta)}$

Figure 2.15: Near tip asymptotic fields for orthotropic material with material orientation, $\theta = 45°$. The crack tip is located at (0.5,0.5).

Based on the generalized Heaviside function, Zi and Belytschko [165] proposed a new crack tip element for modelling cohesive crack growth. This method overcame the difficulty and provided a method for the crack tips to lie within the element. Rabczuk *et al.,* [124] developed a crack tip element for the phantom-node method to model cracks independent of the underlying mesh. The main idea is to use reduced integrated finite elements with hourglass control. With this method, the crack tip can be modelled within an element. This was an advancement to the earlier work by Song *et al.,* [134] who used the phantom node method to simulate dynamic crack growth and shear band propagation. In their approach, the crack has to cross an entire element. Very recently, an isogeometric approach was combined with XFEM to model cohesive cracks in [154].

Dynamic cracks

Réthoré *et al.,* [126] simulated dynamic propagation of arbitrary 2D cracks using an enrichment strategy for time-dependent problems. By adding phantom nodes and superposing elements on the original mesh, Song *et al.,* [134] proposed a new method for modelling dynamic crack and shear band propagation. From the numerical studies, it was observed that the method exhibits almost no mesh dependence once the mesh is sufficiently refined to resolve the relevant physics of the problem. This method was based on the Hansbo and Hansbo approach [69]. XFEM has been applied to concurrent continuum-atomistic simulations of cracks and dislocations by Gracie and Belytschko [67] and Aubertin *et al.,* [6, 7].

Dislocations

Ventura *et al.,* [152] applied the PUM concept for the solution of edge dislocations. As in cracks, the dislocation solutions are characterized by discontinuities and singular points. Gracie *et al.,* [64] used the following approximation for modelling the dislocations:

$$\mathbf{u}^h(\mathbf{x}) = \sum_{I \in \mathcal{N}^{\text{fem}}} N_I(\mathbf{x})\mathbf{q}_I + \mathbf{b} \cdot \sum_{J \in \mathcal{N}^c} N_J(\mathbf{x}) \cdot \psi_{\text{step}}(\mathbf{x}) \tag{2.36}$$

where $\mathbf{b}$ is the Burgers vector, which is a known quantity and closed form solutions are used for enrichment function. Note that Equation (2.36) does not introduce additional unknowns. At the core of the dislocation, the step function ψ_{step} is modified and the rest of the dislocation is modelled by a step function. Gracie *et al.,* [67] computed the enrichment functions by coupling the XFEM with atomistic simulations. This eliminated the need for closed form solutions, which are available only for isotropic materials.

2.4.5 Difficulties in the XFEM

As the method permits arbitrary functions to be incorporated in the FEM approximation basis, the PU enrichment leads to greater flexibility in modelling moving boundary problems, without changing the underlying mesh (see Figure 2.1), while the set of enrichment functions evolve (and/or their supports) with the interface geometry. Although XFEM is robust and applied to a wide variety of moving boundary problems and interface problems, the flexibility provided by this class of methods also leads to associated difficulties:

- **Singular and discontinuous integrands** When the approximation is discontinuous or non-polynomial in an element, special care must be taken to numerically integrate over enriched elements.
- **Blending the different partitions of unity** The local enrichment used in the conventional element leads to oscillations in the results over the elements that are partially enriched.
- **Poor convergence rate** In the conventional XFEM, the obtained convergence error of XFEM remains only in $\sqrt{h}$ [136], when linear finite elements are used, where h is the element size.
- **Stress intensity factor computation** XFEM requires a post-processing stage to extract the stress intensity factors (SIFs) from the computed displacement field. Although not a major difficulty, but this particular point has been addressed by some researchers.
- **Ill-conditioning** The addition of enrichment functions to the FE approximation basis could result in a severely ill-conditioned stiffness matrix.
- **Additional unknowns** With extrinsic enrichment, additional degrees of freedom (dofs) are introduced and the number of additional dofs depends on the number of enrichment functions and the number of such enrichments required.

Blending the different partitions of unity

The regions of high strain gradients or discontinuities are local phenomena. To capture such local phenomena, enrichment functions are added to the FE approximation basis locally (c.f. Section §2.4). In the local enrichment, only a 'small' set of nodes are enriched and this leads to three classification of elements, viz. reproducing (fully enriched), standard and blending elements (partially enriched) (see Figure 2.5). The partition of unity is satisfied in standard elements and in reproducing elements, while it is not satisfied in blending elements. Due to this, the enrichment function cannot be reproduced and some unwanted terms appear in the approximation (see Section 2.5, where the problem with blending element is discussed

with numerical examples). This pathological behaviour has been studied in great detail in the literature:

- Assumed strain blending elements: By using an enhanced strain for the blending elements, Chessa *et al.,* [41] and Gracie *et al.,* [66] proposed new blending elements for crack tip functions and weak discontinuities, respectively.
- Direct coupling of enriched and standard regions: Difficulties in bending elements were circumvented by coupling the standard elements and reproducing elements directly [66, 79]. The continuity between the standard elements and reproducing elements were enforced either point wise [79] or along the interface [35] by via Lagrange multipliers.
- Corrected or Weighted XFEM: Fries [58] suggested that by multiplying the enrichment function with a ramp function, the enrichment vanishes in the elements where only some of the nodes are enriched. The corrected or weighted XFEM approximation is given by

$$\mathbf{u}^h(\mathbf{x}) = \underbrace{\sum_{I\in\mathcal{N}^{\text{fem}}} N_I(\mathbf{x})\mathbf{q}_I}_{\text{Std. FE approx}} + \underbrace{\sum_{J\in\mathcal{N}^{\text{fem}}} N_J(\mathbf{x}) \cdot \underbrace{R(\mathbf{x})}_{\text{Ramp Function}} \cdot[\varrho(\mathbf{x}) - \varrho(\mathbf{x}_J)]\mathbf{a}_J}_{\text{Enrichment}} \tag{2.37}$$

  where $R(\mathbf{x})$ is the ramp function that equals 1 over enriched elements and linearly decreases to 0 in the blending elements.
- Fast integration: Ventura *et al.,* [153] suggested a non-linear form for the ramp function $R(\mathbf{x})$. Given a point $\mathbf{x} \in \Omega$, let $d = d(\mathbf{x})$ be the signed distance function from $\mathbf{x}$ to Γ. The function $R(d)$ is defined by:

$$R(d) = \begin{cases} 1 & 0 \leq |d| \leq d_i \\ (1-g)^n & d_i < |d| < d_e \\ 0 & |d| > d_e \end{cases} \tag{2.38}$$

  where d_i and d_e are chosen such that $R = 1$ for $|d| \leq d_i$ and $R = 0$ for any $|d| > d_e$, n is a positive integer and g is the linear ramp function given by:

$$g = \frac{|d| - d_i}{d_e - d_i} \tag{2.39}$$

  Figure 2.16 shows the choice of two ramp functions to avoid blending problem.

- Hybrid Crack Element-XFEM: By using a hybrid crack element (HCE) in the crack tip region, Xiao and Karihaloo [162, 164] proposed a modification to the conventional XFEM. This resulted in not only estimating the SIFs direction, but also avoided blending problems.
- Enhanced blending elements: Tranacón *et al.,* [150] proposed to use hierarchical shape functions for blending elements and showed that this permits compensating for the unwanted terms in the interpolation.
- Spectral functions: Legay *et al.,* [83] used the XFEM formalism within spectral FEs for modelling strong and weak discontinuities. Their study illustrated that there is no need to employ blending correction for higher order spectral elements if the shape functions used for the local partition of unity are at least one order lower than those of used for the basic approximation. But with lower order spectral element, the blending problem is not alleviated.

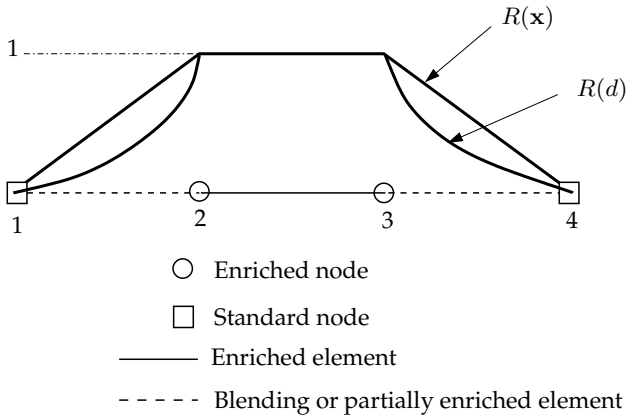

Figure 2.16: Discretized domain in one dimension illustrates reproducing and blending elements. The figure illustrates the choice of ramp function suggested by Fries [58] and Ventura *et al.,* [153]. With $n = 1$ in Equation (2.38) yields a linear ramp function.

Remark: Corrected or weighted XFEM shares similarities with the work of Benzley [22], who proposed to use a function that equals 1 on boundaries adjacent to 'enriched' elements and equals 0 on boundaries adjacent to 'standard' elements, i.e., the value of the function decreases from 1 to 0 in the blending elements (c.f. Section 2.3.2).

Remark: Ventura *et al.,* [153] used a non-linear form for the ramp function. This method shares some similarities with the work of Strang and Fix [136, 137] who used polynomials to merge the coefficients of singular functions smoothly into zero on the boundary of standard elements (c.f. Section 2.3.2).

Numerical integration for enriched approximations

In this section, a brief discussion on various attempts to improve the numerical integration is presented. An additional difficulty related to numerical integration is the requirement to integrate singular functions involving the derivatives of the shape and enrichment functions (which are singular at the tip in LEFM) [79]. This will be revisited in the following sections within the context of strain smoothing, discussed in Chapter 3, Section 3.2.2.

Polar integration The singular functions commonly used in the XFEM requires a high density of integration points. By using polar integration, Laborde *et al.,* [79] and Béchet *et al.,* [13] showed that a concentration of integration points in the vicinity of the singularity improves the results significantly. This process eliminates the singular terms from the quadrature. The idea is to sub-divide into triangles such that each triangle has one node at the singularity. Instead of using triangular quadrature, tensor-product type Gauß points in a quadrilateral reference element are mapped into each triangle such that two nodes of the quadrilateral coincide at the singularity node of each triangle. Figure 2.18 shows the procedure. The proposed technique is well suited for point singularities (for example in 2D), but in the case of 3D, such a mapping is not trivial [13, 79]. Park *et al.,* [118] extended the mapping method introduced by Nagarajan and Mukherjee [108] in 2D to 3D to integrate singular integrands in 2D and 3D. The 2D mapping is given by:

$$T_M : (\rho, \theta) \mapsto (\xi, \eta) \tag{2.40}$$

where, $\xi = \rho \cos^2 \theta$ and $\eta = \rho \sin^2 \theta$. The inverse mapping ($T_M^{-1}$) transforms a right triangle into a rectangle.

Generalized Gaussian quadrature A quadrature in $\mathbb{R}^d$ is a formula of the form

$$\int_\Omega w(\mathbf{x}) f(\mathbf{x})\, d\mathbf{x} \approx \sum_{i=1}^{n} w_i f(\mathbf{x}_i) \tag{2.41}$$

where Ω is the integration region in $\mathbb{R}^d$, f is an integrand defined in Ω, and w is the weight function. Table 2.6 lists the different quadrature rules based on the choice of weight function and the interval over which the integration is performed. The points $\mathbf{x}_i \in \mathbb{R}^d$ are typically called quadrature nodes, and w_i quadrature weights. It can be shown [121] that the evaluation points are just the roots of a polynomial belonging to a class of orthogonal polynomials.
By using the point-elimination scheme with Newton's method, a new quadrature rule was proposed in [161] for triangular and square domains. The point-elimination scheme was

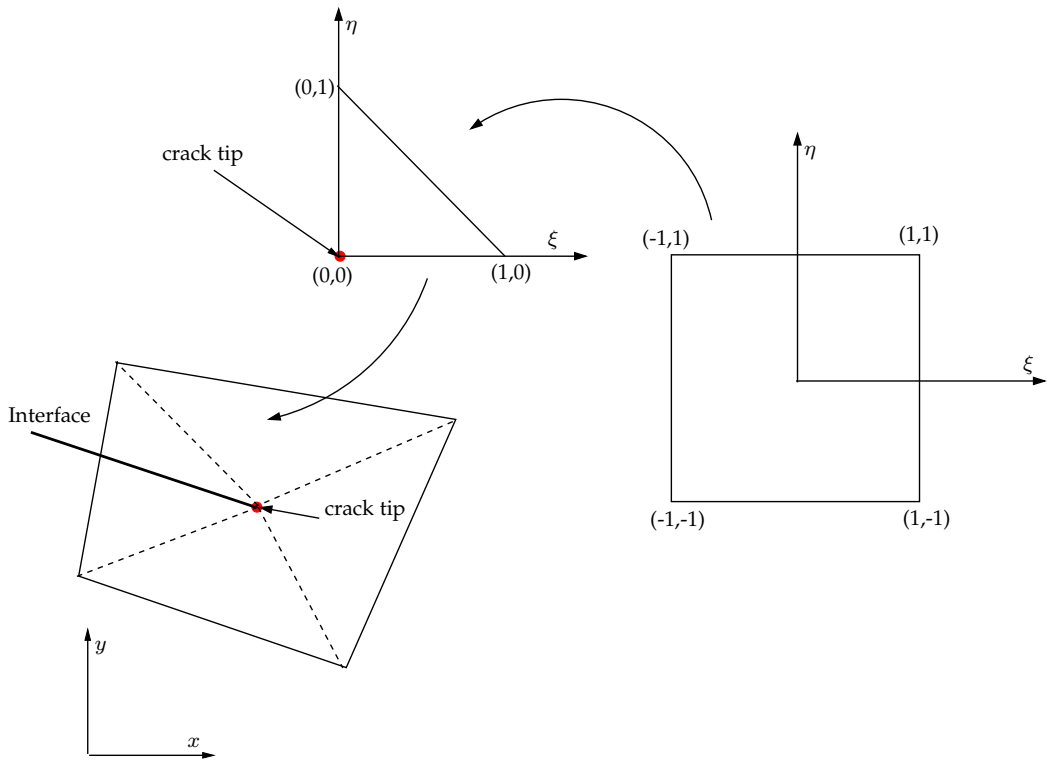

Figure 2.17: Physical element containing a singularity is sub-divided such that each triangular sub-division contains the singular point as one of its nodes. Standard Gauß points from a parent quadrilateral element are projected onto a triangular element.

Table 2.6: Different quadrature rules based on the choice of weight function and the interval over which the integration is performed.

Interval	$w(\mathbf{x})$	Orthogonal Polynomial
$[-1,1]$	1	Legendre Polynomials
$(-1,1)$	$(1-x)^{\alpha}(1+x)^{\beta}, \alpha,\beta >$ -1	Jacobi Polynomials
$(-1,1)$	$\frac{1}{\sqrt{1-x^2}}$	Chebyshev Polynomials (first kind)
$[-1,1]$	$\sqrt{1-x^2}$	Chebyshev Polynomials (second kind)
$[0,\infty)$	e^{-x}	Laguerre Polynomials
$(-\infty,\infty)$	e^{-x^2}	Hermite Polynomials

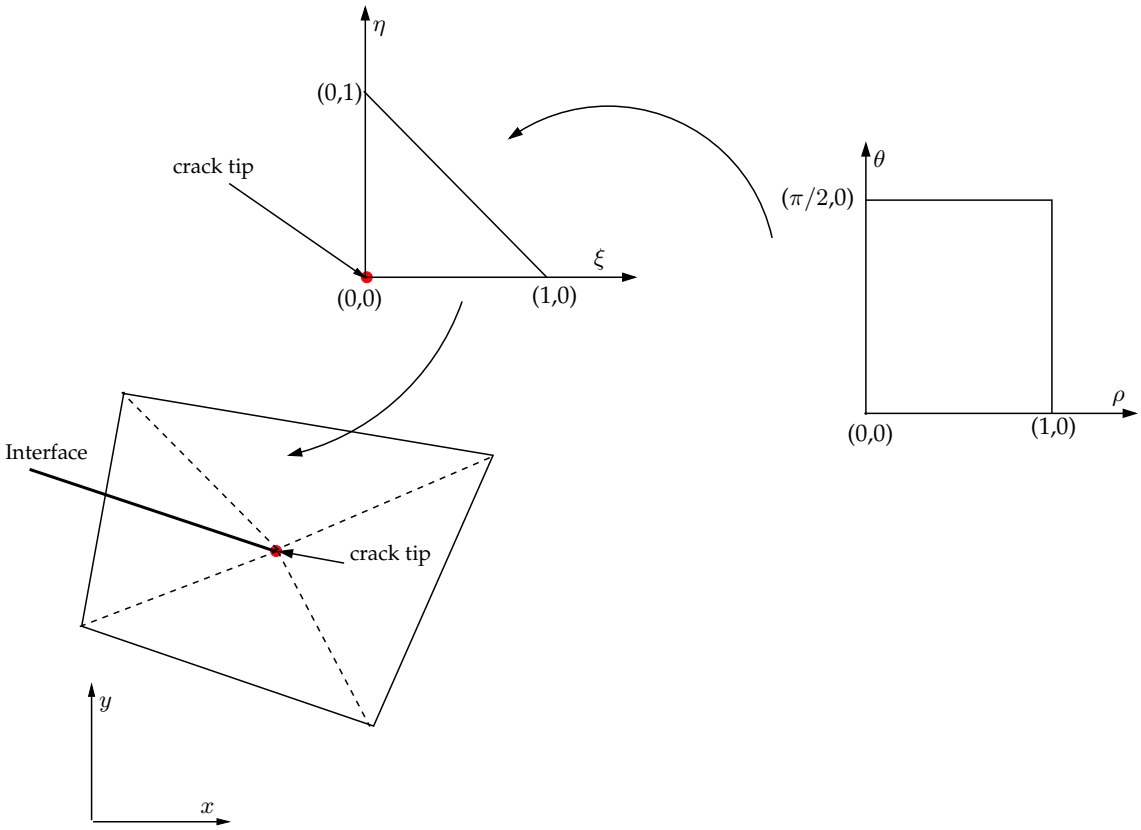

Figure 2.18: Physical element containing a singularity is sub-divided such that each triangular sub-division contains the singular point as one of its nodes. Each sub-triangle is mapped onto a standard triangle in the area co-ordinate system (ξ, η) with crack tip assigned as the origin of the co-ordinate system. Next the triangle is transformed into a rectangular co-ordinate (ρ, θ) system.

later applied to devise efficient quadrature rules on arbitrary polygons [102] and then extended to integrate polynomials and discontinuous functions on irregular convex polygons and polyhedra [103, 104, 105]. They called the scheme as 'Generalized Gaussian quadrature' [133]. The numerical algorithm used to compute the quadrature using point-elimination is [105]:

- Find an initial quadrature[h] $\{\mathbf{x}_i, w_i\}$ for the region of integration Ω, the class of basis functions and appropriate weights that satisfies Equation (2.41).
- Eliminate one of the nodes (e.g., one with the minimum significant factor).
- Solve Equation (2.41) iteratively until convergence is attained. The resulting quadrature now has one less node than the initial one. Continue the above until no additional nodes can be removed. This is the final quadrature.

Equivalent polynomials One of the earlier attempts to improve the integration over enriched elements was by Ventura [151] who focused on the elimination of quadrature sub-cells commonly employed to integrate strongly or weakly discontinuous and non-polynomial functions present in the enriched FE approximation. The objective is to find a polynomial that can reproduce *exactly* the same result as that obtained by the sub-triangulation. The new polynomial is called 'equivalent' polynomial. This facilitates the use of standard Gaussian quadrature over the entire element, but the definition of 'equivalent' polynomials depends on the enrichment and element type. The proposed method is exact for triangular and tetrahedral elements, but for quadrilateral elements, when the opposite sides are not parallel, an additional approximation is introduced.

Higher order shape functions With the conventional Heaviside function, the integration over enriched elements is done by sub-triangulating the intersected domain. Iarve [75] by using a polynomial B-spline approximation, proposed a modification to the Heaviside function. The main advantage is that it does not require modification of the integration domain and the implementation involves integration of the products of the original shape function and its derivatives.

Other integration schemes The elements for which all nodes of the element are enriched, i.e., reproducing elements, Ventura *et al.,* [153] proposed a contour integration for crack and dislocation enrichments in the framework of linear elasticity. In case of 2D, the domain integrals are transformed to contour integrals and in case of 3D, the surface integrals are transformed to domain integrals. The method is only applicable to reproducing elements. Adaptive integration for elements with singularities was used in [90, 138, 163].

[h] The initial quadrature could be the conventional Gaussian quadrature

Improving the convergence rate and direct estimation of SIFs

With the addition of singular fields to the finite element basis, the underlying physics of the problem is captured, but the obtained convergence rate remains in $\sqrt{h}$ in the conventional XFEM. The loss of accuracy in the XFEM occurs in the transition layer between enriched zone and the rest of the domain. Also, to extract the SIFs from the computed displacement field, post-processing is required. This section summarizes the modifications done to the conventional XFEM to improve the convergence rate and to evaluate directly and accurately the SIF.

Higher order XFEM Béchet *et al.,* [13] and Laborde *et al.,* [79] independently proposed a modification to the conventional XFEM approximation in order to improve the convergence rates in the classical XFEM. Béchet *et al.,* called the resulting modification as 'geometric enrichment', while Laborde *et al.,* called it as 'fixed-area enrichment'. In classical XFEM, only the nodes of the element that contains the crack tip are enriched; due to this, as the mesh size h approaches 'zero', the influence of the additional basis functions vanishes. The main idea behind this strategy is to enrich a whole fixed area around the crack tip. Figure 2.19 shows a schematic representation of the conventional XFEM and the XFEM with 'geometric' enrichment or 'fixed-area' enrichment. It was shown in [79] that the convergence rate is improved.

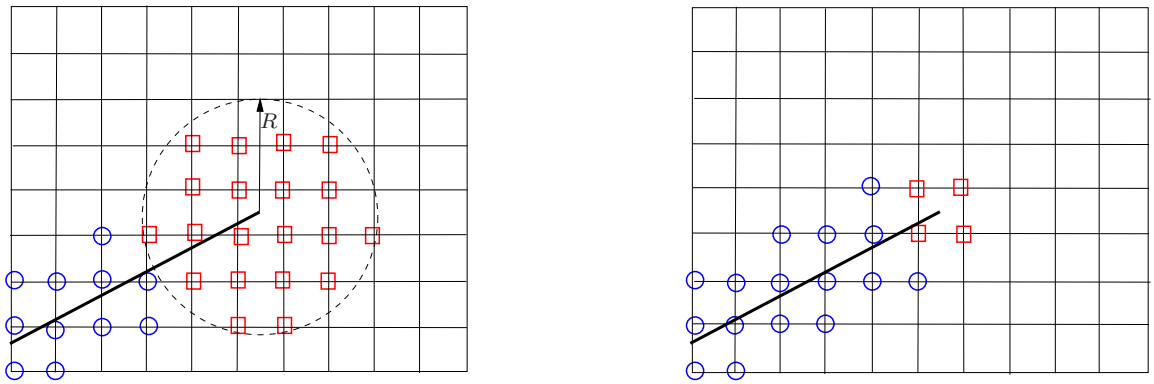

Figure 2.19: Different enrichment strategies in the XFEM: (a) Enrichment with a fixed area for singular functions or 'geometric' enrichment, where R is the enrichment radius ; (b) Topological enrichment. The solid line denotes the crack. The 'circled' nodes are enriched with the Heaviside function and the 'squared' nodes are enriched with the near-tip asymptotic fields.

Hybrid crack element with XFEM Xiao and Karihaloo [164] proposed to combine the highly accurate Hybrid Crack Element (HCE) and the XFEM to improve the accuracy of the

SIFs. They proposed to use HCE for the crack tip region and XFEM formalism in rest of the domain. The XFEM is used to model the crack faces with jump functions. In their approach, the HCE represents the region in the neighbourhood of the crack by *only one* super-element, which is connected compatibly with the other elements. Some of the distinct advantages of this approach are the following:

- avoids blending problem;
- integration is done on the boundary of the HCE, i.e., a contour integration in case of 2D LEFM problems;
- post-processing is not necessary because the SIFs are computed directly from the coefficients of approximating functions.

In its traditional form, the HCE is generally assigned first at the crack tip and then the rest of the domain is meshed by conforming the boundaries of the element to the domain boundary and to the HCE. Xiao and Karihaloo [163] have demonstrated that an HCE element can be constructed from the existing FE background mesh. The degrees of freedom of the unused nodes in the FE mesh are taken care of during the solution process.

Hybrid Analytic XFEM Réthoré *et al.,* [127] in the spirit of the XFEM, proposed a new numerical method to estimate the SIFs directly from the numerical solution. The method relies on partitioning the domain of interest into two overlapping domains Ω_1 and Ω_2, as shown in Figure 2.20. In region Ω_1, the conventional XFEM formalism is adopted to approximate the displacement field, while in region Ω_2, the displacement field is approximated by an analytical form, given by Williams' series [159] expansion for a straight crack. The coupling between these two regions is established by matching the energy. The displacement approximation in region Ω_1 is given by:

$$\mathbf{u}_1^h(\mathbf{x}) = \sum_{I \in \mathcal{N}^{\text{fem}}} N_I(\mathbf{x})\mathbf{q}_I + \sum_{J \in \mathcal{N}^{\text{c}}} N_J(\mathbf{x})H(\mathbf{x})\mathbf{a}_J \tag{2.42}$$

The displacement field in the vicinity of the crack tip (region Ω_2 in Figure 2.20) is given by:

$$\mathbf{u}_2^h(\mathbf{x}) = \frac{1}{2\mu\sqrt{2\pi}} \sum_{n \in [0, n_{\max}]} (\Phi_I^n(\mathbf{x})\mathbf{p}_n + \Phi_{II}^n(\mathbf{x})\mathbf{q}_n) \tag{2.43}$$

where Φ_I and Φ_{II} are the reference fields[i] that form the complete set of linear elastic fields satisfying a zero traction condition along the crack path, μ is Lamé's constant, $\mathbf{p}_n$ and $\mathbf{q}_n$ are the degrees of freedom associated with mode I and mode II functions and $n_{\max}$ is an integer

[i] Obtained from Williams' series expansion for a straight crack [159].

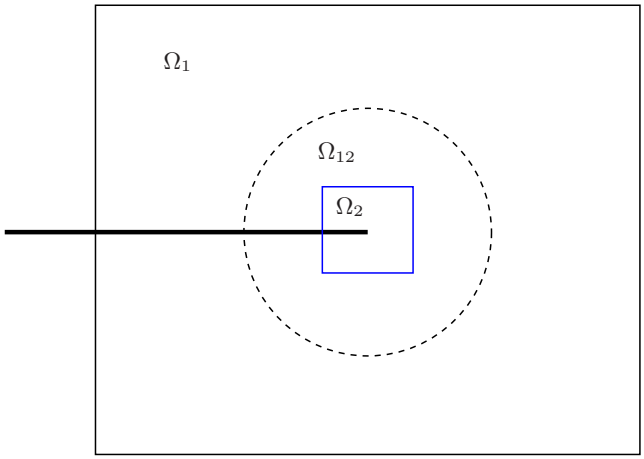

Figure 2.20: HA-XFEM: schematic description, where in Ω_1, finite elements are active and the XFEM formalism is used to represent the discontinuity across the crack face, analytical expressions based on Williams' series [159] are used to represent the displacement field in Ω_2 [127, 128] and Ω_{12} is the coupling zone. The coupling between the two zones is established by partitioning the energy.

that defines the maximum order in the interpolation. When $n = 1$, the stress intensity factors K_I and K_{II} are computed directly from p_1 and q_1 [127, 128]. Numerical results presented in [127] show higher accuracy than the conventional XFEM and the method has been applied to crack growth problems [128]. This shares some similarities with the HCE-XFEM proposed by Xiao and Karihaloo [164].

XFEM with cut-off function In order to improve the convergence properties and robustness of the XFEM, Chahine *et al.,* in a series of papers, proposed the following alternatives to the conventional XFEM. The main idea is to use a cut-off function [136, 137] (c.f. Chapter 8 of the book) to enrich a whole area around the crack tip. The cut-off function, χ satisfies the following property:

$$\begin{cases} \chi(r) = 1 & \text{if } r < r_o \\ 0 < \chi(r) < 1 & \text{if } r_o < r < r_1 \\ \chi(r) = 0 & \text{if } r_1 < r \end{cases} \tag{2.44}$$

where r_o, r_1 are two parameters, that control the size of the cut-off function radius. In their study, χ was chosen to be a fifth degree polynomial. The cut-off function aids is making a smooth transition between the enriched and nonenriched elements [31, 136, 137]. The

enriched approximation of the XFEM with cut-off function takes the form [31, 32]:

$$\mathbf{u}^h = \sum_{I\in\mathcal{N}^{\text{fem}}} N_I\mathbf{q}_I + \sum_{J\in\mathcal{N}^{\text{c}}} N_J H\mathbf{a}_J + \sum_{K\in\mathcal{N}^{f}} N_K \sum_{\alpha=1}^{4} B_\alpha \chi \mathbf{b}_K^\alpha, \tag{2.45}$$

By using the cut-off function, the singular fields are restricted in a region close to the crack tip. Although the method is restricted to 2D, the error in the energy norm and in the displacement norm are improved significantly when compared to the conventional XFEM, that the conditioning number of the system is improved and most importantly a *priori* error estimate showing the optimality of the convergence

Spider XFEM The main idea of Spider XFEM [33] is to approximate the nonsmooth behaviour around the crack tip by another overlapping mesh. To represent the displacement jump across the crack surface, the conventional XFEM is adopted, similar to HAX-FEM [127] and HCE-XFEM [163]. For the region in the vicinity of the crack tip, a circular mesh is adopted and the cut-off function makes a smooth transition between the enriched and the nonenriched regions. The difference between the XFEM with cut-off function [31] and the spider XFEM [33], is that in case of the spider XFEM, an overlapping mesh is used to approximate the displacement fields in the vicinity of the crack tip. The important point is that the enrichment function may be known only partially, i.e., in the radial but not tangential direction.

Reduced basis XFEM Noor and Peters [112] introduced a method that uses pre-computed generic solutions as basis functions for the approximation. Based on this work, Chahine *et al.,* [34] introduced the Reduced Basis-XFEM (RB-XFEM) [34]. The displacement approximation in the RB-XFEM is given by:

$$\mathbf{u}^h = \sum_{I\in\mathcal{N}^{\text{fem}}} N_I\mathbf{q}_I + \sum_{J\in\mathcal{N}^{\text{c}}} N_J H\mathbf{a}_J + \sum_{K=1}^{2} \mathbf{w}_K \chi \mathbf{b}_K \tag{2.46}$$

where $\mathbf{w}_K$ are the pre-computed enrichment functions. This variant of the XFEM is particularly useful when the asymptotic fields ahead of the crack tip are unknown.

Integral matching XFEM It has been shown in [111] that although XFEM with cut-off [31, 32] obtains an optimal convergence rate, the fixed-area enrichment [79] is better than XFEM with a cut-off function. The loss of accuracy is due to the cut-off function itself. Chahine *et al.,* [35] proposed the integral matching XFEM. The idea is to use an integral matching condition on the interface between the enriched zone and the rest of the domain similar to mortar techniques [23]. Note that, Laborde *et al.,* [79] proposed a similar strategy, but the

condition is enforced point-wise. The method yields optimal convergence rate in the displacement norm and in the energy norm with a decrease in the error level when compared with the Std. XFEM and XFEM with fixed-area or geometrical enrichment.

Numerically determined enrichment functions As seen above, special enrichment functions can be added to the FE approximation base that carry information about the local or global behaviour. This requires that these enrichment functions be known in advance in an analytical form. To circumvent this problem, Menk and Bordas [94], proposed a numerical procedure to compute these enrichment functions, especially for anisotropic polycrystals. Although computationally expensive, this method gives a systematic procedure to compute the enrichment functions when their analytical form is not known a priori. The objective of this work closely matches the objective of the RB-XFEM proposed by Chahine *et al.,* [34], in a sense that both approaches aim at applying the XFEM to the problems involving internal boundaries, when their exact nature is not known a priori. It is interesting to note that the idea of cut-off function has been mentioned as early as 1973 by Strang and Fix [136, 137]. The book also provides a discussion on the analytical derivation of the asymptotic fields in the presence of a crack and Kellogg in 1971 [78] studied the crossing of two interfaces.

XS-FEM Lee *et al.,* [82] proposed an alternate formalism by combining the XFEM with the s-method proposed by Fish [52]. The main idea is to use an overlapping mesh consisting of quarter point elements in the region close to the crack tip and to use XFEM for the crack away from the tip. The mesh superposition technique is used to match the near-tip fields with discontinuous displacement field of the underlying mesh.

Ill-conditioning

By incorporating additional functions, the enriched FE basis can model singularities or internal boundaries. The consequence of this is that the stiffness matrix can become ill-conditioned [8, 56, 95, 136]. Various approaches have been developed in the literature to address this issue. Strang and Fix [136], Fix *et al.,* [56] and Béchet *et al.,* [13] applied Cholesky decompositions to submatrices of the stiffness matrix. These submatrices are associated to the degrees of freedom of the enriched nodes. The effect of numerical instability are isolated in the smaller matrices. Strouboulis *et al.,* [138, 139] perturbed the stiffness matrix by an identity matrix of size ε and an iterative method was used to solve the perturbed system. Menk and Bordas [95] proposed a preconditioning technique based on domain decomposition. The method applies the idea of domain decomposition only to the submatrix associated with the enriched degrees of freedom and shares similarity with the finite element tearing and interconnecting (FETI) method [51].

Suppressing additional unknowns

In case of the extrinsic enrichment, the approximation introduces additional unknowns (for example $\mathbf{a}_J$, $\mathbf{b}_K^\alpha$, see Equation (2.23)). These additional unknowns may increase the computational effort. Fries and Belytschko [59] proposed a method that does not use additional unknowns. They called the method the intrinsic XFEM. The main idea is to use special shape functions in the vicinity of discontinuities that captures the physics of the problem. The moving least-squares (MLS) method is used for the construction of the special functions. In this method, the domain is discretized into overlapping subdomains and on each subdomain, a set of shape functions are constructed by means of the MLS technique or by using the standard FE shape functions. A ramp function is used to couple these two domains. Although very appealing, the construction of the MLS approximation increases the computational effort significantly. Song *et al.,* [134] and Rabczuk *et al.,* [124] developed crack tip elements for the phantom-node method. In the phantom-node method, the crack kinematics is captured by overlapping elements. This shares similarities with the proposed by Hansbo and Hansbo [69]. The appealing feature of this method is that no additional degrees of freedoms are involved and is easier to implement into existing FE codes.

2.5 Numerical Examples

In this section, the XFEM is illustrated with examples involving weak discontinuities (material interfaces) to introduce the reader to the concept of enrichment and facilitate the reading and understanding of the following chapters. The first example is a one-dimensional bi-material bar in tension, where imposition of boundary conditions are discussed with and without a shifted approximation basis. The problem with blending elements is also discussed. In the next example, a one-dimensional bar with two interfaces is solved using XFEM, followed by a two dimensional circular inhomogeneity problem, wherein it is illustrated that by using blending correction, optimal convergence rate can be obtained.

2.5.1 One dimensional bi-material bar

To illustrate the solution procedure, the effectiveness and the limitations of the XFEM, a 1D bimaterial bar is considered. The left edge of the bar is clamped and a unit force $F = 1$ N is prescribed at the right end. The material interface is located at $x = x_b = L/2$. Young's moduli for $x \in [0, x_b]$ and $x \in [x_b, L]$ are E_1 = 1 N/m^2 and E_2 = 2 N/m^2, respectively. The area of cross-section for $x \in [0, x_b]$ and $x \in [x_b, L]$ are A_1 = 1 m^2 and A_2 = 1 m^2, respectively. The total length of the bar is $L = 1$ m.

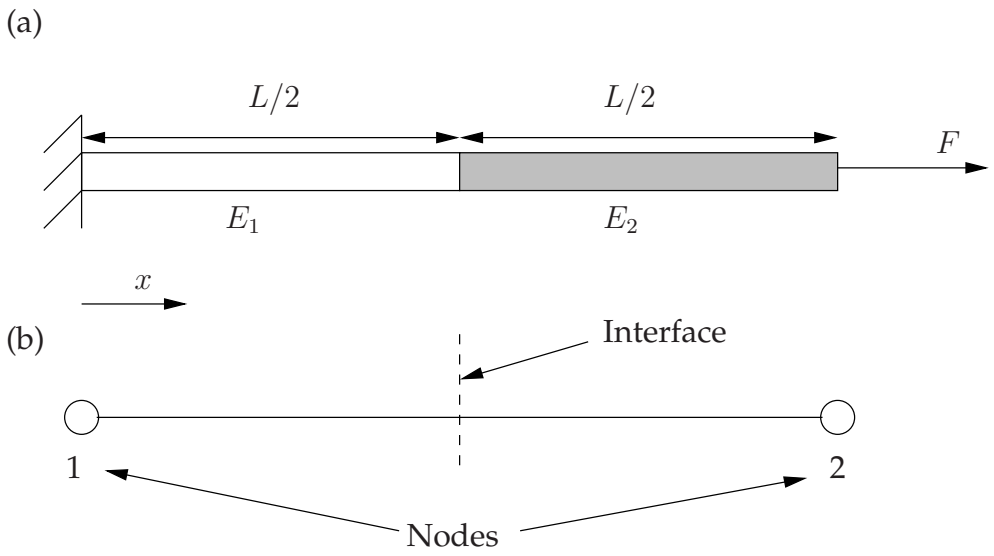

Figure 2.21: Bimaterial bar with a unit force prescribed at the right end: (a) geometry and (b) Finite element.

The effect of nodal subtraction

XFEM without shifting The standard XFEM approximation for the displacement field without shifting is given by:

$$u(x) = N_1(x)u_1 + N_2(x)u_2 + N_3(x)a_1 + N_4(x)a_2 \tag{2.47}$$

where u_1, u_2 are the standard degrees of freedom and a_1, a_2 are the enriched degrees of freedom associated with nodes 1 and 2, respectively. The enrichment functions, N_3 and N_4 are given by:

$$N_3(x) = N_1(x)|\phi_b(x)|, \qquad N_4(x) = N_2(x)|\phi_b(x)| \tag{2.48}$$

where $\phi(x) = x - x_b$ is the enrichment function that has information regarding the local behaviour of the problem. With the two additional functions $N_1\phi$ and $N_2\phi$, the L2 element has four shape functions: standard shape functions $(N_I)_{1\leq I\leq 2}$ and enriched shape functions $(N_I\phi)_{1\leq I\leq 2}$. Associated with these four shape functions come four nodal unknowns: standard unknowns u_1, u_2 and enriched unknowns a_1, a_2. Figure 2.4 shows the variation of the enrichment functions along the length of the bar.
As the first derivative of the solution is discontinuous at $x_b = \mathrm{L}/2$, the domain is split into two regions:

$$\int_0^L f(x)\mathrm{d}x = \int_0^b f(x)\ \mathrm{d}x + \int_b^L f(x)\mathrm{d}x \tag{2.49}$$

The total stiffness matrix for the problem under consideration is given by:

$$\mathbf{K} = \mathbf{K}_1 + \mathbf{K}_2, \tag{2.50}$$

where $\mathbf{K}_1$ and $\mathbf{K}_2$ are given by:

$$\mathbf{K}_1 = \int_0^b \mathbf{B}_1^T E_1 A_1 \mathbf{B}_1 \, \mathrm{d}x, \quad \mathbf{K}_2 = \int_b^L \mathbf{B}_2^T E_2 A_2 \mathbf{B}_2 \, \mathrm{d}x. \tag{2.51}$$

and $\mathbf{B}_1$ and $\mathbf{B}_2$ are given by:

$$\begin{aligned} \forall x \in [0, x_b],\ \mathbf{B}_1(x) &= \begin{bmatrix} -1 & 1 & (x - 1 - \phi(x)) & (-x + \phi(x)) \end{bmatrix} \\ \forall x \in [x_b, L],\ \mathbf{B}_2(x) &= \begin{bmatrix} -1 & 1 & (-x + 1 - \phi(x)) & (x + \phi(x)) \end{bmatrix} \end{aligned} \tag{2.52}$$

Since the enrichment function does not go to zero at the nodes and also because the enrichment function is non-zero within the element, extra effort is required to compute the force vector. The force corresponding to the enriched degrees of freedom has a non-zero entry in the force vector. The elemental force vector can be written as:

$$\mathbf{f}^e = \underbrace{\int_{\Omega^e} \mathbf{N}^{\mathrm{T}} b \, \mathrm{d}x}_{\mathbf{f}^e_\Omega} + \underbrace{\mathbf{N}^{\mathrm{T}} A^e \overline{t}|_{\Gamma^e_t}}_{\mathbf{f}^e_\Gamma} \tag{2.53}$$

where $\mathbf{f}^e_\Omega$ is the body force vector, $\mathbf{f}^e_\Gamma$ is the external local vector, b is the body force and $\overline{t}$ is the traction on the boundary. The boundary conditions are: the displacement at the left end $(x = 0) = 0$ and a unit force applied at the right end $(x = L)$. As the enrichment function is not zero at the nodes, Dirichlet boundary conditions are enforced via Lagrange multipliers. The condition is derived as follows. We require $u(x)|_{x=0} = 0$, so,

$$\begin{aligned} u(x)|_{x=0} &= N_1(x)|_{x=0} u_1 + \underbrace{N_2(x)|_{x=0}}_{=0} u_2 + N_3(x)|_{x=0} a_1 + \underbrace{N_4(x)|_{x=0}}_{=0} a_2 \\ &= N_1(x)|_{x=0} u_1 + \underbrace{N_3(x)|_{x=0}}_{=(|x-x_b|N_1(x)|)_{x=0} \ = \ \frac{1}{2} N_1(x)|_{x=0}} a_1 \\ \implies u(x)|_{x=0} &= 0 = u_1 + (1/2) a_1 \end{aligned} \tag{2.54}$$

The complete system of equations with Lagrange multipliers is given by:

$$\begin{bmatrix} 1.50 & -1.50 & 0.50 & -1.00 & 1.00 \\ -1.50 & 1.50 & -0.50 & 1.00 & 0.00 \\ 0.50 & -0.50 & 0.625 & -0.125 & 0.50 \\ -1.00 & 1.00 & -0.125 & 1.125 & 0.00 \\ 1.00 & 0.00 & 0.50 & 0.00 & 0.00 \end{bmatrix} \begin{Bmatrix} u_1 \\ u_2 \\ a_1 \\ a_2 \\ \lambda \end{Bmatrix} = \begin{Bmatrix} 0 \\ 1 \\ 0 \\ 1/2 \\ 0 \end{Bmatrix} \tag{2.55}$$

and the solution is given by:

$$\begin{Bmatrix} u_1 \\ u_2 \\ a_1 \\ a_2 \\ \lambda \end{Bmatrix} = \begin{Bmatrix} 0.125 \\ 0.875 \\ -0.250 \\ -0.250 \\ 1 \end{Bmatrix} \tag{2.56}$$

Note that the displacement vector obtained by solving the system of equations does not correspond to the nodal values and the actual nodal values are computed by substituting the solution into Equation (2.47).

Computation of true nodal displacements Substituting the functional form for the shape functions and the computed unknown displacements, the actual displacement field is given by:

$$u(x) = 0.125\,(1-x) + 0.875x - 0.25\,(1-x)\,|x - x_b| - 0.25x|x - x_b| \tag{2.57}$$

XFEM with shifting The XFEM displacement approximation at a point $x \in [0,1]$ writes

$$u(x) = N_1(x)u_1 + N_2(x)u_2 + N_3(x)a_1 + N_4(x)a_2 \tag{2.58}$$

where u_1, u_2 are the standard degrees of freedom and a_1, a_2 are the enriched degrees of freedom associated with nodes 1 and 2, respectively. The enrichment functions, N_3 and N_4 are given by:

$$N_3(x) = N_1(x)\,(|\phi_b(x)| - |\phi_b(x_1)|)\,, \qquad N_4(x) = N_2(x)\,(|\phi_b(x)| - |\phi_b(x_2)|) \tag{2.59}$$

where $\phi_b(x) = x - x_b$ is the level set function in 1D. Figure 2.4 shows the variation of enrichment functions along the length of the bar. As the solution's first derivative is discontinuous

at x_b = 0.5, the domain is split into two regions:

$$\int_0^L f(x)\mathrm{d}x = \int_0^b f(x)dx + \int_b^L f(x)\mathrm{d}x \tag{2.60}$$

The total stiffness matrix for the problem under consideration is given by:

$$\mathbf{K} = \mathbf{K}_1 + \mathbf{K}_2, \tag{2.61}$$

where $\mathbf{K}_1$ and $\mathbf{K}_2$ are given by:

$$\mathbf{K}_1 = \int_0^b \mathbf{B}_1^T E_1 A \mathbf{B}_1 \, \mathrm{d}x, \quad \mathbf{K}_2 = \int_b^L \mathbf{B}_2^T E_2 A \mathbf{B}_2 \, \mathrm{d}x. \tag{2.62}$$

and $\mathbf{B}_1$ and $\mathbf{B}_2$ are given by:

$$\begin{aligned} \forall x \in [0, x_b],\ \mathbf{B}_1(x) &= \left[\begin{array}{cccc} -1 & 1 & (x - \phi_b(x) - 1/2) & (\phi_b(x) - 1/2 - x) \end{array} \right], \\ \forall x \in [x_b, 1],\ \mathbf{B}_2(x) &= \left[\begin{array}{cccc} -1 & 1 & (3/2 - x - \phi_b(x)) & (\phi_b(x) - 1/2 + x) \end{array} \right]. \end{aligned} \tag{2.63}$$

The assembled equations after imposing boundary conditions ($u_1 = 0,\ F_2 = 1$) are:

$$\left[\begin{array}{ccc} 1.50 & 0.25 & 0.25 \\ 0.25 & 0.50 & 0.25 \\ 0.25 & 0.25 & 0.50 \end{array} \right] \left\{ \begin{array}{c} u_2 \\ a_1 \\ a_2 \end{array} \right\} = \left\{ \begin{array}{c} 1 \\ 0 \\ 0 \end{array} \right\} \tag{2.64}$$

and the solution is $u_2 = 0.75,\ a_1 = -0.25,\ a_2 = -0.25$. The displacement along the length of the bar is given by, $\forall x \in [0, 1]$:

$$u(x) = 0.75x - 0.25(1 - x)(|x - x_b| - |x_1 - x_b|) - 0.25x(|x - x_b| - |x_2 - x_b|) \tag{2.65}$$

Blending correction

Next, the problem with the blending elements is discussed for the one-dimensional bi-material bar. To study the influence of partially enriched elements, let the domain be discretized with 3 two-noded 1D finite elements, as shown in Figure 2.22, with the material interface located in the second element. The elements on either side of the element containing the interface is partially enriched.

With the displacement approximation given by Equation (2.58), the strain approximation

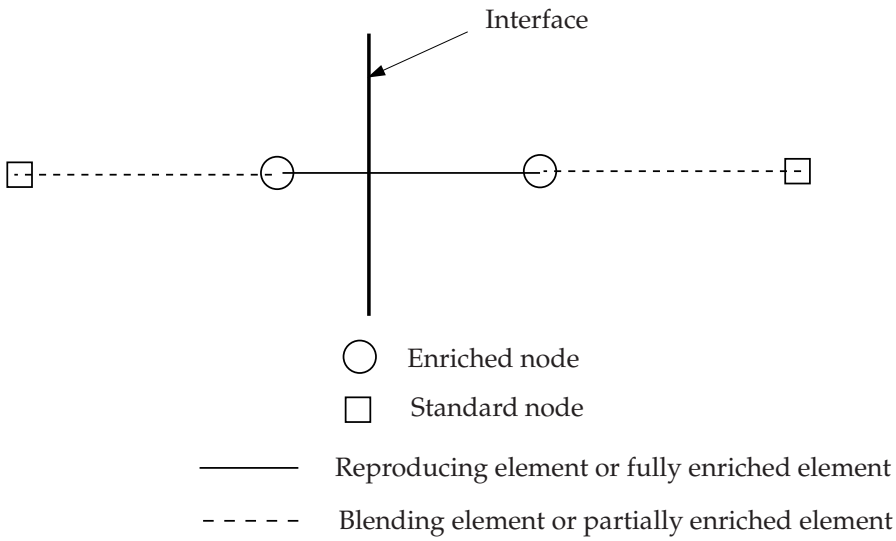

Figure 2.22: Bi-material bar discretized with 3 two-noded 1D finite elements.

in the blending element to the left of the material interface is given by:

$$\varepsilon_x = \frac{\mathrm{d}u}{\mathrm{d}x} = \sum_{I=1}^{2} \frac{\mathrm{d}N_I}{\mathrm{d}x} u_I + \frac{\mathrm{d}N_2}{\mathrm{d}x} \psi a_2 + N_2 \frac{\mathrm{d}\psi}{\mathrm{d}x} a_2 \tag{2.66}$$

The terms ψ and $\frac{\mathrm{d}\psi}{\mathrm{d}x}$ in Equation (2.66) cause the zig-zag behavior seen in Figure 2.23. With a small modification as proposed by Fries [58], it can be seen from Figure 2.23 that the zig-zag behaviour in the blending elements is removed. And with the increase in the number of elements, the performance is improved. The rate of convergence of the XFEM with and without blending correction is studied for a two-dimensional problem, discussed as a last example in this section.

2.5.2 One dimensional multiple interface

In this example, a one-dimensional bar with two material interfaces is considered. The material interfaces are located at $x = x_a = 1/4$ and $x = x_b = 3/4$, as shown in Figure 2.24. The left edge of the bar is clamped and a unit force $F = 1$ is prescribed at the right end. Young's moduli for $x \in [0, x_a)$, $x \in (x_a, x_b)$ and $x > x_b$ are 1 N/m^2, 2 N/m^2 and 1 N/m^2, respectively. The total length of the bar is $L = 1$.

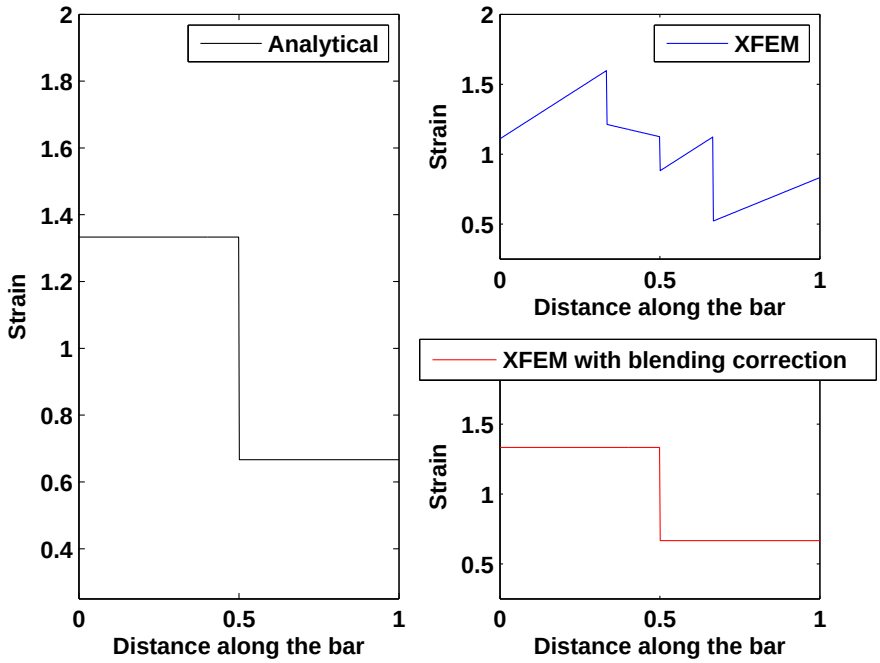

(a) with 3 elements

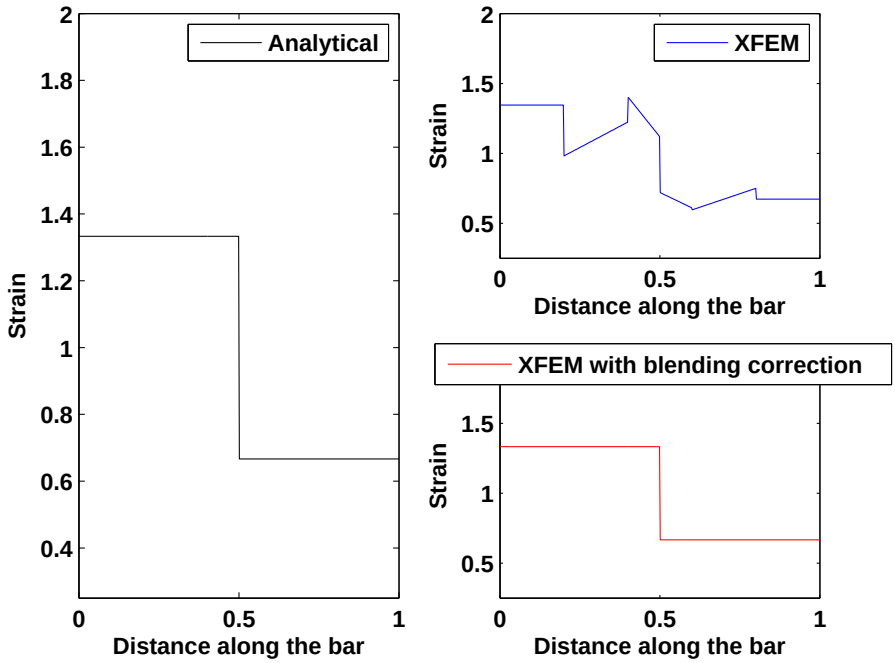

(b) with 5 elements

Figure 2.23: Blending problem for the bimaterial bar: strain along the length of the bar.

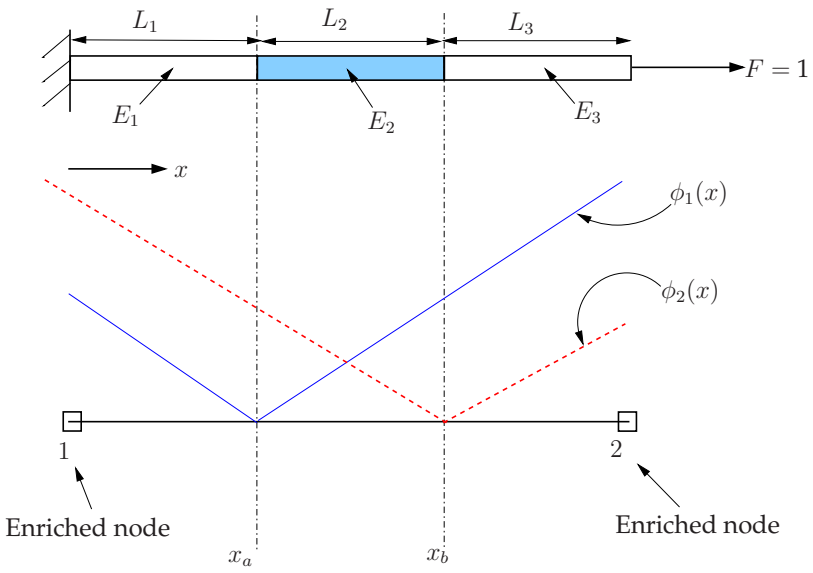

Figure 2.24: One-dimensional bar with multiple interfaces, where x_a and x_b are the location of the material interfaces and L_1, L_2 and L_3 are the length of each segment. A unit force is prescribed at the right end.

The XFEM displacement approximation at a point $x \in [0, 1]$ writes:

$$u(x) = \left[\begin{array}{cccccc} N_1(x) & N_2(x) & N_3(x) & N_4(x) & N_5(x) & N_6(x) \end{array} \right] \left\{ \begin{array}{c} u_1 \\ u_2 \\ a_1 \\ a_2 \\ b_1 \\ b_2 \end{array} \right\} \tag{2.67}$$

where u_1, u_2 are standard degrees of freedom and a_1, a_2, b_1, b_2 are enriched degrees of freedom associated with nodes 1 and 2. N_1, N_2 are the standard FE shape functions, N_3, N_4, N_5 and N_6 are the enriched shape functions, given by, $\forall x \in [0, 1]$:

$$\begin{aligned} N_3(x) &= N_1(x) \left(|\phi_1(x)| - |\phi_1(x_1)| \right) \\ N_4(x) &= N_2(x) \left(|\phi_1(x)| - |\phi_1(x_2)| \right) \\ N_5(x) &= N_1(x) \left(|\phi_2(x)| - |\phi_2(x_1)| \right) \\ N_6(x) &= N_2(x) \left(|\phi_2(x)| - |\phi_2(x_2)| \right) \end{aligned} \tag{2.68}$$

where $\phi_1(x)$ and $\phi_2(x)$ are level set functions for the two material interfaces.
$\phi_1(x_i), \phi_2(x_i), i = 1, 2$ are the values of the level set function evaluated at nodes 1 and 2.

$\phi_1(x) = x - x_a$ is the level set function in 1D and x_a is the location of the first interface from the left end and $\phi_2(x) = x - x_b$ is the level set function for the second interface. An absolute value of the level-set function, given by Equation (2.28) is used as an enrichment function (see Figure 2.24 for a schematic representation). As the solution's first derivative is discontinuous at two locations along the length of the bar, $x_a = 1/4$ and $x_b = 3/4$, the domain is split into three regions:

$$\int_0^L f(x)\,\mathrm{d}x = \int_0^{x_a} f(x)\,\mathrm{d}x + \int_{x_a}^{x_b} f(x)\,\mathrm{d}x + \int_{x_b}^{L} f(x)\,\mathrm{d}x. \tag{2.69}$$

The total stiffness matrix for the problem under consideration is given by

$$\mathbf{K} = \mathbf{K}_1 + \mathbf{K}_2 + \mathbf{K}_3, \tag{2.70}$$

where $\mathbf{K}_1$, $\mathbf{K}_2$ and $\mathbf{K}_3$ are given by

$$\begin{aligned}
\mathbf{K}_1 &= \int_0^b \mathbf{B}_1^{\mathrm{T}}\, E_1 A\, \mathbf{B}_1\,\mathrm{d}x \\
\mathbf{K}_2 &= \int_b^L \mathbf{B}_2^{\mathrm{T}}\, E_2 A\, \mathbf{B}_2\,\mathrm{d}x \\
\mathbf{K}_3 &= \int_b^L \mathbf{B}_3^{\mathrm{T}}\, E_3 A\, \mathbf{B}_3\,\mathrm{d}x,
\end{aligned} \tag{2.71}$$

and $\mathbf{B}_i, i = 1, 2, 3$ are the strain-displacement matrices. The terms in Equation (2.71) are computed as outlined earlier for the bi-material problem. The assembled system of equations is given by:

$$\begin{bmatrix} 1.5 & 0.25 & 0 & 0 & -0.25 \\ 0.25 & 0.5 & 0 & 0.0208 & -0.2708 \\ 0 & 0 & 0.3750 & 0.3542 & 0.0208 \\ 0 & 0.0208 & 0.3542 & 0.3750 & 0 \\ -0.25 & -2708 & 0.0208 & 0 & 0.5 \end{bmatrix} \begin{Bmatrix} u_2 \\ a_1 \\ a_2 \\ b_1 \\ b_2 \end{Bmatrix} = \begin{Bmatrix} 1 \\ 0 \\ 0 \\ 0 \\ 0 \end{Bmatrix} \tag{2.72}$$

with boundary conditions $u_1 = 0$, $F_1 = 1$. The solution is given by $u_2 = 0.75$, $a_1 = -0.25$, $a_2 = -0.25$, $b_1 = 0.25$, $b_2 = 0.25$. The displacement function is given by:

$$\forall x \in [0,1],\;\; u(x) = 0.75N_2(x) - 0.25N_3(x) - 0.25N_4(x) + 0.25N_5(x) + 0.25N_6(x) \tag{2.73}$$

Figure 2.25 shows the displacement along the length of the bar for the XFEM and for the conforming FEM. In the case of the FEM, three elements are used to solved the problem. Thanks to the local PU and enrichment functions, the XFEM with one element is able to

capture the weak discontinuities along the length of the bar. Note that, the number of unknowns in case of the XFEM is 6 (two standard dofs and four enriched dofs) while in the case of the FEM, its only 4 (one for each node). Although the number of unknowns in case of the XFEM is increased, the advantage is that the mesh does not conform to the material interface. Hence, the influence of the location of the material interface on the solution can be solved without changing the underlying mesh by using appropriate values of the location of the interfaces x_a and x_b while evaluating the integrals given by Equation (2.71).

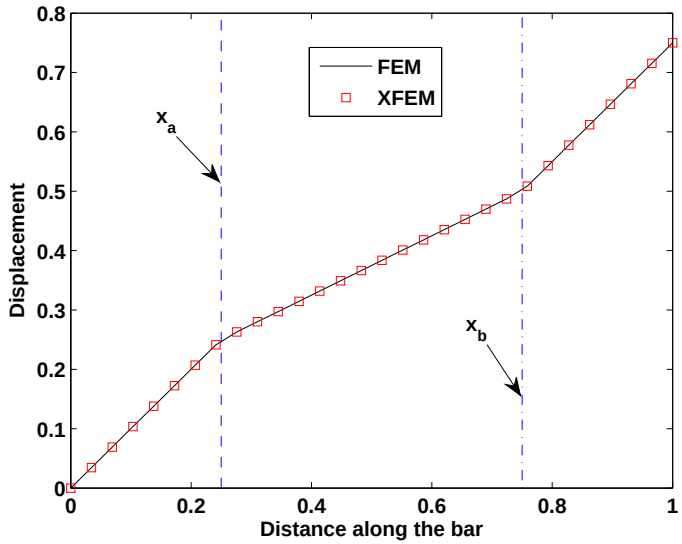

Figure 2.25: Displacement along the length of the bar. Three elements are used in case of the FEM, while one element is used in case of the XFEM. x_a and x_b denote the material interfaces.

2.5.3 Two dimensional circular inhomogeneity

In this example, the enriched finite element solutions for the elastostatic response of a circular material inhomogeneity under radially symmetric loading, as shown in Figure 2.26 is examined within the framework of the XFEM. The effect of modifying the approximation in the blending elements is studied. Plane strain conditions are assumed. The material properties are constant within each domain, Ω_1 and Ω_2, but there is a material discontinuity across the interface, $\Gamma_1(r = a)$. The Lamé constants in Ω_1 and Ω_2 are: $\lambda_1 = \mu_1 = 0.4$ and λ_2 =5.7692, μ_2 =3.8461, respectively. These correspond to E_1 =1, ν =0.25 and E_2 =10, ν_2 =0.3. A linear displacement field: $u_1 = x_1, u_2 = x_2$ $(u_r = r, u_\theta = 0)$ on the boundary $\Gamma_2(r = b)$ is imposed [41, 58, 145]. The governing equations, the exact displacement solutions, the strain and the stress fields are given in Appendix A.
For the present numerical study, a square domain of size $L \times L$ with $L = 2$ is considered.

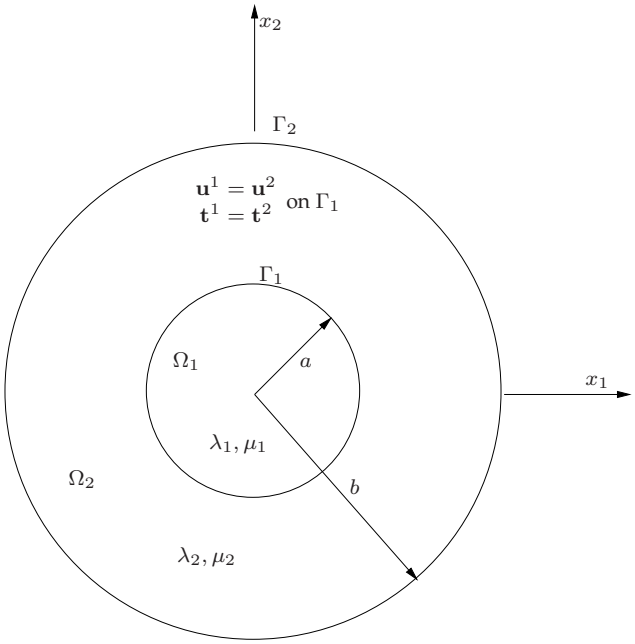

Figure 2.26: Bi-material boundary value problem

Along the outer boundary, closed-form displacements are imposed. Meshes with characteristic element sizes of $h \in \{0.2, 0.1, 0.05, 0.025\}$ are used. Figure 2.27 shows the rate of convergence in the displacement norm (L^2) and in the energy norm. It can be seen that the XFEM without blending corrections achieves sub-optimal convergence rates, i.e., 0.95 in L^2 and 0.71 in the energy norm. By using the enrichment function proposed by Fries [58], the method achieves a convergence rates of 1.80 in the L^2 norm and 1.16 in the energy norm. The error level is also smaller than the XFEM without blending correction.

2.6 Summary

This chapter gave an overview of the partition of unity methods and the XFEM in particular. The usefulness of the enrichment technique and the way the system matrices are modified due to the addition of new functions is discussed in detail using the one-dimensional bi-material bar example. The effect of nodal subtraction and blending corrections were also discussed in a didactic manner to help the reader appreciate the essential points required to understand the basis of the method.

Motivation The salient feature of the XFEM is that known information can be added to the FE approximation basis to improve the performance of the finite elements using piecewise polynomials. If the enrichment functions are not smooth or polynomial functions, addi-

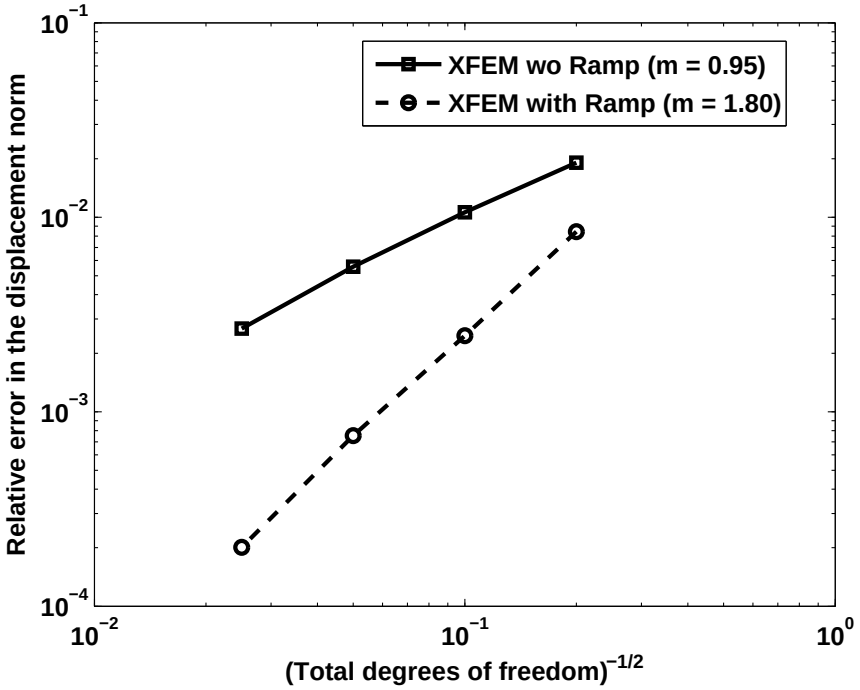

(a) Relative error in the displacement norm

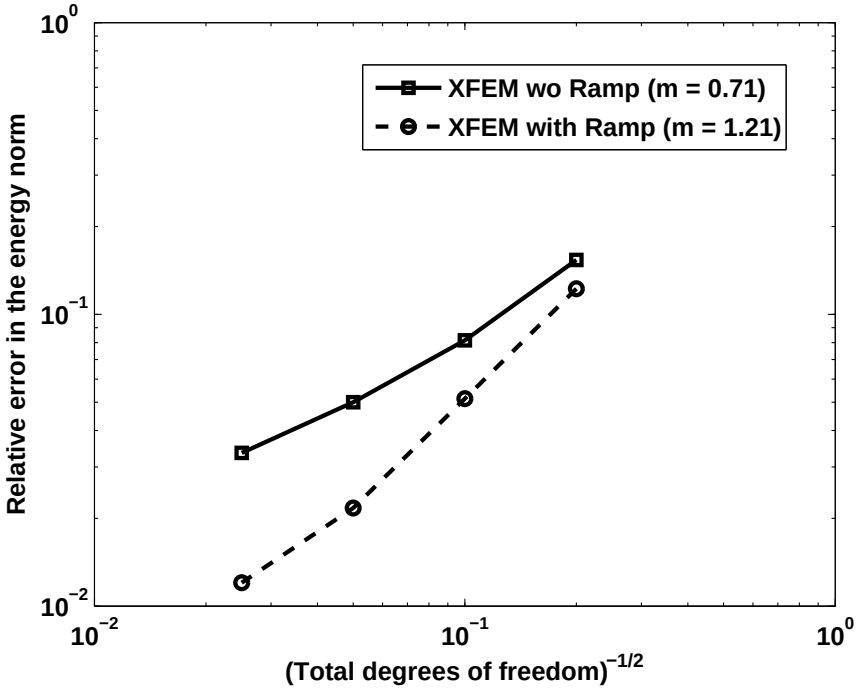

(b) Relative error in the energy norm

Figure 2.27: Bi-material circular inhomogeneity problem: the rate of convergence in L^2 and in the energy norm. m is the rate of convergence. It can be seen that the rate of convergence in both the displacement norm and in the energy norm increases by using a ramp enrichment.

tional care has to be taken in numerically integrating over the elements that are intersected by the discontinuity surface (for example, $\sqrt{r}$ in case of the LEFM). Significant amount of work has been done to improve the integration as discussed in Section 2.4.5. Some of these methods eliminate the singularities present in the XFEM stiffness matrix in the LEFM, for example, polar integration [79] and special mapping techniques [118]. Numerical integration techniques using adaptive methods were proposed, but an adaptive control of the integration error is very time-consuming [163]. Note that, all the above techniques still require a sub-triangulation of the polygonal region intersected by the discontinuity surface. Other methods proposed in the literature, focussed on integrating over the elements that are intersected by the discontinuity surface but do not contain the crack tip. For example, replacing the product of the shape functions and the enrichment functions by an equivalent polynomial [151] or by using higher order shape functions [75].

This study is motivated by the need to improve numerical integration over enriched elements. Two new methods are proposed in Chapter 3. The accuracy of the proposed methods is discussed in Chapter 4.

Bibliography

[1] P. M. A. Areias and T. Belytschko. A comment on the article: a finite element method for simulation of strong and weak discontinuities in solid mechanics by A. Hanbso and P. Hansbo [comput. methods appl. mech. engrg. 193 (2004)]. *Computer Methods in Applied Mechanical and Engineering*, 195:1275–1276, 2006.

[2] A. Asadpoure and S. Mohammadi. A new approach to simulate the crack with the extended finite element method in orthotropic media. *International Journal for Numerical Methods in Engineering*, 69:2150–2172, 2007.

[3] A. Asadpoure and S. Mohammadi. Crack analysis in orthotropic media using the extended finite element method. *Thin Walled Structures*, 44:1031–1038, 2007.

[4] S. N. Atluri, A. S. Kobayashi, and M. O. Nakagaki. An assumed displacement hybrid finite element model for linear fracture mechanics. *International Journal of Fracture*, 11:257–271, 1975.

[5] S. N. Atluri, H. G. Kim, and J. Y. Cho. A critical assessment of the meshless local Petrov-Galerkin (MLPG) and local boundary integral equation (LBIE) methodds. *Computational Mechanics*, 24:348–372, 1999.

[6] P. Aubertin, J. Réthoré, and R. de Borst. A coupled molecular dynamics and extended finite element method for dynamic crack propagation. *International Journal for Multiscale Computational Engineering*, 81:72–88, 2009.

[7] P. Aubertin, J. Réthoré, and R. de Borst. Dynamic crack propagation using a combined molecular dynamics/extended finite element approach. *International Journal for Multiscale Computational Engineering*, 2:221–235, 2010.

[8] I. Babuška and U. Banerjee. Stable generalized finite element method (SGFEM). Technical Report 11-07, Institute for Computational Engineering and Sciences, 2011.

[9] I. Babuška and J. Melenk. The partition of unity finite element method. *International Journal for Numerical Methods in Engineering*, 40:727–758, 1997.

[10] I. Babuška, G. Caloz, and J. E. Osborn. Special finite element methods for a class of second order elliptic problems with rough coefficients. *SIAM Journal of Numerical Analysis*, 31:945–981, 1994.

[11] R. S. Barsoum. Triangular quarter-point elements as elastic and perfectly-plastic crack tip elements. *International Journal for Numerical Methods in Engineering*, 11:85–98, 1977.

[12] K. J. Bathe. *Finite Element Procedures*. Cambridge, MA, Englewood Cliffs, NJ, 1996.

[13] E. Béchet, H. Minnebo, N. Moës, and B. Burgardt. Improved implementation and robustness study of the X-FEM for stress analysis around cracks. *International Journal for Numerical Methods in Engineering*, 64(8):1033–1056, 2005. doi: 10.1002/nme.1386.

[14] E. Béchet, M. Scherzer, and M. Kuna. Application of the x-fem to the fracture of piezoelectric materials. *International Journal for Numerical Methods in Engineering*, 77:1535–1565, 2009.

[15] T. Belytschko and T. Black. Elastic crack growth in finite elements with minimal remeshing. *International Journal for Numerical Methods in Engineering*, 45:601–620, 1999.

[16] T. Belytschko, J. Fish, and B. E. Englemann. A finite element with embedded localization zones. *Computer Methods in Applied Mechanical and Engineering*, 70:59–89, 1988.

[17] T. Belytschko, J. Fish, and A. Bayliss. The spectral overlay on finite elements for problems with high gradients. *Computer Methods in Applied Mechanical and Engineering*, 81:71–89, 1990.

[18] T. Belytschko, Y. Y. Lu, and L. Gu. Element-free Galerkin methods. *International Journal for Numerical Methods in Engineering*, 37:229–256, 1994.

[19] T. Belytschko, N. Moës, S. Usui, and C. Parimi. Arbitrary discontinuities in finite elements. *International Journal for Numerical Methods in Engineering*, 50(4):993–1013, Jan 2001.

[20] T. Belytschko, S. P. Xiao, and C. Parimi. Topology optimization with implicit functions and regularization. *International Journal for Numerical Methods in Engineering*, 57(8):1177–1196, 2003. ISSN 1097-0207.

[21] T. Belytschko, R. Gracie, and G. Ventura. A review of extended/generalized finite element methods for material model. *Modelling and simulation in Materials Science and Engineering*, 17: 1–24, 2009.

[22] S. E. Benzley. Representation of singularities with isoparametric finite elements. *International Journal for Numerical Methods in Engineering*, 8:537–545, 1974.

[23] C. Bernardi, Y. Maday, and A. Patera. *Nonlinear partial differential equations and their applications*, chapter A new nonconforming approach to domain decomposition, pages 13–51. Longman Scientific and Technical, 1994.

[24] S. Bordas and B. Moran. Enriched finite elements and level sets for damage tolerance assessment of complex structures. *Engineering Fracture Mechanics*, 73:1176–1201, 2006.

[25] S. Bordas, H. Ronald, W. Hoppe, and S. Petrova. Mechanical failure in microstructural heterogeneous materials. *Lecture notes in computer science (LNCS) post-proceedings. Proceedings of the sixth international conference on numerical methods and applications*, 6:24–26, 2006.

[26] S. Bordas, V. P. Nguyen, C. Dunant, A. Guidoum, and H. Nguyen-Dang. An extended finite element library. *International Journal for Numerical Methods in Engineering*, 71:703–732, 2007.

[27] S. Bordas, T. Rabczuk, and G. Zi. Three-dimensional crack initiation, propagation, branching and junction in non-linear materials by an extended meshfree method without asymptotic enrichment. *Engineering Fracture Mechanics*, 75(5):943–960, March 2008. doi: 10.1016/j.engfracmech.2007.05.010.

[28] S. P. A. Bordas and S. Natarajan. On the approximation in the smoothed finite element method (SFEM). *International Journal for Numerical Methods in Engineering*, 81:660–670, 2010.

[29] J. P. Boyd. *Chebyshev and Fourier Spectral Methods*. Dover Publications Inc, 2000.

[30] E. Byskov. The calculation of stress intensity factors using the finite elemnet method with cracked elements. *International Journal of Fracture*, 6:159–167, 1970.

[31] E. Chahine, P. Laborde, and Y. Renard. A quais-optimal convergence result for fracture mechanics with XFEM. *Comptes Rendus Mathematique*, 1342:527–532, 2006.

[32] E. Chahine, P. Laborde, and Y. Renard. Crack tip enrichment in the (XFEM) using a cutoff function. *International Journal for Numerical Methods in Engineering*, 75:629–646, 2008.

[33] E. Chahine, P. Laborde, and Y. Renard. Spider-XFEM: an extended finite element variant for partially unknown crack-tip displacement. *European Journal of Computational Mechanics*, 15: 625–636, 2008.

[34] E. Chahine, P. Laborde, and Y. Renard. A reduced basis enrichment for the eXtended Finite Element Method. *Mathematical Modelling Natural Phenomena*, 4:88–105, 2009.

[35] E. Chahine, P. Laborde, and Y. Renard. A non-conformal eXtended Finite Eelement approach: Integral matchin Xfem. *Applied Numerical Mathematics*, 61:322–343, 2011.

[36] J. S. Chen, C. Pan, T. C. Wu, and W. K. Liu. Reproducing kernel particle methods for large deformation analysis of non-linear structures. *Applied Mechanics and Engineering*, 139:195–228, 1996.

[37] X. Chen, S. Yang, J. Ma, and Z. He. The construction of wavelet finite element and its application. *Finite Elements in Analysis and Design*, 40:541–554, 2004.

[38] K. W. Cheng and T. P. Fries. Higher-order XFEM for curved strong and weak discontinuities. *International Journal for Numerical Methods in Engineering*, 82:564–590, 2010.

[39] J. Chessa and T. Belytschko. An enriched finite element method and level sets for axisymmetric two-phase flow with surface tension. *International Journal for Numerical Methods in Engineering*, 58(13):2041–2064, 2003.

[40] J. Chessa, P. Smolinski, and T. Belytschko. The extended finite element method (XFEM) for solidification problems. *International Journal for Numerical Methods in Engineering*, 53(8):1959–1977, Jan 2002. doi: 10.1002/nme.386.

[41] J. Chessa, H. Wang, and T. Belytschko. On the construction of blending elements for local partition of unity enriched finite elements. *International Journal for Numerical Methods in Engineering*, 57:1015–1038, 2003.

[42] D. L. Chopp and N. Sukumar. Fatigue crack propagation of multiple coplanar cracks with the coupled extended finite element/fast marching method. *International Journal of Engineering Science*, 41(8):845–869, 2003.

[43] K. Y. Dai, G. R. Liu, and T. T. Nguyen. An n-sided polygonal smoothed finite element method (nSFEM) for solid mechanics. *Finite Elements in Analysis and Design*, 43:847–860, 2007.

[44] J. Dolbow, N. Moës, and T. Belytschko. Modeling fracture in Mindlin - Reissner plates with the extended finite element method. *International Journal of Solids and Structures*, 37(48-50): 7161–7183, 2000. doi: 10.1016/S0020-7683(00)00194-3.

[45] C. A. Duarte, O. N. Hamzeh, T. J. Liszka, and W. W. Tworzydlo. A generalized finite element method for the simulation of three-dimensional dynamic crack propagation. *Computer Methods in Applied Mechanical and Engineering*, 190:2227–2262, 2001.

[46] R. Duddu, S. P. A. Bordas, D. Chopp, and B. Moran. A combined extended finite element and level set method for biofilm growth. *International Journal for Numerical Methods in Engineering*, 74(5):848–870, Jan 2008. doi: 10.1002/nme.2200.

[47] M. Duflot. A study of the representation of cracks with level sets. *International Journal for Numerical Methods in Engineering*, 70:1261–1302, 2007.

[48] M. Duflot. The extended finite element method in thermoelastic fracture mechanics. *International Journal for Numerical Methods in Engineering*, 74:827–847, 2008.

[49] M. S. Edke and K.-H. Chang. Shape optimization for 2D mixed-mode fracture using extended FEM (XFEM) and level set method (LSM). *Structural and Multidisciplinary Optimization*, 2011. doi: 10.1007/s00158-010-0616-5.

[50] T. Elguedj, A. Gravouil, and A. Combescure. Appropriate extended functions for XFEM simulation of plastic fracture mechanics. *Computer Methods in Applied Mechanical and Engineering*, 195:501–515, 2006.

[51] C. Farhat and F. Roux. A method of finite element tearing and interconnecting and its parallel solution algorithm. *International Journal for Numerical Methods in Engineering*, 32:1205–1227, 1991.

[52] J. Fish. The s-version of the finite element method. *Computers and Structures*, 43:539–547, 1992.

[53] J. Fish and T. Belytschko. Elements with embedded localization zones for large deformation problems. *Computers and Structures*, 30:247–256, 1988.

[54] J. Fish and T. Belytschko. A general finite element procedure for problems with high gradients. *Computers and Structures*, 35:309–319, 1990.

[55] G. J. Fix. High-order Rayleigh-Ritz approximations. *Journal of Mathematics and Mechanics*, 18: 645–657, 1969.

[56] G. J. Fix, S. Gulati, and G. I. Wakoff. On the use of singular functions with finite element approximations. *Journal of Computational Physics*, 13:209–228, 1973.

[57] L. Franca, C. Farhat, and I. Harari. The discontinuous enrichment method. *Computer Methods in Applied Mechanical and Engineering*, 190:6455–6479, 2001.

[58] T.-P. Fries. A corrected XFEM approximation without problems in blending elements. *International Journal for Numerical Methods in Engineering*, 75:503–532, 2008.

[59] T.-P. Fries and T. Belytschko. The intrinsic partition of unity method. *Computational Mechanics*, 40:803–814, 2007.

[60] O. Garcia, E. Fancello, C. Barcellos, and C. Duarte. Hp clouds in mindlin's thick plate model. *International Journal for Numerical Methods in Engineering*, 47:1381–1400, 2000.

[61] A. Gerstenberger and W. Wall. An extended finite element method/Lagrange multiplier based approach for fluid-structure interaction. *Computer Methods in Applied Mechanics and Engineering*, 197(19-20):1699–1714, 2008. ISSN 0045-7825.

[62] S. Ghosh. *Micromechanical analysis and multi-scale modeling using the Voronoi cell Finite element method*. CRC Press, 2010.

[63] S. Ghosh and R. L. Mallett. Voronoi cell finite elements. *Computers and Structures*, 50:33–46, 1994.

[64] R. Gracie, G. Ventura, and T. Belytschko. A new fast finite element method for dislocations based on interior discontinuities. *International Journal for Numerical Methods in Engineering*, 69: 423–441, 2007.

[65] R. Gracie, J. Oswald, and T. Belytschko. On a new extended finite element method for dislocations: core enrichment and nonlinear formulation. *Journal of the Mechanics and Physics of Solids*, 56(1):200–214, 2008. ISSN 0022-5096.

[66] R. Gracie, H. Wang, and T. Belytschko. Blending in the extended finite element method by discontinuous Galerkin and assumed strain methods. *International Journal for Numerical Methods in Engineering*, 74:1645–1669, 2008.

[67] R. Gracie, J. Oswald, and T. Belytschko. Concurrently coupled atomistic and XFEM models for dislocations and cracks. *International Journal for Numerical Methods in Engineering*, 78:354–378, 2009.

[68] M. Griebel and M. A. Schweitzer, editors. *Meshfree Methods for Partial Differential Equations*. Springer, 2003.

[69] A. Hansbo and P. Hansbo. A finite element method for the simulation of strong and weak discontinuities in solid mechanics. *Computer Methods in Applied Mechanical and Engineering*, 193:3523–3540, 2004.

[70] T. Hettich, A. Hung, and E. Ramm. Modeling of failure in composites by X-FEM and level-sets within a multiscale framework. *Computer Methods in Applied Mechanical and Engineering*, 197: 414–424, 2008.

[71] T. J. R. Hughes. Multiscale phenomena: Green's function, the Dirichlet-to-Neumann formulation, subgrid scale models, bubbles and the origins of stabilized methods. *Computer Methods in Applied Mechanical and Engineering*, 127:387–401, 1995.

[72] T. J. R. Hughes, G. R. Feijóo, L. Mazzei, and J.-B. Quincy. The variational multiscale method - a paradigm for computational mechanics. *Computer Methods in Applied Mechanical and Engineering*, 166:3–24, 1998.

[73] T. J. R. Hughes, J. A. Cottrell, and Y. Bazilevs. Isogeometric analysis: CAD, finite elements, NURBS, exact geometry and mesh refinement. *Computer Methods in Applied Mechanical and Engineering*, 194:4135–4195, 2005.

[74] D. B. P. Huynh and T. Belytschko. The extended finite element method for fracture in composite materials. *International Journal for Numerical Methods in Engineering*, 77:214–239, 2009.

[75] E. V. Iarve. Mesh independent modelling of cracks by using higher order shape functions. *International Journal for Numerical Methods in Engineering*, 56:869–882, 2003.

[76] S. Jun, W. K. Liu, and T. Belytschko. Explicit reproducing kernel particle methods for large deformation problems. *International Journal for Numerical Methods in Engineering*, 41:137–166, 1998.

[77] P. Kaufmann, S. Martin, M. Botsch, E. Grinspun, and M. Gross. Enrichment textures for detailed cutting of shells. *ACM Transactions on Graphics (TOG)*, 28(3):1–10, 2009. ISSN 0730-0301.

[78] R. B. Kellogg. *Numerical Solution of Partial Differential Equations II*, chapter Singularities in interface problems, pages 351–400. Academic Press, Inc: New York, 1971.

[79] P. Laborde, J. Pommier, Y. Renard, and M. Salaün. High-order extended finite element method for cracked domains. *International Journal for Numerical Methods in Engineering*, 64(3):354–381, September 2005. doi: 10.1002/nme.1370.

[80] J. Lasry, J. Pommier, Y. Renard, and M. Salaün. eXtended finite element methods for thin cracked plates with Kirchoff-Love theory. *International Journal for Numerical Methods in Engineering*, 84:1115–1138, 2010.

[81] B. Lecampion. An extended finite element method for hydraulic fracture problems. *Communications in Numerical Methods in Engineering*, 25:121–133, 2009.

[82] S.-H. Lee, J.-H. Song, Y.-C. Yoon, G. Zi, and T. Belytschko. Combined extended and superimposed finite element method for cracks. *International Journal for Numerical Methods in Engineering*, 59:1119–1136, 2004.

[83] A. Legay, H. W. Wang, and T. Belytschko. Strong and weak arbitrary discontinuities in spectral finite elements. *International Journal for Numerical Methods in Engineering*, 64:991–1008, 2005.

[84] G. Legrain, N. Moës, and A. Huerta. Stability of incompressible formulations enriched with XFEM. *Computer Methods in Applied Mechanical and Engineering*, 197:1835–1849, 2008.

[85] S. Li and W. K. Liu. *Meshfree Particle methods*. Springer, 2004.

[86] S. Li, W. Hao, and W. K. Liu. Numerical simulations of large deformation of thin shell structures using meshfree methods. *Computational Mechanics*, 25:102–116, 2000.

[87] G. R. Liu, T. T. Nguyen, K. Y. Dai, and K. Y. Lam. Theoretical aspects of the smoothed finite element method (SFEM). *International Journal for Numerical Methods in Engineering*, 71:902–930, 2007.

[88] S. J. Liu, H. Wang, and H. Zhang. Smoothed finite elements large deformation analysis. *International Journal of Computational Methods*, 7:513–524, 2010.

[89] W. K. Liu, S. Jun, and Y. Zhang. Reproducing Kernel Particle Method. *International Journal for Numerical Methods in Engineering*, 20:1081–1106, 1995.

[90] X. Y. Liu, Q. Z. Xiao, and B. L. Karihaloo. XFEM for direct evaluation of mixed mode SIFs in homogeneous and bi-materials. *International Journal for Numerical Methods in Engineering*, 59: 1103–1118, 2004.

[91] H. R. Lotfi and P. B. Shing. Embedded representation of fracture in concrete with mixed finite elements. *International Journal for Numerical Methods in Engineering*, 38:1307–1325, 1995.

[92] J. M. Melenk. *On generalized finite element methods*. PhD thesis, University of Maryland, College Park, MD, 1995.

[93] J. M. Melenk and I. Babuška. The partition of unity finite element method: Basic theory and applications. *Computer Methods in Applied Mechanical and Engineering*, 139:289–314, 1996.

[94] A. Menk and S. Bordas. Numerically determined enrichment function for the extended finite element method and applications to bi-material anisotropic fracture and polycrystals. *International Journal for Numerical Methods in Engineering*, 83:805–828, 2010.

[95] A. Menk and S. Bordas. A robust preconditioning technique for the extended finite element method. *International Journal for Numerical Methods in Engineering*, 85:1609–1632, 2011.

[96] J. Mergheim. A variational multiscale method to model crack propagation at finite strains. *International Journal for Numerical Methods in Engineering*, 80:269–289, 2009.

[97] N. Moës and T. Belytschko. Extended finite element method for cohesive crack growth. *Engineering Fracture Mechanics*, 69:813–833, 2002.

[98] N. Moës, J. Dolbow, and T. Belytschko. A finite element method for crack growth without remeshing. *International Journal for Numerical Methods in Engineering*, 46(1):131–150, 1999.

[99] N. Moës, M. Cloirec, P. Cartraud, and J.-F. Remacle. A computational approach to handle complex microstructure geometries. *Computer Methods in Applied Mechanics and Engineering*, 192(28):3163–3177, 2003. doi: 10.1016/S0045-7825(03)00346-3.

[100] C. D. Mote. Glocal-local finite element. *International Journal for Numerical Methods in Engineering*, 3:565–574, 1971.

[101] M. Moumnassi, S. Belouettar, E. Béchet, S. Bordas, D. Quoirin, and M. Potier-Ferry. Finite element analysis on implicitly defined domains: an accurate representation based on arbitrary parametric surfaces. *Computer Methods in Applied Mechanical and Engineering*, 200:774–796, 2011.

[102] S. E. Mousavi and N. Sukumar. Numerical integration of polynomials and discontinuous functions on irregular convex polygons and polyhedrons. *Computational Mechanics*, 2010. doi: 10.1007/s00466-010-0562-5.

[103] S. E. Mousavi and N. Sukumar. Generalized Gaussian quadrature rules for discontinuities and crack singularities in the extended finite element method. *Computer Methods in Applied Mechanical and Engineering*, 199:3237–3249, 2010.

[104] S. E. Mousavi and N. Sukumar. Generalized duffy transformation for integrating vertex singularities. *Computational Mechanics*, 45:127–140, 2010.

[105] S. E. Mousavi, H. Xiao, and N. Sukumar. Generalized Gaussian quadrature rules on arbitrary polygons. *International Journal for Numerical Methods in Engineering*, 82:99–113, 2010.

[106] A. A. Munjiza. *The combined finite-discrete element method*. Wiley Publishers, 2004.

[107] V. Murti, S. Valliappan, and I. K. Lee. Stress intensity factor using quarter point element. *Journal of Engineering Mechanics*, 111:203–217, 1985.

[108] A. Nagarajan and S. Mukherjee. A mapping method for numerical evaluation of two-dimensional integrals with $1/r$ singularity. *Computational Mechanics*, 12:19–26, 1993.

[109] V. P. Nguyen, T. Rabczuk, S. Bordas, and M. Duflot. Meshless methods: A review and computer implementation aspects. *Mathematics and Computers in Simulation*, 79:763–813, 2008.

[110] H. Nguyen-Xuan, S. P. A. Bordas, and H. Nguyen-Dang. Smooth finite element methods: convergence, accuracy and properties. *International Journal for Numerical Methods in Engineering*, 74:175–208, 2008.

[111] S. Nicaise, Y. Renard, and E. Chahine. Optimal convergence analysis for the extended finite element method. *International Journal for Numerical Methods in Engineering*, 86:528–548, 2011.

[112] A. K. Noor and J. M. Peters. Reduced basis techniques for nonlinear analysis of structures. *AIAA Journal*, 18:455–462, 1980.

[113] J. Oliver, A. E. Huespe, and E. Samaniego. A study on finite elements for capturing strong discontinuities. *International Journal for Numerical Methods in Engineering*, 56:2135–2161, 2003.

[114] J. Oliver, A. E. Huespe, and P. J. Sánchez. A comparitive study on finite elements for capturing strong discontinuities: E-FEM vs X-FEM. *Computer Methods in Applied Mechanical and Engineering*, 195:4732–4752, 2006.

[115] M. Ortiz, Y. Leroy, and A. Needleman. A finite element method for localization failure analysis. *Computer Methods in Applied Mechanical and Engineering*, 61:189–214, 1988.

[116] S. Osher and J. Sethian. Fronts propagating with curvature-dependent speed: Algorithms based on Hamilton-Jacobi formulations. *Journal of Computational Physics*, 79:12–49, 1988.

[117] S. G. Papaiannou, P. D. Hilton, and R. A. Lucas. A finite element method for calculating stress intensity factors and its application to composites. *Engineering Fracture Mechanics*, 6:807–823, 1974.

[118] K. Park, J. P. Pereira, C. A. Duarte, and G. H. Paulino. Integration of singular enrichment functions in the generalized/extended finite element method for three-dimensional problems. *International Journal for Numerical Methods in Engineering*, 78:1220–1257, 2008.

[119] S. V. Patankar. *Numerical Heat Transfer and Fluid Flow*. Taylor & Francis, 1980.

[120] C. Pozrikidis. *Introduction to Finite and Spectral element methods*. Chapman & Hall/CRC, 2005.

[121] W. H. Press and B. P. Flannery. *Gausian quadratures and Orthogonal Polynomials*. Numerical Recipes in C (2nd ed.) Cambridge University Press, 1988.

[122] S. M. Quraishi and K. Sandeep. A second generation wavelet based finite elements on triangulations. *Computational Mechanics*, 2011. doi: 10.1007/s00466-011-0586-5.

[123] T. Rabczuk, S. Bordas, and G. Zi. A three-dimensional meshfree method for continuous crack initiation, nucleation and propagation in statics and dynamics. *Computational Mechanics*, 40 (3):473–495, August 2007. doi: 10.1007/s00466-006-0122-1.

[124] T. Rabczuk, G. Zi, A. Gerstenberger, and W. A. Wall. A new crack tip element for the phantom-node method with arbitrary cohesive cracks. *International Journal for Numerical Methods in Engineering*, 75:577–599, 2008.

[125] F. K. F. Radtke, A. Simone, and L. J. Sluys. A partition of unity finite element method for simulating non-linear debonding and matrix failure in thin fibre composites. *International Journal for Numerical Methods in Engineering*, 86:453–476, 2011.

[126] J. Réthoré, A. Gravouil, and A. Combescure. An energy-conserving scheme for dynamic crack growth using the extended finite element method. *International Journal for Numerical Methods in Engineering*, 63:631–659, 2005.

[127] J. Réthoré, S. Roux, and F. Hild. Hybrid analytical and extended finite element method (HAX-FEM) : A new enrichment algorithm for cracked solids. *International Journal for Numerical Methods in Engineering*, 81:269–285, 2010.

[128] J. Réthoré, S. Roux, and F. Hild. Mixed-mode crack propagation using a Hybrid Analytical and eXtended Finite Element Method. *Comptes Rendus Mécanique*, 338:121–126, 2010.

[129] R. Rojas-Díaz, N. Sukumar, A. Sáez, and F. García-Sánchez. Crack analysis in magnetoelectroelastic media using the extended finite element method. In *International Conference on Extended Finite Element Methods*, 2009.

[130] S. A. Sauter and C. Schwab. *Boundary element methods*. Springer-Verlag Berlin Heidelberg, 2011.

[131] J. A. Sethian. *Level Set Methods and Fast Marching Methods: Evolving Interfaces in Computational Geometry, Fuid mechanics, Computer vision and Material science*. Cambridge University Press, 1999.

[132] A. Simone. Partition of unity-based discontinuous elements for interface phenomena: computational issues. *Communications in Numerical Methods in Engineering*, 20:465–478, 2004.

[133] A. H. Soemadi. Generalized Gaussian quadrature. Master's thesis, Texas Tech University, 1989.

[134] J.-H. Song, P. M. Areias, and T. Belytschko. A method for dynamic crack and shear band propagation with phantom nodes. *International Journal for Numerical Methods in Engineering*, 67:868–893, 2006.

[135] M. Stolarska, D. L. Chopp, N. Moës, and T. Belytschko. Modelling crack growth by level sets in the extended finite elemet method. *International Journal for Numerical Methods in Engineering*, 51:943–960, 2001.

[136] G. Strang and G. J. Fix. *An Analysis of the Finite Element Method*. Prentice-Hall, 1973.

[137] G. Strang and G. J. Fix. *An Analysis of the Finite Element Method*. Wellesley-Cambridge Press, second edition, 2008.

[138] T. Strouboulis, I. Babuška, and K. Copps. The design and analysis of the generalized finite element method. *Computer Methods in Applied Mechanical and Engineering*, 181:43–69, 2000.

[139] T. Strouboulis, K. Copps, and I. Babuška. The generalized finite element method. *Computer Methods in Applied Mechanical and Engineering*, 190:4081–4193, 2001.

[140] M. C. Sukop. *Lattice Boltzmann Modeling: An Introduction for Geoscientists and Engineers*. Springer, 2006.

[141] N. Sukumar. Construction of polygonal interpolants: A maximum entropy approach. *International Journal of Numerical Methods in Engineering*, 61(12):2159–2181, 2004.

[142] N. Sukumar and E. Malsch. Recent advances in the construction of polygonal finite element interpolants. *Archives of Computational Methods in Engineering*, 13(1):129–163, 2006.

[143] N. Sukumar and J.-H. Prévost. Modeling quasi-static crack growth with the extended finite element method part i: Computer implementation. *International Journal of Solids and Structures*, 40:7513–7537, 2003.

[144] N. Sukumar, N. Moës, B. Moran, and T. Belytschko. Extended finite element method for three-dimensional crack modelling. *International Journal for Numerical Methods in Engineering*, 48:1549–1570, 2000.

[145] N. Sukumar, D. L. Chopp, N. Moës, and T. Belytschko. Modeling holes and inclusions by level sets in the extended finite-element method. *Computer Methods in Applied Mechanical and Engineering*, 190:6183–6200, 2001.

[146] N. Sukumar, D. L. Chopp, and B. Moran. Extended finite element method and fast marching method for three-dimensional fatigue crack propagation. *Engineering Fracture Mechanics*, 70: 29–48, 2003.

[147] S. Tanaka, H. Okada, S. Okazawa, and M. Fujikubo. Analysis of elastostatic crack problems using B-spline wavelet finite element method. In *Proceedings of the Eighteenth International offshore and polar engineering conference, Vancouver, Canada, July 6 - 11*, 2008.

[148] P. Tong, T. H. H. Pian, and S. J. Lasry. A hybrid-element approach to crack problems in plane elasticity. *International Journal for Numerical Methods in Engineering*, 7:297–308, 1973.

[149] D. M. Tracey. Finite elements for determination of crack-tip elastic stress intensity factors. Technical Report AD0732837, Army materials and mechanisc research center watertown mass, 1971.

[150] J. E. Tranacón, A. Vercher, E. Giner, and F. J. Feuenmayor. Enhanced blending elemetns for XFEM applied to linear elastic fracture mechanics. *International Journal for Numerical Methods in Engineering*, 77:126–148, 2009.

[151] G. Ventura. On the elimination of quadrature subcells for discontinuous functions in the extended finite-element method. *International Journal for Numerical Methods in Engineering*, 66(5): 767–795, 2006.

[152] G. Ventura, B. Moran, and T. Belytschko. Dislocations by partition of unity. *International Journal for Numerical Methods in Engineering*, 62:1463–1487, 2005.

[153] G. Ventura, R. Gracie, and T. Belytschko. Fast integration and weight function blending in the extended finite element method. *International Journal for Numerical Methods in Engineering*, 77: 1–29, 2009. doi: 10.1002/nme.2387.

[154] C. V. Verhoosel, M. A. Scott, R. de Borst, and T. J. R. Hughes. An isogeometric analysis to cohesive zone modeling. *International Journal for Numerical Methods in Engineering*, 10.1002/nme.3061, 2010. doi: 10.1002/nme.3061.

[155] R. Wait and A. R. Mitchell. Corner singularities in elliptic problems by finite element methods. *Journal of Computational Physics*, 8:45–52, 1971.

[156] G. N. Wells and L. J. Sluys. A new method for modelling cohesive cracks using finite elements. *International Journal for Numerical Methods in Engineering*, 50:2667–2682, 2001.

[157] G. N. Wells, L. J. Sluys, and R. de Borst. Simulating the propagation of displacement discontinuities in a regularized strain-softening medium. *International Journal for Numerical Methods in Engineering*, 53(5):1235–1256, 2002. ISSN 1097-0207.

[158] J. R. Whiteman and J. E. Akin. Finite elements, singularities and fracture. In *The Mathematics of finite elements applications III*, pages 35–54, 1978.

[159] M. Williams. On the stress distribution at the base of a stationary crack. *ASME Journal of Applied Mechanics*, 24:109–114, 1957.

[160] E. Wyart, D. Coulon, M. Duflot, T. Pardoen, J.-F. Remacle, and F. Lani. A substructured FE shell/XFE 3D method for crack analysis. *International Journal for Numerical Methods in Engineering*, 72(7):757–779, 2007. doi: 10.1002/nme.2029.

[161] H. Xiao and Z. Gimbutas. A numerical algorithm for the construction of efficient quadrature rules in two and higher dimensions. *Computers and Mathematics with Applications*, 59:663–676, 2010.

[162] Q. Z. Xiao and B. L. Karihaloo. Direct evaluation of accurate coefficients of the linear elastic crack tip asymptotic field. *Fatigue & Fracture of Engineering Materials & Structures*, 26:719–729, 2003.

[163] Q. Z. Xiao and B. L. Karihaloo. Improving the accuracy of XFEM crack tip fields using higher order quadrature and statically admissible stress recovery. *International Journal for Numerical Methods in Engineering*, 66(9):1378–1410, 2006.

[164] Q. Z. Xiao and B. L. Karihaloo. Implementation of hybrid crack element on a general finite element mesh and in combination with XFEM. *Computer Methods in Applied Mechanical and Engineering*, 196:1864–1873, 2007.

[165] G. Zi and T. Belytschko. New crack-tip elements for (XFEM) and applications to cohesive cracks. *International Journal for Numerical Methods in Engineering*, 57:2221–2240, 2003.

[166] O. C. Zienkiewicz, R. L. Taylor, and J. Z. Zhu. *The finite element method: its basics and fundamentals*. Elsevier Butterworth Heinemann, 6^{th} edition, 2000.

3

Advances in numerical integration techniques for enriched FEM

This chapter presents some advances in numerical integration over enriched elements in XFEM. Two new numerical integration techniques are presented in this chapter that can complement the conventional XFEM. The first method relies on conformal mapping and is restricted to 2D problems, while the second method relies on strain smoothing. Both methods are unrelated in their spirit, but aim at improving numerical integration in the conventional XFEM. The development of both methods is motivated by the following:

- **Decreasing the complexity of sub-integration in the XFEM**
  - by conformally mapping the enriched elements onto a unit disk and using cubature on this unit disk.
  - by integrating over the boundary of the elements intersected by the discontinuities (material interfaces, cracks, voids).
- **Avoiding the need to integrate the singular functions** present in the XFEM stiffness matrix in the LEFM. With the strain smoothing technique, the derivatives of the shape functions are no longer necessary, hence, the $1/r$ [3, 24, 32] term does not appear in the integral.

This chapter is organized as follows. Section 3.1 discusses the basic idea behind using the conformal mapping to integrate over any arbitrary polygon and over enriched elements. After giving a brief overview of the strain smoothing in the FEM, the coupling of the strain smoothing technique with partition of unity enrichment is developed in Section 3.2. The resulting method is called the Smoothed eXtended Finite Element Method (SmXFEM). The salient features of the proposed methods are summarized in the last section.

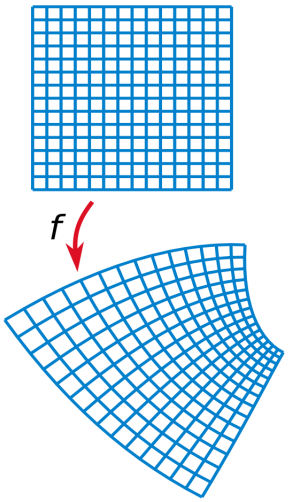

Figure 3.1: A rectangular grid (top) and its image under a conformal map f (bottom). It can be seen that f maps pairs of lines intersecting at 90° to pairs of curves intersecting at 90°. In general, a conformal map preserves oriented angles.

3.1 Numerical integration based on conformal mapping

In this section, a new numerical integration technique based on a conformal mapping for arbitrary polygons that can be used for the elements intersected by a discontinuity surface is presented. The proposed method eliminates the need to sub-triangulate the polygonal region intersected by the discontinuity or to sub-triangulate the polygonal element. A conformal maps transforms any pair of curves intersecting at a point in the region so that the image curves intersect at the same angle (see Figure 3.1).

3.1.1 Conformal mapping

Definition: A mapping that preserves the angles between the intersecting arcs when mapping one open region in the complex plane $\mathbb{C}$ onto another by a function which is analytic and one-to-one and has a 'nonzero' derivative everywhere is called a conformal map.

This follows from the Riemann mapping theorem, which states that:

Riemann mapping theorem: If U is a non-empty simply connected open subset of the complex number plane $\mathbb{C}$, then there exists a biholomorphic (bijective[a] and holomorphic[b]) mapping

[a] is a function f from a set X to a set Y with the property that, for every y in Y, there is exactly one x in X such that $f(x) = y$.

[b] Also called analytic function, regular function, differentiable function, complex differentiable function and holomorphic map [23]. The word derives from the Greek 'holos', meaning 'whole'.

f from U onto the open unit disk D.

$$D = \{z \in \mathbb{C} \colon |z| < 1\} \tag{3.1}$$

Corollary: Any two simply connected open subsets of the Riemann Sphere [c] can be conformally mapped into each other.
A map

$$w = f(z) \tag{3.2}$$

is called conformal at a point z_o if it preserves oriented angles between the curves through z_o.

Example A conformal map can be used to convert a circular cylinder into a family of aerofoil shapes. This transformation is called the Joukowsky transform and finds important applications in the study of two-dimensional potential flow around aerofoils. The transform is given by:

$$w = f(z) = z + \frac{1}{z} \tag{3.3}$$

where $z = x + iy$ is a complex variable in the transformed space and $w = \xi + i\eta$ is a complex variable in the physical space and $\xi = \xi(x, y), \eta = \eta(x, y)$.

Jacobian of an analytic function of a complex variable

Consider a general function of a complex variable $w = f(z)$ where $z = x+iy$ and $w = \xi+i\eta$. In a region where the function f is analytic, the Jacobian of the transformation is given by:

$$\begin{vmatrix} \xi_{,x} & \xi_{,y} \\ \eta_{,x} & \eta_{,y} \end{vmatrix} = |f(z)_{,z}|^2 \tag{3.4}$$

where subscript 'comma' represents the partial derivative with respect to the spatial coordinate succeeding it.If f is analytic in a region, then it satisfies Cauchy-Riemann equations, given by:

$$\begin{aligned} \xi_{,x} &= \eta_{,y} \\ \xi_{,y} &= -\eta_{,x} \end{aligned} \tag{3.5}$$

[c] Named after mathematician Bernhard Riemann, is the sphere obtained from the complex plane by adding a point at infinity.

Thus,

$$\begin{vmatrix} \xi_{,x} & \xi_{,y} \\ \eta_{,x} & \eta_{,y} \end{vmatrix} = \begin{vmatrix} \xi_{,x} & \xi_{,y} \\ -\xi_{,y} & \xi_{,x} \end{vmatrix} = |f(z)_{,z}|^2 \tag{3.6}$$

It follows that the transformation is one-to-one in regions where $f(z)_{,z} = \frac{df(z)}{dz} \neq 0$. The Riemann mapping theorem [9] describes an existence of such a mapping but does not tell us how to explicitly construct the mapping. The recipe for such a mapping is given by the Schwarz-Christoffel transformation, discussed next.

3.1.2 Schwarz-Christoffel Conformal Mapping (SCCM)

The Schwarz-Christoffel formula was proposed independently by Christoffel in 1867 [8] and Schwarz in 1869 [41]. The Schwarz-Christoffel transformation is based on the following postulate:

Theorem: Let U be the interior of a polygon Γ having vertices $w_1, w_2, \cdots, w_n$ and interior angles $\pi\alpha_1, \pi\alpha_2, \cdots, \pi\alpha_n$ in counter-clockwise order. Let f be any conformal map from the unit disk D to U, then the Schwarz-Christoffel formula for a disk is given by:

$$w = f(z) = A + C \int_0^z \prod_{k=1}^{n} \left(1 - \frac{\varsigma}{z_k}\right)^{\alpha_k - 1} \mathrm{d}\varsigma \tag{3.7}$$

where A and C are complex constants $(C \neq 0)$. Here $z = x + iy$ corresponds to a point in the complex plane and $w = \xi + i\eta$ is its corresponding map in the complex polygonal plane. The function f maps the unit disk in the complex plane conformally onto a polygonal plane U (see Figure 3.2). An inverse mapping also exists [44, 45] and since the map is conformal, the positivity of the Jacobian is ensured.
For example, $n = 1$ is a line with vertex $w_1 = \infty$ and $\alpha_1 = -1$. Applying the Schwarz-Christoffel formula, given by Equation (3.7), leads to:

$$w = f(z) = A + C \int_0^z \left(1 - \frac{\varsigma}{z_k}\right)^{-2} \mathrm{d}\varsigma = A - \frac{C}{1 - \frac{z}{z_1}} \tag{3.8}$$

The above equation maps the interior of the disk onto a half-plane and this is a Möbius transformation[d]. There are two degrees of freedom still unspecified, for example, the complex constants A and C. The SCCM is semi-explicit since the pre-vertices are not given and cannot in general be found analytically [40, 44]. A conformal map between the two domains is not unique unless these constants are fixed (e.g., A and C). Two common choices are to

[d] Also called bilinear, linear functional transformation. A transformation of the form $w = \frac{az+b}{cz+d}$ is called a Möbius transformation, where $ad - bc \neq 0$ and a, b, c, d are complex numbers

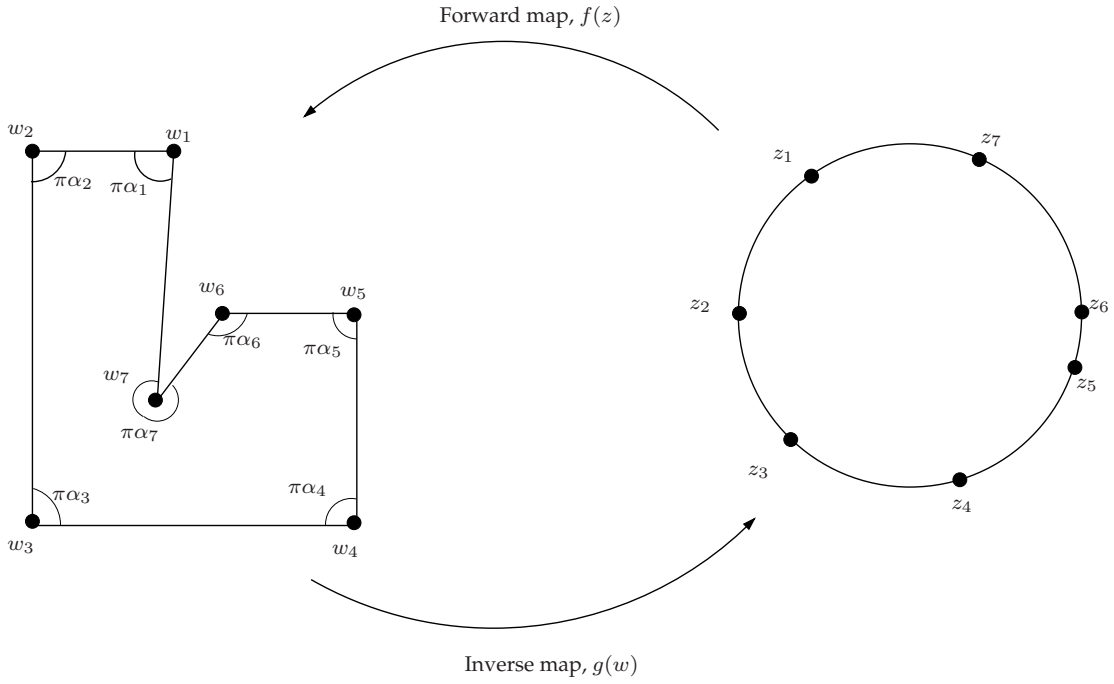

Figure 3.2: Notational conventions of the SCCM.

fix any three pre-vertices, e.g., $z_1 = -1, z_2 = -i$ and $z_3 = 1$ or to fix the conformal center, $f(0) = w$ and $f'(0) > 0$. For problems with more vertices, unless the polygon is symmetric, in general, the SCCM integral in Equation (3.7) has no closed-form solution [1, 43, 44, 45]. In such cases, the SCCM involves the following three numerical steps:

1. Finding points z_k (see Figure 3.2), known as parameter problem; these unknown parameters can be found by solving a system of non-linear equations that assert that the side lengths of the polygon are correct.

2. Calculating the SCCM integral in Equation (3.7). Numerical evaluation of the integral is done by a *Compound Gauß Jacobi quadrature*.

3. By using Newton iterations, the inverse of the map is computed.

The steps involved in the numerical conformal mapping are illustrated in Figure 3.3. All these numerical steps are implemented in the open source MATLAB toolbox [14]. Figure 3.4 shows a conformal mapping of an arbitrary polygon onto a unit disk. The mapping is made with respect to a point in the complex plane, which forms the conformal center. Either the geometric center of the polygon is specified or it could be user specified.

Jacobian of the mapping Let the conformal mapping be given by Equation (3.2) and the Schwarz-Christoffel formula given by Equation (3.7). The differential form of the Schwarz-

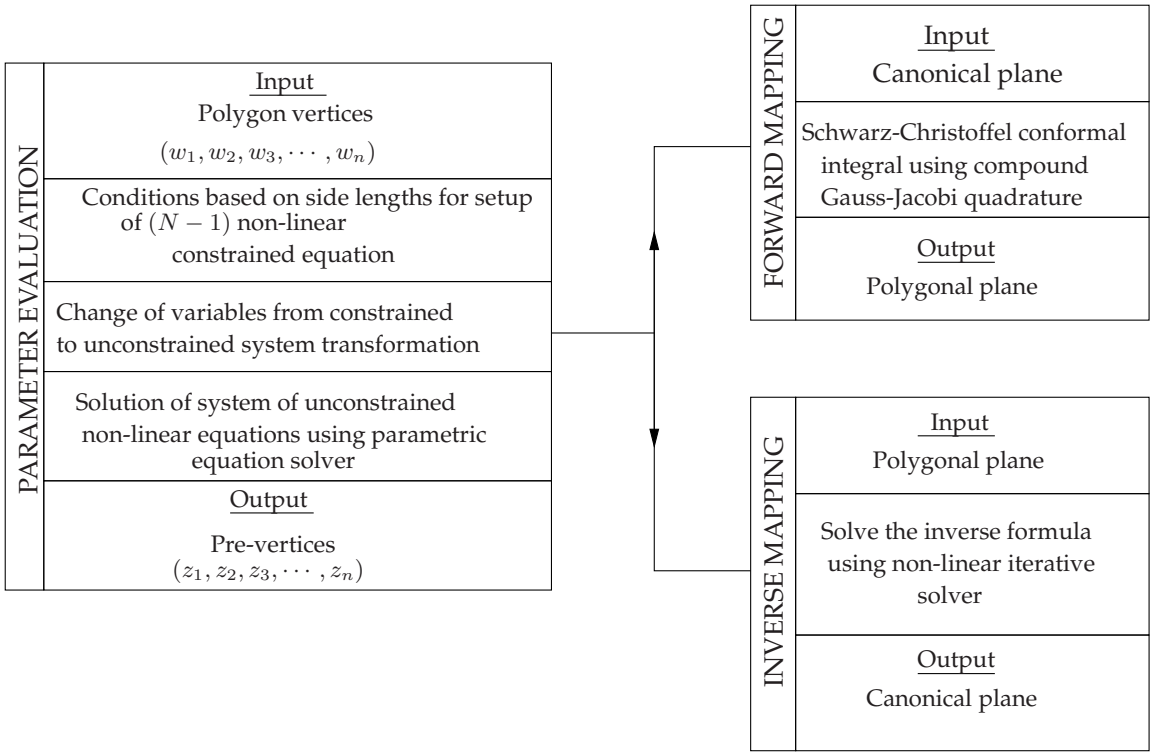

Figure 3.3: Steps involved in the implementation of numerical conformal mapping.

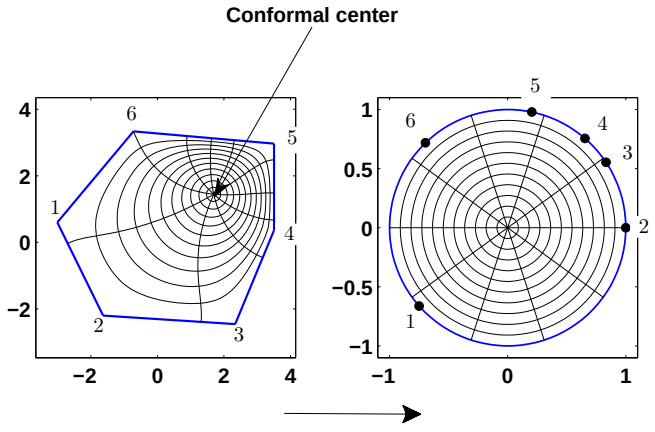

Figure 3.4: Mapping of the physical domain onto a unit disk. This picture was produced with the MATLAB SC toolbox [14]. The SCCM maps the interior of the polygon onto the disk. A pair of lines intersecting at an angle in the polygon is mapped to a pair of lines inside the disk, intersecting at the same angle.

Christoffel formula is given by [14]:

$$\frac{df(z)}{dz} = C \prod_{k=1}^{n} \left(1 - \frac{\varsigma}{z_k}\right)^{\alpha_k - 1}. \tag{3.9}$$

The Jacobian of the mapping can be computed by inverting Equation (3.9). The numerical implementation of this inversion is discussed in [15] and implemented in the toolbox [14].

3.1.3 Numerical integration rule

In this section, cubature rules based on midpoint rule [13] and product rule [38] on the unit disk are discussed.

Midpoint Rule

De and Bathe [13] proposed a simple quadrature rule by subdividing the disk into concentric circles and radial lines and implemented a midpoint quadrature rule for the interior of the disk. The integral is evaluated on each of the subdomains as the area of the subdomain multiplied by the integrand evaluated at the centroid of the subdomain (see Figure 3.5). To integrate $f(x, y)$ on a disk (Ω) of radius R_o,

$$\int\int_{\Omega} f(x,y)dxdy \simeq \sum_{i=1}^{n_\theta} \sum_{j=1}^{n_r} A_j f(r_j \cos\theta_i, r_j \sin\theta_i) \tag{3.10}$$

where n_θ is the number of sectors in which the disk is partitioned and n_r is the number of radial sub-divisions. Here,

$$\begin{aligned} r_j &= \frac{j^2 - j + 1/3}{j - 1/2}\Delta r; \qquad \theta_i = (i - 1/2)\Delta\theta \\ \Delta r = \frac{R_o}{n_r};\ \ \Delta\theta = \frac{2\pi}{n_\theta}; &\qquad A_j = \left(j - \frac{1}{2}\right)\Delta\theta(\Delta r)^2 \end{aligned} \tag{3.11}$$

where r and θ are the polar coordinates and A_{ij} is the corresponding weight of the integration point.

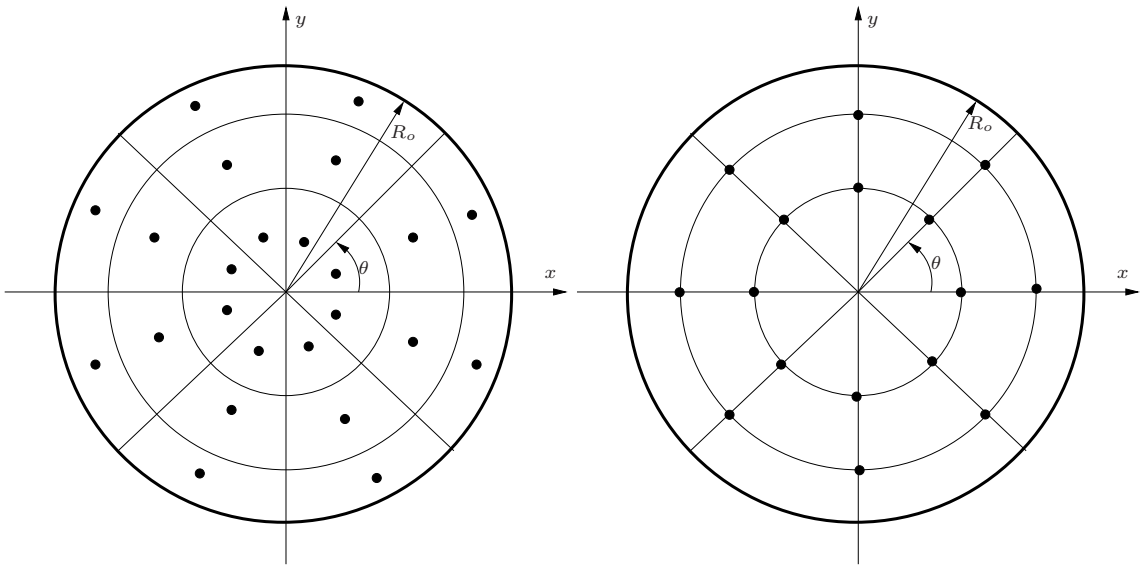

(a) Midpoint rule (b) Gauß - Chebyshev rule

Figure 3.5: Quadrature rule on a disk.

Gauß-Chebyshev Rule

Peirce [38] proposed the following approximation to evaluate the integral over a planar annulus based on Legendre polynomials[e] and Chebyshev nodes[f]:

$$\int\int_{\Omega} f(x,y)dxdy \simeq \sum_{i=1}^{4(m+1)} \sum_{j=1}^{m+1} A_j f(r_j \cos\theta_i, r_j \sin\theta_i) \tag{3.12}$$

where

1. $\theta_i = \frac{i\pi}{2(m+1)}$, $i = 1, 2, \cdots 4(m+1)$, $m = 0, 1, 2, \cdots$
2. $A_j = \frac{\pi}{4(m+1)P'_{m+1}r_j^2} \int_0^{R_0^2} \frac{P_{m+1}r^2}{r^2 - r_j^2}\ \mathrm{d}r$, $j = 1, 2, \cdots, m+1$
3. r_i^2 are the $m+1$ zeros of $P_{m+1}(r^2)$, the Legendre polynomial in r^2 of degree $m+1$, orthogonalized on $\left[0, R_o^2\right]$ (R_o defined in Figure 3.5).

where θ_i are the Chebyshev nodes. The integration points are on equally spaced radii and the weights are independent of the angular position. The distributions of the integration

[e]Legendre polynomials are defined by the following recurrence relation: $P_o(x) = 1$, $P_1(x) =$ x and $(n+1)P_{n+1}(x) = (2n+1)xP_n(x) - nP_{n-1}(x)$.

[f]Chebyshev nodes are the roots of the Chebhyshev polynomial of the first kind. The Chebyshev polynomials of the first kind are defined by the following recurrence relation: $T_o(x) = 1$, $T_1(x) = x$ and $T_{n+1}(x) = 2xT_n(x) - T_{n-1}(x)$

points for the midpoint quadrature and for the Gauß-Chebyshev quadrature are illustrated in Figure 3.5. For all the numerical examples presented in this work, a midpoint quadrature rule is used. Other cubature rules on a unit disk based on orthogonal polynomials are given in [10, 11, 25, 39].

3.1.4 Numerical integration over polygons and discontinuous elements

The SCCM combined with the midpoint quadrature can be used to integrate over arbitrary polygons and over the elements intersected by the discontinuity. This basic idea is discussed in this section.

Integration over arbitrary polygons

In the context of polygonal finite elements[g], one potential solution for the purpose of numerical integration over arbitrary polygons as described by Sukumar and Tabaraei [42] is to sub-divide the physical element into triangles and then use well-known quadrature rules on a triangle. In this study, this method is called the sub-triangulation method. As described in [42], the purpose of sub-dividing into triangles is solely for the purpose of numerical integration and does not introduce new degrees of freedom.

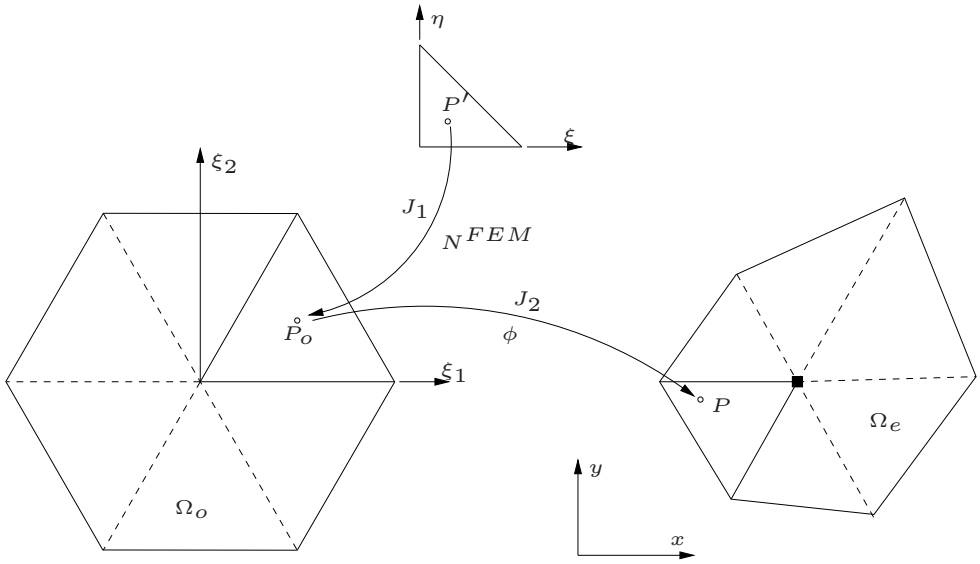

Figure 3.6: Numerical integration based on the partition of the physical element, where J_1 and J_2 are the Jacobian that corresponds to the two level mapping.

The sequence of transformations used is illustrated in Figure 3.6. For a polygon with $n > 4$, where n is the number of sides of the polygon, the centroid of the element is used to par-

[g]In polygonal finite elements, the number of sides of the element is not limited to four in 2D [33, 42].

tition it into n triangles. The method involves two levels of isoparametric mapping. By using the SCCM, an arbitrary polygon can be mapped onto a unit disk and cubature rules described above can be used for the purpose of numerical integration. This eliminates the need for sub-dividing the polygon and the need for a two level isoparametric mapping. Figure 3.7 shows the location of the integration points on different polygonal elements for the sub-triangulation method and the SCCM combined with the midpoint quadrature rule. The efficiency of the proposed numerical integration technique is illustrated by computing the integral of a few polynomial functions over different polygonal domains. The numerical results are given in Table 3.1 and are compared with the sub-triangulation method. It can be seen that for low order polygons such as quadrilaterals, the relative error in the computed value between the sub-triangulation and the SCCM midpoint rule is about 4%, but with the increase in the number of sides of the polygon, the error between the methods decreases and is within 2%. Natarajan *et al.,* [33] used SCCM to integrate over arbitrary polygons in the context of polygonal FE and applied it to solve elasticity problems. Some results pertaining to this study are presented in Appendix B.

Table 3.1: Numerical Integration of polynomial functions over polygonal domains: comparison between the sub-triangulation method and the SCCM combined with midpoint quadrature rule. A total of 20 integration points for both methods is used in evaluating the integral.

Region	Method	Polynomial function			
		1	x^2	$(xy)^2$	$(x+y)^2$
Quadrilateral	Triangulation	4.0000	1.3333	0.4630	2.6667
	Midpoint	3.9483	1.2860	0.4010	2.5472
Hexagon	Triangulation	2.5981	0.5413	0.0744	1.0825
	Midpoint	2.5946	0.5404	0.0752	1.0822
Octagon	Triangulation	2.8284	0.6381	0.0944	1.2761
	Midpoint	2.8286	0.6381	0.0954	1.2745
Decagon	Triangulation	2.9389	0.6880	0.1054	1.3759
	Midpoint	2.9379	0.6870	0.1073	1.3766

Integration over enriched elements

In the conventional XFEM, the numerical integration over the elements intersected by the discontinuity is done by sub-dividing the elements in to sub-domains (triangular sub-domains in this case). This poses two problems:

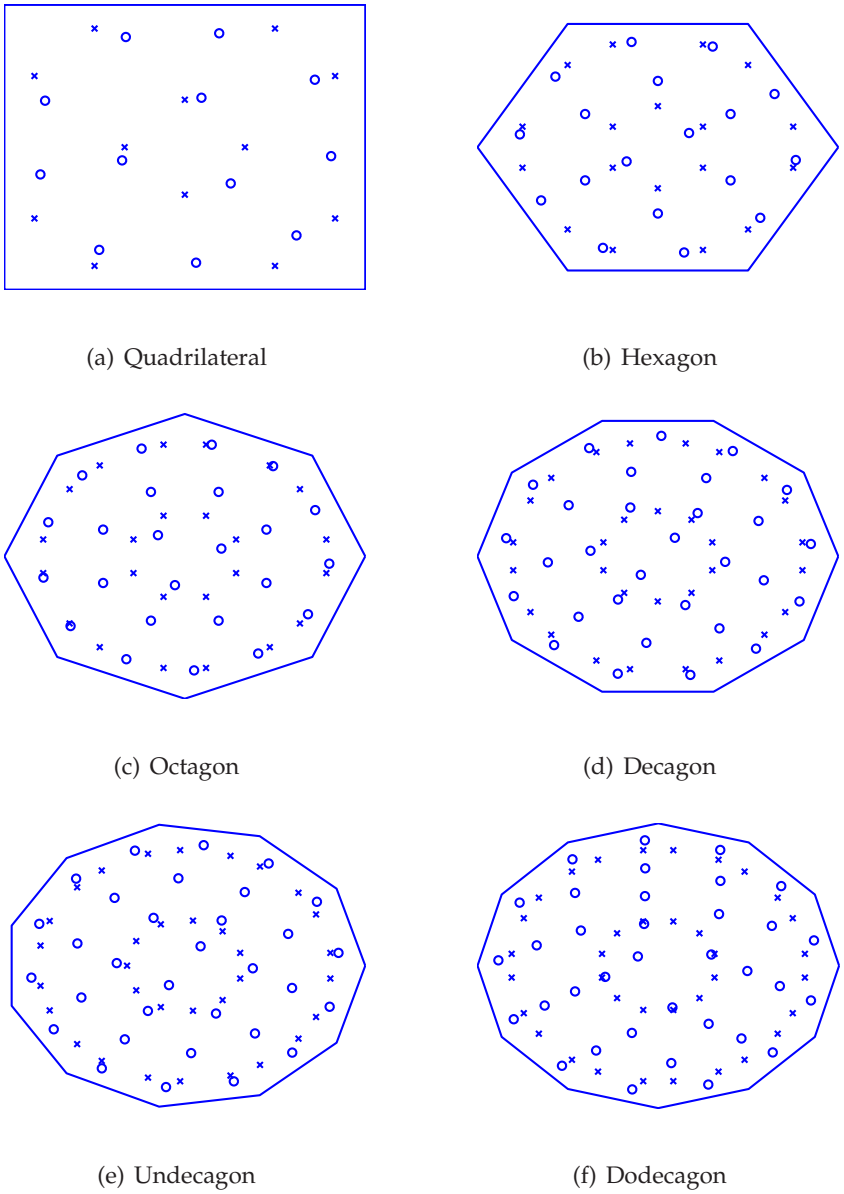

(a) Quadrilateral (b) Hexagon

(c) Octagon (d) Decagon

(e) Undecagon (f) Dodecagon

Figure 3.7: The distribution of integration points on different polygonal elements, '×' denotes the location of the integration points for the sub-triangulation method and '○' denotes the location of the integration points for the SCCM combined with mid point quadrature rule.

- The sub-triangulation introduces a 'mesh' requirement (c.f. Section 2.4.5).
- Involves two level isoparametric mapping.

By employing the SCCM, the above two steps can be circumvented. By conformally mapping each part of the element intersected by the discontinuous surface, the 'mesh' requirement is suppressed. Figure 3.8 illustrates the above idea for the split and the tip element. Conformal (same form or shape) mapping is an important technique used in complex analysis and has many applications in different physical solutions. Trukrov and Novak [46] computed the effective elastic properties of materials with irregular shaped heterogeneities using a numerical conformal mapping. Ishikawa and Kohno [21] have used the conformal mapping to analyse the stress singularity at the corner of a rigid square inclusion in an infinite plate. Tiwary *et al.,* [43] analysed the stress distribution in the microstructures having arbitrary shaped heterogeneities using the numerical conformal mapping combined with the Voronoi cell finite element method. In their work, the shape based stress functions were computed by the Schwarz-Christoffel Conformal Mapping (SCCM). Markovic *et al.,* [31] used SCCM to determine the 2D magnetic field in a square magnetic circuit. By transforming the pipe into a strip using SCCM, Fyrillas [17] optimized the conduction rate in a solid slab embedded in a pipe of general cross-section. Elcart and Hu [16] used SCCM combined with electrostatic measurements to detect surface and interior cracks. SCCM techniques have been used to generate FE meshes in two-dimensional fracture mechanics problems [18] and multiple connected regions [26]. Wu *et al.,* [50] reduced the mixed boundary value problem of interfacial crack between two elastic strips to the standard Riemann-Hilbert[h] problem using a conformal mapping technique. Barra *et al.,* [2] used conformal maps to study the geometrical characteristics of quasistatic fractures in brittle materials. In this study, the conformal mapping will be used to integrate over arbitrary polygons and over the enriched elements. A detailed discussion on the effectiveness and the robustness is presented in Chapter 4.

3.2 Strain smoothing in FEM and XFEM

Stabilized Conformal Nodal Integration (SCNI) [7] was constituted to suppress the instabilities arising in nodally integrated mesh-free methods by avoiding the computation of the derivatives of the shape functions, which vanish at the nodes. Liu *et al.,* [27] extended the idea of SCNI to finite element approximations and named the resulting method the Smoothed Finite Element Method (SFEM). In this section, after recalling the basics of strain smoothing in the FEM, the basic theory behind the coupling of the SSM with partition of unity enrichment is presented.

[h] are a class of problems that arise in the study of differential equations in the complex plane.

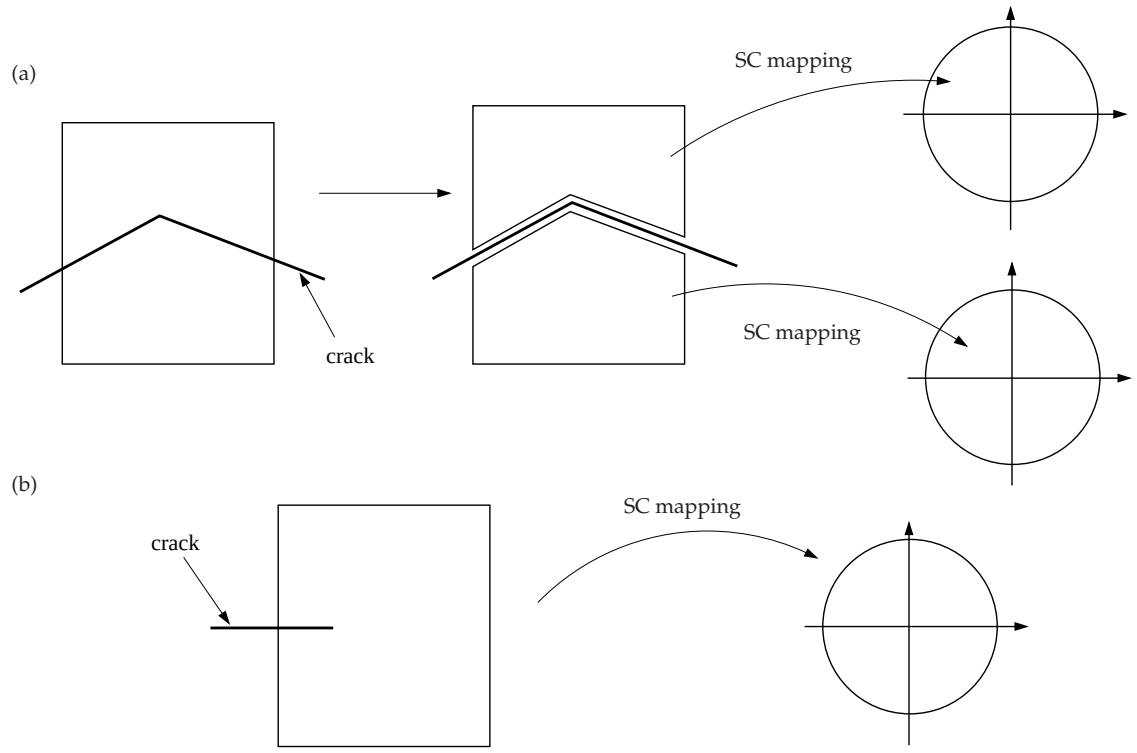

Figure 3.8: Integration over an element with discontinuity (Solid line): (a) with kinked discontinuity, representing the split element and (b) strong discontinuity, representing the tip element. In the case of split element, each sub-polygon is mapped conformally onto the unit disk and in case of the tip element, the resulting polygon is mapped conformally onto the unit disk using Schwarz-Christoffel conformal mapping.

3.2.1 Strain smoothing in the FEM

By incorporating the SSM into the FEM, Liu *et al.,* have formulated a series of SFEMs named as cell-based SFEM (CS-FEM) [6, 12, 27, 36], node-based SFEM (NS-FEM) [30], edge-based SFEM (ES-FEM) [29], face-based SFEM (FS-FEM) [35] and alpha-FEM [28].
Since the inception of the SFEM in 2006, the convergence, the stability, the accuracy and the computational complexity of this method was studied in [6, 27, 36]. The CS-FEM has been applied to various problems in mechanics such as plates [37], shells [34], acoustic problems [20, 52], nonlinear analysis [48], fluid-structure interactions [19] and heat transfer analysis [22, 49] . Yet, to date, all work on the CS-FEM has been restricted to linear complete bases and bi-linear shape functions. Some preliminary results on the extension of SSM to higher order elements is given in Appendix C.
The smoothing allows to transform the volume integration into surface integration in case of 3D and surface into contour integration in case of 2D by the divergence theorem[i]. It is observed that when the SSM is applied to a linear triangular element, the CS-FEM yields identical results to its FEM counterpart, irrespective of the number of smoothing cells. This is true for any linear approximation (2 noded bar element, 4 noded tetrahedron element, etc.,). For a bi-linear element, the solution of the SFEM differs from that of the FEM, because the gradient of the shape functions is not a constant. On the contrary, other smoothing methods, such as, the ESFEM and the FSFEM are shown to improve the accuracy of the triangular or tetrahedral elements [29, 35]. However, the bandwidth of the stiffness matrix in case of the NS-FEM, ES-FEM and FS-FEM is found to be greater than the FEM, while the band width of CS-FEM is the same as that of the FEM. Other advantages of strain smoothing include a low sensitivity to mesh distortion and absence of volumetric locking. These nice properties motivated the study of the behaviour of strain smoothing for enriched approximation (see Section 3.2.2) and [4, 5].

Description of the theory

In the SCNI, the strain field used to construct the stiffness matrix is written as the divergence of a spatial average of the standard (compatible) strain field –i.e. symmetric gradient of the displacement field. Elements are divided into subcells, as shown in Figures (3.9), (3.10) and (3.11). Different numbers of smoothing cells per element confer the method with different properties [6, 12, 27, 36]. The strain field $\tilde{\varepsilon}_{ij}^h$, used to compute the stiffness matrix is computed by a weighted average of the standard strain field ε_{ij}^h. At a point $\mathbf{x}_C$ in an element Ω^h,

[i] If $\mathbf{F}$ is a continuously differentiable vector field defined on a neighbourhood of V, then we have $\int_V \nabla \cdot \mathbf{F}\, \mathrm{d}V = \oint_S \mathbf{F} \cdot \mathbf{n}\, \mathrm{d}S$, where $V \subset \mathbb{R}^n$.

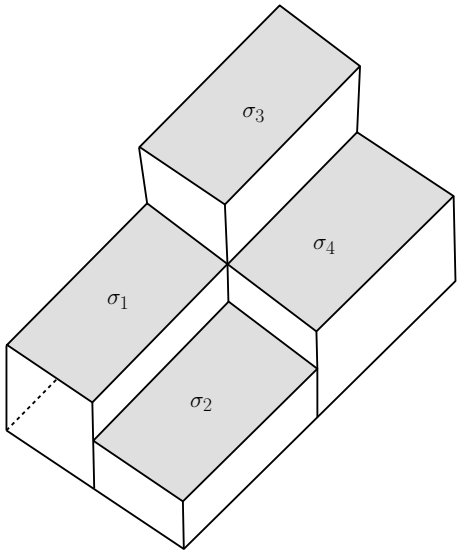

Figure 3.9: Stress field in a smoothed finite element. The stress is constant over each smoothing cell, but discontinuous across cells. On the contrary, the displacement field is continuous within an element. $\sigma_i, i = 1, 2, 3, 4$ are the stresses within each subcell.

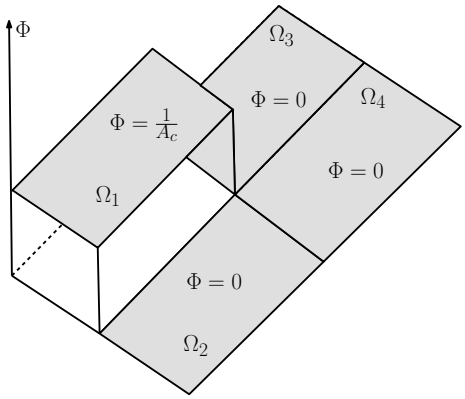

Figure 3.10: The weight function or the smoothing function is defined for each subcell as constant equal to the inverse of the area of the subcell and zero elsewhere. This permits transforming the domain integral into a boundary integral over the boundary of the subcell. If a single subcell is used, integration over the boundary of the finite element is recovered. This figure shows the weight function Φ used for subcell Ω_{C}.

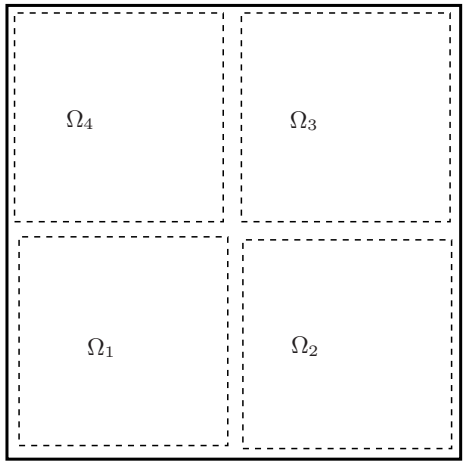

$$\Omega^h = \Omega_1 \cup \Omega_2 \cup \Omega_3 \cup \Omega_4$$

$$\tilde{\mathbf{K}}^e = \sum_{C=1}^{4} \tilde{\mathbf{B}}_C^{\mathrm{T}} \mathbf{D} \tilde{\mathbf{B}}_C A_C$$

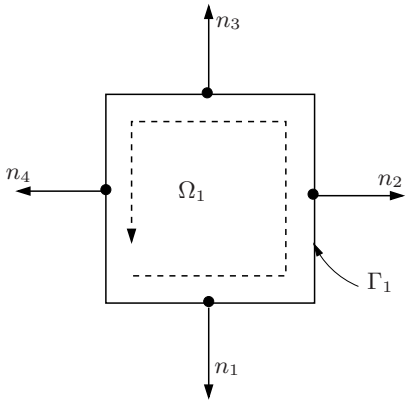

$$\tilde{\mathbf{B}}_1 = \frac{1}{A_1} \int_{\Gamma_1} \mathbf{n}^{\mathrm{T}} N_I(\mathbf{x}) \, \mathrm{d}\Gamma$$

Figure 3.11: Calculation of the smoothed discretized gradient operator. The integration is performed along the boundary of each subcell. The smoothing cells are represented by dashed lines, where $\mathbf{n}$ is the unit outward normal to the smoothing cell Ω_{C}. The location of the integration point is represented by a filled circle.

$$\tilde{\varepsilon}_{ij}^{h}(\mathbf{x}_C) = \int_{\Omega^h} \varepsilon_{ij}^{h}(\mathbf{x})\Phi(\mathbf{x}-\mathbf{x}_C)\mathrm{d}\mathbf{x}, \tag{3.13}$$

where Φ is a smoothing function that generally satisfies the following properties [53] (See Figure 3.10):

$$\Phi \geq 0 \quad \text{and} \quad \int_{\Omega^h} \Phi(\mathbf{x})\mathrm{d}\mathbf{x} = 1. \tag{3.14}$$

One possible choice of Φ is given by:

$$\Phi = \frac{1}{A_C} \quad \text{in} \quad \Omega_{\mathrm{C}} \quad \text{and} \quad \Phi = 0 \quad \text{elsewhere.} \tag{3.15}$$

where A_C is the area of the subcell. To use Equation (3.13), the subcell containing the point $\mathbf{x}_C$ must first be located in order to compute the correct value of the weight function Φ. The discretized strain field is computed, through the smoothed discretized gradient operator or the smoothed strain-displacement operator, $\tilde{\mathbf{B}}$, defined by (see Figure 3.11 for a schematic representation of the construction):

$$\tilde{\boldsymbol{\varepsilon}}^{h}(\mathbf{x}_C) = \tilde{\mathbf{B}}_C(\mathbf{x}_C)\mathbf{q} \tag{3.16}$$

where $\mathbf{q}$ are the unknown displacements coefficients defined at the nodes of the finite element, as usual. The smoothed element stiffness matrix for element e is computed by the *sum of the contributions of the subcells* (Figure 3.11)[j]:

$$\tilde{\mathbf{K}}^{e} = \sum_{C=1}^{nc} \int_{\Omega_{\mathrm{C}}} \tilde{\mathbf{B}}_C^{\mathrm{T}}\mathbf{D}\tilde{\mathbf{B}}_C \mathrm{d}\Omega = \sum_{C=1}^{nc} \tilde{\mathbf{B}}_C^{\mathrm{T}}\mathbf{D}\tilde{\mathbf{B}}_C \int_{\Omega_{\mathrm{C}}} \mathrm{d}\Omega = \sum_{C=1}^{nc} \tilde{\mathbf{B}}_C^{\mathrm{T}}\mathbf{D}\tilde{\mathbf{B}}_C A_C \tag{3.17}$$

where nc is the number of the smoothing cells of the element. The strain-displacement matrix $\tilde{\mathbf{B}}_C$ is constant over each Ω_{C} and is of the following form:

$$\tilde{\mathbf{B}}_C = \left[\begin{array}{cccc} \tilde{\mathbf{B}}_{C1} & \tilde{\mathbf{B}}_{C2} & \tilde{\mathbf{B}}_{C3} & \tilde{\mathbf{B}}_{C4} \end{array} \right] \tag{3.18}$$

where for all shape functions $I \in \{1,\ldots,4\}$, the 3×2 submatrix $\tilde{\mathbf{B}}_{CI}$ represents the contribution to the strain displacement matrix associated with shape function I and cell C and writes (see Figure 3.11),

$$\forall I \in \{1,2,\ldots,4\}, \forall C \in \{1,2,\ldots nc\} \tilde{\mathbf{B}}_{CI} = \int\limits_{\Gamma_C} \left[\begin{array}{cc} n_x & 0 \\ 0 & n_y \\ n_y & n_x \end{array} \right] (\mathbf{x}) N_I(\mathbf{x}) \mathrm{d}\Gamma \tag{3.19}$$

[j] The subcells Ω_{C} form a partition of the element Ω^h.

or, since Equation (3.19) is computed on the boundary of Ω_C and one Gauß point is sufficient for an exact integration (in the case of a bilinear approximation):

$$\tilde{\mathbf{B}}_{CI}(\mathbf{x}_C) = \frac{1}{A_C}\sum_{b=1}^{nb}\begin{pmatrix} N_I\left(\mathbf{x}_b^G\right)n_x & 0 \\ 0 & N_I\left(\mathbf{x}_b^G\right)n_y \\ N_I\left(\mathbf{x}_b^G\right)n_y & N_I\left(\mathbf{x}_b^G\right)n_x \end{pmatrix} l_b^C \tag{3.20}$$

where $\mathbf{n} = (n_x, n_y)$ is the outward normal to the smoothing cell Ω_C, n_b is number of edges of the subcell, $\mathbf{x}_b^G$ and l_b^C are the center point (Gauß point) and the length of Γ_b^C, respectively. Figure 3.12 shows a possible subdivision of a quadrilateral element into subcells and the location of the integration points. The general procedure for the SFEM consists of the following steps:

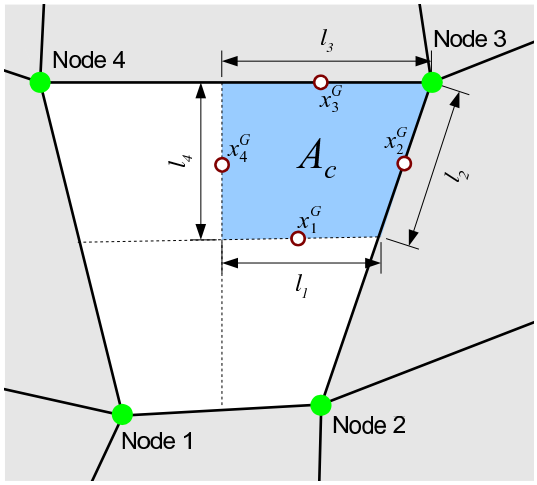

Figure 3.12: SFEM: description of the subcells and the integration points. The boundary of the subcell is denoted by dashed lines.

1. Discretize the problem into finite elements.
2. Create a displacement field through the construction of the shape functions. The displacement approximation in case of the SFEM is identical to that of the FEM.
3. Construct the smoothed strain field over the elements. This is computed by integrating over the boundaries of the subcells.
4. Using the weak form of the governing differential equations, establish the discrete linear algebraic system of equations.
5. Impose essential boundary conditions, which is exactly the same as in the FEM.
6. Solution methodologies and post-processing are the same as in the FEM.

It can be seen that the only difference between the conventional FEM and the SFEM is in the computation of the stiffness matrix. For SFEM, the need for an isoparametric mapping is eliminated and a non-mapped shape function is used to compute the smoothed stiffness matrix. To compute the smoothed stiffness matrix, the underlying FE mesh is sub-divided into non-overlapping smoothing domains. The smoothing domains can be quadrilateral or triangular in shape (see Figure 3.13).

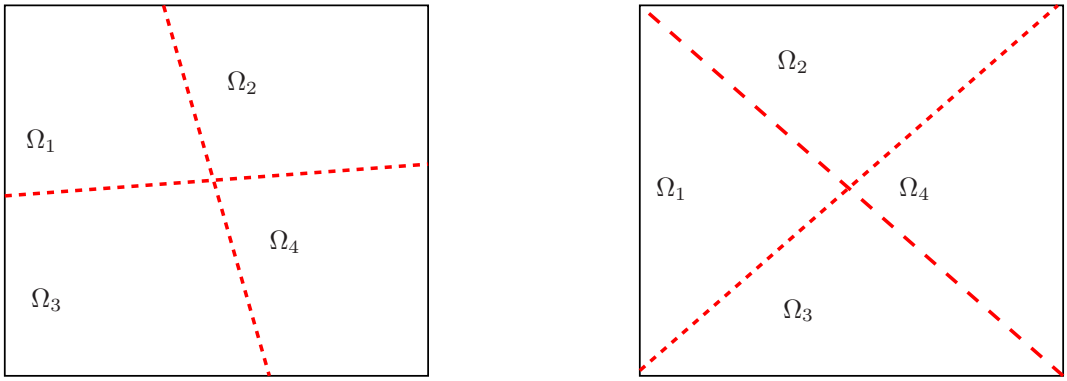

Figure 3.13: Division of a quadrilateral element into smoothing domains: (a) quadrilateral smoothing cells and (b) triangular smoothing cells, where $\Omega_i (i = 1, 2, 3, 4)$ are the smoothing cells. The property of the element depends on the number of smoothing cells [6, 12, 27, 36].

Basic properties of the SFEM

The following are a few properties of the cell based SFEM:

- A *priori* error bounds were derived for linear triangular elements [51].
- The resulting matrix is symmetric positive definite and sparse.
- No isoparametric mapping is required, since integration is performed on the boundary of the smoothing cells. In the case of bilinear shape functions, one integration point on each edge is sufficient.
- The shape functions need to be computed along the edges of the smoothing cells. This is done by simple linear interpolation of the underlying element shape functions [6, 36]. Shape functions can also be computed in the physical space by using Wachspress interpolants [6, 47]. This lack of isoparametric mapping confers SFEMs with a relative insentivity to mesh distortion.

- If the shape functions of the underlying element are linear (two-noded bar, three-noded triangle, four-noded tetrahedron), SFEM coincides exactly with FEM [27].
- The one-subcell version of the four-noded quadrilateral (Q4) SFEM is equivalent to an under integrated Q4 [27] and to a quasi-equilibrium element. It is therefore insensitive to locking, but exhibits zero-energy modes, while improving the accuracy of the stress field.
- In the limit where the number of subcells goes to infinity, the SFEM tends toward the standard displacement-based FEM.

3.2.2 Strain smoothing in the XFEM

In this section, the strain smoothing discussed above is combined with the enrichment in the FEM presented in Chapter 2 to construct the Smoothed eXtended Finite Element Method (SmXFEM). The SmXFEM uses a similar approximation for the displacement field as the XFEM, given by Equation (2.23) (c.f Chapter 2.4 Section 2.4). As in the SFEM, subcells are employed to smooth the strain field and calculate the stiffness matrix. All elements are divided into a number of subcells, which can vary from element to element. Typically, elements that are split by a discontinuity (weak or strong) will be divided into only two subcells, one on either side of the discontinuity. Elements in which non-polynomial approximations are present are divided into a larger number of subcells, similar to the case of the standard XFEM.
The Heaviside function for the SmXFEM is as follows:

$$H(\mathbf{x}) = \begin{cases} +1 & \text{if the center of the subcell is above the crack face,} \\ -1 & \text{if the center of the subcell is below the crack face.} \end{cases} \tag{3.21}$$

Given a point $\mathbf{x}$, the center of the subcell, we name $\mathbf{x}^*$ the closest point on the crack to $\mathbf{x}$ (Figure 3.14). At $\mathbf{x}^*$, construct the tangential vector, $\mathbf{e}_s$ and the normal vector $\mathbf{e}_n$ to the curve. The Heaviside function is then given by the sign of the scalar product $(\mathbf{x} - \mathbf{x}^*) \cdot \mathbf{e}_n$.

Remark: As in the XFEM, apart from standard elements, four types of elements should be considered (c.f. Chapter 2, Section 2.4, Figure 2.5).

Computation of the stiffness matrix

Let us now derive the enriched stiffness matrix of the SmXFEM, assuming all nodes in $\mathcal{N}^{\text{enr}}$ are enriched with function ϱ. Denote by $\boldsymbol{\varepsilon}^h = \varepsilon_{ij}^h$ the discretized enriched strain field deduced by differentiation of Equation (2.23), given by:

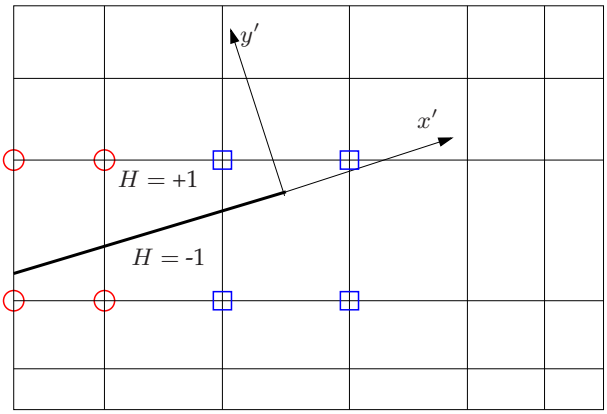

(a)

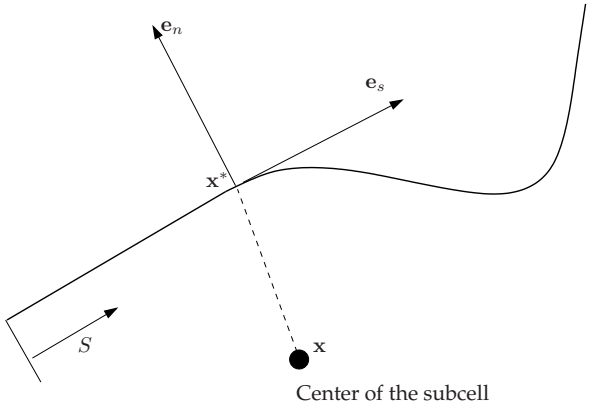

(b)

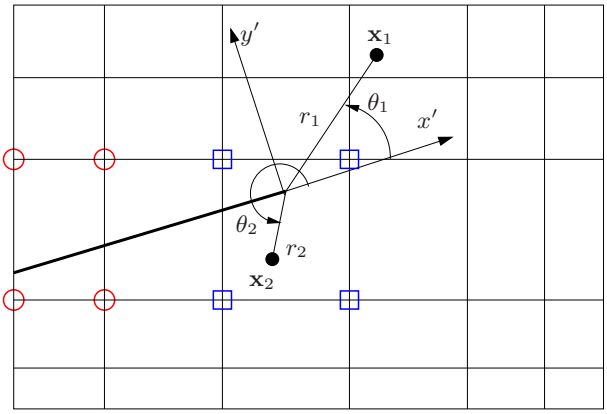

(c)

Figure 3.14: (a) The value of the Heaviside function. The solid line represents the crack or discontinuity in general. The circled nodes are enriched with the Heaviside function and the squared nodes are enriched with the near-tip asymptotic fields. The Heaviside function takes the value $+1$ above the crack and -1 below the crack. The local co-ordinate (x', y') is centered at the crack tip; (b) Normal and tangential coordinates for the crack and (c) Local polar coordinates (r, θ) at the crack tip.

$$\begin{aligned} \boldsymbol{\varepsilon}^h(\mathbf{x}) &= \sum_{I\in\mathcal{N}^{\text{fem}}} B_{I\text{fem}}(\mathbf{x})\mathbf{q}_I + \sum_{J\in\mathcal{N}^{\text{enr}}} B_{J\text{enr}}(\mathbf{x})\mathbf{a}_J = [\mathbf{B}_{\text{fem}}|\mathbf{B}_{\text{enr}}][\mathbf{q}] \\ \boldsymbol{\varepsilon}^h(\mathbf{x}) &= [\mathbf{B}_{\text{xfem}}][\mathbf{q}] \end{aligned} \tag{3.22}$$

where $\mathcal{N}^{\text{fem}}$ is the set of all nodes in the finite element mesh, $\mathcal{N}^{\text{enr}}$ is the set of nodes that are enriched with Heaviside function and near tip asymptotic fields. The $\mathbf{B}_{\text{xfem}}$ matrix in Equation (3.22) includes two terms $\mathbf{B}_{\text{fem}}$ and $\mathbf{B}_{\text{enr}}$ corresponding to the standard nodes and the enriched nodes. The $\mathbf{B}_{\text{fem}}$ term contains the first derivatives of the standard finite element shape functions:

$$\mathbf{B}_{\text{fem}} = \begin{bmatrix} \frac{\partial N_I}{\partial x} & 0 \\ 0 & \frac{\partial N_I}{\partial y} \\ \frac{\partial N_I}{\partial y} & \frac{\partial N_I}{\partial x} \end{bmatrix}. \tag{3.23}$$

The $\mathbf{B}_{\text{enr}}$ term is composed of the first derivatives of the product of the finite element shape functions with the enrichment functions:

$$\mathbf{B}_{\text{enr}} = \begin{bmatrix} \frac{\partial}{\partial x}[N_J(\varrho(\mathbf{x}) - \varrho(\mathbf{x}_J))] & 0 \\ 0 & \frac{\partial}{\partial y}[N_J(\varrho(\mathbf{x}) - \varrho(\mathbf{x}_J))] \\ \frac{\partial}{\partial y}[N_J(\varrho(\mathbf{x}) - \varrho(\mathbf{x}_J))] & \frac{\partial}{\partial x}[N_J(\varrho(\mathbf{x}) - \varrho(\mathbf{x}_J))] \end{bmatrix}. \tag{3.24}$$

The smoothed strain field at an arbitrary point $\mathbf{x}_{\text{C}}$ is defined as for the standard SFEM:

$$\widetilde{\boldsymbol{\varepsilon}}^h_{ij}(\mathbf{x}_{\text{C}}) = \int_\Omega \varepsilon^h_{ij}(\mathbf{x})\Phi(\mathbf{x}-\mathbf{x}_{\text{C}})\,\mathrm{d}\mathbf{x}, \tag{3.25}$$

where Φ is a smoothing function defined exactly as in the SFEM:

$$\begin{aligned} \Phi \geq 0 \quad \text{and} \quad \int_\Omega \Phi(\mathbf{x})\,\mathrm{d}\mathbf{x} = 1, \\ \Phi\left(\mathbf{x}-\mathbf{x}_{\text{C}}\right) = \begin{cases} 1/A_{\text{C}}, & \mathbf{x}\in\Omega_{\text{C}} \\ 0, & \mathbf{x}\notin\Omega_{\text{C}} \end{cases}. \end{aligned} \tag{3.26}$$

Substituting Equation (3.22) into Equation (3.25) and using Equations (3.23), (3.24) and (3.26), we obtain:

$$\widetilde{\boldsymbol{\varepsilon}}^h(\mathbf{x}_{\text{C}}) = \int_\Omega \mathbf{B}_{\text{xfem}}\mathbf{q}\,\Phi(\mathbf{x}-\mathbf{x}_{\text{C}})\,\mathrm{d}\mathbf{x} = \widetilde{\mathbf{B}}_{\text{xfem}}\mathbf{q}\,, \tag{3.27}$$

where the smoothed matrix $\widetilde{\mathbf{B}}_{\text{xfem}}$ in Equation (3.27) is defined by:

$$\widetilde{\mathbf{B}}_{\text{xfem}} = \frac{1}{A_{\text{C}}} \int_{\Omega_{\text{C}}} \mathbf{B}_{\text{xfem}}(\mathbf{x})\, \mathrm{d}\mathbf{x}. \tag{3.28}$$

The $\widetilde{\mathbf{B}}_{\text{xfem}}$ in Equation (3.28) includes two terms: $\widetilde{\mathbf{B}}_{\text{fem}}$ and $\widetilde{\mathbf{B}}_{\text{enr}}$ corresponding to the standard nodes and enriched nodes. The $\widetilde{\mathbf{B}}_{\text{fem}}$ term is given by:

$$\widetilde{\mathbf{B}}_{I\text{fem}} = \frac{1}{A_{\text{C}}} \int_{\Omega_{\text{C}}} \begin{bmatrix} \frac{\partial N_I}{\partial x} & 0 \\ 0 & \frac{\partial N_I}{\partial y} \\ \frac{\partial N_I}{\partial y} & \frac{\partial N_I}{\partial x} \end{bmatrix} \mathrm{d}\Omega. \tag{3.29}$$

By using the divergence theorem and noting $\mathbf{n} = (n_x, n_y)$ the outward normal to the smoothing cell Ω_{C} and Γ_{C}, Equation (3.29) can be written as:

$$\widetilde{\mathbf{B}}_{I\text{fem}} = \frac{1}{A_{\text{C}}} \int_{\Gamma_{\text{C}}} \begin{bmatrix} n_x N_I & 0 \\ 0 & n_y N_I \\ n_y N_I & n_x N_I \end{bmatrix} \mathrm{d}\Gamma. \tag{3.30}$$

Performing the same operations for $\widetilde{\mathbf{B}}_{\text{enr}}$, we obtain:

$$\widetilde{\mathbf{B}}_{J\text{enr}} = \frac{1}{A_{\text{C}}} \int_{\Omega_{\text{C}}} \begin{bmatrix} \frac{\partial}{\partial x}[N_J(\varrho(\mathbf{x}) - \varrho(\mathbf{x}_J))] & 0 \\ 0 & \frac{\partial}{\partial y}[N_J(\varrho(\mathbf{x}) - \varrho(\mathbf{x}_J))] \\ \frac{\partial}{\partial y}[N_J(\varrho(\mathbf{x}) - \varrho(\mathbf{x}_J))] & \frac{\partial}{\partial x}[N_J(\varrho(\mathbf{x}) - \varrho(\mathbf{x}_J))] \end{bmatrix} \mathrm{d}\Omega. \tag{3.31}$$

Using the divergence theorem to transform area integration into line integration, we obtain:

$$\widetilde{\mathbf{B}}_{J\text{enr}} = \frac{1}{A_{\text{C}}} \int_{\Gamma_{\text{C}}} \begin{bmatrix} n_x[N_J(\varrho(\mathbf{x}) - \varrho(\mathbf{x}_J))] & 0 \\ 0 & n_y[N_J(\varrho(\mathbf{x}) - \varrho(\mathbf{x}_J))] \\ n_y[N_J(\varrho(\mathbf{x}) - \varrho(\mathbf{x}_J))] & n_x[N_J(\psi(\mathbf{x}) - \psi(\mathbf{x}_J)] \end{bmatrix} \mathrm{d}\Gamma. \tag{3.32}$$

The smoothed enriched stiffness matrix for subcell C, $\widetilde{\mathbf{K}}^{\text{C}}_{\text{xfem}}$ is computed by

$$\widetilde{\mathbf{K}}^{\text{C}}_{\text{xfem}} = \int_{\Omega_{\text{C}}} \underbrace{\widetilde{\mathbf{B}}^{\text{T}}_{\text{C}} \mathbf{D} \widetilde{\mathbf{B}}_{\text{C}}}_{=\text{constant}}\, \mathrm{d}\Omega = \widetilde{\mathbf{B}}^{\text{T}}_{\text{C}} \mathbf{D} \widetilde{\mathbf{B}}_{\text{C}} A_{\text{C}} \tag{3.33}$$

where $\widetilde{\mathbf{B}}_C \equiv \widetilde{\mathbf{B}}_{\text{xfem}}$ and A_{C} is the area of the subcell. The smoothed enriched element stiffness matrix $\widetilde{\mathbf{K}}^{e}_{\text{xfem}}$ is the sum of the $\widetilde{\mathbf{K}}^{C}_{\text{xfem}}$, for all subcells, C

$$\widetilde{\mathbf{K}}^{\text{e}} = \sum_{C=1}^{nc} \widetilde{\mathbf{B}}^{\text{T}}_{\text{C}} \mathbf{D} \widetilde{\mathbf{B}}_{\text{C}} \int_{\Omega_{\text{C}}} \mathrm{d}\Omega = \sum_{C=1}^{nc} \widetilde{\mathbf{B}}^{\text{T}}_{\text{C}} \mathbf{D} \widetilde{\mathbf{B}}_{\text{C}} A_{\text{C}} \tag{3.34}$$

where $C \in \{1, 2, \cdots nc\}$ is the number of subcell Ω_{C}, $A_{\mathrm{C}} = \int_{\Omega_{\mathrm{C}}} \mathrm{d}\Omega$ is the area of the subcell Ω_{C}. Note that in Equation (3.34), the stiffness matrix is rewritten as the sum of the contributions from the individual subcell, because all the entries in matrix $\tilde{\mathbf{B}}_{\mathrm{C}}$ are constants over each subcell Ω_{C} - each of these entries are line integrals calculated along the boundaries of the subcells.

Remark: It is clear from Equations (3.32) and (3.34) that the derivatives of the shape functions are not needed to compute the stiffness matrix. Intuitively, this leads to believe that strain smoothing could find applications where higher order derivatives are needed (e.g. gradient elasticity). Moreover, when $\sqrt{r}$ enrichment is used, the singular terms normally present in the stiffness matrix integrand (c.f Chapter 2.4 Section 2.4) disappear.

Numerical Integration

The XFEM allows the mesh to be independent of the geometry. Hence, special care has to be taken while numerically integrating over the elements intersected by the discontinuity (c.f. Chapter 2, Section 2.4.5). For the elements that are enriched, the standard Gaussian quadrature is not appropriate and the integration scheme has to be adapted to properly integrate the enriched terms. Figure 3.15 shows the process of numerical integration in the conventional XFEM and in case of the strain smoothing. To locate the integration point in the tip elements, the following procedure is adopted:

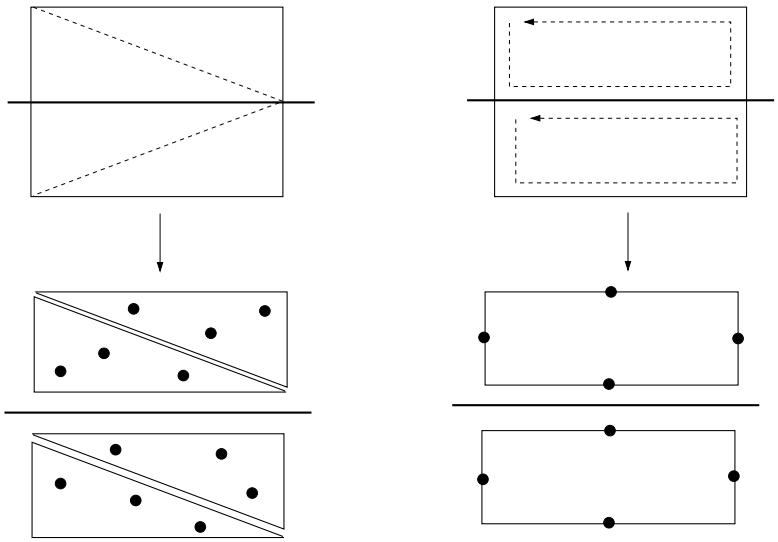

Figure 3.15: Integration in an element with a straight discontinuity (solid line). (left) Standard decomposition of an element for integration of a discontinuous weak form for XFEM: Gauß points are introduced within each (dotted lines) triangle to ensure proper integration of the discontinuous displacement field. (right) Absence of decomposition allowed by the strain smoothing technique.

The co-ordinates of the Gauß points on the boundary of the subcells for tip elements are computed in the following way:

1. The Newton-Raphson method is used to determine the position of the crack tip in the natural co-ordinate system.
2. For each Gauß point along the edge of the subcell, the natural co-ordinate η' and its corresponding weight W are determined in one dimension.
3. This one-dimensional co-ordinate is then transformed into the local two-dimensional natural co-ordinate system (ξ_1, η_1) on the subcell edge.
4. Depending on the position of the subcell edge in this local natural co-ordinate system, the values of (ξ, η) in the two-dimensional natural co-ordinate system are determined based on the triangular element.

Figure 3.16 illustrates the necessary steps to determine the co-ordinates of the Gauß points on the boundary of the subcells.

3.3 Summary

In this chapter, two new numerical integration techniques were presented. One method is based on the conformal mapping of the elements intersected by the discontinuity surface onto a unit disk and then using the cubature rule on the unit disk to evaluate the terms in the stiffness matrix. The other method, coined as the SmXFEM, relies on smoothing the compatible strain field. Both methods aim at improving the integration in the conventional XFEM. Some of the key features of the proposed techniques are listed below.

SCCM By conformally mapping the polygonal sub-domain obtained by the intersection of the discontinuity with the element onto a unit disk, the need for sub-triangulation is eliminated. The positivity of the Jacobian is always ensured. Additionally, quadrature rules of any order can be easily generated. A toolbox (in FORTRAN and MATLAB) to carry out the conformal mapping is available as an open source [14, 15] and can be easily combined with any existing FE code.

SmXFEM The method is a result of combining the strain smoothing technique and the XFEM. The SmXFEM shares properties both with the SFEM and the XFEM. By using the divergence theorem, the derivatives of the shape and the enrichment functions are replaced by products with normals, which suppresses the need to compute and integrate singular

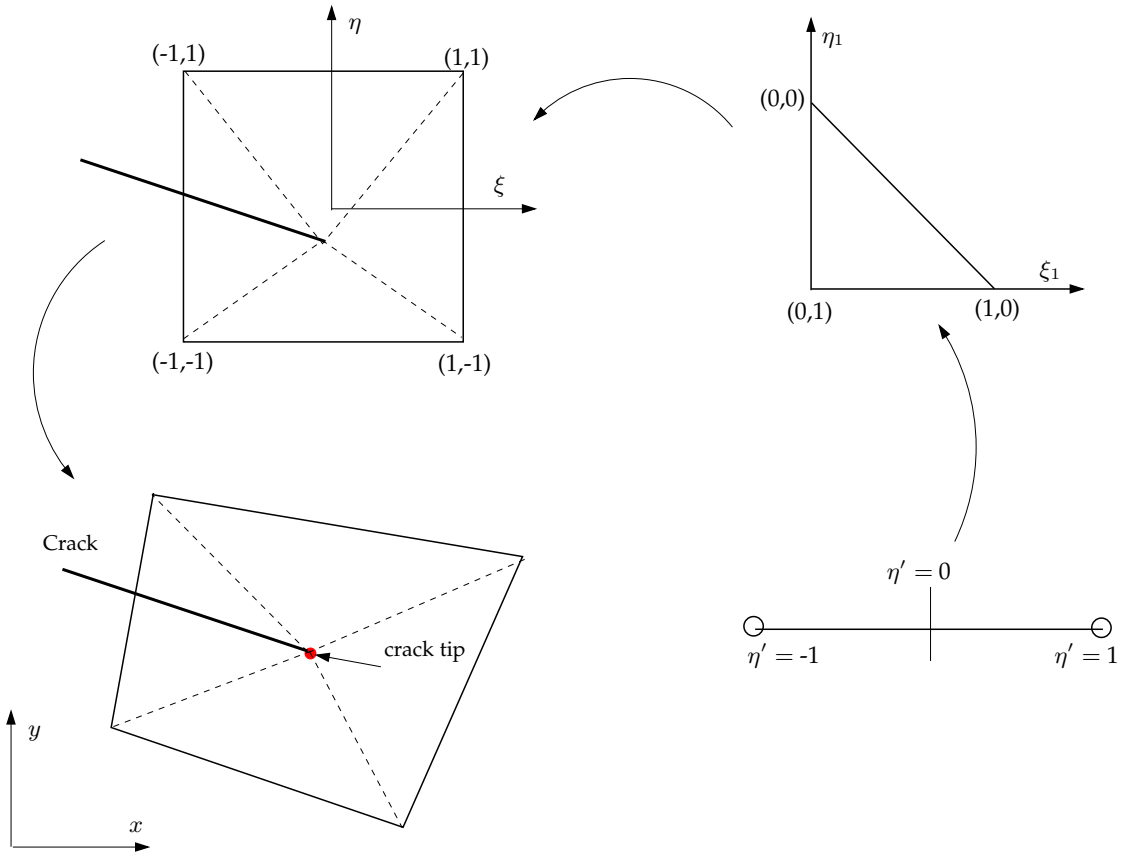

Figure 3.16: Necessary steps in computing the Gauß points along the boundaries of a subcell. The solid line denotes the crack face.

functions usually appearing in the stiffness matrix in linear elastic fracture mechanics applications of the XFEM. Additionally, since the integration is performed along the boundary of the finite elements or the smoothing cells, the need for an isoparametric mapping is eliminated. In this method, the weak form is integrated on the boundary of the smoothing cells, forming a partition of the element. For elements split by a weak or strong discontinuity, one subcell above and below the interface are sufficient, and thus lead to the suppression of integration using triangular subcells. The formulation as presented here is restricted to the case of bi-linear quadrilateral element.

The efficiency and accuracy of the proposed methods are discussed in detail with numerical examples involving weak and strong discontinuities in Chapter 4.

Bibliography

[1] G. Balachandran, A. Rajagopal, and S. M. Sivakumar. Mesh free Galerkin method based on natural neighbors and conformal mapping. *Computational Mechanics*, 42:885–905, 2008.

[2] F. Barra, H. G. E. Hentschel, A. Levermann, and I. Procaccia. Quasistatic fractures in brittle media and iterated conformal maps. *Physical Review E*, 65:045101–1 – 045101–4, 2002.

[3] E. Béchet, H. Minnebo, N. Moës, and B. Burgardt. Improved implementation and robustness study of the X-FEM for stress analysis around cracks. *International Journal for Numerical Methods in Engineering*, 64(8):1033–1056, 2005. doi: 10.1002/nme.1386.

[4] S. Bordas, T. Rabczuk, H. Nguyen-Xuan, V. P. Nguyen, S. Natarajan, T. Bog, D. M. Quan, and V. H. Nguyen. Strain smoothing in FEM and XFEM. *Computers & Structures*, 88:1419–1443, 2010.

[5] S. Bordas, S. Natarajan, P. Kerfriden, C. Augarde, D. R. Mahapatra, T. Rabczuk, and S. D. Pont. On the performance of strain smoothing for quadratic and enriched finite element approximations (XFEM/GFEM/PUFEM). *International Journal for Numerical Methods in Engineering*, 86: 637–666, 2011.

[6] S. P. A. Bordas and S. Natarajan. On the approximation in the smoothed finite element method (SFEM). *International Journal for Numerical Methods in Engineering*, 81:660–670, 2010.

[7] J. S. Chen, C. T. Wu, S. Yoon, and Y. You. A stabilized conforming nodal integration for Galerkin mesh-free methods. *International Journal for Numerical Methods in Engineering*, 50:435–466, 2001.

[8] E. B. Christoffel. Sul problema delle temperature stazionarie e la rappresentazione di una data superficie. *Annali Di Mathematica Pura ed Applicata*, 1:89–103, 1867.

[9] H. Cohn. *Conformal mapping on Riemann surfaces*. Dover Publications Inc, 1967.

[10] R. Cools. An encyclopaedia of cubature formulas. *Journal of Complexity*, 19:445–453, 2003.

[11] R. Cools and K. J. Kim. A survey of known and new cubature formulas for the unit disk. *Journal of Applied Mathematics and Computing*, 7:477–485, 2000.

[12] K. Y. Dai, G. R. Liu, and T. T. Nguyen. An n-sided polygonal smoothed finite element method (nSFEM) for solid mechanics. *Finite Elements in Analysis and Design*, 43:847–860, 2007.

[13] S. De and K.-J. Bathe. The method of finite spheres with improved numerical integration. *Computers and structures*, 79(22):2183–2196, 2001.

[14] T. A. Driscoll and L. N. Trefethen. Algorithms 756: A matlab toolbox for schwarz christoffel mapping. *ACM Transactions on Mathematical Software*, 22(2):168–186, 1996.

[15] T. A. Driscoll and L. N. Trefethen. *Schwarz-Christoffel Mapping*, volume 8. Cambridge University Press, 2002.

[16] A. R. Elcart and C. Hu. Determination of surface and interior cracks from electrostatic measurements using Schwarz-Christoffel tranformations. *International Journal of Engineering Science*, 34: 1165–1181, 1996.

[17] M. M. Fyrillas. Heat conduction in a solid slab embedded with a pipe of general cross-section: Shape Factor and Shape Optimization. *International Journal of Engineering Science*, 46:907–916, 2008.

[18] O. Haber, H. Grebner, and A. Höfler. Application of conformal mapping for mesh generation in two-dimensional elasto-plastic fracture mechanics problems. *Engineering Fracture Mechanics*, 33:897–905, 1989.

[19] Z. C. He, G. Liu, Z. Zhong, G. Zhang, and A. Cheng. A coupled ES-FEM/BEM method for fluid-structure interaction problems. *Engineering Analysis with Boundary Elements*, 35:140–147, 2011.

[20] Z. G. He, G. Liu, Z. Zhong, G. Zhang, and A. Cheng. Coupled analysis of 3D structural-acoustic problems using the edge-based smoothed finite element method/finite element method. *Finite Elements in Analysis and Design*, 46:1114–1121, 2010.

[21] H. Ishikawa and Y. Kohno. Analysis of stress singularities at the corner of square hole and rigid square inclusion in elastic plate by conformal mapping. *International Journal of Engineering Science*, 31:1197–1213, 1993.

[22] M. J. Kazemzadeh-Parsi and F. Daneshmand. Solution of geometric inverse heat conduction problems by smoothed fixed grid finite element method. *Finite Elements in Analysis and Design*, 45:599–611, 2009.

[23] S. G. Krantz. *Handbook of Complex Variables*. Birkhäuser, Boston, 1999.

[24] P. Laborde, J. Pommier, Y. Renard, and M. Salaün. High-order extended finite element method for cracked domains. *International Journal for Numerical Methods in Engineering*, 64(3):354–381, September 2005. doi: 10.1002/nme.1370.

[25] F. G. Lether. A generalized product rule for the circle. *SIAM Journal of Numerical Analysis*, 8: 249–253, 1971.

[26] B. Lin and S. N. Chandler-Wilde. Numerical conformal mapping and mesh generation for polygonal and multiply-connected regions. *Journal of Hydroinformatics*, 2:255–267, 2000.

[27] G. R. Liu, T. T. Nguyen, K. Y. Dai, and K. Y. Lam. Theoretical aspects of the smoothed finite element method (SFEM). *International Journal for Numerical Methods in Engineering*, 71:902–930, 2007.

[28] G. R. Liu, T. Nguyen-Thoi, and K. Y. Lam. A novel alpha finite element method (αFEM) for exact solution to mechanics problems using triangular and tetrahedral elements. *Computer Methods in Applied Mechanics and Engineering*, 197:3883–3897, 2008.

[29] G. R. Liu, T. Nguyen-Thoi, and K. Y. Lam. An edge-based smoothed finite element method (ES-FEM) for static, free and forced vibration analyses of solids. *Journal of Sound and Vibration*, 320:1100–1130, 2009.

[30] G. R. Liu, T. Nguyen-Thoi, H. Nguyen-Xuan, and K. Y. Lam. A node based smoothed finite element method (NS-FEM) for upper bound solution to solid mechanics problems. *Computers and Structures*, 87:14–26, 2009.

[31] M. Markovic, M. Jufer, and Y. Perriard. A square magnetic circuit analysis using Schwarz-Christoffel mapping. *Mathematics and Computers in Simulation*, 71:460–465, 2006.

[32] N. Moës, J. Dolbow, and T. Belytschko. A finite element method for crack growth without remeshing. *International Journal for Numerical Methods in Engineering*, 46(1):131–150, 1999.

[33] S. Natarajan, S. Bordas, and D. R. Mahapatra. Numerical integration over arbitrary polygonal domains based on Schwarz-Christoffel conformal mapping. *International Journal for Numerical Methods in Engineering*, 80:103–134, 2009.

[34] N. T. Nguyen, T. Rabczuk, H. Nguyen-Xuan, and S. Bordas. A smoothed finite element method for shell analysis. *Computer Methods in Applied Mechanics and Engineering*, 198:165–177, 2008.

[35] T. Nguyen-Thoi, G. R. Liu, K. Y. Lam, and G. Y. Zhang. A face-based smoothed finite element method (FS-FEM) for 3D linear and nonlinear solid mechanics using 4-node tetrahedral elements. *International Journal for Numerical Methods in Engineering*, 78:324–353, 2009.

[36] H. Nguyen-Xuan, S. P. A. Bordas, and H. Nguyen-Dang. Smooth finite element methods: convergence, accuracy and properties. *International Journal for Numerical Methods in Engineering*, 74: 175–208, 2008.

[37] H. Nguyen-Xuan, T. Rabczuk, S. Bordas, and J. F. Debongnie. A smoothed finite element method for plate analysis. *Computer Methods in Applied Mechanics and Engineering*, 197:1184–1203, 2008.

[38] W. H. Peirce. Numerical integration over the planar annulus. *Journal of the Society of Industrial and Applied Mathematics*, 5(2):66–73, 1957.

[39] J. C. Santos-León. Error bounds for interpolatory quadrature rules on the unit circle. *Mathematics of Computation*, 70:281–296, 2000.

[40] R. Schinzinger and P. A. Laura. *Conformal mapping: Methods and Applications*. Dover Publications Inc, 2003.

[41] H. A. Schwarz. Conforme abbildung der oberfläche eines Tetraeders auf die Oberfläche einer Kugel. *Journal für die reine and angewandte Mathematik*, 70:121–136, 1869.

[42] N. Sukumar and A. Tabarraei. Conforming polygonal finite elements. *International Journal of Numerical Methods in Engineering*, 61:2045–2066, 2004.

[43] A. Tiwary, C. Hu, and S. Ghosh. Numerical conformal mapping method based Voronoi cell finite element model for analyzing microstructures with irregular heterogeneities. *Finite Elements in Analysis and Design*, 43:504–520, 2007.

[44] L. N. Trefethen. Numerical computation of the Schwarz-Christoffel transformation. Technical report, Department of Computer Science, Stanford University, 1979.

[45] L. N. Trefethen. Numerical conformal mapping. *SIAM J Sci Stat Comput*, 1(1):82–102, 1980.

[46] I. Trukrov and J. Novak. Effective elastic properties of solids with defects of irregular shapes. *International Journal of Solids and Structures*, 39:1539–1555, 2002.

[47] E. L. Wachspress. *A rational basis for function approximation*. Academic Press, Inc: New York, 1975.

[48] S. Wang, G. R. Liu, Z. A. Zhang, and L. Chen. Nonlinear 3D numerical computations for the square membrane versus experimental data. *Engineering Structures*, 33:1828–1837, 2011.

[49] S. C. Wu, G. R. Liu, X. Y. Cui, T. T. Nguyen, and G. Y. Zhang. An edge-based smoothed point interpolation method (ES-PIM) for heat transfer analysis of rapid manufacturing system. *International Journal of Heat and Mass Transfer*, 53:1938–1950, 2010.

[50] X. F. Wu, E. Lilla, and W. S. Zou. A semi-infinite interfacial crack between two bonded dissimilar elastic strips. *Archive of Applied Mechanics*, 72:630–636, 2002.

[51] Z. Xuan, T. Lassila, G. Rozza, and A. Quarteroni. On computing upper and lower bounds on the outputs of linear elasticity problems approximated by the smoothed finite element method. *International Journal for Numerical Methods in Engineering*, 83:174–195, 2010.

[52] L. Y. Yao, D. J. Yu, X. Y. Cui, and X. G. Zang. Numerical treatment of acoustic problems with the smoothed finite element method. *Applied Acoustics*, 71:743–753, 2010.

[53] J. W. Yoo, B. Moran, and J. S. Chen. Stabilized conforming nodal integration in the natural-element method. *International Journal of Numerical Methods in Engineering*, 60:861–890, 2004.

4

Enriched FEM to model strong and weak discontinuities

In this chapter, the application of the XFEM and the SmXFEM to problems in small displacements, two-dimensional elastostatics, in the absence of body forces, involving weak discontinuities (e.g., material interfaces) and strong discontinuities, (e.g., plate with a crack) is presented. The numerical integration over the elements intersected by the discontinuity is done with the conventional sub-triangulation method, the SCCM and the SmXFEM (c.f. Chapter 3). The relative merits of the different numerical integration techniques are discussed. In all the numerical examples, a bi-linear quadrilateral element with 4 nodes and with two degrees of freedom per node is used. The numerical results from the two new techniques are compared with the conventional XFEM and with the analytical solutions wherever available.

4.1 Numerical integration over the enriched elements

In the following examples, the sub-triangulation method (denoted as Std. XFEM), the SCCM (denoted as XFEM + SC Map) and the SmXFEM are employed to numerically integrate over the elements intersected by the discontinuities. The following conventions are used for the purpose of numerical integration, unless otherwise mentioned.

XFEM with SCCM Each subdomain of the intersected element is conformally mapped onto a unit disk and the cubature rule on a unit disk is used. The SCCM is applied only to the enriched elements. Figure 3.8 shows the mapping of the split element and the element containing the crack tip onto a unit disk using the SCCM. For standard elements, a 2×2 integration rule is used.

Std. XFEM The conventional sub-triangulation is employed to numerically evaluate the terms in the stiffness matrix.

SmXFEM The elements intersected by the discontinuities are subdivided into subcells. In this study, for weak discontinuity problems, three variants of subcells are used:

- One subcell above and below the interface (denoted by SmXFEM 1 subcell).
- Two subcells above and below the interface (denoted by SmXFEM 2 subcell).
- Four subcells above and below the interface (denoted by SmXFEM 4 subcell).

Figures 4.1 and 4.2, show a schematic representation of the subdivision of an element intersected by a discontinuity in case of the split element and the element containing the crack tip, respectively. The integration rules used for the current study are given in Table 4.1

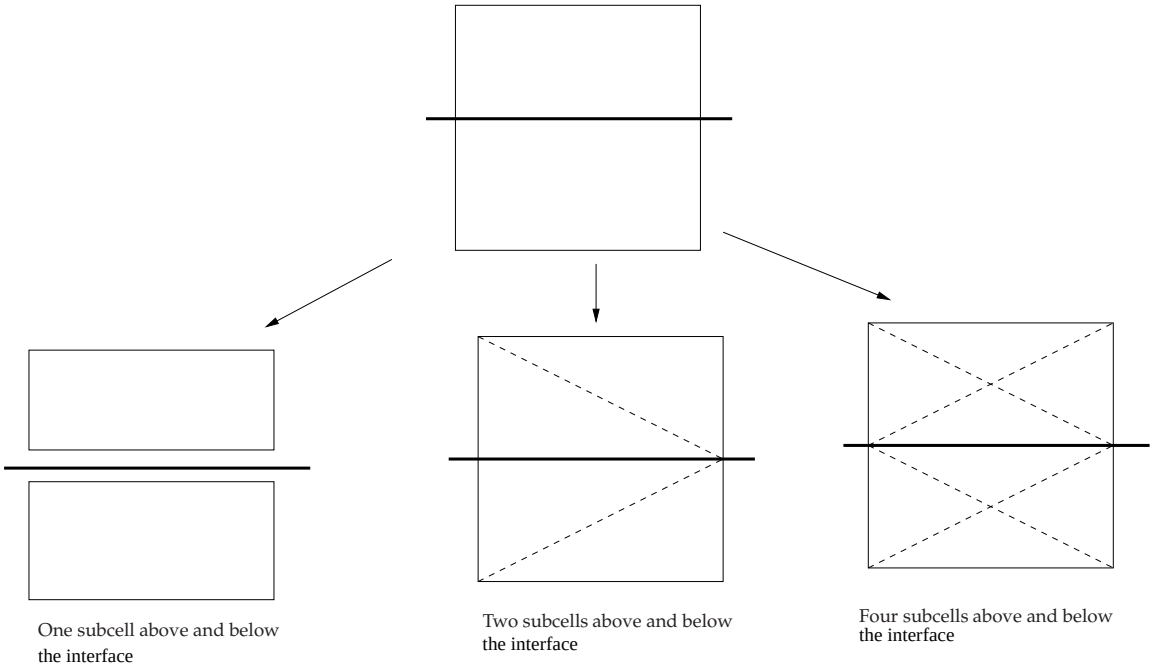

Figure 4.1: SmXFEM: A schematic partition of split element into subcells. The solid line represents the discontinuity and the dashed lines denote the boundaries of the subcell (c.f Chapter 3 Section 3.2.2).

4.2 Numerical Examples

The error in the displacement norm is measured in terms of $||L^2||$ norm and is defined as:

$$||\mathbf{u}||_{L^2} = \sqrt{(\mathbf{u}^h - \mathbf{u}^{\text{ex}}) \cdot (\mathbf{u}^h - \mathbf{u}^{\text{ex}})} \tag{4.1}$$

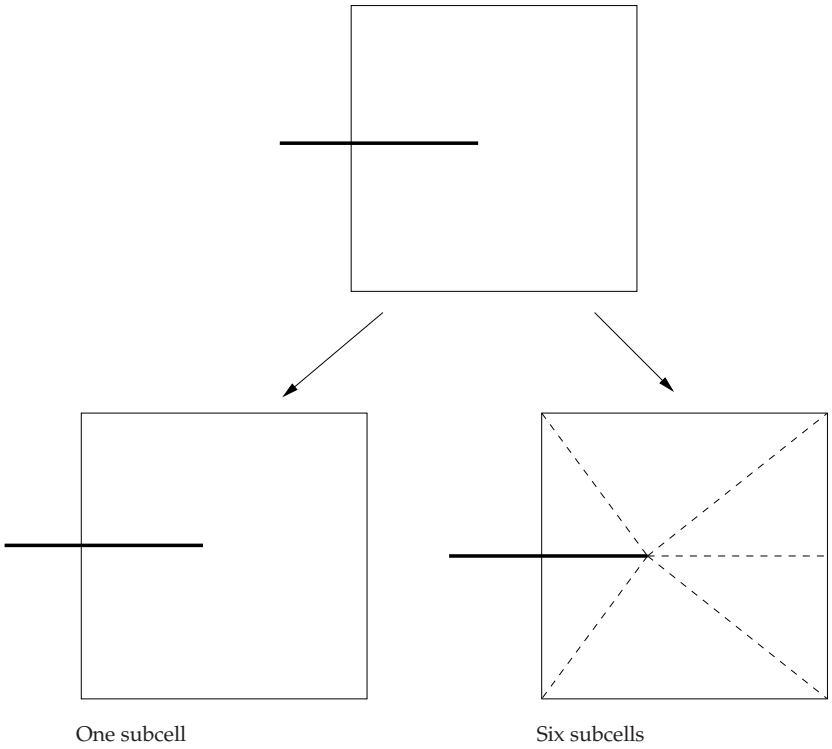

Figure 4.2: SmXFEM: A schematic partition of elements intersected by a discontinuity into subcells (tip element). The solid line represents the discontinuity and the dashed lines denote the boundaries of the subcell (c.f Chapter 3 Section 3.2.2).

Table 4.1: Integration rules for enriched and non-enriched elements. In the SmXFEM triangular subcells with four Gauß points along each edge of the subcell are used.

Element Type	Std. XFEM (Gauß points)	XFEM + SC Map (Gauß points)	SmXFEM (Subcells)
Non-enriched element	4	4	4
Tip element	13 per triangle	80	1, 6, 12
Tip blending element	16	16	4
Split element	3 per triangle	6	2
Split blending element	4	4	4
Split-Tip blending element	4 per triangle	8	2

The relative error in the energy norm is defined by:

$$||\mathbf{u}||_e = \sqrt{\int_\Omega (\boldsymbol{\varepsilon}^h - \boldsymbol{\varepsilon}^{\text{ex}}) : \mathbf{D} : (\boldsymbol{\varepsilon}^h - \boldsymbol{\varepsilon}^{\text{ex}})\, d\Omega} \tag{4.2}$$

where $\mathbf{u}^{\text{ex}}$ and $\mathbf{u}^h$ in Equations (4.1) and (4.2) are the exact and the numerical displacement solution, respectively. In this study, the domain integral method [18, 19], in conjunction with the interaction energy integrals is used to determine the mixed-mode stress intensity factors (SIFs). A detailed description is given in Appendix D. In this chapter, the following classes of problems are considered:

- Weak discontinuities: multi-material problems.
- Strong discontinuities and singularities: linear elastic fracture mechanics (LEFM).
- A combination of the above problems: crack-inclusion interaction in an elastic medium.
- Crack growth around an inclusion.

4.2.1 Weak Discontinuity

One-dimensional: Bi-material problem

As a first example, consider a 1D bi-material bar in tension (see Figure 4.3). The problem is solved with the SmXFEM and a step-by-step solution procedure is presented. The XFEM solution to this problem is given in Chapter 2, Section 2.5.1. The left edge of the bar is clamped and a unit force is prescribed at the right end. The total length of the bar is $L(= L_1 + L_2) = 1$. The material interface is assumed to be at $x = x_b = 0.5$. Young's moduli for $x < x_b$ and $x > x_b$ are $E_1 = 1$ and $E_2 = 2$, respectively. For the current study, a 1D two-noded element with each node having one degree of freedom is considered.

SmXFEM solution The displacement approximation for the SmXFEM is identical to that of the XFEM. For a two-noded element, the XFEM/SmXFEM displacement approximation at a point $x \in [0, 1]$ writes:

$$u(x) = N_1(x)u_1 + N_2(x)u_2 + N_3(x)a_1 + N_4(x)a_2 \tag{4.3}$$

where u_1, u_2 are the standard degrees of freedom and a_1, a_2 are the enriched degrees of freedom associated with nodes 1 and 2, respectively. The enrichment functions, N_3 and N_4 are given by:

$$N_3(x) = N_1(x)\left(|\phi_b(x)| - |\phi_b(x_1)|\right), \qquad N_4(x) = N_2(x)\left(|\phi_b(x)| - |\phi_b(x_2)|\right) \tag{4.4}$$

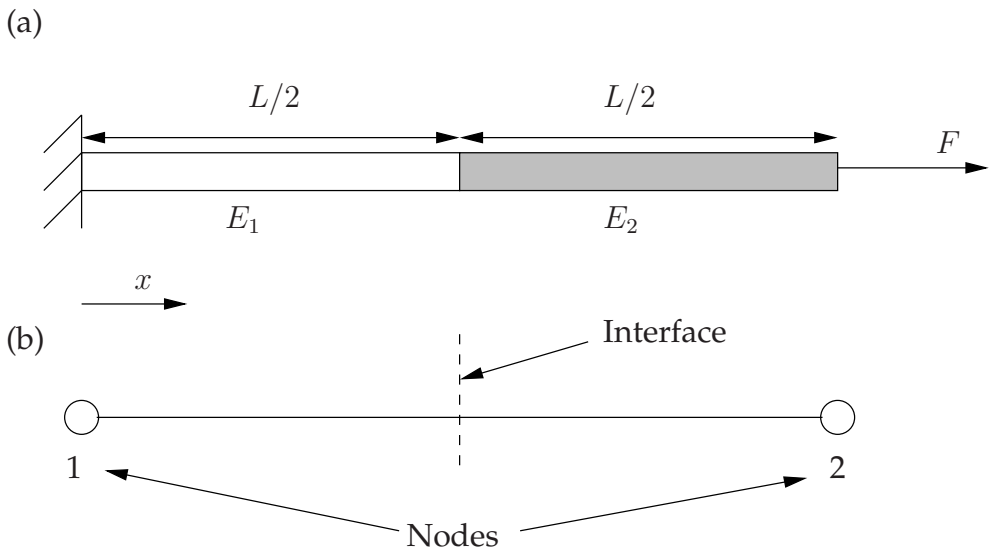

Figure 4.3: Bi-material bar: (a) geometry and boundary conditions and (b) finite element.

where, $\phi_b(x) = x - x_b$ is the level set function in 1D. One of the main ideas in the SFEM or the SmXFEM, is to change the boundary integral to a line integral by the using the divergence theorem. In 1D, this reduces to evaluating the function at the domain boundary. The influence of the number of subcells on the solution of the bi-material problem is studied next.

One subcell In this case, the entire domain is treated with only one subcell. The material discontinuity is embedded within the subcell. The corresponding strain-displacement matrix is given by:

$$\tilde{\mathbf{B}} = \frac{1}{L}\left[\begin{array}{cccc} N_1 & N_2 & N_3 & N_4 \end{array}\right]|_{x=0}^{x=L}, \tag{4.5}$$

where, in Equation (4.5) the shape functions are evaluated at the domain boundary. The strain-displacement matrix for one subcell is given by:

$$\tilde{\mathbf{B}} = \frac{1}{L}\left[\begin{array}{cccc} -1 & 1 & 0 & 0 \end{array}\right]. \tag{4.6}$$

It is clear that the contribution from the enriched shape functions to the strain-displacement matrix is *'zero'*, because the enriched shape functions are 'zero' on the boundary of the subcell. This leads to a singular stiffness matrix, $\tilde{\mathbf{K}}$.

Two subcells Now the bi-material bar is split into two subcells, with the subcell boundary conforming to the material interface. The strain displacement matrix for each subcell is given by:

$$\begin{aligned}\tilde{\mathbf{B}}_1 &= \frac{1}{L}\begin{bmatrix} -1 & 1 & -L/2 & -L/2 \end{bmatrix}, \text{ along } \mathrm{L}_1 \\ \tilde{\mathbf{B}}_2 &= \frac{1}{L}\begin{bmatrix} -1 & 1 & L/2 & L/2 \end{bmatrix}, \text{ along } \mathrm{L}_2, \end{aligned} \tag{4.7}$$

where, L_1 and L_2 are the lengths of the corresponding subcells. It can be easily verified that the above strain-displacement matrices lead to a singular stiffness matrix, $\tilde{\mathbf{K}}$. The stiffness matrix is given by:

$$\tilde{\mathbf{K}} = \begin{bmatrix} 1.50 & -1.50 & -0.25 & -0.25 \\ -1.50 & 1.50 & 0.25 & 0.25 \\ -0.25 & 0.25 & 0.375 & 0.375 \\ -0.25 & 0.25 & 0.375 & 0.375 \end{bmatrix}. \tag{4.8}$$

Next, instead of subdividing into an 'odd' number of subcells, the domain is divided into an 'even' number of subcells and such that the subcell boundaries conform to the material interface. With an odd number of subcells, the analytical integration of the strain displacement matrix is not a difficulty, but assigning the proper material property to the subcell is not straight forward. This can be handled by using the numerical integration. This is implemented for higher dimensions.

Four subcells Here, the bi-material bar is split into four subcells. The strain-displacement matrix for each of the subcell is computed as outlined earlier. The assembled equations are:

$$\begin{bmatrix} 1.50 & -1.50 & -0.25 & -0.25 \\ -1.50 & 1.50 & 0.25 & 0.25 \\ -0.25 & 0.25 & 0.468 & 0.281 \\ -0.25 & 0.25 & 0.281 & 0.468 \end{bmatrix} \begin{Bmatrix} u_1 \\ u_2 \\ a_1 \\ a_2 \end{Bmatrix} = \begin{Bmatrix} F_1 \\ F_2 \\ 0 \\ 0 \end{Bmatrix} \tag{4.9}$$

with the boundary conditions $u_1 = 0$ and $F_2 = 1$, the solution is $u_2 = 0.75$, $a_1 = -0.25$, $a_2 = -0.25$.

Remark From the above test cases, it is clear that there is a minimum number of subcells required. And the following can be concluded:

- One subcell and two subcells lead to a singular $\tilde{\mathbf{K}}$ matrix.
- Four subcells :
  - Lead to a proper $\tilde{\mathbf{K}}$ matrix, i.e., avoid spurious zero energy modes.

  - The solution is identical to the analytical solution.
  - The XFEM stiffness matrix, $\mathbf{K}$ and the SmXFEM stiffness matrix, $\tilde{\mathbf{K}}$ are not the same, but both lead to identical solutions.

- Increasing the number of subcells (beyond 2) and keeping this number evenly distributed in each subdomain has no effect on the solution.

Two-dimensional: Bi-material problem

Next, consider a one-dimensional bi-material bar discretized with 2D quadrilateral elements. A two-dimensional square domain $\Omega = \Omega_1 \cup \Omega_2$ of length $L = 2$ with the material interface Γ located at b is considered for this study, as shown in Figure 4.4. The Young's modulus and Poisson's ratio in $\Omega_1 = [-1, b] \times [-1, 1]$ are $E_1 = 1$, $\nu = 0$, and that in $\Omega_2 = [b, 1] \times [-1, 1]$ are $E_2 = 10$, $\nu = 0$. The exact displacement solution in the absence of body forces is given in Appendix A. The left end of the bar is clamped and a unit force is prescribed at the right end.

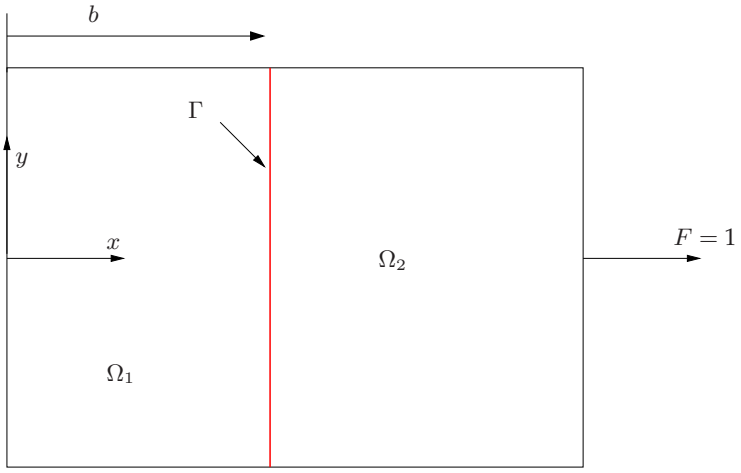

Figure 4.4: Bi-material bar problem. The material interface is located at a distance b from the left end.

Numerical results are computed on a regular 11×11 finite element mesh with six different locations of the interface: $b = 0, 0.01, 0.05, 0.1, 0.15$ and 0.19. From Table 4.2 it can be seen that the smoothed XFEM and the XFEM with SCCM both yield comparable results to the conventional XFEM.

Bi-material boundary value problem - elastic circular inhomogeneity

In this example, the enriched finite element solutions for the elastostatic response of a circular material inhomogeneity under radially symmetric loading, as shown in Figure 4.5 is

Table 4.2: Relative error in the energy norm for the bi-material bar problem for a regular 11 $\times$ 11 finite element mesh and material interface parallel to the mesh lines.

Interface location	Std. XFEM	XFEM+SCCM	SmXFEM		
b			1 subcell	2 subcell	4 subcell
0.00	8.7×10^{-8}	8.7×10^{-8}	3.9×10^{-8}	8.3×10^{-8}	3.3×10^{-8}
0.01	4.8×10^{-8}	4.8×10^{-8}	1.9×10^{-8}	2.9×10^{-8}	3.8×10^{-8}
0.05	1.4×10^{-8}	1.4×10^{-8}	9.6×10^{-8}	7.6×10^{-8}	1.1×10^{-8}
0.10	2.3×10^{-8}	2.3×10^{-8}	6.8×10^{-8}	7.5×10^{-8}	4.6×10^{-8}
0.15	7.1×10^{-8}	7.1×10^{-8}	5.4×10^{-8}	4.8×10^{-8}	6.2×10^{-8}
0.19	3.9×10^{-8}	3.9×10^{-8}	7.9×10^{-8}	1.4×10^{-8}	9.7×10^{-8}

examined within the framework of the XFEM and the SmXFEM. Plane strain conditions are assumed. The material properties are constant within each domain, Ω_1 and Ω_2, but there is a material discontinuity across the interface, $\Gamma_1(r = a)$. The Lamé constants in Ω_1 and Ω_2 are: $\lambda_1 = \mu_1 = 0.4$ and λ_2 =5.7692, μ_2 =3.8461, respectively. These correspond to E_1 =1, ν =0.25 and E_2 =10, ν_2 =0.3. A linear displacement field: $u_1 = x_1, u_2 = x_2$ $(u_r = r, u_\theta = 0)$ on the boundary $\Gamma_2(r = b)$ is imposed [9, 12, 22]. The governing equations, the exact displacement solutions, the strain and the stress fields are given in Appendix A. In this study, the problem due to partially enriched elements are alleviated by using the corrected or weighted XFEM [12] (c.f Section 2.4.5).

For the present numerical study, a square domain of size $L \times L$ with $L = 2$ is considered. Along the outer boundary, closed-form displacements are imposed. Meshes with characteristic element sizes of h={0.2, 0.1, 0.05, 0.025} are used and the results are shown in Figures 4.6 and 4.7. These figures show the decrease in the error in the displacement and the energy for the following different cases:

- eXtended Finite element solution with sub-domain integration (denoted as Std. XFEM) with blending correction [12].
- eXtended Finite element solution with SCCM (denoted as XFEM with SCCM) with blending correction.
- Smoothed XFEM solution (with blending correction) with 1,2 and 4 subcells above and below the material interface (see Figure 4.1) (denoted as SmXFEM 1 subcell, SmXFEM 2 subcells and SmXFEM 4 subcells)(see Figure 4.1).

From Figures 4.6 and 4.7, it may be seen that the convergence rate is not constant and both the Std. XFEM and the XFEM with SCCM obtains an average convergence rate of 1.22 in

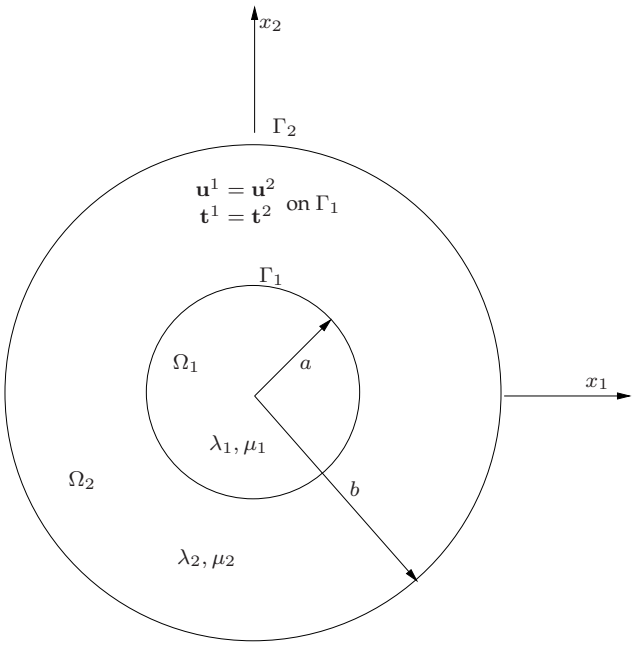

Figure 4.5: Bi-material boundary value problem

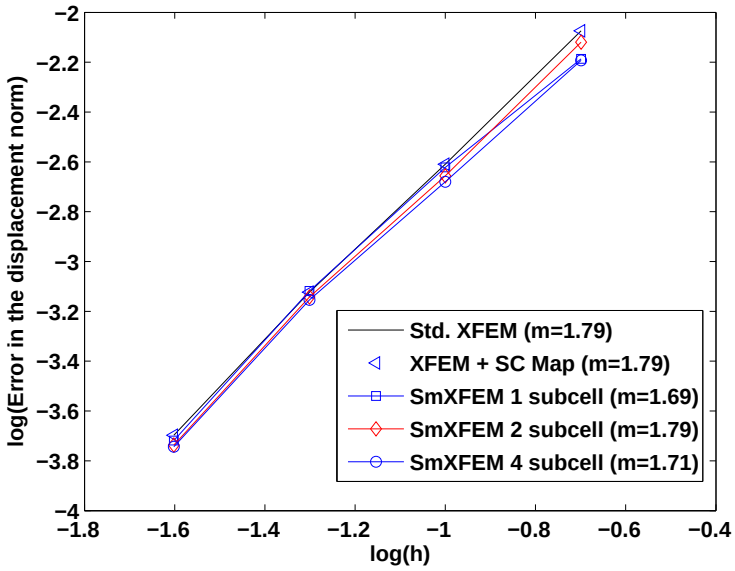

Figure 4.6: Bi-material circular inhomogeneity: the rate of convergence. The error is measured in displacement L^2 norm. Note that the behaviour of the XFEM + SC Map is approximately identical to the conventional XFEM. m is the average slope.

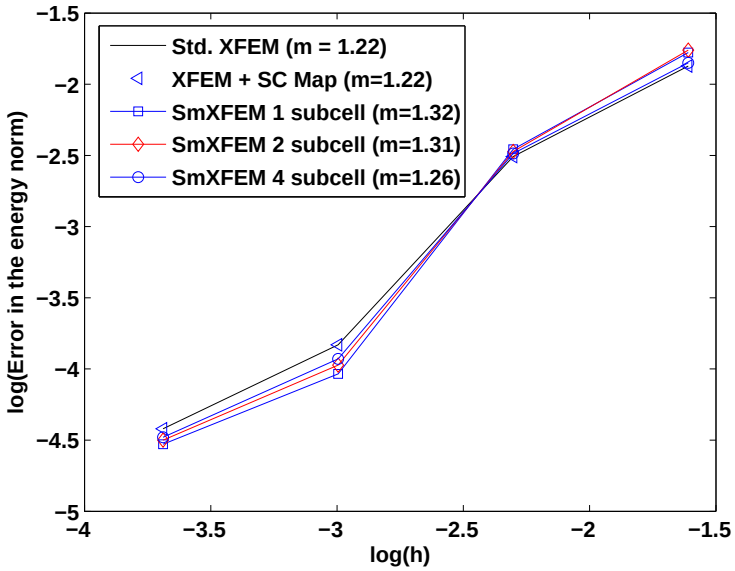

Figure 4.7: The convergence rate in the energy norm for the bi-material circular inhomogeneity problem. m is the average slope.

the energy norm and 1.79 in L^2. The SmXFEM with one, two and four subcells obtains an average convergence rate of 1.32, 1.31 and 1.26 in the energy norm and 1.69, 1.79 and 1.71 in L^2, respectively. The number of subcells does not have a significant influence on the average convergence rate. Based on the above two examples on weak discontinuities, it can be concluded that the behaviour of the SSM is very close to that of the conventional XFEM. On the other hand, the XFEM with SCCM yields identical results to the conventional XFEM. The main advantage of the strain smoothing and the SCCM is that sub-triangulation of the elements intersected by the discontinuity is eliminated.

4.2.2 Strong discontinuities

Infinite plate with a center crack under tension

As a first example, let us consider an infinite plate containing a straight crack of length a and loaded by a remote uniform stress field σ, as shown in Figure 4.8. Along ABCD, the closed-form near-tip displacements are imposed. The closed-form stress fields in terms of polar coordinates in a reference frame (r, θ) centered at the crack tip are given in Appendix A. All simulations are performed with $a = 100$ mm and $\sigma = 10^4$ N/mm^2 on a square mesh with sides of length 10 mm.

Before illustrating the efficiency and the accuracy of the XFEM with SCCM and the SmXFEM, the influence of the following parameters on the numerically computed SIF is studied:

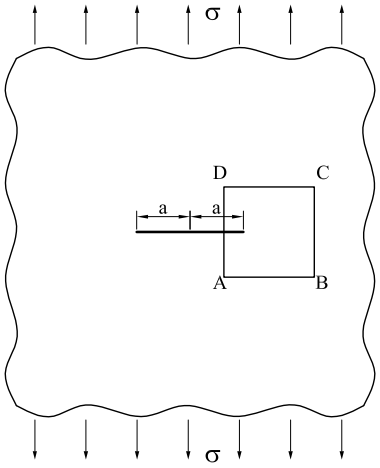

Figure 4.8: Infinite plate with a center crack under remote tension: geometry and loads.

- the number of integration points in the tip element in case of the XFEM with SCCM ;
- the number of integration points along each edge of the subcell and the number of subcells in the tip element in case of the SmXFEM.

For other elements, the integration rule given in Table 4.1 is used. A structured quadrilateral mesh (60×60) is used for the study. The number of integration points and the number of subcells are varied until the difference between two consecutive computations is less than a specified tolerance.

XFEM with SCCM: The convergence of the numerical SIF with the number of integration points in the tip element is shown in Figure 4.9. It is seen that with the increase in the number of integration points, the SIF reaches a constant value beyond 60 integration points. In this study, 80 integration points for the tip element are used (see Table 4.1).

SmXFEM: Figure 4.10 shows the influence of the number of integration points and the number of subcells on the numerical SIF. It can be seen that increasing the number of integration points beyond 2, along each edge of the subcell has very little influence on the numerical SIF, whereas, increasing the number of subcells in the tip element, increases the numerical SIF. In this example, the accuracy of the SmXFEM is studied for different number of subcells in the tip element, for example, 1, 2 and 6 subcells (see Table 4.1).
The rate of convergence of the relative error in the displacement (L^2) norm and the relative error in the SIF is shown in Figure 4.11 for the two numerical integration methods proposed in Chapter 3, along with the XFEM with sub-triangulation. It is seen that for the same number of integration points, the XFEM with SCCM outperforms (although *only*

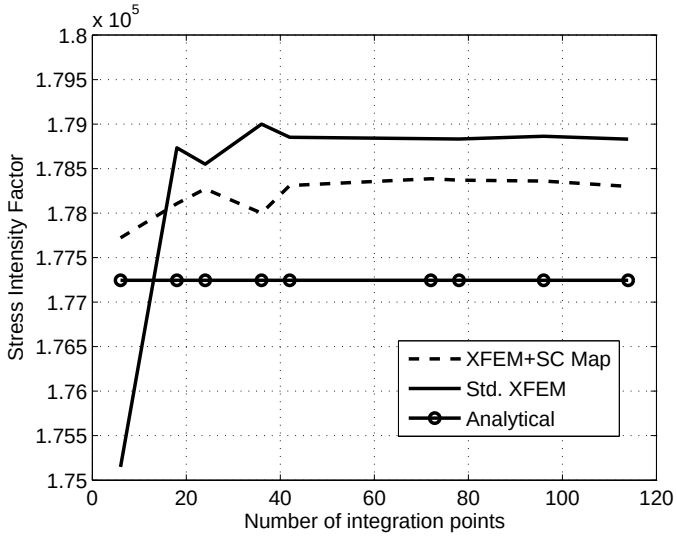

Figure 4.9: Griffith problem: the convergence of the numerical SIF with the number of integration points in the tip element. A structured quadrilateral mesh (60×60) is used.

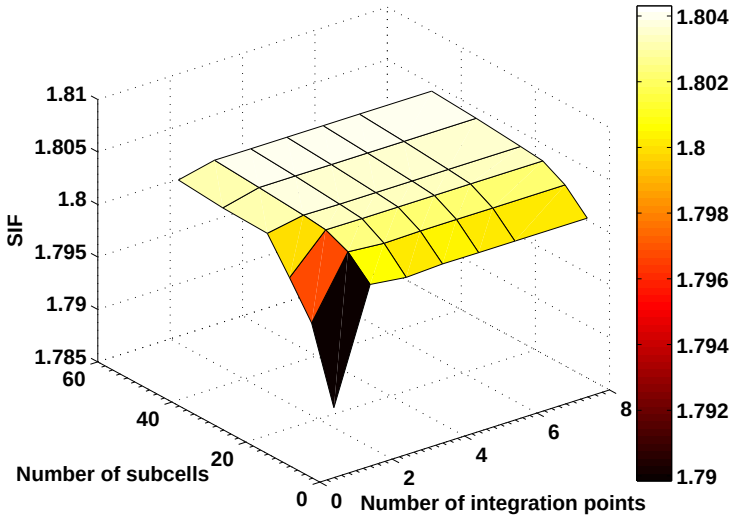

Figure 4.10: Griffith problem: the influence of the number of subcells in the tip element and the number of integration points along each edge of the subcell on the numerical stress intensity factor. Four subcells are used for standard elements and one subcell above and below the crack face is used for the split elements.

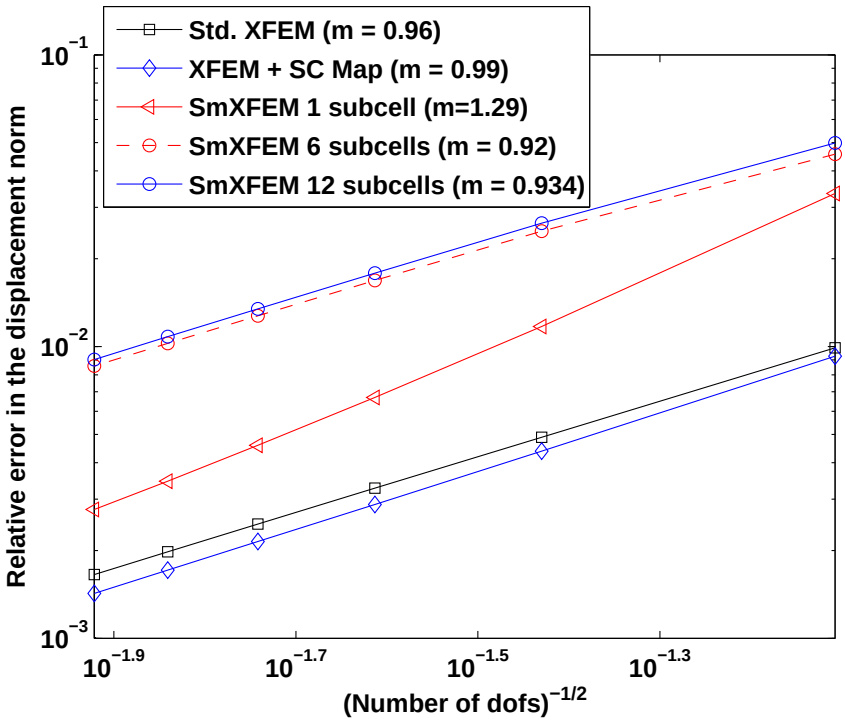

(a) Relative error in the displacement norm

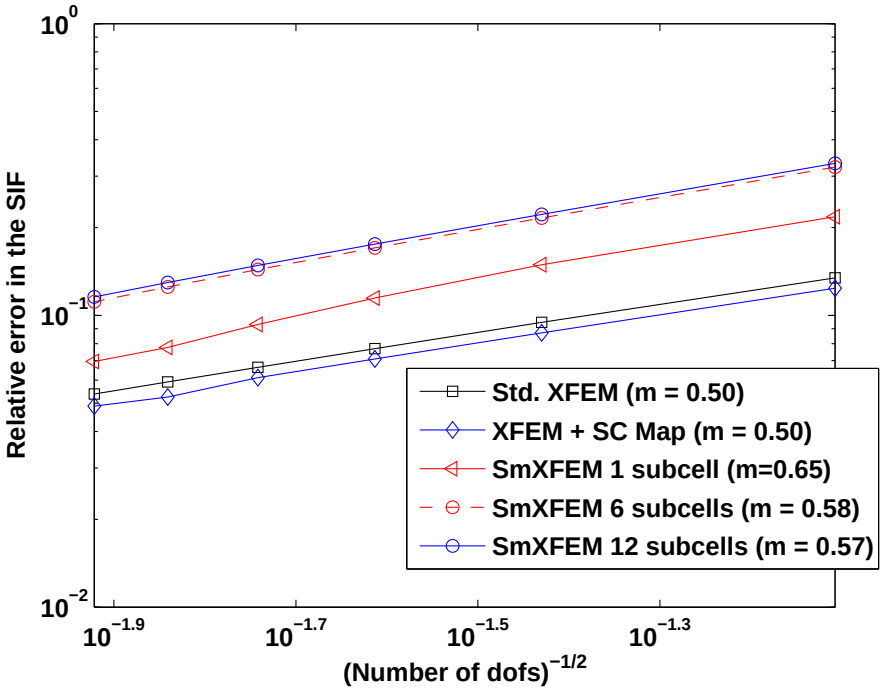

(b) Relative error in the SIF

Figure 4.11: Infinite plate under far field tension: Convergence results in L^2 and in the SIF. The rate of convergence is also given in the figure.

slightly) the conventional XFEM. The SmXFEM on the other hand, leads to slightly superior convergence rates, the error in the solution is greater than its XFEM counterpart. It can also be observed that with an increase in the number of subcells in the tip element, the error in the solution increases. But with decreasing mesh size, both techniques of numerical integration, viz., SmXFEM and XFEM with SCCM, approach the analytical solution.
Examining Figure 4.11 shows that the convergence rates in the SIFs and in the displacement norm (L^2) are suboptimal for the XFEM with standard integration, the XFEM with SCCM and the SmXFEM. This is because in this study only the tip element is enriched (topological enrichment) [2, 14, 24], which asymptotically reduces the XFEM approximation space to the standard FEM approximation space, this limits the optimal convergence rate to 0.5 in the presence of a square root singularity.
The main idea behind the strain smoothing is to write the strain field as a non-local weighted average of the compatible strain field. When strain smoothing is employed to smooth functions, the method outperforms the conventional FEM [5, 10, 16, 17]. In case of the weak discontinuity problem, the SmXFEM performs at least as well as the conventional XFEM. When applied to the functions of the form $r^{\frac{1}{\lambda}}, \lambda > 1$, the SSM eliminates the singularity by the use of the divergence theorem and the choice of the weighting function. To understand the influence of the enrichment functions of the form $r^{\lambda}\sin(\lambda\theta)$, a similar problem (to the above) is solved without these enrichment functions. In this case, the discontinuity cuts through the element and the crack tip falls on the element edge (see Figure 4.12). The elements that are cut entirely by the crack faces are identified as split elements and Heaviside enrichment is used to capture the jump across the crack faces. One subcell above and below the crack face are used for the split elements. For the tip element, the number of subcells is varied, for example, in this study, 1, 6 and 12 subcells are used. The convergence of the relative error in the displacement norm and the energy norm is shown in Figures 4.13 and 4.14. It can be seen that in general, the SmXFEM very slightly outperforms the conventional XFEM. Both methods with vanishing mesh size, converge to the analytical solution. It can also be observed that, with the increase in the number of subcells, the SmXFEM approaches the conventional XFEM solution, as seen in case of the SFEM without enrichment [5, 10, 16, 17] (see Figures 4.13 and 4.14).
From the above example, it can be seen that some of the basic properties of the SFEM[a] (c.f. Section 3.2) are recovered when only discontinuous (weakly or strongly) enrichment is used. The main advantage is that sub-triangulation of the elements intersected by the discontinuity is eliminated and for the elements that are completely cut by the crack faces, one subcell above and below is sufficient. To make use of the salient features of the SmXFEM, the SmXFEM is combined with the SCCM and the resulting technique is denoted as SmXFEM with SCCM. For the rest of this study, the strain smoothing is performed over the regions

[a] for example, by increasing the number of subcells, the FEM solution is recovered.

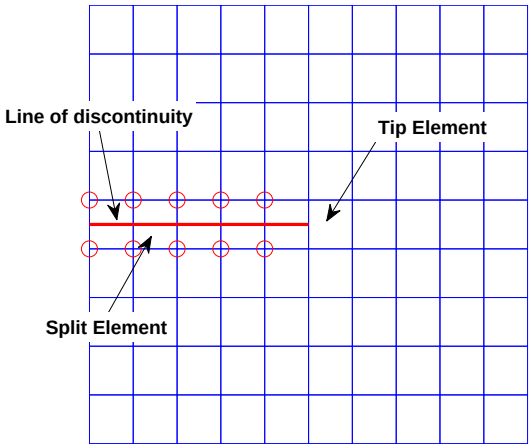

Figure 4.12: Domain discretized with finite elements. The red line denotes the crack face, the 'circled' nodes are enriched with Heaviside function. No near-tip asymptotic fields are used.

which are not enriched with asymptotic functions and the following convention is used for the purpose of numerical integration, unless stated otherwise:

- *Split elements*: SmXFEM, with one subcell above and below the crack face.
- *Tip element*: XFEM with SCCM.
- *Tip-blending elements*: standard XFEM.
- *Split-blending elements*: standard XFEM.
- *Standard elements*: SFEM with four subcells [17].

Edge crack under tension

In the next example, consider a plate of dimension $1\times$ 2, subjected to a tensile load, $\sigma = 1$. The geometry, loading and boundary conditions are shown in Figure 4.15. The reference mode I SIF is given by [1, 7]:

$$K_I = F\left(\frac{a}{W}\right)\sigma\sqrt{\pi a} \tag{4.10}$$

where a is the crack half-length, W is the plate width, L is the length of the plate and $F(\frac{a}{W})$ is an empirical function given as (For $(\frac{a}{W}) \leq 0.6$)

$$F\left(\frac{a}{W}\right) = 1.12 - 0.231\left(\frac{a}{W}\right) + 10.55\left(\frac{a}{W}\right)^2 - 21.72\left(\frac{a}{W}\right)^3 + 30.39\left(\frac{a}{W}\right)^4 \tag{4.11}$$

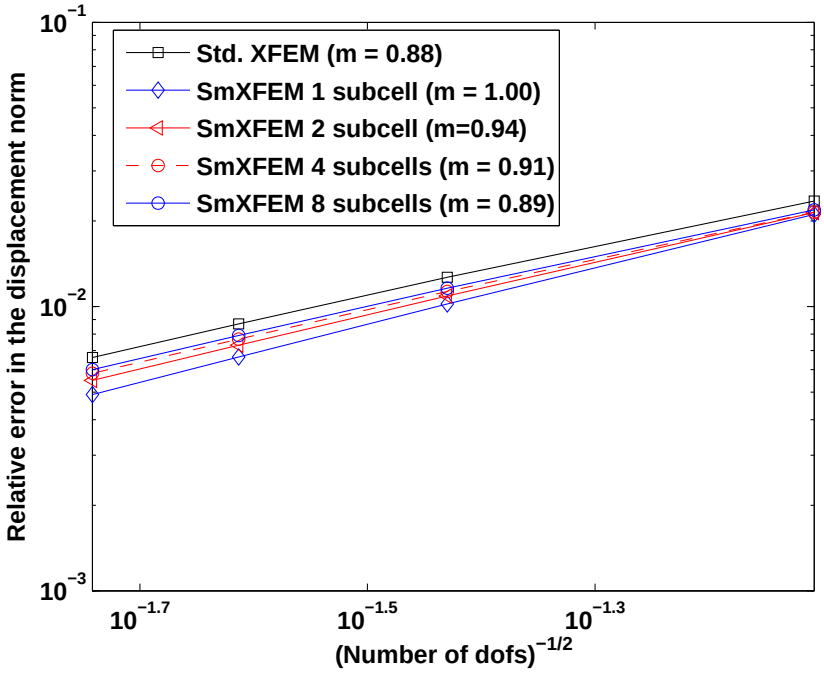

(a)

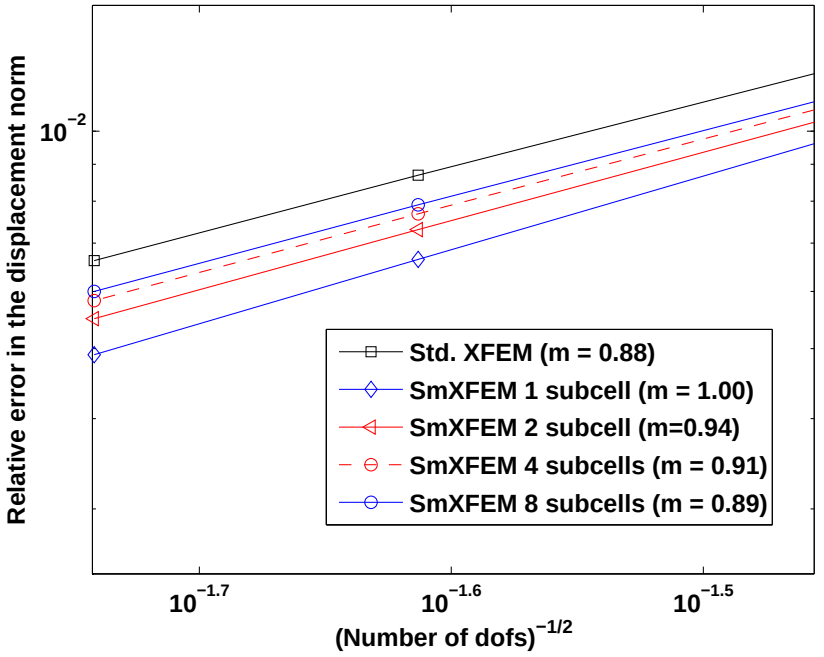

(b)

Figure 4.13: Infinite plate under far field tension: Convergence results for the relative error in the displacement norm (L^2) without the near-tip asymptotic functions: (a) the rate of convergence and (b) a zoomed in view. Note that as the number of subcells is increased, the strain smoothing approaches the XFEM solution. The rate of convergence (m) is also given in the figure.

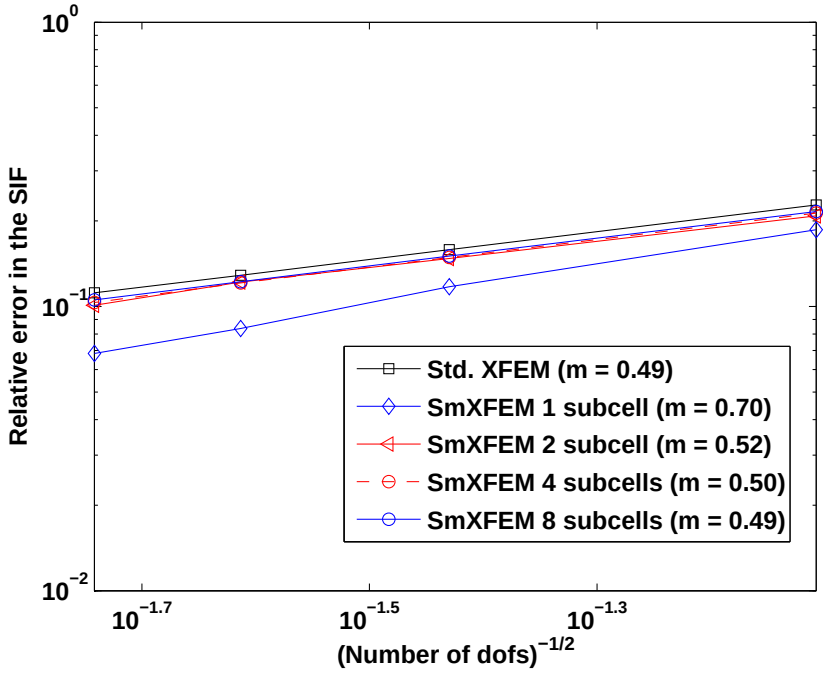

(a)

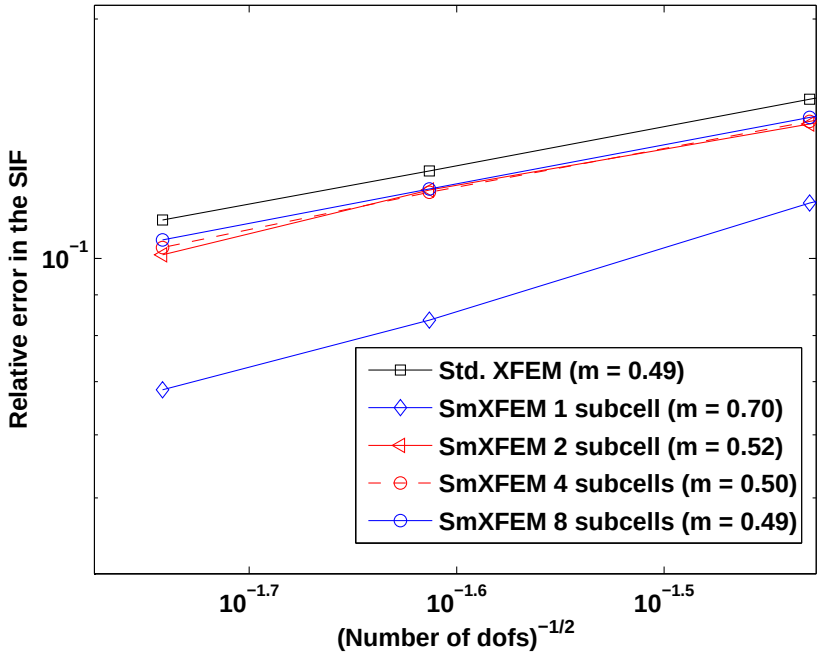

(b)

Figure 4.14: Infinite plate under far field tension: Convergence results for the relative error in the SIF without the near-tip asymptotic functions: (a) the rate of convergence and (b) a zoomed in view. The rate of convergence (m) is also given in the figure.

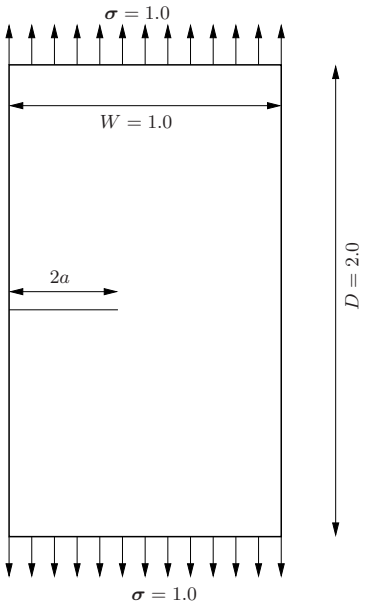

Figure 4.15: Plate with an edge crack under tension.

The convergence of the mode I SIF with mesh size and the rate of convergence of the SIF for a plate with an edge crack is shown in Figure 4.16. It is seen that with decreasing mesh size, both methods approach the analytical solution. Also, the proposed method performs slightly better than the standard XFEM with sub-triangulation.
In the above two examples, the background FE mesh is made up of regular quadrilateral elements. The numerical integration of the stiffness matrix over regular quadrilateral elements is not a difficult task. The real challenge is when the background mesh is made up of polygons or when the crack faces are irregular, i.e., when the crack faces cut the elements in such a way that at least one of the sub-domains, created by the intersection of the geometry with the mesh, is a polygon with more than 4 edges. To demonstrate the usefulness of the proposed integration technique, let us consider the problem of an inclined crack in tension with bi-linear quadrilateral element as background FE mesh. In the forthcoming examples, the results are presented only for the SmXFEM with SCCM.

Inclined crack in tension

Consider a plate with an angled crack subjected to a far field uni-axial stress field, $\boldsymbol{\sigma}$ (see Figure 4.17). In this example, mode I and mode II SIFs, K_I and K_{II}, respectively, are obtained as a function of the crack angle β. For the loads shown, the analytical stress intensity factors are given by [20]:

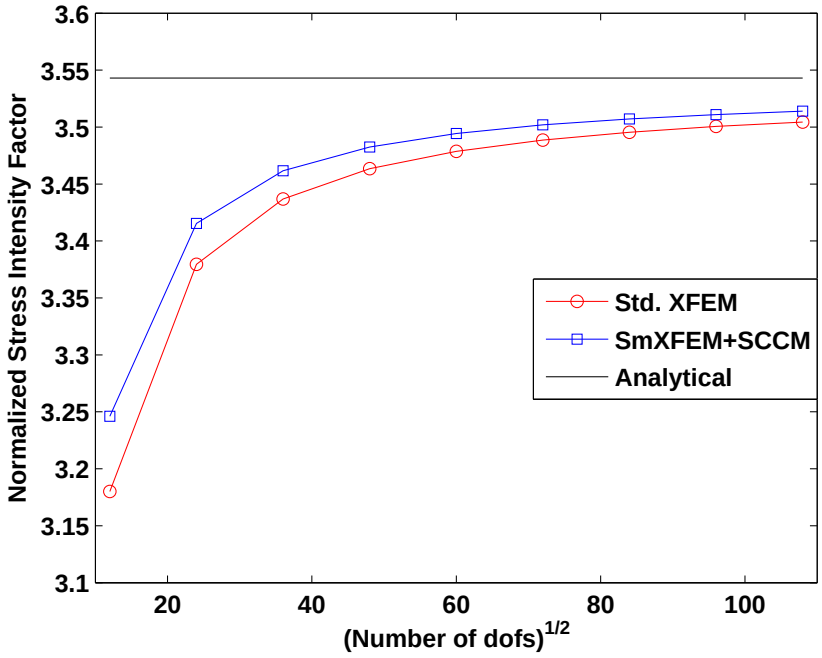

(a)

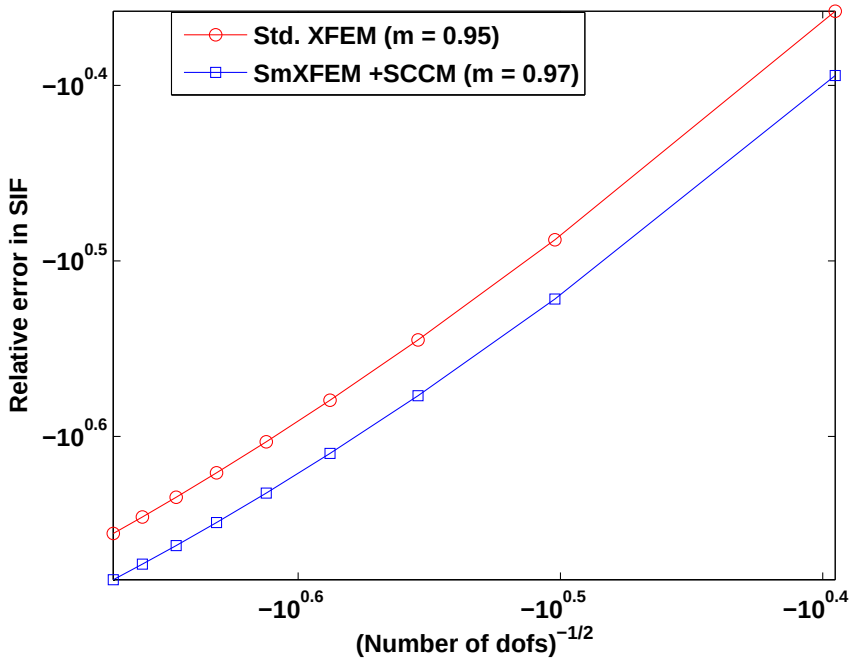

(b)

Figure 4.16: Edge crack problem: the convergence of the numerical stress intensity factor to the analytical stress intensity factor and the convergence rate.

$$K_I = \sigma\sqrt{\pi a}\cos\beta\cos\beta, \quad K_{II} = \sigma\sqrt{\pi a}\cos\beta\sin\beta. \tag{4.12}$$

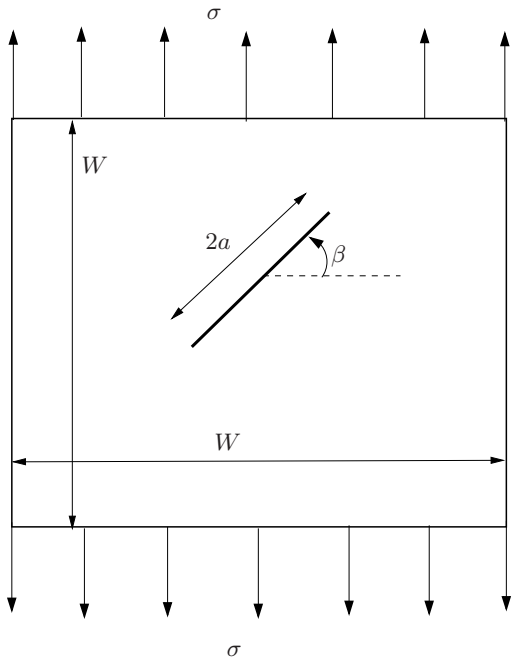

Figure 4.17: Inclined crack in tension.

The influence of the crack angle, β on the SIFs is shown in Figure 4.18. A structured mesh (100×100) is used for the study. For crack angles, $0^\circ < \beta < 90^\circ$, the crack face intersects the elements in such a way that one region of the split elements (either above or below the crack face) is a polygon. It is seen from Figure 4.18 that the numerical results from the proposed techniques are comparable with the analytical solution.

Multiple cracks in tension

In the next example, consider a plate with two cracks. The geometry and the boundary conditions of the problem are shown in Figure 4.19. The material properties are: Young's modulus $E = 3 \times 10^7$ N/mm^2 and Poisson's ratio, $\nu = 0.3$. A mesh size of 72×144 is used for the current study with crack size, $2a_1 = 0.2$. The length of the other crack $2a_2$ is varied. Figure 4.20 shows the variation of the mode I SIF for different H_x/V_y ratios and for different ratio of the crack lengths[b] with $\theta_1 = 0$ and $\theta_2 = 0$, where θ_1 and θ_2 are the angles subtended

[b] crack length ratio = $\frac{2a_2}{2a_1}$

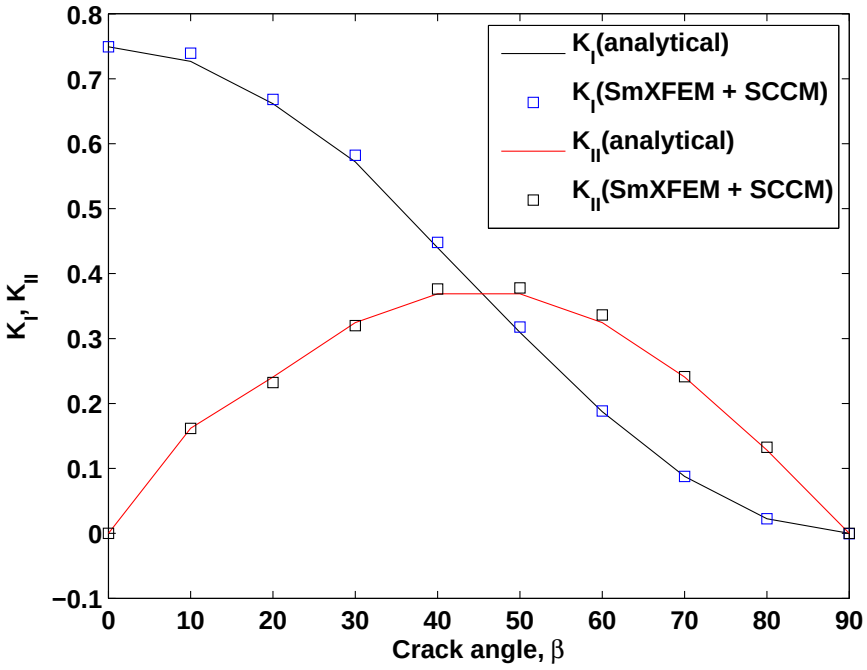

Figure 4.18: Variation of stress intensity factors K_I and K_{II} with crack angle, β.

by the crack faces with the horizontal (see Figure 4.19). The normalized mode I SIF[c] is plotted for the point A in Figure 4.19. This is done to non-dimensionalize the results. Also, the value of $K_{I_{\text{analytical}}}$ is taken as the value for a plate with a center crack given by:

$$K_I = \sigma\sqrt{\pi a \sec\left(\frac{\pi a}{2w}\right)} \tag{4.13}$$

where a is the half crack length, $w = \frac{W}{2}$ is the half width of the plate, and $\boldsymbol{\sigma}$ is the far field tensile load.

It can be seen that with the increase in the H_x/V_y ratio, the interaction between the cracks decreases, which is as expected. It is also seen from Figure 4.20 that as the ratio of the crack lengths increases, the normalized mode I SIF increases. And as the H_x/V_y ratio increases, the influence between the cracks decreases and the numerical SIF approaches a value that corresponds to a plate with a center crack.

Next, the influence of the relative angle between the cracks on the mode I and the mode II SIF for a crack length of $2a_1 = 2a_2 = 0.2$, with the distance between the cracks: $H_x = 0.1$ and $V_y = 0.2$ is studied. Figure 4.21 shows the variation of mode I and mode II SIF with the angle subtended by the cracks to the horizontal axis. It is seen that with an increase in the

[c] $K_{I_{\text{normalized}}} = \frac{K_{I_{\text{numerical}}}}{K_{I_{\text{analytical}}}}$

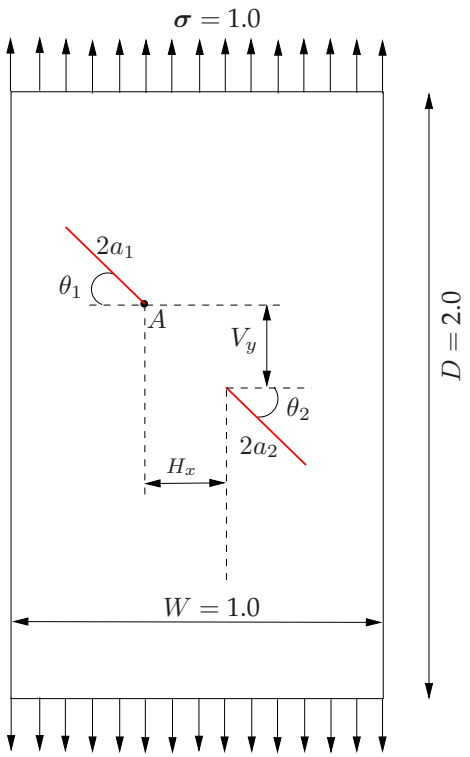

Figure 4.19: Plate with multiple cracks: geometry and loads. The length of the cracks are $2a_1$ and $2a_2$. θ_1 and θ_2 are the angles subtended by the crack faces with the horizontal.

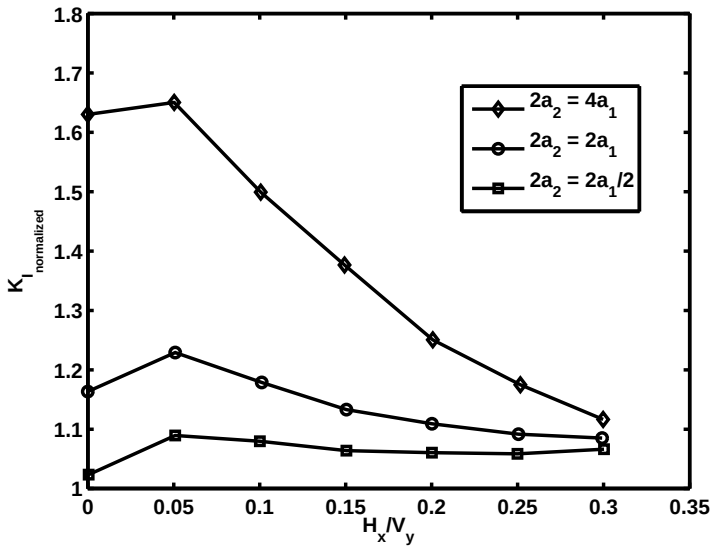

Figure 4.20: Influence of H_x/V_y ratio and the ratio of crack lengths, $2a_2/2a_1$ on the numerical mode I SIF.

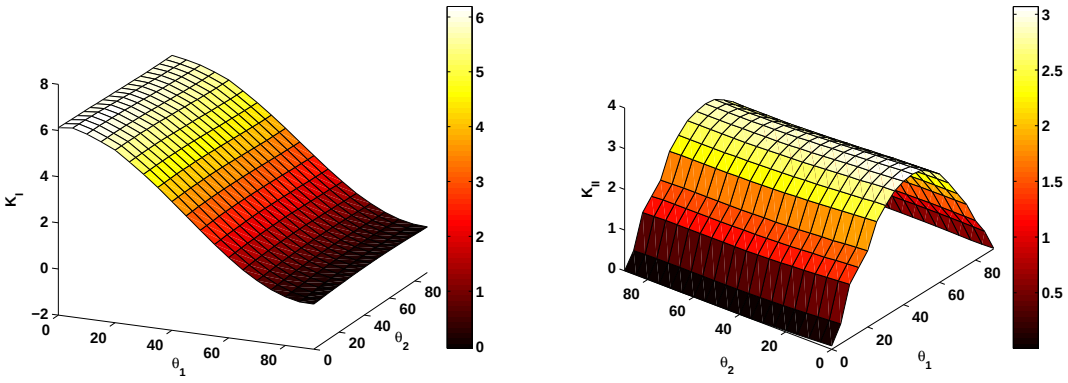

(a) mode I (b) mode II

Figure 4.21: Plate with two cracks: the variation of mode I SIF and mode II SIF with respect to angle between the cracks for crack lengths $2a_1 = 0.2$ and $2a_2 = 0.2$. The distance between the cracks are $H_x = 0.1$ and $V_y = 0.2$.

crack angle, (θ_1 and θ_2), the mode I SIF decreases and approaches zero for $\theta_1 = \theta_2 = 90°$. While the mode II SIF, initially increases with an increase in the crack angle and reaches the maximum for the crack angle $\theta_1 = \theta_2 = 45°$ and then decreases with further increase in the crack angle. Note that when $\theta_1 = \theta_2 = 90°$, the crack is aligned to the loading direction.

4.2.3 Inclusion-crack interaction

As a last example in this chapter, the interaction between a crack and an inclusion in particle reinforced composite is numerically studied. Both the crack and the inclusion are represented independent of the background mesh using level sets (c.f. Chapter 2, Section 2.4) and appropriate enrichment functions are used to capture the underlying physics. The enriched approximation for this problem, takes the following form:

$$\mathbf{u}^h(\mathbf{x}) = \sum_{I\in\mathcal{N}^{\text{fem}}} N_I(\mathbf{x})\mathbf{q}_I + \underbrace{\sum_{J\in\mathcal{N}^c} N_J(\mathbf{x})H(\mathbf{x})\mathbf{a}_J + \sum_{K\in\mathcal{N}^f} N_K(\mathbf{x})\sum_{\alpha=1}^{4} B_\alpha(\mathbf{x})\mathbf{b}_K^\alpha}_{\text{for cracks}} + \underbrace{\sum_{L\in\mathcal{N}^{\text{inc}}} N_L(\mathbf{x})\Psi(\mathbf{x})\mathbf{c}_L}_{\text{for inclusions}} \tag{4.14}$$

where $\mathcal{N}^{\text{fem}}$ is the set of all nodes in the finite element mesh, $\mathcal{N}^c, \mathcal{N}^f$ and $\mathcal{N}^{\text{inc}}$ are the set of nodes enriched with a Heaviside function, the near-tip asymptotic fields and the absolute value function. $\mathbf{a}_J$ and $\mathbf{b}_K^\alpha$ are the nodal degrees of freedom corresponding to the Heaviside function H and the near-tip functions, $\{B_\alpha\}_{1\leq\alpha\leq4}$, given by Equations (2.30) and (2.32). $\mathbf{c}_L$

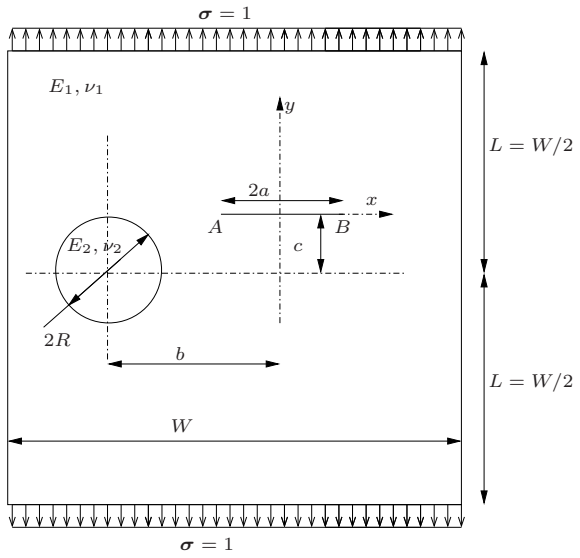

Figure 4.22: A plate with a horizontal crack in the neighbourhood of a circular inclusion: geometry and boundary conditions.

is the nodal degrees of freedom that corresponds to the absolute value function, Ψ, given by Equation (2.28) to capture the material discontinuity. The SIFs are computed by using the domain form of the interaction integral. The conventional form is modified to account for the material discontinuity. The main advantage of the new form is that it does not require any derivative of the material property parameters [25]. This is discussed in Appendix D.

Effect of the distance between the crack and the inclusion

Figure 4.22 shows a square plate of side W with a horizontal crack of length $2a$ in the neighbourhood of a circular inclusion of radius R. The following parameters are chosen for the current study: $W = 100; a/W = 0.01; b/a = (3, 4, 6, 8, 10); R = 2a; E_1 = 1, E_2 = 10^4; \nu_1 = \nu_2 = 0.35; \sigma_o = 1; K_o = \sigma_o\sqrt{\pi a}$. Tables 4.3 and 4.4 show the variation of the crack tip SIF (normalized SIF)[d] as a function of the distance to the center of the circular inclusion. It can be seen that as the distance between the crack and the inclusion increases, the effect of the inclusion on the crack tip SIF decreases. In other words, the crack tip SIF increases with increasing distance from the inclusion. The results show good agreement with the results available in the literature [23, 25].

[d]Normalized SIF = $K_{\text{numerical}}/K_o$

Table 4.3: Normalized SIFs at left tip (A) for a plate with a crack and a circular inclusion under far field tension σ_o.

b/a	K_I			K_{II}		
	Ref [23]	Ref [25]	Present	Ref [23]	Ref [25]	Present
3	0.5810	0.5908	0.5916	0.0636	0.0652	0.0592
4	0.8199	0.8174	0.8185	-0.0661	-0.0671	-0.0646
6	0.9506	0.9505	0.9517	-0.0368	-0.0373	-0.0359
8	0.9787	0.9785	0.9798	-0.0173	-0.0179	-0.0172
10	0.9878	0.9877	0.9889	-0.0091	-0.0101	-0.0117

Table 4.4: Normalized SIFs at right tip (B) for a plate with a crack and a circular inclusion under far field tension σ_o.

b/a	K_I			K_{II}		
	Ref [23]	Ref [25]	Present	Ref [23]	Ref [25]	Present
3	0.7995	0.8011	0.7916	-0.0733	-0.0711	-0.0684
4	0.9068	0.9065	0.8957	-0.0560	-0.0568	-0.0555
6	0.9684	0.9687	0.9572	-0.0252	-0.0255	-0.0245
8	0.9842	0.9844	0.9727	-0.0125	-0.0129	-0.0124
10	0.9901	0.9903	0.9924	-0.0069	-0.0076	-0.0069

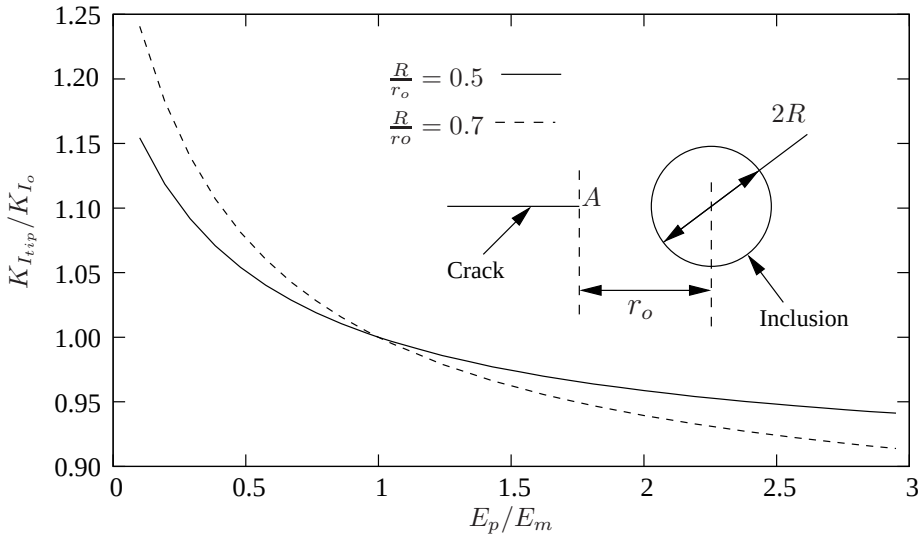

Figure 4.23: Normalized crack tip SIF (mode I) $(K_{I_{tip}}/K_{I_o})$ at point A as a function of ratio of Young's modulus (E_p/E_m).

Effect of the mismatch in the Young's modulus

Figure 4.23 shows the normalized crack tip SIF as a function of the mismatch of Young's modulus between the inclusion and the matrix for different distances between the crack tip and the center of the inclusion. For a particular distance from the crack tip to the inclusion, with increase in the mismatch of the Young's modulus, the SIF decreases. The decrease in the crack tip SIF is due to the presence of the inclusion and this decrease in SIF indicates toughening due to the shielding of the inclusion.

Crack tip shielding & amplification

Next, the crack tip shielding in the presence of an inclusion is studied. When the inclusion is perfectly bonded to the matrix, the crack deflection is a prominent toughening mechanism. The crack deflection depends on the inclusion size, the inclusion eccentricity, the number of inclusions surrounding the crack, the orientation of crack, to name a few. A rigid inclusion in a relatively compliant matrix shields the crack tip as it is approached. Also, shielding depends on the aforementioned factors. The geometry and boundary conditions are shown in Figure 4.24. The radius of the inclusion, $R = W/20$ is considered, where W is the width of the plate.

The variation of the energy release rate (ERR), G with respect to the crack length and the elastic moduli is studied. The ratio of the elastic moduli E_p/E_m is varied from 2 to 8 as in the literature [8, 13], where E_p is the Young's modulus of the inclusion and E_m is the Young's modulus of the matrix. The ERR, G is calculated using the SIFs by the following

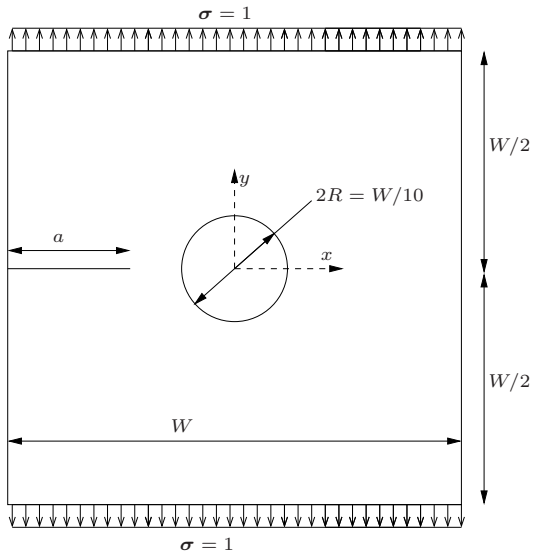

Figure 4.24: A plate with a horizontal edge crack in the neighbourhood of a circular inclusion: geometry and boundary conditions.

equation:

$$G = \frac{\kappa + 1}{8\mu}(K_I^2 + K_{II}^2) \tag{4.15}$$

where the Kolosov coefficient, κ is $(3 - 4\nu)$ for plane strain and $(3 - \nu)/(1 + \nu)$ for plane stress. The Poisson's ratio for the inclusion and the matrix are assumed to be $\nu = 0.33$ and 0.17, respectively. The variation of the nondimensional ERR, G/G_o for different crack lengths and the elastic moduli is shown in Figure 4.25, where G_o is the ERR for the matrix without the inclusion. With an increasing ratio of the elastic moduli, the nondimensional ERR decreases. From Figure 4.25, it can been that the crack senses the rigid inclusion infront of it at least from a distance of ≈ 5 times the radius of the inclusion [8, 13]. The observed variation of the ERR agree with the results reported in the literature.

Effect of a pair of inclusions

The effect of a pair of circular inclusions in the crack path on the ERR is studied next. A symmetrically located pair of inclusions with respect to the crack, as shown in Figure 4.26 leads to crack growth under mode I conditions. The length of the crack is a and the inclusions are located at $p/W = 0.25$ from the crack tip. The separation distance 's' between the inclusions is varied between $W/8$ to W. Figure 4.27 shows the variation of the ERR as a function of the crack length for various position of the inclusions. It can be seen that by increasing the crack length, the ERR decreases indicating the crack shielding and maximum

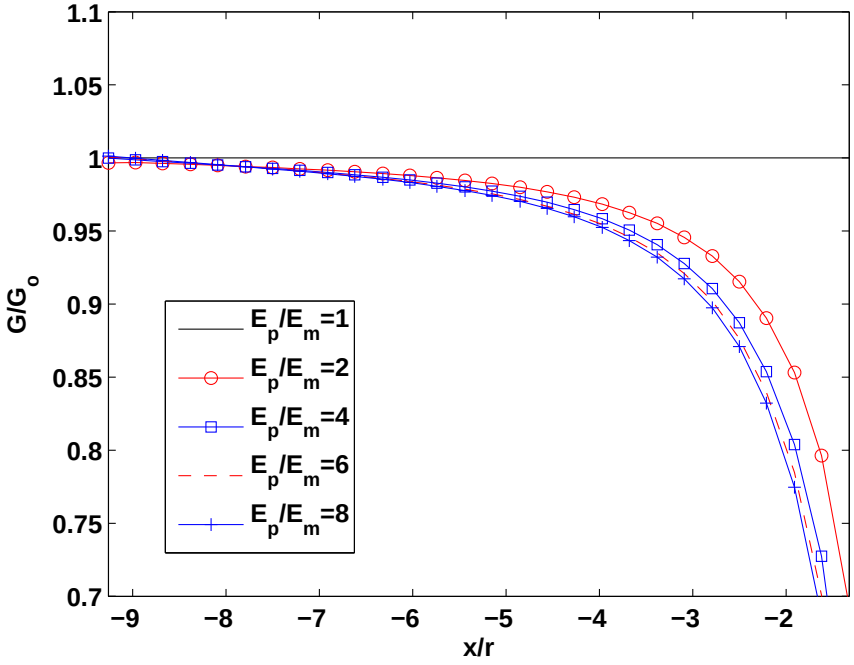

(a)

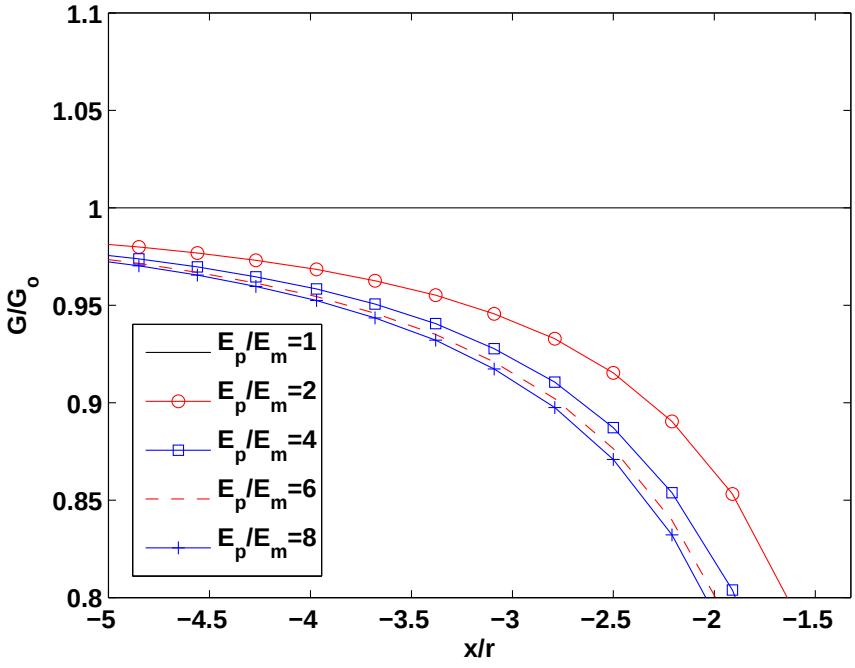

(b)

Figure 4.25: Variation of non-dimensionalized ERR for various ratio of elastic moduli, E_p/E_m, where E_p is the Young's modulus of the inclusion and E_m is the Young's modulus of the matrix. It can be seen that the crack senses the inclusion at a distance of ≈ 5 times the radius of the inclusion [8, 13].

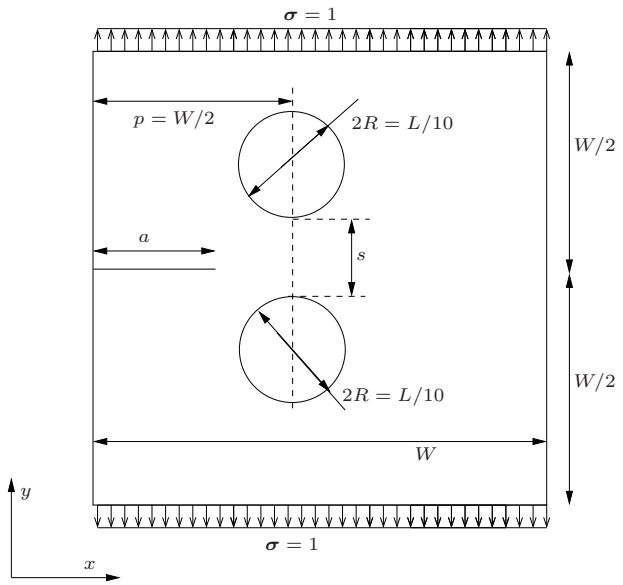

Figure 4.26: A plate with a horizontal edge crack in the neighbourhood of symmetrically located two circular inclusions, geometry and boundary conditions.

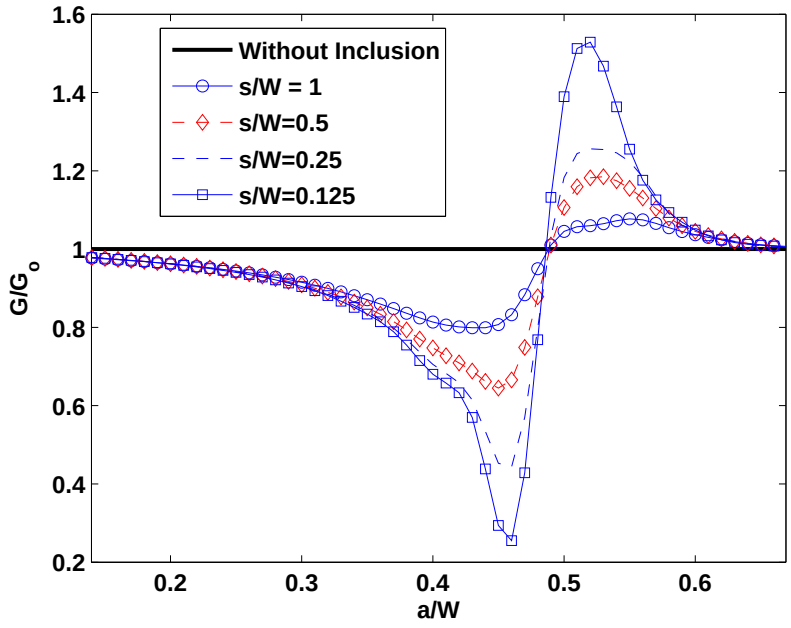

Figure 4.27: Crack tip shielding and amplification factors due to pair of symmetrically situated inclusions in the crack path.

shielding occurs when the crack tip is approximately at a distance of $W/2$ in front of the center of the inclusion. With further increase in the crack length, the crack shielding decreases and approaches unity when the crack length approaches p/W (the center of the inclusions). And with further increase, an amplification of the ERR can be seen. This is because, when the crack length, a is greater than p/W, the effect of the inclusion below the crack is small, as the crack experiences the majority of the far field tension. The amplification decreases with further increase in the crack length. The observed crack shielding/amplification effects agree well with the results reported in the literature [8, 13, 15].

4.2.4 Crack growth

In this section, the proposed method is applied to study a quasi-static crack growth. The crack growth is governed by the maximum hoop stress criterion [11], which states that the crack will propagate from its tip in the direction θ_c where the circumferential (hoop) stress $\sigma_{\theta\theta}$ is maximum. The critical angle is computed by solving the following equation:

$$K_I \sin(\theta_c) + K_{II}(3\cos(\theta_c) - 1) = 0 \tag{4.16}$$

Solving Equation (4.16) gives the crack propagation angle [21]:

$$\theta_c = 2\arctan\left[\frac{-2\left(\frac{K_{II}}{K_I}\right)}{1+\sqrt{1+8\left(\frac{K_{II}}{K_I}\right)^2}}\right] \tag{4.17}$$

In this study, the amount by which the crack advances at each step is fixed in advance, as opposed to being computed at each step based on some crack growth law.

Double cantilever beam

In this example, the crack growth in a pre-notched double cantilever beam (DCB) subjected to an end load is studied. The dimensions of the DCB (see Figure 4.28) are 6×2 m and the initial pre-crack with length of $a = 2.05$ m is considered. The material properties are taken to be Young's modulus, $E = 100$ N/m^2 and Poisson's ratio, $\nu = 0.3$. And the load P is taken to be unity. By symmetry, a crack on the mid-plane of the beam is under pure mode I and the crack would propagate in a straight line, however, due to small perturbations in the crack geometry, the crack takes a curvilinear path [3].
The crack growth increment, Δa is taken to be 0.15 for this study and the crack growth is simulated for 8 steps. The domain is discretized with a structured mesh consisting of 1200 elements. The crack path is simulated using both methods and is shown in Figure 4.29. The crack path qualitatively agrees with the published results [3].

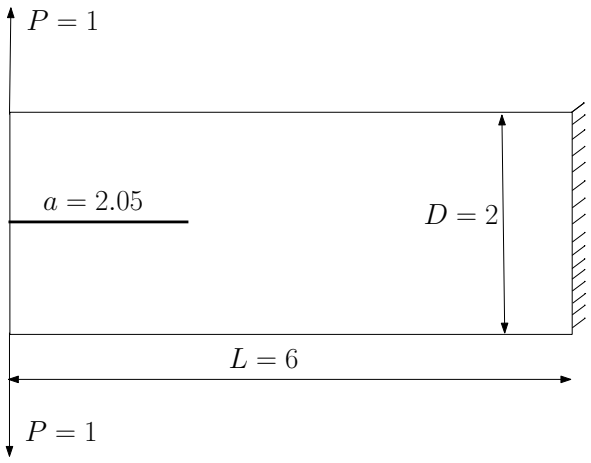

Figure 4.28: Geometry and loads of a double cantilever beam

Crack inclusion interaction

In this example, crack growth in presence of an inclusion is studied. Consider a plate of dimension 4×8, subjected to a tensile load, $\sigma = 1$. The geometry, loading and boundary conditions are shown in Figure 4.30. The plate is pre-notched and has an off-centered inclusion. Let $E_{\text{ratio}} = E_{\text{matrix}}/E_{\text{inclusion}}$ be the ratio of Young's modulus between the matrix and the inclusion. The crack growth around the inclusion is studied for two different ratios of Young's modulus: (a) soft inclusion ($E_{\text{ratio}} = 0.1$) and (b) hard inclusion ($E_{\text{ratio}} = 10$). A mesh size of 100×100 is used for the current study. Figure 4.31 shows the calculated crack path for the soft inclusion and for the hard inclusion using both the methods, i.e., Std. XFEM and SmXFEM + SCCM. It can be seen that both methods yield identical crack paths. In case of the soft inclusion, the crack is attracted towards the inclusion, on the other hand, the crack is deflected in the presence of a hard inclusion. The obtained results are consistent with the results available in the literature [4, 6]

4.3 Conclusions

In this chapter, the accuracy and the efficiency of the methods proposed in Chapter 3 are illustrated by solving a few problems involving weak and strong discontinuities. Both methods yield comparable results to their counterpart standard XFEM with sub-domain integration. The interaction between a crack and an inclusion is numerically studied. The crack tip energetics such as 'shielding' and 'amplification' effects are captured accurately.

SmXFEM is shown numerically that as long as only discontinuous (weak or strong) enrichment, i.e., discontinuities in the unknown, the smoothed version of the XFEM performs

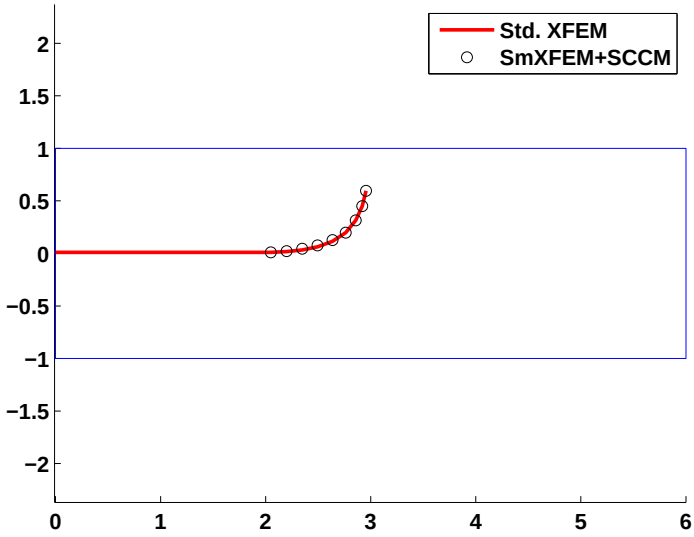

(a)

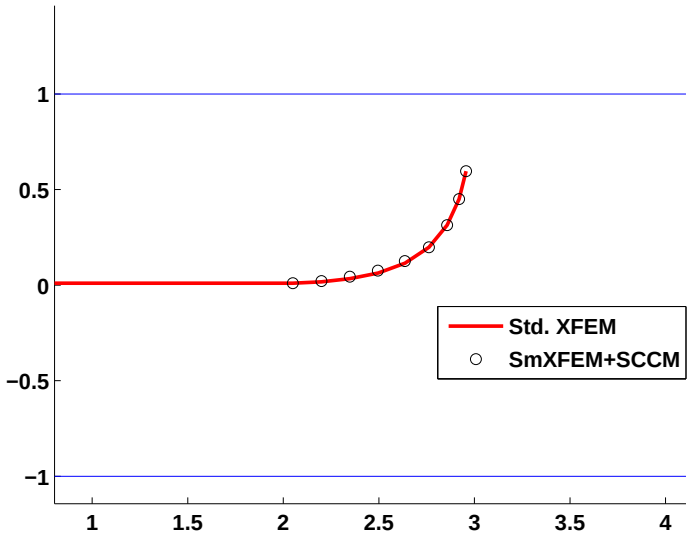

(b)

Figure 4.29: Double cantilever beam: (a) comparison of crack path between the two numerical integration methods and (b) a zoomed in view

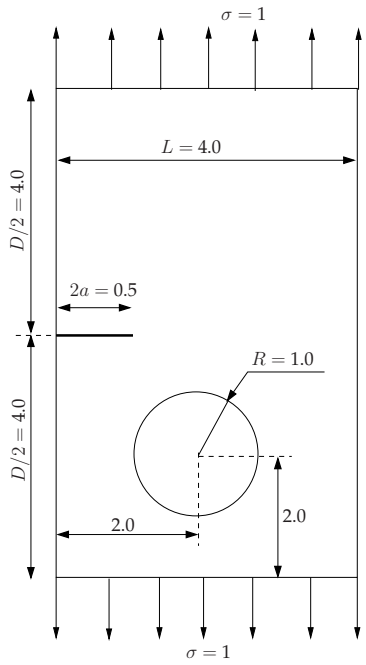

Figure 4.30: Crack inclusion interaction: geometry and boundary conditions.

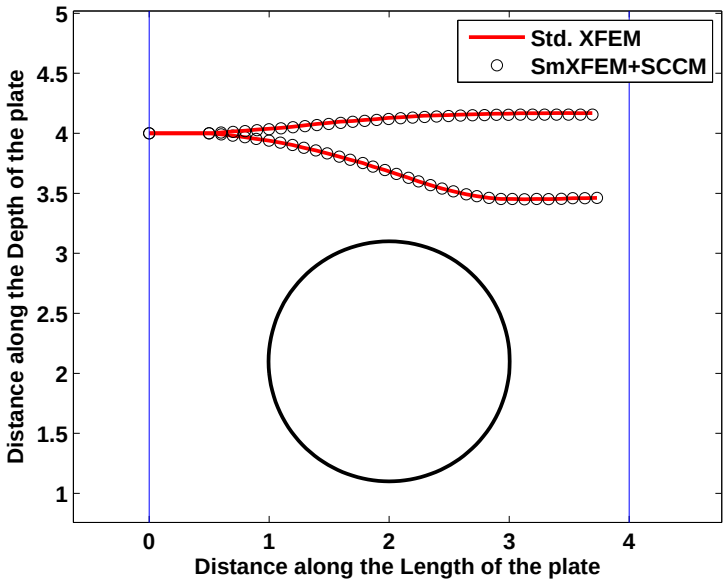

Figure 4.31: Numerically computed crack path using the Std. XFEM and the SmXFEM + SCCM. The top curve denotes the case of the hard inclusion while the lower curve corresponds to the soft inclusion.

at least as well as the XFEM. The potential advantages of the smoothed XFEM are that no subdivision of the split elements is required and that the derivatives of the shape functions (including the enrichment functions) is not required. In the case of enrichment schemes for LEFM enrichment, however, numerical examples indicate that while the convergence rate obtained with SmXFEM is equal or superior to that of the XFEM, the error level is greater. But with reducing mesh size, the SmXFEM approaches the analytical solution.

XFEM with SCCM eliminates the need to sub-divide the elements cut by strong or weak discontinuities or containing the crack tip. It is seen that for similar number of integration points, the XFEM with SCCM slightly outperforms the convention integration method based on sub-division. With mesh refinement, the XFEM with SCCM provides convergence of the SIFs to the analytical SIFs. Owing to its simplicity, the XFEM with SCCM can be easily integrated in any existing code.

To improve the efficiency of the smoothed XFEM, a new technique is proposed that makes use of the best of all the three methods, i.e., the XFEM with SCCM for tip elements, the XFEM with sub-domain integration for blending elements, the SmXFEM for split elements and the SFEM for standard elements. The resulting technique, in this thesis, is named as the SmXFEM + SCCM. The method yields comparable results to that of the conventional XFEM. The main advantage is that the sub-triangulation of elements intersected by the discontinuity is eliminated.

Bibliography

[1] T. L. Anderson. *Fracture mechanics: Fundamentals and Applications*. CRC Press, 1995.

[2] E. Béchet, H. Minnebo, N. Moës, and B. Burgardt. Improved implementation and robustness study of the X-FEM for stress analysis around cracks. *International Journal for Numerical Methods in Engineering*, 64(8):1033–1056, 2005. doi: 10.1002/nme.1386.

[3] T. Belytschko and T. Black. Elastic crack growth in finite elements with minimal remeshing. *International Journal for Numerical Methods in Engineering*, 45:601–620, 1999.

[4] S. Bordas, V. P. Nguyen, C. Dunant, A. Guidoum, and H. Nguyen-Dang. An extended finite element library. *International Journal for Numerical Methods in Engineering*, 71:703–732, 2007.

[5] S. P. A. Bordas and S. Natarajan. On the approximation in the smoothed finite element method (SFEM). *International Journal for Numerical Methods in Engineering*, 81:660–670, 2010.

[6] P. O. Bouchard, F. Bay, and Y. Chastel. Numerical modelling of crack propagation: automatic remeshing and comparison of different criteria. *Computer Methods in Applied Mechanical and Engineering*, 192:3887–3908, 2003.

[7] D. Broek. *The practical use of fracture mechanics*. Kluwer Academic Press, 1988.

[8] M. B. Bush. The interaction between a crack and a particle cluster. *International Journal of Fracture*, 88:215–232, 1997.

[9] J. Chessa, H. Wang, and T. Belytschko. On the construction of blending elements for local partition of unity enriched finite elements. *International Journal for Numerical Methods in Engineering*, 57:1015–1038, 2003.

[10] K. Y. Dai, G. R. Liu, and T. T. Nguyen. An n-sided polygonal smoothed finite element method (nSFEM) for solid mechanics. *Finite Elements in Analysis and Design*, 43:847–860, 2007.

[11] F. Erdogan and G. C. Sih. On the crack extension in plates under plane loading and transverse shear. *Journal of Basic Engineering*, 85:519–527, 1963.

[12] T.-P. Fries. A corrected XFEM approximation without problems in blending elements. *International Journal for Numerical Methods in Engineering*, 75:503–532, 2008.

[13] R. Kitey, A.-V. Phan, H. V. Tippur, and T. Kaplan. Modeling of crack growth through particle clusters in brittle matrix by symmetric-galerkin boundary element method. *International Journal of Fracture*, 141:11–25, 2006.

[14] P. Laborde, J. Pommier, Y. Renard, and M. Salaün. High-order extended finite element method for cracked domains. *International Journal for Numerical Methods in Engineering*, 64(3):354–381, September 2005. doi: 10.1002/nme.1370.

[15] R. Li and A. Chudnovsky. Energy analysis of crack interaction with an elastic inclusion. *International Journal of Fracture*, 63:247–261, 2003.

[16] G. R. Liu, T. T. Nguyen, K. Y. Dai, and K. Y. Lam. Theoretical aspects of the smoothed finite element method (SFEM). *International Journal for Numerical Methods in Engineering*, 71:902–930, 2007.

[17] H. Nguyen-Xuan, S. P. A. Bordas, and H. Nguyen-Dang. Smooth finite element methods: convergence, accuracy and properties. *International Journal for Numerical Methods in Engineering*, 74: 175–208, 2008.

[18] G. P. Nikishkov and S. N. Atluri. Calculation of fracture mechanics parameters for an arbitrary three-dimensional crack by the equivalent domain integral method. *International Journal for Numerical Methods in Engineering*, 24:851–867, 1987.

[19] C. F. Shih, B. Moran, and T. Nakamura. Energy release rate along a three-dimensional crack front in a thermally stressed body. *International Journal of Fracture*, 30:79–102, 1986.

[20] G. C. Sih. Energy-density concept in fracture mechanics. *Engineering Fracture Mechanics*, 5: 1037–1040, 1973.

[21] N. Sukumar and J.-H. Prévost. Modeling quasi-static crack growth with the extended finite element method part i: Computer implementation. *International Journal of Solids and Structures*, 40:7513–7537, 2003.

[22] N. Sukumar, D. L. Chopp, N. Moës, and T. Belytschko. Modeling holes and inclusions by level sets in the extended finite-element method. *Computer Methods in Applied Mechanical and Engineering*, 190:6183–6200, 2001.

[23] Y. B. Wang and K. T. Chou. A new boundary element method for mixed boundary value problems involving cracks and holes: interactions between rigid inclusions and cracks. *International Journal of Fracture*, 110:387–406, 2001.

[24] Q. Z. Xiao and B. L. Karihaloo. Improving the accuracy of XFEM crack tip fields using higher order quadrature and statically admissible stress recovery. *International Journal for Numerical Methods in Engineering*, 66(9):1378–1410, 2006.

[25] H. Yu, L. Wu, S. Du, and Q. He. Investigation of mixed-mode stress intensity factors for non-homogeneous materials using an interaction integral method. *International Journal of Solids and Structures*, 46:3710–3724, 2009.

5

Free vibration analysis of cracked plates

In this chapter, the dynamic characteristics of cracked Functionally Graded Material (FGM) plates based on the First order Shear Deformation Theory (FSDT) is studied. The crack geometry is modelled independent of the underlying mesh by using the XFEM (c.f. Chapter 2, Section 2.4) [4, 7, 8]. The numerical integration over the elements intersected by the discontinuity surface is performed using the new integration technique, i.e., SmXFEM with SCCM (c.f. Chapter 4, §4.2.2). In the presence of flaws such as through-the-thickness cracks, the fundamental frequency will decrease with an increase in the flaw size. This severely affects the performance of plate structures. A crack in a vibrating structure results in stiffness decrease, which is a function of the crack location and the crack size. Earlier studies on the vibration of cracked plates using the FEM [23, 32] were restricted to a limited number of configurations, because the mesh has to conform to the geometry. The flexibility provided by the XFEM in handling internal discontinuities is exploited here to study the influence of the cracks on the fundamental frequency of the plate structure. This chapter is organized as follows. The next section presents a short summary of the different numerical methods and the different plate theories used to study the dynamic characteristics of FGM plates. Section 5.2 will give an introduction to FGMs. A brief overview of the FSDT, also called the Reissner-Mindlin plate theory is presented in Section 5.3. Section 5.4 illustrates the basic idea of the XFEM as applied to plates. A systematic parametric study on the influence of the various parameters, such as the gradient index, the boundary conditions, the crack and the plate geometry on the natural frequencies of the FGM plates using the 4-noded shear flexible element based on the field and the edge consistency approach [42] is presented in Section 5.5, followed by concluding remarks.

5.1 Background

Engineered materials, such as laminated composites are widely used in the automotive and aerospace industry due to their excellent strength-to and stiffness-to-weight ratios and the

possibility of tailoring their properties to optimize their structural response. But due to the sudden change in the material properties between the layers in laminated composites, these materials suffer from premature failure or the decay of the stiffness characteristics because of delaminations and chemically unstable matrix and lamina adhesives. The emergence of FGMs [21, 22] has revolutionized the aerospace and the aerocraft industry. FGMs used initially as thermal barrier materials for aerospace structural applications and fusion reactors are now developed for general use as structural components in high temperature environment. FGMs are manufactured by combining metals and ceramics. These materials are inhomogeneous, in the sense that the material properties vary smoothly and continuously in one or more directions. FGMs combine the best properties of metals and ceramics. FGMs are characterized by the volume fraction of its constituent materials, which depends on the gradient index n. In the literature, $n = 0$, corresponds to a pure ceramic material, $n = \infty$, corresponds to a pure metal and any other value of n corresponds to a mixture of a ceramic and a metal. FGMs are strongly considered as a potential material candidate for a certain class of aerospace structures exposed to a high temperature environment.

5.1.1 Dynamic characteristics of FGMs

It is seen from the literature that the amount of work carried out on the vibration characteristics of FGMs is considerable [11, 14, 24, 26, 28, 46, 47, 54]. Vel and Batra [46] have accounted for the variation of material properties through the thickness according to a power-law distribution and studied the thermoelastic deformation of thick FGM plates. The locally effective material properties were obtained using the Mori-Tanaka homogenization scheme [27]. He *et al.,* [14] presented a finite element formulation based on the thin plate theory for the vibration control of FGM plates with integrated piezoelectric sensors and actuators under mechanical load. Liew *et al.,* [24] have analysed the active vibration control of plates subjected to a thermal gradient using the shear deformation theory. Ng *et al.,* [28] have investigated the parametric resonance of plates based on Hamilton's principle and the assumed mode technique. Yang and Shen [53] have analysed the dynamic response of thin FGM plates subjected to impulsive loads using a Galerkin procedure coupled with the modal superposition method. Yang and Shen [54] studied the transient response of FGM plates in a thermal environment based on the shear deformation theory with temperature dependent material properties. Their study concluded that temperature affects the dynamic response of FGM plates. Qian *et al.,* [33] studied the static deformation and the vibration of FGM plates based on the higher-order shear deformation theory using the meshless local Petrov-Galerkin method (MLPG). Matsunaga [26] presented analytical solutions for simply supported rectangular FGM plates based on the second-order shear deformation theory. Vel and Batra [47] proposed three-dimensional solutions for vibration of simply supported

rectangular plates. Reddy [36] presented a finite element solution for the dynamic analysis of a FGM plate and Ferreira *et al.,* [11] performed a dynamic analysis of FGM plates based on the higher order shear and normal deformable plate theory using the MLPG. Akbari *et al.,* [34] studied two-dimensional wave propagation in FGM solids using the MLPG. It is observed that, in general, increasing the gradient index decreases the fundamental frequency due to the increase in the metallic volume fraction.

5.1.2 Vibration of cracked plates

It is known that cracks or local defects affect the dynamic response of a structural member. This is because, the presence of a crack introduces local flexibility and anisotropy. Moreover, the crack will open and close depending on the vibration amplitude. The vibration of cracked plates was studied as early as 1969 by Lynn and Kumbasar [25], who used a Green's function approach. Later, in 1972, Stahl and Keer [43] studied the vibration of cracked rectangular plates using elasticity methods. The other numerical methods that are used to study the dynamic response and the instability of plates with cracks or local defects are: (1) the Finite Fourier series transform [41]; (2) the Rayleigh-Ritz Method [19]; (3) the harmonic balance method [50]; and (4) the FEM [23, 32]. FGM plates or in general plate structures, may develop flaws during manufacturing or after they have been subjected to cyclic loading. Hence it is important to understand the dynamic response of a FGM plate with an internal flaw. Recently, Huang *et al.,* [15] proposed solutions for the vibrations of side-cracked FGM thick plates based on Reddy's Third-order Shear Deformation Theory (TSDT) using the Ritz technique. Kitipornchai *et al.,* [20] studied the non-linear vibration of an edge cracked functionally graded Timoshenko beams using the Ritz method. Yang *et al.,* [52] studied the non-linear dynamic response of FGM plates with a through-width crack based on Reddy's TSDT using a Galerkin method. Very recently, the XFEM has been applied to study the vibration of cracked isotropic plates [1, 2, 45]. An enriched 4-noded mixed interpolated tensorial components (MITC4) [3] element was used to compute the fundamental frequencies. Their study focussed on centre and edge cracks with simply supported and clamped boundary conditions.

5.2 Functionally Graded Materials

Consider a rectangular FGM plate with co-ordinates x, y along the in-plane directions and z along the thickness direction as shown in Figure 5.1. The material on the top surface ($z = h/2$) of the plate is ceramic and is graded to metal at the bottom surface of the plate ($z = -h/2$) by a power-law distribution. The homogenized material properties are computed using the Mori-Tanaka Scheme [5, 27].

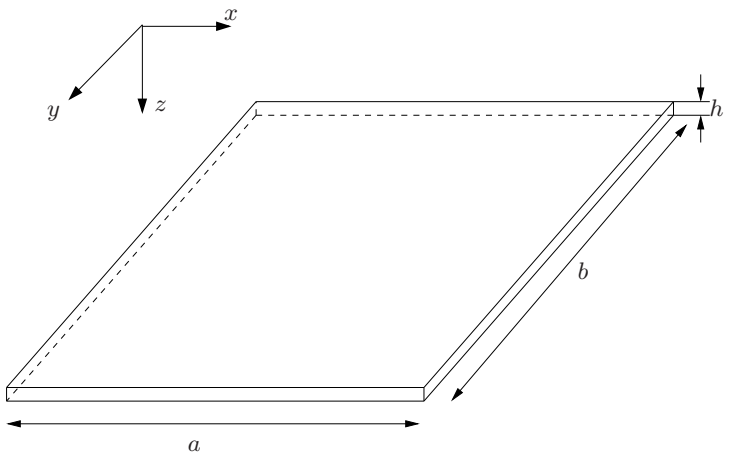

Figure 5.1: Co-ordinate system of a rectangular FGM plate, where a, b and h are the length, the width and the thickness of the plate, respectively.

Estimation of mechanical and thermal properties

Based on the Mori-Tanaka homogenization method, the effective bulk modulus K and the shear modulus G of the FGM are evaluated as [5, 9, 27, 33]:

$$\begin{aligned} \frac{K - K_m}{K_c - K_m} &= \frac{V_c}{1 + (1 - V_c)\frac{3(K_c - K_m)}{3K_m + 4G_m}} \\ \frac{G - G_m}{G_c - G_m} &= \frac{V_c}{1 + (1 - V_c)\frac{(G_c - G_m)}{G_m + f_1}}, \end{aligned} \tag{5.1}$$

where

$$f_1 = \frac{G_m(9K_m + 8G_m)}{6(K_m + 2G_m)}. \tag{5.2}$$

Here, V_i $(i = c, m)$ is the volume fraction of the phase material. The subscripts c and m refer to the ceramic and the metal phases, respectively. The volume fractions of the ceramic and the metal phases are related by $V_c + V_m = 1$, and V_c is expressed as:

$$V_c(z) = \left(\frac{2z + h}{2h}\right)^n, \quad n \geq 0 \tag{5.3}$$

where n in Equation (5.3) is the volume fraction exponent, also referred to as the gradient index in the literature. The variation of the volume fraction of the ceramic phase in the thickness direction is shown in Figure 5.2. It can be seen that with the increase in the gradient index n, the metallic volume fraction increases and by tailoring the gradient index, n, a suitable FGM can be designed for a particular application.

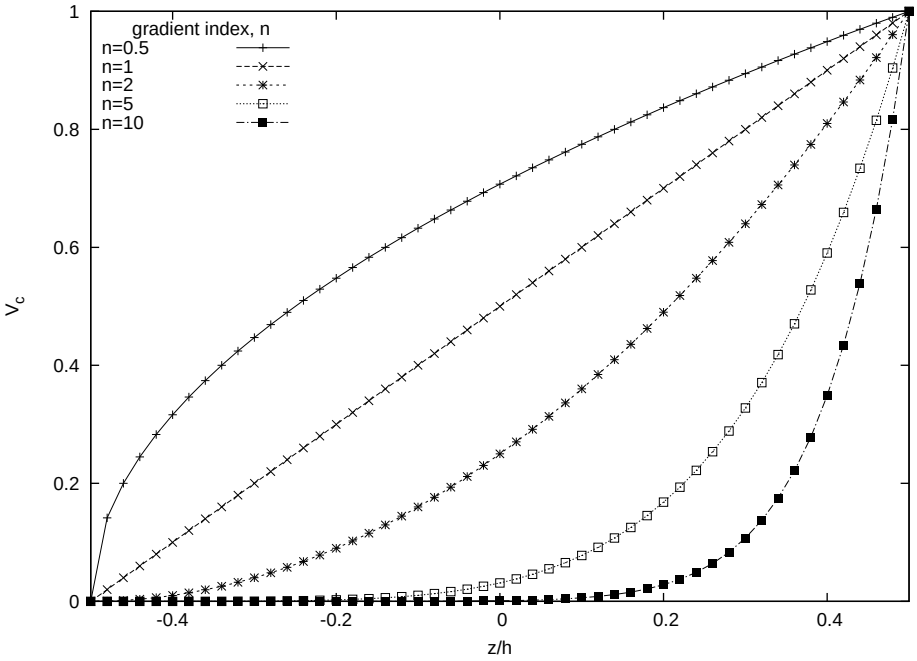

Figure 5.2: Through the thickness variation of the ceramic volume fraction. A higher value of gradient index n corresponds to a metallic plate.

The effective Young's modulus, E and Poisson's ratio, ν are computed from the following expressions:

$$\begin{aligned} E &= \frac{9KG}{3K+G} \\ \nu &= \frac{3K-2G}{2(3K+G)}. \end{aligned} \tag{5.4}$$

The effective mass density, ρ is given by the rule of mixtures as [47]:

$$\rho = \rho_c V_c + \rho_m V_m. \tag{5.5}$$

The effective heat conductivity coefficient κ and the coefficient of thermal expansion α is given by [13, 38]:

$$\begin{aligned} \frac{\kappa-\kappa_m}{\kappa_c-\kappa_m} &= \frac{V_c}{1+(1-V_c)\frac{(\kappa_c-\kappa_m)}{3\kappa_m}} \\ \frac{\alpha-\alpha_m}{\alpha_c-\alpha_m} &= \frac{\left(\frac{1}{K}-\frac{1}{K_m}\right)}{\left(\frac{1}{K_c}-\frac{1}{K_m}\right)} \end{aligned} \tag{5.6}$$

The material properties P[a] that are temperature dependent can be written as [37]:

$$P = P_o(P_{-1}T^{-1} + 1 + P_1T + P_2T^2 + P_3T^3) \tag{5.7}$$

where $P_o, P_{-1}, P_1, P_2, P_3$ are the coefficients of the temperature T and are unique to each constituent material phase. The temperature variation is assumed to occur in the thickness direction only and the temperature field is considered to be constant in the xy-plane. In such a case, the temperature distribution along the thickness can be obtained by solving the following steady state heat transfer equation:

$$-\frac{d}{dz}\left[\kappa(z)\frac{dT}{dz}\right] = 0, \quad T = T_c \text{ at } z = h/2; \;\; T = T_m \text{ at } z = -h/2 \tag{5.8}$$

The solution of Equation (5.8) is obtained by means of a polynomial series [51] as:

$$T(z) = T_m + (T_c - T_m)\eta(z,h) \tag{5.9}$$

where,

$$\begin{aligned}\eta(z,h) = \frac{1}{C}\Bigg[&\left(\frac{2z+h}{2h}\right) - \frac{\kappa_{cm}}{(n+1)\kappa_m}\left(\frac{2z+h}{2h}\right)^{n+1} + \\ &\frac{\kappa_{cm}^2}{(2n+1)\kappa_m^2}\left(\frac{2z+h}{2h}\right)^{2n+1} - \frac{\kappa_{cm}^3}{(3n+1)\kappa_m^3}\left(\frac{2z+h}{2h}\right)^{3n+1} \\ &+ \frac{\kappa_{cm}^4}{(4n+1)\kappa_m^4}\left(\frac{2z+h}{2h}\right)^{4n+1} - \frac{\kappa_{cm}^5}{(5n+1)\kappa_m^5}\left(\frac{2z+h}{2h}\right)^{5n+1}\Bigg];\end{aligned} \tag{5.10}$$

$$\begin{aligned}C = 1 - \frac{\kappa_{cm}}{(n+1)\kappa_m} + \frac{\kappa_{cm}^2}{(2n+1)\kappa_m^2} - \frac{\kappa_{cm}^3}{(3n+1)\kappa_m^3} \\ + \frac{\kappa_{cm}^4}{(4n+1)\kappa_m^4} - \frac{\kappa_{cm}^5}{(5n+1)\kappa_m^5}\end{aligned} \tag{5.11}$$

where $\kappa_{cm} = \kappa_c - \kappa_m$ and $T_c,\ T_m$ denote the temperature of the ceramic and the metallic phases, respectively.

5.3 Reissner-Mindlin Formulation

Using the Mindlin formulation, the displacements u, v, w at a point (x, y, z) in the plate (see Figure 5.1) from the medium surface are expressed as functions of the mid-plane dis-

[a]The material property P could be the Young's modulus, E, Poisson's ratio ν, the Bulk modulus K, the shear modulus G, the mass density ρ, the coefficient of thermal expansion α or the coefficient of heat conductivity κ.

placements u_o, v_o, w_o and independent rotations β_x, β_y of the normal in yz and xz planes, respectively, as

$$\begin{aligned} u(x,y,z,t) &= u_o(x,y,t) + z\beta_x(x,y,t) \\ v(x,y,z,t) &= v_o(x,y,t) + z\beta_y(x,y,t) \\ w(x,y,z,t) &= w_o(x,y,t), \end{aligned} \tag{5.12}$$

where t is the time. The strains in terms of the mid-plane deformation can be written as:

$$\boldsymbol{\varepsilon} = \left\{ \begin{array}{c} \boldsymbol{\varepsilon}_p \\ 0 \end{array} \right\} + \left\{ \begin{array}{c} z\boldsymbol{\varepsilon}_b \\ \boldsymbol{\varepsilon}_s \end{array} \right\}. \tag{5.13}$$

The mid-plane strain $\boldsymbol{\varepsilon}_p$, the bending strain $\boldsymbol{\varepsilon}_b$, the shear strain $\boldsymbol{\varepsilon}_s$ in Equation (5.13) are written as:

$$\boldsymbol{\varepsilon}_p = \left\{ \begin{array}{c} u_{o,x} \\ v_{o,y} \\ u_{o,y} + v_{o,x} \end{array} \right\}, \qquad \boldsymbol{\varepsilon}_b = \left\{ \begin{array}{c} \beta_{x,x} \\ \beta_{y,y} \\ \beta_{x,y} + \beta_{y,x} \end{array} \right\},$$

$$\boldsymbol{\varepsilon}_s = \left\{ \begin{array}{c} \beta_x + w_{o,x} \\ \beta_y + w_{o,y} \end{array} \right\}, \tag{5.14}$$

where the subscript 'comma' represents the partial derivative with respect to the spatial coordinate succeeding it. The membrane stress resultants, $\mathbf{N}^{st}$ and the bending stress resultants, $\mathbf{M}^{st}$ can be related to the membrane strain, $\boldsymbol{\varepsilon}_p$ and the bending strain, $\boldsymbol{\varepsilon}_b$ through the following constitutive relations:

$$\begin{aligned} \mathbf{N}^{st} &= \left\{ \begin{array}{c} N_{xx} \\ N_{yy} \\ N_{xy} \end{array} \right\} = \mathbf{A_e}\boldsymbol{\varepsilon}_p + \mathbf{B}_{be}\boldsymbol{\varepsilon}_b \\ \mathbf{M}^{st} &= \left\{ \begin{array}{c} M_{xx} \\ M_{yy} \\ M_{xy} \end{array} \right\} = \mathbf{B}_{be}\boldsymbol{\varepsilon}_p + \mathbf{D_b}\boldsymbol{\varepsilon}_b, \end{aligned} \tag{5.15}$$

where the matrices $\mathbf{A}_e = A_{ij}, \mathbf{B}_{be} = B_{ij}$ and $\mathbf{D_b} = D_{ij}; (i,j = 1,2,6)$ are the extensional,

the bending-extensional coupling and the bending stiffness coefficients. These stiffness coefficients are defined as:

$$\{A_{ij},\ B_{ij},\ D_{ij}\} = \int_{-h/2}^{h/2} \overline{Q}_{ij}\left\{1,\ z,\ z^2\right\}\ \mathrm{d}z. \tag{5.16}$$

Similarly, the transverse shear force $\overline{\overline{Q}} = \{\overline{\overline{Q}}_{xz}, \overline{\overline{Q}}_{yz}\}$ is related to the transverse shear strain $\boldsymbol{\varepsilon}_s$, through the following equation:

$$\overline{\overline{Q}}_{ij} = \tilde{Q}_{ij}\boldsymbol{\varepsilon}_s \tag{5.17}$$

where $\tilde{\mathbf{Q}} = \tilde{Q}_{ij} = \int_{-h/2}^{h/2} \overline{Q}_{ij}\upsilon_i\upsilon_j\ dz;\ (i,j=4,5)$ is the transverse shear stiffness coefficient, υ_i, υ_j are the transverse shear correction factors for the non-uniform shear strain distribution through the plate thickness. The stiffness coefficients $\overline{Q}_{ij}$ are defined as:

$$\begin{aligned} \overline{Q}_{11} = \overline{Q}_{22} = \frac{E}{1-\nu^2}; \qquad \overline{Q}_{12} = \frac{\nu E}{1-\nu^2}; \qquad \overline{Q}_{16} = \overline{Q}_{26} = 0; \\ \overline{Q}_{44} = \overline{Q}_{55} = \overline{Q}_{66} = \frac{E}{2(1+\nu)}, \end{aligned} \tag{5.18}$$

where the modulus of elasticity, E and Poisson's ratio, ν are given by Equation (5.4). The strain energy function U is given by:

$$U(\boldsymbol{\delta}) = \frac{1}{2}\int_{\Omega}\left\{\boldsymbol{\varepsilon}_p^{\mathrm{T}}\mathbf{A}_e\boldsymbol{\varepsilon}_p + \boldsymbol{\varepsilon}_p^{\mathrm{T}}\mathbf{B}_{be}\boldsymbol{\varepsilon}_b + \boldsymbol{\varepsilon}_b^{\mathrm{T}}\mathbf{B}_{be}\boldsymbol{\varepsilon}_p + \boldsymbol{\varepsilon}_b^{\mathrm{T}}\mathbf{D}_{\mathbf{b}}\boldsymbol{\varepsilon}_b + \boldsymbol{\varepsilon}_s^{\mathrm{T}}\tilde{\mathbf{Q}}\boldsymbol{\varepsilon}_s\right\}\ \mathrm{d}\Omega \tag{5.19}$$

where $\boldsymbol{\delta} = \{u_o, v_o, w_o, \beta_x, \beta_y\}$ is the vector of the degrees of freedom associated to the displacement field in a finite element discretization. Following the procedure given in [35, 55], the strain energy function U given by the Equation (5.19) can be rewritten as:

$$U(\boldsymbol{\delta}) = \frac{1}{2}\boldsymbol{\delta}^{\mathrm{T}}\mathbf{K}\boldsymbol{\delta}, \tag{5.20}$$

where $\mathbf{K}$ is the linear stiffness matrix. The kinetic energy of the plate is given by:

$$T(\boldsymbol{\delta}) = \frac{1}{2}\int_{\Omega}\left\{I_o(\dot{u}_o^2 + \dot{v}_o^2 + \dot{w}_o^2) + I_1(\dot{\beta}_x^2 + \dot{\beta}_y^2)\right\}\ \mathrm{d}\Omega, \tag{5.21}$$

where $I_o = \int_{-h/2}^{h/2}\rho(z)\ dz,\ I_1 = \int_{-h/2}^{h/2} z^2\rho(z)\ dz$ and $\rho(z)$ is the mass density that varies through the thickness of the plate, given by Equation (5.5). The Lagrangian equations of motion is given by:

$$\frac{d}{dt}\left[\frac{\partial(T-U)}{\partial\dot{\boldsymbol{\delta}}}\right] - \left[\frac{\partial(T-U)}{\partial\boldsymbol{\delta}}\right] = 0 \tag{5.22}$$

.

Substituting Equations (5.20) - (5.21) in the Lagrangian equations of motion, Equation (5.22), the following governing equation is obtained:

$$\mathbf{M}\ddot{\boldsymbol{\delta}} + \mathbf{K}\boldsymbol{\delta} = \mathbf{0}, \tag{5.23}$$

where $\mathbf{M}$ is the consistent mass matrix. After, substituting the characteristic of the time function [12, 55] $\ddot{\boldsymbol{\delta}} = -\omega^2\boldsymbol{\delta}$, the following generalized eigenvalue problem is obtained:

$$\left[\mathbf{K} - \omega^2\mathbf{M}\right]\boldsymbol{\delta} = \mathbf{0}. \tag{5.24}$$

where ω is the natural frequency. In solving for the eigenvalues, the QR algorithm, based on the QR decomposition is used [49].

5.4 Field consistent quadrilateral element

The plate element employed here is a $\mathcal{C}^0$ continuous shear flexible field consistent element with five degrees of freedom $(u_o, v_o, w_o, \beta_x, \beta_y)$ at four nodes in a 4-noded quadrilateral (QUAD-4) element. The displacement field within the element is approximated by:

$$\{u_o^e, v_o^e, w_o^e, \beta_x^e, \beta_y^e\} = \sum_{J=1}^{4} N_J\{u_{oJ}, v_{oJ}, w_{oJ}, \beta_{xJ}, \beta_{yJ}\}, \tag{5.25}$$

where $u_{oJ}, v_{oJ}, w_{oJ}, \beta_{xJ}, \beta_{yJ}$ are the nodal variables and N_J are the shape functions for the bi-linear QUAD-4 element, given by:

$$\begin{aligned} N_1(\xi,\eta) &= \frac{1}{4}(1-\xi)(1-\eta), & N_2(\xi,\eta) &= \frac{1}{4}(1+\xi)(1-\eta) \\ N_3(\xi,\eta) &= \frac{1}{4}(1+\xi)(1+\eta), & N_4(\xi,\eta) &= \frac{1}{4}(1-\xi)(1+\eta). \end{aligned} \tag{5.26}$$

where $-1 \leq \xi \leq 1$ and $-1 \leq \eta \leq 1$. If the interpolation functions, given by Equation (5.26) for a QUAD-4 are used directly to interpolate the five variables $(u_o, v_o, w_o, \beta_x, \beta_y)$ in deriving the shear strains and the membrane strains, the element will lock and show oscillations in the shear and the membrane stresses. The oscillations are due to the fact that the derivative functions of the out-of plate displacement, w_o do not match that of the rotations (β_x, β_y) in the shear strain definition, given by Equation (5.14). To alleviate the locking phenomenon, the terms corresponding to the derivative of the out-of plate displacement, w_o must be consistent with the rotation terms, β_x and β_y. The different techniques by which the locking phenomenon can be suppressed are:

- Retain the original interpolations given by Equation (5.26) and subsequently use an

optimal integration rule for evaluating the bending and the shear terms;

- Mixed interpolation technique [3];
- Use field redistributed substitute shape functions [12, 42];
- Discrete shear gap method [6];
- Stabilized conforming nodal integration [48], i.e., strain smoothing, SFEM [29, 30].
- Enhanced assumed strain method [39] ;
- Use p-adaptivity, for example Moving Least Square approximations [18] or Non-Uniform Rational B-Splines [17].

In this study, field redistributed shape functions are used. The field consistency requires that the transverse shear strains and the membrane strains must be interpolated in a consistent manner. Thus, the β_x and β_y terms in the expressions for the shear strain $\boldsymbol{\varepsilon}_s$ have to be consistent with the derivative of the field functions, $w_{o,x}$ and $w_{o,y}$. If the element has edges which are aligned with the coordinate system (x, y), the section rotations β_x, β_y in the shear strain are approximated by [42]:

$$\begin{aligned} \beta_x^e &= \sum_{J=1}^{4} \tilde{N}_{1J} \beta_{xJ} \\ \beta_y^e &= \sum_{J=1}^{4} \tilde{N}_{2J} \beta_{yJ} \end{aligned} \tag{5.27}$$

where β_{xJ} and β_{yJ} are the nodal variables, $\tilde{N}_{1J}$ and $\tilde{N}_{2J}$ are the substitute shape functions, given by [42]:

$$\begin{aligned} \tilde{N}_1(\eta) &= \frac{1}{4} \left[\begin{array}{cccc} 1-\eta & 1-\eta & 1+\eta & 1+\eta \end{array} \right] \\ \tilde{N}_2(\xi) &= \frac{1}{4} \left[\begin{array}{cccc} 1-\xi & 1+\xi & 1+\xi & 1-\xi \end{array} \right]. \end{aligned} \tag{5.28}$$

It can be seen that the field redistributed shape functions, given by Equation (5.28) are consistent with the derivative of the shape functions, given by Equation (5.26) used to approximate the out-of plate displacement, w_o. Note that, no special integration rule is required for evaluating the shear terms. A numerical integration based on the 2×2 Gaussian rule is used to evaluate all the terms.

Enriched Q4 element

Consider a mesh of field consistent Q4 elements and an independent crack geometry as shown in Figure 2.5. The following enriched approximation proposed by Dolbow et al., [10] for the plate displacements are used:

$$\begin{aligned}(u^h, v^h, w^h)(\mathbf{x}) = \sum_{I\in\mathcal{N}^{\text{fem}}} N_I(\mathbf{x})(u_I^s, v_I^s, w_I^s) + \sum_{J\in\mathcal{N}^{\text{c}}} N_J(\mathbf{x})H(\mathbf{x})(b_J^u, b_J^v, b_J^w) + \\ \sum_{K\in\mathcal{N}^{\text{f}}} N_K(\mathbf{x})\left(\sum_{l=1}^{4}(c_{Kl}^u, c_{Kl}^v, c_{Kl}^w)G_l(r,\theta)\right)\end{aligned} \tag{5.29}$$

The section rotations are approximated by:

$$\begin{aligned}\beta_x^h(\mathbf{x}) &= \sum_{I\in\mathcal{N}^{\text{fem}}} \tilde{N}_{1I}(\mathbf{x})\beta_{x_I}^s + \sum_{J\in\mathcal{N}^{\text{c}}} \tilde{N}_{1J}(\mathbf{x})H(\mathbf{x})b_J^{\beta_x} + \sum_{K\in\mathcal{N}^{\text{f}}} \tilde{N}_{1K}(\mathbf{x})\left(\sum_{l=1}^{4} c_{Kl}^{\beta_x}F_l(r,\theta)\right), \\ \beta_y^h(\mathbf{x}) &= \sum_{I\in\mathcal{N}^{\text{fem}}} \tilde{N}_{2I}(\mathbf{x})\beta_{y_I}^s + \sum_{J\in\mathcal{N}^{\text{c}}} \tilde{N}_{2J}(\mathbf{x})H(\mathbf{x})b_J^{\beta_y} + \sum_{K\in\mathcal{N}^{\text{f}}} \tilde{N}_{2K}(\mathbf{x})\left(\sum_{l=1}^{4} c_{Kl}^{\beta_y}F_l(r,\theta)\right).\end{aligned} \tag{5.30}$$

where $\mathcal{N}^{\text{fem}}$ is a set of all the nodes in the finite element mesh, $\mathcal{N}^{\text{c}}$ is a set of nodes that are enriched with the Heaviside function and $\mathcal{N}^{\text{f}}$ is a set of nodes that are enriched with near-tip asymptotic fields. In Equations (5.29) and (5.30), $(u_I^s, v_I^s, w_I^s, \beta_{x_I}^s, \beta_{y_I}^s)$ are the nodal unknown vectors associated with the continuous part of the finite element solution, b_J is the nodal enriched degree of freedom vector associated with the Heaviside (discontinuous) function, and c_{Kl} is the nodal enriched degree of freedom vector associated with the elastic asymptotic near-tip functions. The asymptotic functions, G_l and F_l in Equations (5.29) and (5.30) are given by ([10]):

$$\begin{aligned}G_l(r,\theta) &\equiv \left\{\sqrt{r}\sin\left(\frac{\theta}{2}\right), \sqrt[3]{r}\sin\left(\frac{\theta}{2}\right), \sqrt[3]{r}\cos\left(\frac{\theta}{2}\right), \sqrt[3]{r}\sin\left(\frac{3\theta}{2}\right), \sqrt[3]{r}\cos\left(\frac{3\theta}{2}\right)\right\}, \\ F_l(r,\theta) &\equiv \sqrt{r}\left\{\sin\left(\frac{\theta}{2}\right), \cos\left(\frac{\theta}{2}\right), \sin\left(\frac{\theta}{2}\right)\sin(\theta), \cos\left(\frac{\theta}{2}\right)\sin(\theta)\right\}.\end{aligned} \tag{5.31}$$

Here (r,θ) are the polar coordinates in the local coordinate system with the origin at the crack tip.

Discretized equations for the enriched Q4 plate element

Now, substituting the displacement field approximated by Equations (5.29) - (5.30) in Equation (5.19) and Equation (5.21), the following modified generalized eigenvalue problem is obtained:

$$\left(\tilde{\mathbf{K}} - \omega^2 \tilde{\mathbf{M}}\right) \tilde{\boldsymbol{\delta}} = \mathbf{0}, \tag{5.32}$$

where $\tilde{\mathbf{K}}$ is the enriched stiffness matrix, $\tilde{\mathbf{M}}$ is the enriched mass matrix and $\tilde{\boldsymbol{\delta}}$ is the vector of nodal unknown vector consisting of the continuous part of the finite element solution, $(u_I^s, v_I^s, w_I^s, \beta_{x_I}^s, \beta_{y_I}^s)$ and the enriched degrees of freedom, b_J and c_{Kl}. The nodes, whose support is intersected by the discontinuous surface are selected based on the procedure outlined in Chapter 2, Section 2.4. The numerical integration technique presented in Chapter 3 is used to numerically integrate over the elements that are intersected by the discontinuity surface and the following convention is used:

- *Split elements*: SmXFEM, with one subcell above and below the crack face.
- *Tip element*: XFEM with SCCM.
- *Tip-blending elements*: standard XFEM.
- *Split-blending elements*: standard XFEM.
- *Standard elements*: SFEM with four subcells.

For the elements that are not enriched, a standard 2×2 Gaussian quadrature rule is used.

5.5 Numerical Examples

Based on the above formulation, a MATLAB code is developed and a systematic parametric study is performed to study the influence of the following parameters on the fundamental frequency of the cracked FGM plate:

- Plate thickness (a/h) - three different ratios (10, 20, 100) are chosen;
- Boundary conditions - simply supported and clamped condition;
- Gradient index, n - five different gradient indices (0, 1, 2, 5, 10) are chosen;
- Crack geometry - crack length (d), crack location (c_y), crack orientation (θ) and number of cracks.

The temperature of the ceramic and the metallic phase is assumed to be constant and for this study, the temperature is taken as $T_c = T_m = 300$K. The ambient temperature T_{amb} is also assumed to be at 300K. The material properties are evaluated at this temperature using the expression given in Equation (5.7). In all the cases, the non dimensionalized free flexural frequencies, unless specified otherwise is presented as:

$$\overline{\Omega} = \omega \left(\frac{b^2}{h}\right) \sqrt{\frac{\rho_c}{E_c}} \tag{5.33}$$

where E_c, ν_c are the Young's modulus and Poisson's ratio of the ceramic material, and ρ_c is the mass density of the ceramic phase. In order to be consistent with the existing literature, properties of the ceramic phase are used for normalization. Based on a progressive mesh refinement, a 33×33 structured mesh is found to be adequate to model the full plate for the present analysis (see Figure 5.3). The convergence of the mode 1 and the mode 2 frequencies for a square isotropic plate with and without a crack is shown in Figure 5.4. The material properties used for the FGM components are listed in Table 5.1.

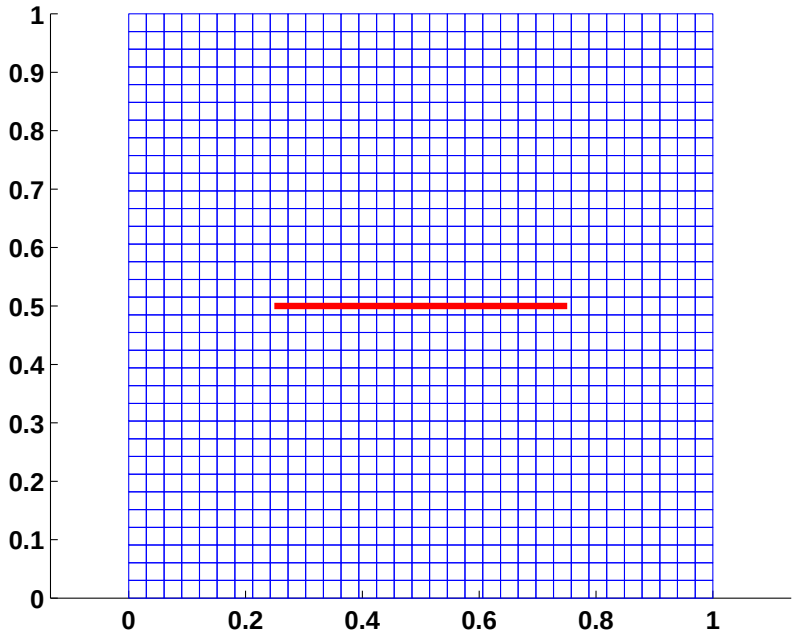

Figure 5.3: A typical finite element mesh used for this study. 'Solid line' denotes the crack.

Before proceeding with the detailed study on the effect of different parameters on the natural frequency, the formulation developed herein is validated against the available results pertaining to the linear frequencies of cracked isotropic and FGM plates with different boundary conditions. The computed frequencies for the cracked isotropic simply sup-

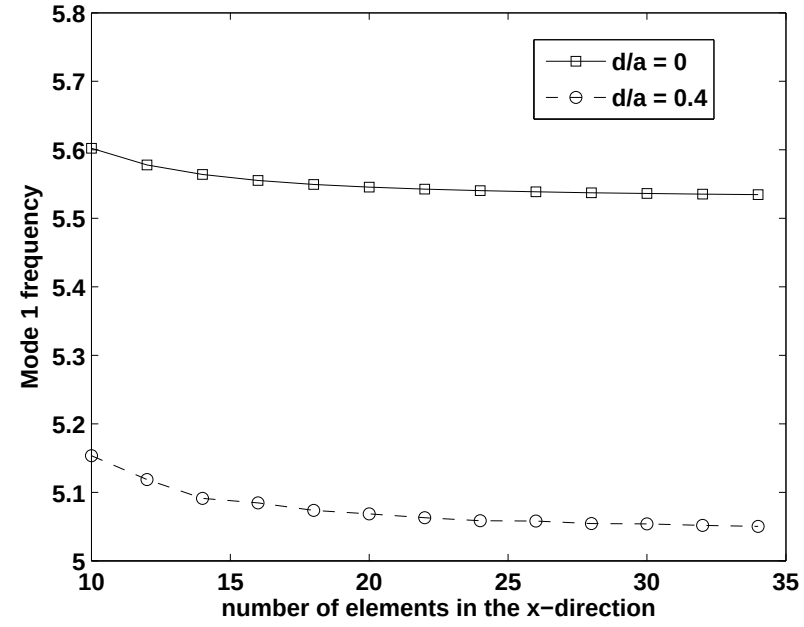

(a) mode 1

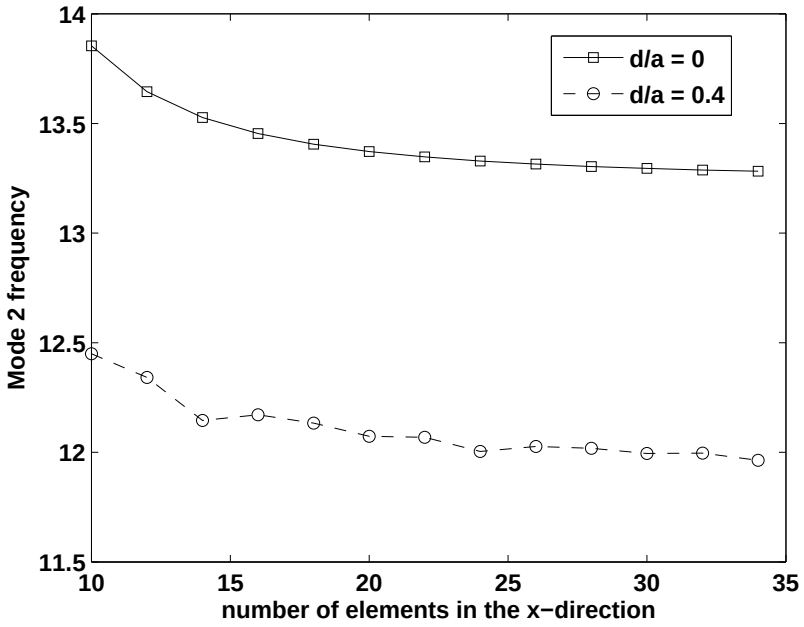

(b) mode 2

Figure 5.4: Convergence of the mode 1 and the mode 2 frequency with increasing mesh density for a ceramic plate with and without a crack. The crack is assumed to be at the center of the plate and horizontally oriented with a simply supported boundary condition. The other parameters of the plate are: $n = 0$, $a/b = 1$, $a/h = 10$.

ported rectangular plate is given in Table 5.3. Tables 5.4 and 5.5 gives a comparison of the computed frequencies for a simply supported square plate with a side crack and a cantilevered plate with a side crack, respectively. It can be seen that the numerical results from the present formulation are found to be in good agreement with existing solutions.
The FGM plate considered here consists of silicon nitride (Si_3N_4) and stainless steel (SUS304). The material properties are considered to be temperature dependent and the temperature coefficients corresponding to Si_3N_4/SUS304 are listed in Table 5.2 [37, 44]. The mass density (ρ) and thermal conductivity (K) are: ρ_c=2370 kg/m^3, K_c=9.19 W/mK for Si_3N_4 and ρ_m = 8166 kg/m^3, K_m = 12.04 W/mK for SUS304. Poisson's ratio ν is assumed to be constant and taken as 0.28 for the current study [31, 44]. Here, the modified shear correction factor obtained based on energy equivalence principle as outlined in [40] is used. The boundary conditions for the simply supported and the clamped condition are (see Figure 5.5):
Simply supported boundary conditions:

$$\begin{aligned} u_o = w_o = \theta_y = 0 \qquad & \text{on } x = 0, a \\ v_o = w_o = \theta_x = 0 \qquad & \text{on } y = 0, b \end{aligned} \tag{5.34}$$

Clamped boundary conditions:

$$\begin{aligned} u_o = w_o = \theta_y = v_o = \theta_x = 0 \qquad & \text{on } x = 0, a \\ u_o = w_o = \theta_y = v_o = \theta_x = 0 \qquad & \text{on } y = 0, b \end{aligned} \tag{5.35}$$

Table 5.1: Material properties of the FGM components. †Ref [15], *Ref [37, 44]

Material	Properties		
	E(GPa)	ν	ρ (kg/m^3)
Aluminum (Al)†	70.0	0.30	2702
Alumina (Al_2O_3)†	380.0	0.30	3800
Zirconia (ZrO_2)†	200.0	0.30	5700
Steel (SUS304)*	201.04	0.28	8166
Silicon Nitride (Si_3N_4)*	348.43	0.28	2370

Table 5.2: Temperature dependent coefficients for material SI_3N_4/SUS304, Ref [37, 44].

Material	Property	P_o	P_{-1}	P_1	P_2	P_3
SI_3N_4	E(Pa)	348.43e^9	0.0	-3.070e^{-4}	2.160e^{-7}	-8.946e^{-11}
	α (1/K)	5.8723e^{-6}	0.0	9.095e^{-4}	0.0	0.0
SUS304	E(Pa)	201.04e^9	0.0	3.079e^{-4}	-6.534e^{-7}	0.0
	α (1/K)	12.330e^{-6}	0.0	8.086e^{-4}	0.0	0.0

Table 5.3: Comparison of frequency parameters, $\omega(b^2/h)\sqrt{\rho_c/E_c}$ for a simply supported homogeneous rectangular thin plate with a horizontal crack $(a/b = 2, b/h = 100, c_y/b = 0.5, d/a = 0.5, \theta = 0)$.

mode	Ref [43]	Ref [16]	Ref [15]	Present
1	3.050	3.053	3.047	3.055
2	5.507	5.506	5.503	5.508
3	5.570	5.570	5.557	5.665
4	9.336	9.336	9.329	9.382
5	12.760	12.780	12.760	12.861

Table 5.4: Non-dimensionalized natural frequency for a simply supported square Al/Al_2O_3 plate with a side crack $(a/b = 1, a/h = 10)$. Crack length $d/a = 0.5$.

gradient	Mode 1		Mode 2		Mode 3	
index, n	Ref [15]	Present	Ref [15]	Present	Ref [15]	Present
0	5.379	5.387	11.450	11.419	13.320	13.359
0.2	5.001	5.028	10.680	10.659	12.410	12.437
1	4.122	4.122	8.856	8.526	10.250	10.285
5	3.511	3.626	7.379	7.415	8.621	8.566
10	3.388	3.409	7.062	7.059	8.289	8.221

Table 5.5: Fundamental frequency, $\omega b^2/h\sqrt{\rho_c/E_c}$ for a cantilevered square Al/ZrO_2 FGM plates with a horizontal size crack $(b/h = 10, c_y/b = 0.5, d/a = 0.5)$.

a/b	Mode		gradient index, n				
			0	0.2	1	5	10
1	1	Ref [15]	1.0380	1.0080	0.9549	0.9743	0.9722
		Present	1.0380	1.0075	0.9546	0.9748	0.9722
	2	Ref [15]	1.7330	1.6840	1.5970	1.6210	1.6170
		Present	1.7329	1.6834	1.5964	1.6242	1.6194
	3	Ref [15]	4.8100	4.6790	4.4410	4.4760	4.4620
		Present	4.8231	4.6890	4.4410	4.4955	4.4845

5.5.1 Plate with a center crack

Consider a plate of uniform thickness, h and with length and width as a and b, respectively. Figure 5.5 shows a plate with all the edges simply supported and with a center crack of length d, located at a distance of c_y from the $x-$axis.

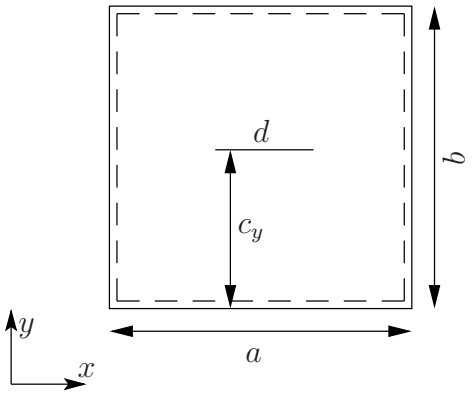

Figure 5.5: Simply supported plate with a center crack. The dotted line denotes the support.

Effect of the crack length, the crack orientation and the gradient index

The influence of the crack length d/a, the crack orientation, θ and the gradient index, n on the fundamental frequency for a simply supported square FGM plate with thickness a/h =10 is shown in Tables 5.6 and 5.7. It is observed that as the crack length increases, the frequency decreases. This is due to the fact that increasing the crack length increases the local flexibility and thus decreases the frequency. Also, with an increase in the gradient index n, the frequency decreases. This is because of the stiffness degradation due to the

increase in the metallic volume fraction. It can be seen that the combined effect of increasing the crack length and the gradient index is to lower the fundamental frequency. Further, it is observed that the frequency is lowest for a crack orientation, $\theta = 45^o$. The frequency values tend to be symmetric with respect to a crack orientation, $\theta = 45^o$. This is also shown in Figure 5.6 for the gradient index $n = 5$ and the crack length $d/a = 0.8$.

Table 5.6: Fundamental frequency, $\omega(b^2/h)\sqrt{\rho_c/E_c}$ for a simply supported Si_3N_4/SUS304 FGM square plate. †denotes change in trend.

gradient index, n	Crack orientation, θ	Crack length, d/a. 0	0.4	0.6	0.8
	0	5.5346	5.0502	4.7526	4.5636
	10	5.5346	5.0453	4.7386	4.5337
	20	5.5346	5.0379	4.7043	4.4509
	30	5.5346	5.0278	4.6640	4.3528
	40	5.5346	5.0207	4.6370	4.2849
0	**45**†	**5.5346**	**5.0173**	**4.6342**	**4.2754**
	50	5.5346	5.0204	4.6370	4.2849
	60	5.5346	5.0278	4.6640	4.3528
	70	5.5346	5.0380	4.7043	4.4509
	80	5.5346	5.0453	4.7384	4.5337
	90	5.5346	5.0503	4.7527	4.5636
	0	3.3376	3.0452	2.8657	2.7518
	10	3.3376	3.0422	2.8571	2.7337
	20	3.3376	3.0376	2.8362	2.6833
	30	3.3376	3.0315	2.8117	2.6237
	40	3.3376	3.0271	2.7953	2.5825
1	**45**†	**3.3376**	**3.0252**	**2.7936**	**2.5767**
	50	3.3376	3.0270	2.7953	2.5824
	60	3.3376	3.0315	2.8117	2.6237
	70	3.3376	3.0377	2.8363	2.6833
	80	3.3376	3.0422	2.8571	2.7337
	90	3.3376	3.0452	2.8657	2.7518

Effect of crack location

Next, the influence of the crack location on the natural frequency of a square plate with thickness, $a/h = 10$ and the crack length, $d/a = 0.2$ is studied. In this case, the crack is assumed to be horizontal, i.e., $\theta = 0$. The results are presented in Figure 5.7. It is observed

Table 5.7: Fundamental frequency, $\omega b^2/h\sqrt{\rho_c/E_c}$ for a simply supported Si_3N_4/SUS304 FGM square plate. †denotes change in trend.

gradient	Crack	Crack length, d/a.			
index, n	orientation, θ	0	0.4	0.6	0.8
	0	3.0016	2.7383	2.5769	2.4747
	10	3.0016	2.7356	2.5692	2.4583
	20	3.0016	2.7315	2.5504	2.4130
	30	3.0016	2.7259	2.5283	2.3594
	40	3.0016	2.7220	2.5136	2.3223
2	**45**†	**3.0016**	**2.7202**	**2.5120**	**2.3170**
	50	3.0016	2.7219	2.5135	2.3222
	60	3.0016	2.7259	2.5283	2.3594
	70	3.0016	2.7315	2.5504	2.4130
	80	3.0016	2.7356	2.5692	2.4583
	90	3.0016	2.7383	2.5770	2.4747
	0	2.7221	2.4833	2.3371	2.2445
	10	2.7221	2.4809	2.3302	2.2297
	20	2.7221	2.4772	2.3131	2.1887
	30	2.7221	2.4722	2.2932	2.1402
	40	2.7221	2.4686	2.2798	2.1067
5	**45**†	**2.7221**	**2.4670**	**2.2785**	**2.1019**
	50	2.7221	2.4685	2.2798	2.1066
	60	2.7221	2.4722	2.2932	2.1402
	70	2.7221	2.4772	2.3132	2.1887
	80	2.7221	2.4809	2.3301	2.2297
	90	2.7221	2.4833	2.3371	2.2445

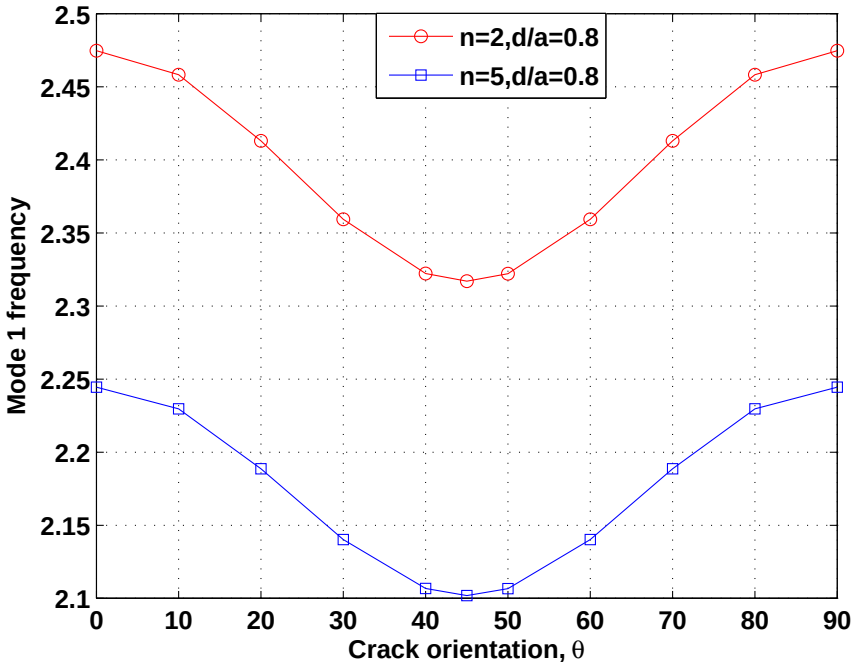

Figure 5.6: Variation of the fundamental frequency with orientation of the crack for a simply supported square FGM plate, $a/h = 10$.

that the natural frequency of the plate monotonically decreases as the crack moves along the edges and towards the center of these edges. The natural frequency of the plate is maximum when the damage is situated at the corner. As the crack moves along the center lines of the plate from the edges and towards the center of the plate, the natural frequency increases up to a certain distance and then decreases. When the crack is situated at the center of the plate, the frequency is minimum.

Effect of the aspect ratio, the thickness and the boundary conditions

The influence of the plate aspect ratio b/a, the plate thickness a/h and the boundary condition on a cracked FGM plate with a horizontal center crack is shown in Table 5.8. Two types of boundary conditions are studied: Simply Supported (SS) and Clamped Condition (CC). For a given crack length and for a given crack location, decreasing the plate thickness and increasing the plate aspect ratio, increases the frequency. The increase in the stiffness is the reason for the increase in the frequency when the boundary condition is changed from SS to CC for a fixed aspect ratio and the plate thickness.

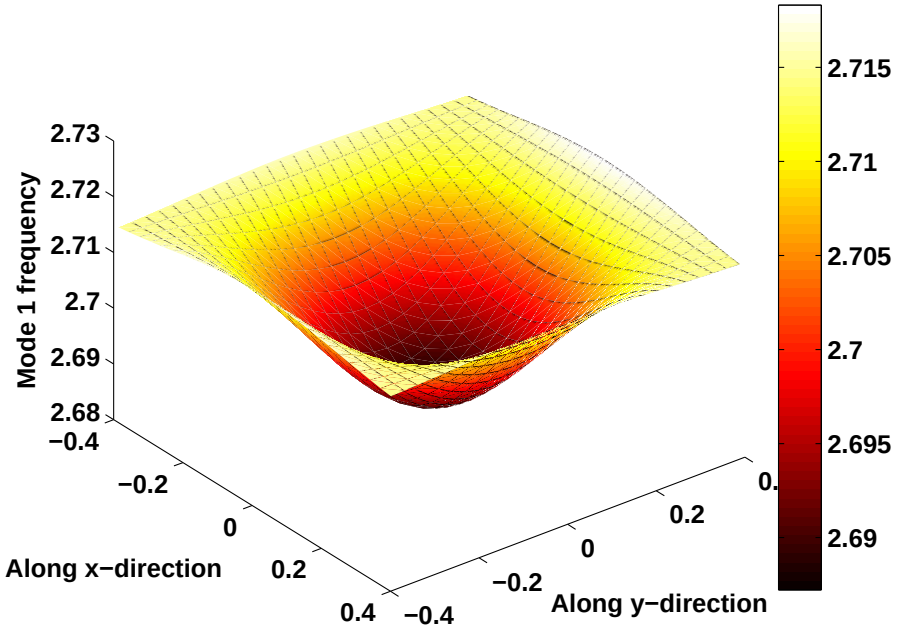

(a)

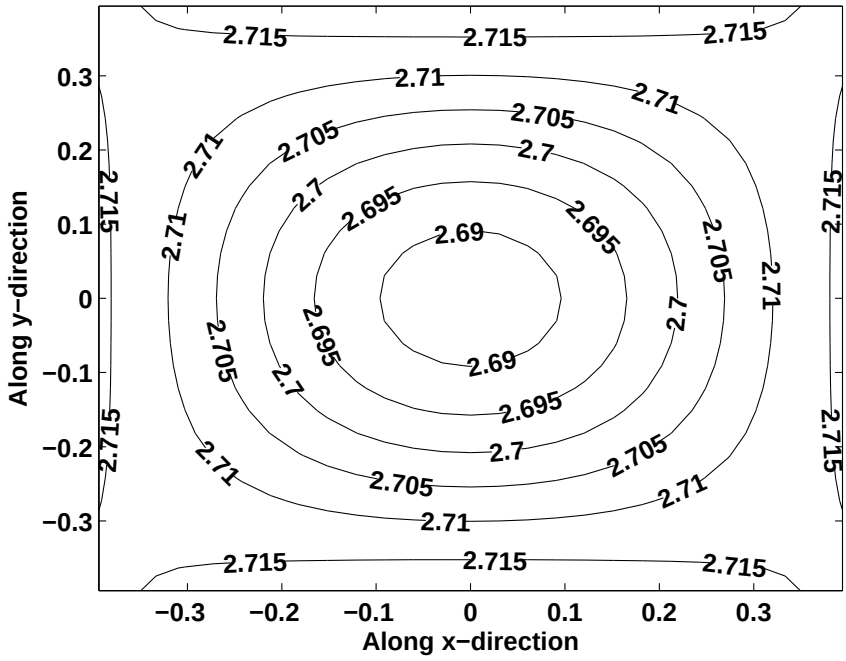

(b)

Figure 5.7: Variation of the fundamental frequency as a function of crack position for a simply supported square FGM plate. The crack orientation, θ is taken to be 0°, i.e., horizontal crack.

Table 5.8: Effect of the plate aspect ratio b/a, the plate thickness a/h and the boundary condition on the fundamental frequency, $\omega b^2/h\sqrt{\rho_c/E_c}$ for Si_3N_4/SUS304 FGM plate with a horizontal center crack ($c_y/b = 0.5, d/a = 0.5$). †Simply Supported, *Clamped Condition.

b/a	a/h	Mode 1		Mode 2	
		SS†	CC*	SS†	CC*
0.5	10	1.1205	2.2202	2.1586	2.8588
	20	1.1974	2.5043	2.5482	3.4621
	100	1.2625	2.6748	2.6593	4.0903
1	10	2.4051	4.1624	5.2792	6.6286
	20	2.4831	4.4592	5.8338	7.6464
	100	2.5473	4.6311	6.2765	8.5774
2	10	6.6864	12.7513	10.5295	15.9115
	20	6.8101	13.4551	10.8647	17.0301
	100	6.8847	13.7540	11.0392	17.6030

5.5.2 Plate with multiple cracks

Figure 5.8 shows a plate with two cracks with lengths a_1 and a_2 and with orientations θ_1 and θ_2 they subtend with the horizontal. The effect of the crack orientations on the fundamental frequency for a simply supported FGM plate is numerically studied. The horizontal (H_x) and the vertical (V_y) separation (see Figure 5.8) between the crack tips is set to a constant value, $H_x = 0.2$ and $V_y = 0.1$, respectively. Table 5.9 shows the variation of the fundamental frequency for a plate with a gradient index $n = 5$ and the crack lengths $a_1 = a_2 = 0.2$ as a function of the crack orientations. Figure 5.9 shows the variation of the frequency as a function of orientation of one of the crack for different orientations of the other crack. It can be seen that with an increase in the crack orientation, the frequency initially decreases until it reaches a minimum at $\theta = 45^o$. With further increase in the crack orientation, the frequency increases and reaches maximum at $\theta_1 = \theta_2 = 90^o$. The frequency value at $\theta = 0^o$ is not the same as that at $\theta = 90^o$ as expected. This is because when $\theta_1 = \theta_2 = 90^o$, the crack is located away from the center of the plate and the presence of the crack disturbs the mode shape slightly.

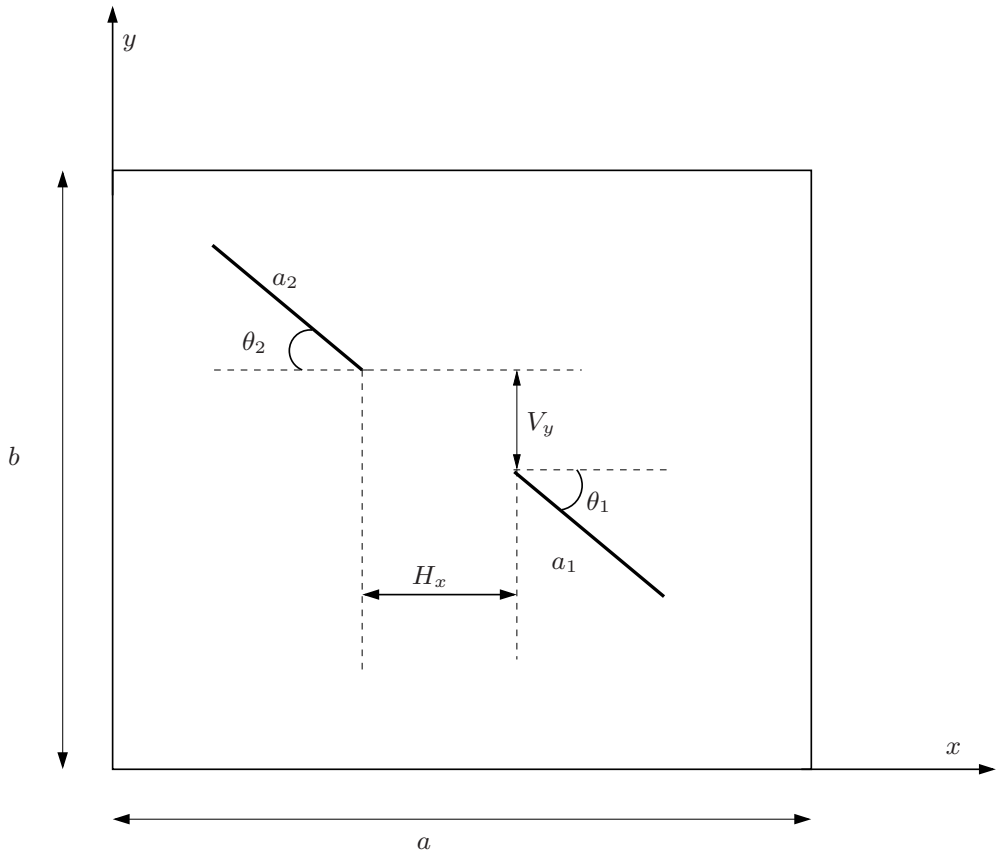

Figure 5.8: Plate with multiple cracks: geometry. H_x and V_y are the horizontal and the vertical separation between the crack tips, a_1, a_2 are the crack lengths and θ_1, θ_2 are the crack orientations they subtend with the horizontal.

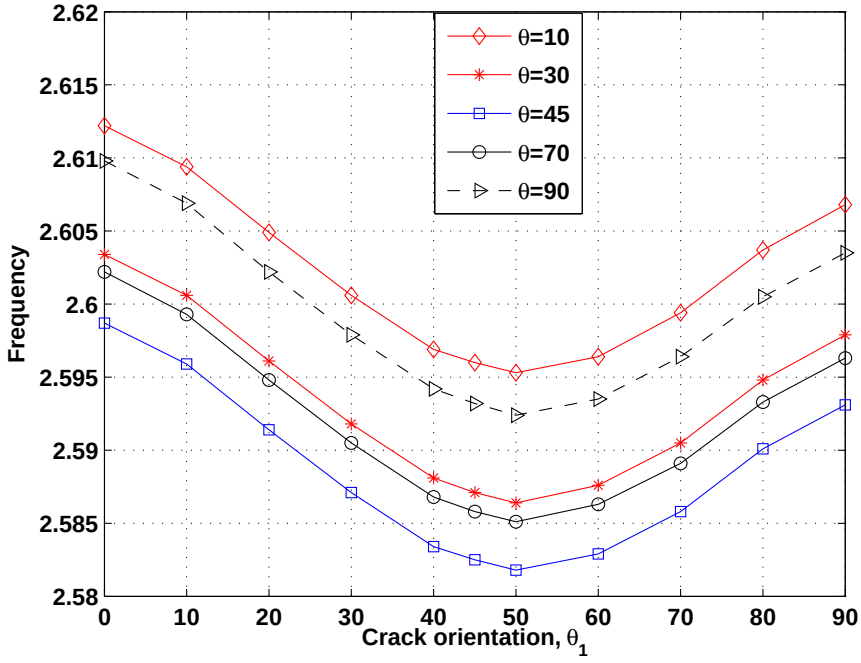

(a)

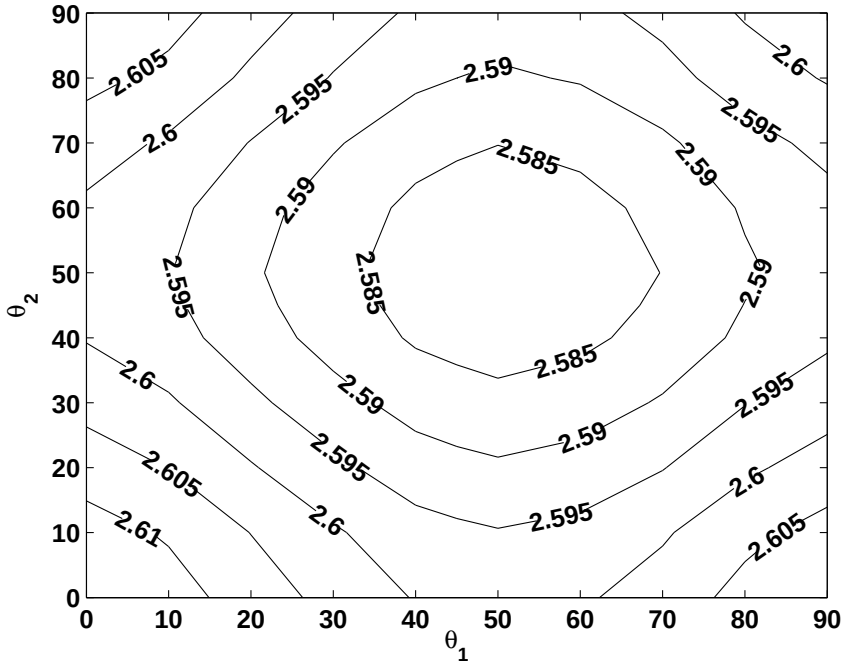

(b)

Figure 5.9: Variation of the fundamental frequency for a simply supported square Si_3N_4/SUS304 FGM plate with a center crack as a function crack orientation with $H_x = 0.2$, $V_y = 0.1$ and $a/h = 10$ (see Figure 5.8).

Table 5.9: Fundamental frequency, $\omega b^2/h\sqrt{\rho_c/E_c}$ for a simply supported Si_3N_4/SUS304 FGM square plate, gradient index, $n = 5$. †denotes change in trend.

Crack	Crack orientation, θ_2.										
Orientation, θ_1	0	10	20	30	40	45	**50**†	60	70	80	90
0	2.6149	2.6122	2.6077	2.6034	2.5997	2.5988	**2.5981**	2.5993	2.6023	2.6066	2.6098
10	2.6122	2.6094	2.6049	2.6006	2.5969	2.5960	**2.5953**	2.5964	2.5994	2.6037	2.6068
20	2.6077	2.6049	2.6004	2.5961	2.5924	2.5914	**2.5907**	2.5919	2.5948	2.5991	2.6022
30	2.6034	2.6006	2.5961	2.5918	2.5881	2.5871	**2.5864**	2.5876	2.5905	2.5948	2.5979
40	2.5997	2.5969	2.5924	2.5881	2.5844	2.5835	**2.5827**	2.5839	2.5868	2.5910	2.5941
45	2.5987	2.5959	2.5914	2.5871	2.5834	2.5825	**2.5818**	2.5829	2.5858	2.5901	2.5931
50†	**2.5980**	**2.5952**	**2.5907**	**2.5864**	**2.5827**	**2.5818**	**2.5811**	**2.5822**	**2.5851**	**2.5893**	**2.5924**
60	2.5992	2.5964	2.5918	2.5876	2.5839	2.5829	**2.5822**	2.5834	2.5863	2.5905	2.5935
70	2.6022	2.5993	2.5948	2.5905	2.5868	2.5858	**2.5851**	2.5863	2.5891	2.5933	2.5963
80	2.6065	2.6036	2.5990	2.5947	2.5910	2.5900	**2.5893**	2.5904	2.5933	2.5974	2.6004
90	2.6098	2.6069	2.6022	2.5979	2.5942	2.5932	**2.5924**	2.5935	2.5964	2.6005	2.6035

5.5.3 Plate with a side crack

Consider a plate of uniform thickness, h, with length and width as a and b, respectively. Figure 5.10 shows a cantilevered plate with a side crack of length d, located at a distance of c_y from the $x-$axis and at an angle θ with respect to the $x-$axis. The influence of the plate thickness, the crack orientation and the gradient index on the fundamental frequency is shown in Table 5.10 and in Figure 5.11. With an increase in the gradient index n, the frequency decreases for all crack orientations and for different plate thickness. With an increase in the crack orientation from $\theta = -60^\circ$ to $\theta = 60^\circ$, the frequency initially decreases until $\theta = -40^\circ$ and then reaches the maximum when the crack is horizontal. And with further increase in the crack orientation, the frequency decreases. This is because, when the crack is horizontal $(\theta = 0)$, the crack is aligned to the first mode shape and the response of the plate is similar to a cantilevered plate without a crack. The frequency of the plate without a crack is greater than a plate with a crack. Figures 5.12 and 5.13 shows the first two mode shapes for a cantilevered plate with and without a horizontal crack. As explained earlier, the frequency and the first mode shape for a plate with and without a crack are very similar. For any other crack orientation, the mode shape is influenced by the presence of the crack. Figures 5.14 and 5.15 shows the first mode shape of a cantilevered plate with a side crack with orientations, $\theta = \pm 40^\circ$ and $\theta = \pm 60^\circ$, respectively.

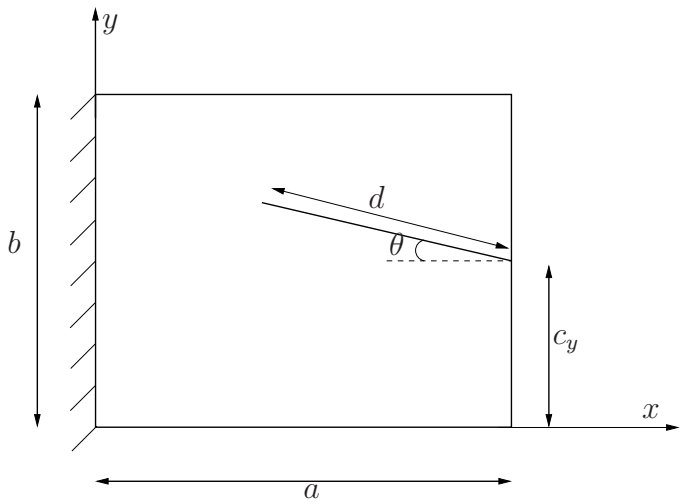

Figure 5.10: Cantilevered plate with a side crack: geometry

5.6 Conclusions

The natural frequencies of a cracked FGM plate is studied using the XFEM. The formulation is based on the FSDT and the 4-noded shear flexible, field consistent enriched element is

Table 5.10: Fundamental frequency, $\omega b^2/h\sqrt{\rho_c/E_c}$ for a cantilevered square plate Si_3N_4/SUS304 FGM plate with a side crack $(c_y/b = 0.5, d/a = 0.5)$ as a function of crack angle and gradient index. †denotes a change in trend.

a/h	crack angle, θ	gradient index, n				
		0	1	2	5	10
	-60	0.9859	0.5918	0.5322	0.4838	0.4610
	-50	0.9840	0.5906	0.5312	0.4829	0.4601
	-40†	**0.9838**	**0.5905**	**0.5311**	**0.4828**	**0.4600**
	-30	0.9862	0.5919	0.5323	0.4840	0.4611
	-20	0.9900	0.5943	0.534	0.4859	0.4630
	-10	0.9936	0.5964	0.5364	0.4876	0.4646
10	**0†**	**0.9951**	**0.5973**	**0.5372**	**0.4884**	**0.4653**
	10	0.9936	0.5964	0.5364	0.4876	0.4646
	20	0.9900	0.5943	0.5344	0.4859	0.4630
	30	0.9862	0.5919	0.5323	0.4840	0.4611
	40†	**0.9838**	**0.5905**	**0.5311**	**0.4828**	**0.4600**
	50	0.9840	0.5906	0.5312	0.4829	0.4601
	60	0.9859	0.5918	0.5322	0.4838	0.4610
	-60	0.9949	0.5972	0.5371	0.4883	0.4653
	-50	0.9927	0.5959	0.5359	0.4872	0.4643
	-40†	**0.9924**	**0.5957**	**0.5357**	**0.4871**	**0.4641**
	-30	0.9944	0.5969	0.5368	0.4881	0.4651
	-20	0.9979	0.5989	0.5387	0.4898	0.4667
	-10	1.0011	0.6009	0.5404	0.4913	0.4682
20	**0†**	**1.0024**	**0.6016**	**0.5411**	**0.4920**	**0.4688**
	10	1.0011	0.6009	0.5404	0.4913	0.4682
	20	0.9979	0.5989	0.5387	0.4898	0.4667
	30	0.9944	0.5969	0.5368	0.4881	0.4651
	40†	**0.9924**	**0.5957**	**0.5357**	**0.4871**	**0.4641**
	50	0.9927	0.5959	0.5359	0.4872	0.4643
	60	0.9949	0.5972	0.5371	0.4883	0.4653

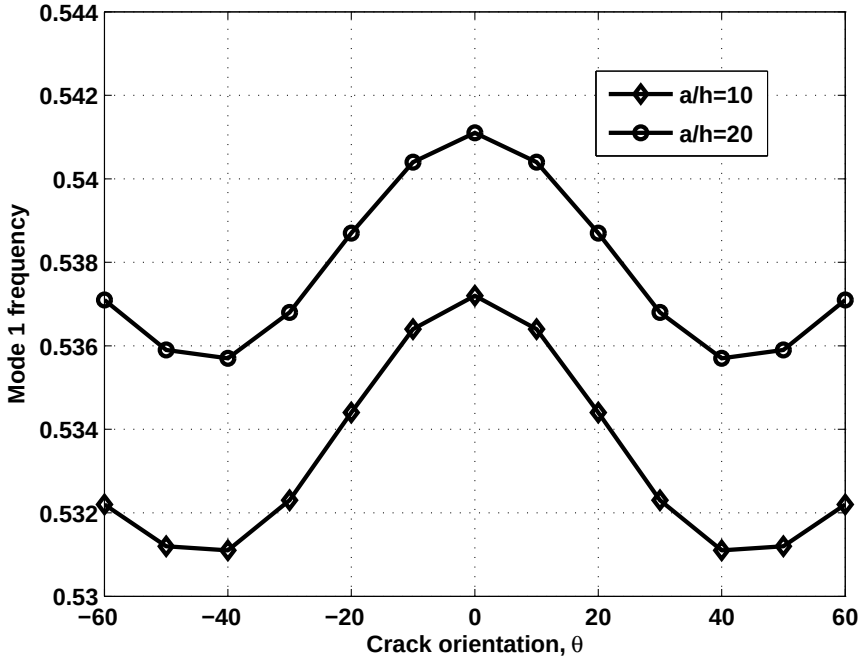

(a) Effect of aspect ratio, a/h

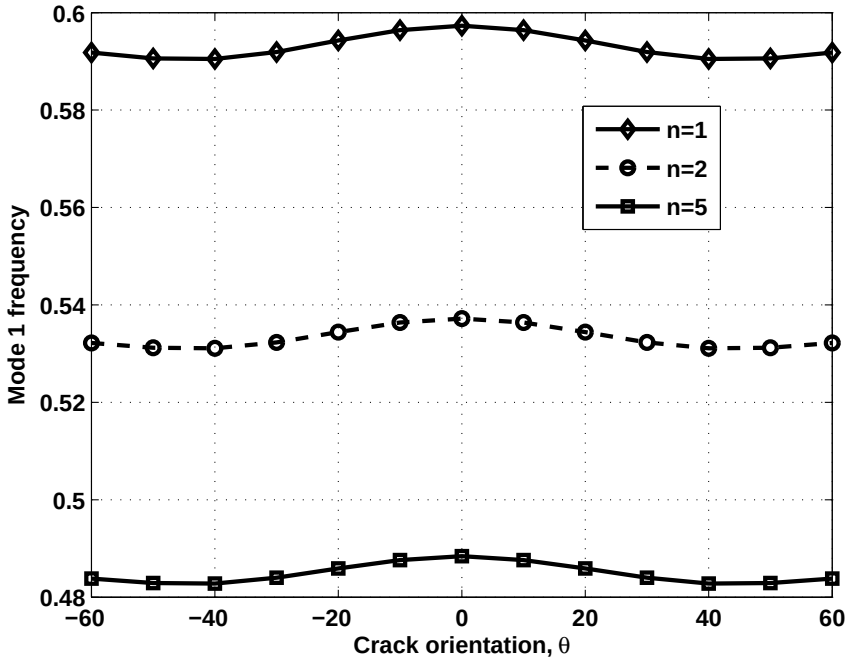

(b) Effect of gradient index, n

Figure 5.11: Variation of the fundamental frequency for a cantilevered square Si_3N_4/SUS304 FGM plate with a side crack as a function of crack orientation. $d/a = 0.5$, $c_y/a = 0.5$.

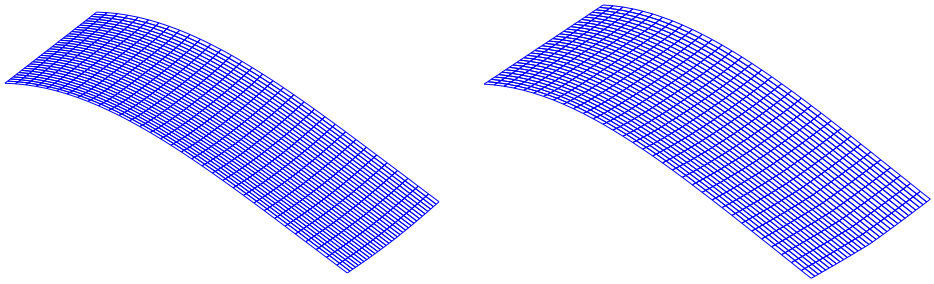

(a) Without crack, $\overline{\Omega}_1 = 0.4885$ (b) With crack, $\overline{\Omega}_1 = 0.4883$

Figure 5.12: First Mode shape for a cantilevered plate with a side crack with $\theta = 0°, n = 5, c_y/b = 0.5, d/a = 0.5, a/h = 10, b/a = 1$.

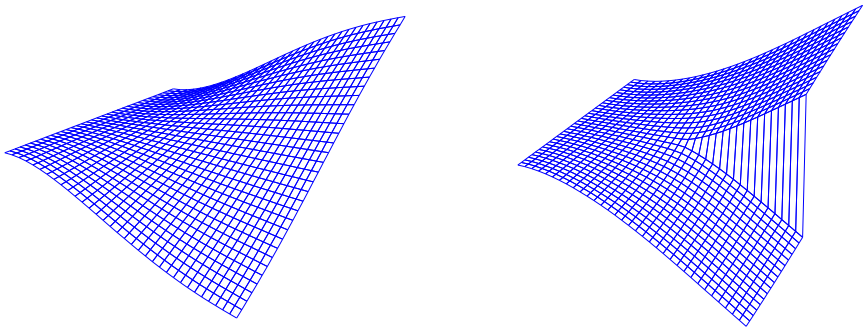

(a) Without crack, $\overline{\Omega}_2 = 1.1608$ (b) With crack, $\overline{\Omega}_2 = 0.8223$

Figure 5.13: Second Mode shape for a cantilevered plate with a side crack with $\theta = 0, n = 5, c_y/b = 0.5, d/a = 0.5, a/h = 10, b/a = 1$.

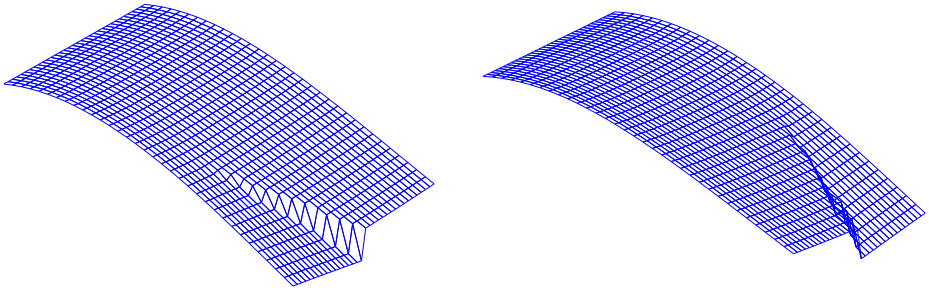

(a) $\theta = 40°$ (b) θ = -40°

Figure 5.14: First Mode shape ($\overline{\Omega}_1 = 0.4828$) for a cantilevered plate with a side crack with $n = 5, c_y/b = 0.5, d/a = 0.5, a/h = 10, b/a = 1$.

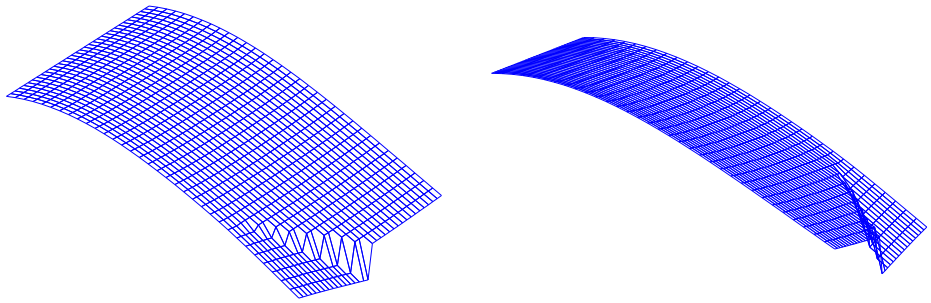

(a) $\theta = 60^\circ$ (b) θ = -60°

Figure 5.15: First Mode shape ($\overline{\Omega}_1 = 0.4838$) for a cantilevered plate with a side crack with $n = 5, c_y/b = 0.5, d/a = 0.5, a/h = 10, b/a = 1$.

used. The material is assumed to be graded only in the thickness direction. Numerical experiments have been conducted to bring out the effect of various parameters, such as the gradient index, the crack geometry, the boundary condition and the plate geometry on the natural frequency of the FGM plate. Also, the influence of multiple cracks and their relative orientation on the natural frequency is studied. From the detailed numerical study, the following can be concluded:

- Increasing the crack length decreases the natural frequency. This is due to the reduction in the stiffness of the material structure. The frequency is lowest when the crack is located at the center of the plate.
- Increasing the gradient index, n decreases the natural frequency. This is due to the increase in the metallic volume fraction.
- Decreasing the plate thickness, a/h and increasing the aspect ratio, b/a increases the fundamental frequency.
- For a cantilevered plate with a side crack, the frequency is maximum when the crack is horizontal, i.e., $\theta = 0$. The response of the plate is symmetric with respect to this crack orientation and the trend changes at $\theta = \pm 40^\circ$.
- Crack orientation, $\theta = 45^\circ$ has been observed to be a critical angle. At this crack orientation, the frequency changes its trend for a square plate.
- Increasing the number of cracks, decreases the overall stiffness of the plate and thus decreases the frequency. The frequency is lowest when both the cracks are oriented at $\theta = 50^\circ$.

Bibliography

[1] M. Bachene, R. Tiberkak, and S. Rechak. Vibration analysis of cracked plates using the extended finite element method. *Arch. Appl. Mech.*, 79:249–262, 2009.

[2] M. Bachene, R. Tiberkak, S. Rechak, G. Maurice, and B. K. Hachi. Enriched finite element for modal analysis of cracked plates. In *Damage and Fracture Mechanics: Failure Analysis and Engineering Materials and Structures*, pages 463–471. Springer Science, 2009.

[3] K. J. Bathe and E. Dvorkin. A four node plate bending element based on Mindlin - Reissner plate theory and mixed interpolation. *International Journal for Numerical Methods in Engineering*, 21:367–383, 1985.

[4] T. Belytschko and T. Black. Elastic crack growth in finite elements with minimal remeshing. *International Journal for Numerical Methods in Engineering*, 45:601–620, 1999.

[5] Y. Benvensite. A new approach to the application of Mori - Tanaka's theory in composite materials. *Mechanics of Materials*, 6:147–157, 1987.

[6] K. U. Bletzinger, M. Bischoff, and E. Ramm. A unified approach for shear-locking free triangular and rectangular shell finite elements. *International Journal for Numerical Methods in Engineering*, 75:321–334, 2000.

[7] S. Bordas and A. Legay. Enriched finite element short course: class notes. In *The extended finite element method, a new approach to numerical analysis in mechanics: course notes*. Organized by S. Bordas and A. Legay through the EPFL school of continuing education, Lausanne, Switzerland, 2005.

[8] S. Bordas and A. Legay. Enriched finite element short course: class notes. In *The extended finite element method, a new approach to numerical analysis in mechanics: course notes*. Organized by S. Bordas and A. Legay through the EPFL school of continuing education, Lausanne, Switzerland, 2007.

[9] J. S. Chen, H. P. Wang, S. Yoon, and Y. You. Some recent improvements in meshfree methods for incompressible finite elasticity boundary value problems with contact. *Computational Mechanics*, 25:137–156, 2000.

[10] J. Dolbow, N. Moës, and T. Belytschko. Modeling fracture in Mindlin - Reissner plates with the extended finite element method. *International Journal of Solids and Structures*, 37(48-50):7161–7183, 2000.

[11] A. J. M. Ferreira, R. C. Batra, C. M. C. Roque, L. K. Qian, and R. M. N. Jorge. Natural frequencies of functionally graded plates by a meshless method. *Composite Structures*, 75:593–600, 2006.

[12] M. Ganapathi, T. K. Varadan, and B. S. Sarma. Nonlinear flexural vibrations of laminated orthotropic plates. *Computers and Structures*, 39:685–688, 1991.

[13] H. Hatta and M. Taya. Effective thermal conductivity of a misoriented short fiber composite. *Journal of Applied Physics*, 58:2478–2486, 1985.

[14] X. Q. He, T. Y. Ng, S. Sivashanker, and K. M. Liew. Active control of FGM plates with integrated piezoelectric sensors and actuators. *International Journal of Solids and Structures*, 38:1641–1655, 2001.

[15] C. S. Huang, O. G. M. III, and M. J. Chang. Vibrations of cracked rectangular FGM thick plates. *Commposite Structures*, 2011.

[16] C. S. Huang and A. W. Lieissa. Vibration analysis of rectangular plates with side cracks via the Ritz method. *Journal of Sound and Vibration*, 323:974–988, 2009.

[17] T. J. R. Hughes, J. A. Cottrell, and Y. Bazilevs. Isogeometric analysis: CAD, finite elements, NURBS, exact geometry and mesh refinement. *Computer Methods in Applied Mechanical and Engineering*, 194:4135–4195, 2005.

[18] W. Kanok-Nukulchai, W. Barry, K. Saran-Yasoontorn, and P. H. Bouillard. On elimination of shear locking in the element-free Galerkin method. *International Journal for Numerical Methods in Engineering*, 52:705–725, 2001.

[19] S. E. Khadem and M. Rezaee. Introduction of modified comparison functions for vibration analysis of a rectangular cracked plate. *Journal of Sound and Vibration*, 236(2):245–258, 2000.

[20] S. Kitipornchai, L. L. Ke, J. Yang, and Y. Xiang. Nonlinear vibration of edge cracked functionally graded Timoshenko beams. *Journal of Sound and Vibration*, 324:962–982, 2009.

[21] M. Koizumi. The concept of FGM. *Ceram. Trans. Funct. Graded Mater*, 34:3–10, 1993.

[22] M. Koizumi. FGM activities in Japan. *Composites*, 28:1–4, 1997.

[23] H. P. Lee and S. P. Lim. Vibration of cracked rectangular plates including transverse shear deformation and rotary inertia. *Computers and Structures*, 49(4):715–718, 1993.

[24] K. M. Liew, X. Q. He, T. Y. Ng, and S. Sivashanker. Active control of FGM plates subjected to a temperature gradient: modeling via finite element method based on FSDT. *International Journal for Numerical Methods in Engineering*, 52:1253–1271, 2001.

[25] P. P. Lynn and N. Kumbasar. Free vibrations of thin rectangular plates having narrow cracks with simply supported edges. *Developments in Mechanics*, 4:928–991, 1967.

[26] H. Matsunaga. Free vibration and stability of functionally graded plates according to a 2-D higher-order deformation theory. *Composite Structures*, 82:499–512, 2008.

[27] T. Mori and K. Tanaka. Average stress in matrix and average elastic energy of materials with misfitting inclusions. *Acta Metallurgica*, 21:571–574, 1973.

[28] T. Y. Ng, K. Y. Lam, and K. M. Liew. Effect of FGM materials on parametric response of plate structures. *Computer Methods in Applied Mechanics and Engineering*, 190:953–962, 2000.

[29] N. T. Nguyen, T. Rabczuk, H. Nguyen-Xuan, and S. Bordas. A smoothed finite element method for shell analysis. *Computer Methods in Applied Mechanics and Engineering*, 198:165–177, 2008.

[30] H. Nguyen-Xuan, T. Rabczuk, S. Bordas, and J. F. Debongnie. A smoothed finite element method for plate analysis. *Computer Methods in Applied Mechanics and Engineering*, 197:1184–1203, 2008.

[31] T. Prakash, N. Sundararajan, and M. Ganapathi. On the nonlinear axisymmetric dynamic buckling behavior of clamped functionally graded spherical caps. *Journal of Sound and Vibration*, 299: 36–43, 2007.

[32] G. L. Qian, S. N. Gu, and J. S. Jiang. A finite element model of cracked plates and application to vibration problems. *Computers and Structures*, 39(5):483–487, 1991.

[33] L. C. Qian, R. C. Batra, and L. M. Chen. Static and dynamic deformations of thick functionally graded elastic plates by using higher order shear and normal deformable plate theory and meshless local Petrov Galerkin method. *Composites Part B: Engineering*, 35:685–697, 2004.

[34] A. A. Rahimabadi, A. Bagri, S. Bordas, and T. Rabczuk. Analysis of thermoelastic waves in a two-dimensional functionally graded materials domain by the meshless local Petrov-Galerkin method. *Computer Modelling in Engineering and Science*, 65:27–74, 2010.

[35] S. Rajasekaran and D. W. Murray. Incremental finite element matrices. *ASCE Journal of Structural Divison*, 99:2423–2438, 1973.

[36] J. N. Reddy. Analysis of functionally graded plates. *International Journal for Numerical Methods in Engineering*, 47:663–684, 2000.

[37] J. N. Reddy and C. D. Chin. Thermomechanical analysis of functionally graded cylinders and plates. *Journal of Thermal Stresses*, 21:593–629, 1998.

[38] B. Rosen and Z. Hashin. Effective thermal expansion coefficients and specific heat of composite materials. *International Journal of Engineering Science*, 8:157–173, 1970.

[39] J. C. Simo and M. S. Rifai. A class of mixed assumed strain methods and the method of incompatible modes. *International Journal for Numerical Methods in Engineering*, 29:1595–1638, 1990.

[40] M. K. Singh, T. Prakash, and M. Ganapathi. Finite element analysis of functionally graded plates under transverse load. *Finite Elements in Analysis and Design*, 47:453–460, 2011.

[41] R. Solecki. Bending vibration of rectangular plate with arbitrarly located rectilinear crack. *Engineering Fracture Mechanics*, 22(4):687–695, 1985.

[42] B. R. Somashekar, G. Prathap, and C. R. Babu. A field-consistent four-noded laminated anisotropic plate/shell element. *Computers and Structures*, 25:345–353, 1987.

[43] B. Stahl and L. M. Keer. Vibration and stability of cracked rectangular plates. *International Journal of Solids and Structures*, 8:69–91, 1972.

[44] N. Sundararajan, T. Prakash, and M. Ganapathi. Nonlinear free flexural vibrations of functionally graded rectangular and skew plates under thermal environments. *Finite Elements in Analysis and Design*, 42:152–168, 2005.

[45] R. Tiberkak, M. Bachene, B. K. .Hachi, S. Rechak, and M. Haboussi. Dynamic response of cracked plate subjected to impact loading using the extended finite element method. In *Damage and Fracture Mechanics: Failure Analysis and Engineering Materials and Structures*, pages 297–306. Springer Science, 2009.

[46] S. S. Vel and R. C. Batra. Exact solutions for thermoelastic deformations of functionally graded thick rectangular plates. *AIAA J*, 40:1421–1433, 2002.

[47] S. S. Vel and R. C. Batra. Three-dimensional exact solution for the vibration of functionally graded rectangular plates. *Journal of Sound and Vibration*, 272:703–730, 2004.

[48] D. Wang and J. S. Chen. Locking-free stabilized conforming nodal integration for mesh-free Mindlin-Reissner plate formulation. *Computer Methods in Applied Mechanical and Engineering*, 193:1065–1083, 2004.

[49] D. S. Watkins. *Fundamentals of matrix computations*. Wiley Publishers, 2002.

[50] G. Y. Wu and Y. S. Shih. Dynamic instability of rectangular plate with an edge crack. *Computers and Structures*, 84(1-2):1–10, 2005.

[51] L. Wu. Thermal buckling of a simply supported moderately thick rectangular FGM plate. *Composite Structures*, 64:211–218, 2004.

[52] J. Yang, Y. X. Hao, W. Zhang, and S. Kitipornchai. Nonlinear dynamic response of a functionally graded plate with a through-width surface crack. *Nonlinear Dynamics*, 59:207–219, 2010.

[53] J. Yang and H. S. Shen. Dynamic response of initially stressed functionally graded rectangular thin plates. *Composite Structures*, 54:497–508, 2001.

[54] J. Yang and H. S. Shen. Vibration characteristic and transient response of shear-deformable functionally graded plates in thermal environments. *Journal of Sound and Vibration*, 255:579–602, 2002.

[55] O. C. Zienkiewicz, R. L. Taylor, and J. Z. Zhu. *The finite element method: its basics and fundamentals*. Elsevier Butterworth Heinemann, 6^{th} edition, 2000.

6 Conclusions

Detailed conclusions were drawn at the end of each chapter. Some important conclusions and contributions are summarized below.

6.1 Conclusions & Future Work

This thesis presented two new numerical integration techniques (c.f. Chapter 3) to integrate over the elements intersected by a discontinuity surface. The first method relies on SCCM, where the regions intersected by the discontinuity surface are mapped onto a unit disk and cubature rule on this unit disk is used to numerically evaluate the system matrices, i.e., the stiffness matrix, the mass matrix and the force vector. The same technique is also applied to integrate over arbitrary polygons in the context of polygonal finite element method. One of the main advantage of this technique is that this eliminates the need for a two level iso-parametric mapping and suppresses the need for 'mesh' alignment with the discontinuity surface, which is inevitable in other techniques such as discussed in Chapter 2, Section 2.4.5. Additionally, the positivity of the Jacobian is ensured and quadrature rules of any order can be easily obtained. The flexibility provided by the method also suffers from the following drawback: (i) the SC mapping technique, with current state-of-the-art, remains to two-dimensional problems and (ii) the integration points have to be computed for each polygonal element in the domain.

The second method relies on strain smoothing applied to discontinuous finite element approximations. By writing the strain field as a non-local weighted average of the compatible strain field, integration on the surface of the finite elements is transformed into contour integration. A sub-division is still required for the elements that are intersected by the discontinuity surface, but with strain smoothing, the integration is performed along the boundaries of the subcells. One of the potential advantages of the smoothed XFEM is that no subdivision of the split elements is required.

The efficiency and the accuracy of both methods are illustrated with numerical examples involving weak and strong discontinuities in Chapter 4. From the numerical examples presented, it can be seen that the numerical integration performed with SCCM slightly outperforms the conventional integration method based on sub-division. However, for the SmXFEM, the numerical examples presented for the case with asymptotic enrichment, indicate that the convergence rate obtained with SmXFEM is equal or superior to that of the XFEM, but the error level is greater. This can be attributed to the asymptotic fields. To make use of the salient features of the strain smoothing, the SmXFEM is combined with the SCCM. This eliminates the need to sub-triangulate the elements completely cut by the crack. It can be inferred from the numerical examples that the proposed technique behaves at least as well as the Std. XFEM. The XFEM is applied to crack growth problems, where the results obtained from the numerical study qualitatively agrees with the published results. The linear free flexural vibrations of cracked FGM plates are studied in Chapter 5. The crack geometry is modelled independent of the underlying mesh and the influence of the crack geometry on the fundamental frequency is numerically studied.

Application to 3D The method based on SC mapping for numerical integration is restricted to 2D, as there is no such mapping available in case of the 3D. In case of the 2D, it eliminates the need for sub-division of elements interested by the discontinuous surface. The second method alleviates the need to integrate singular functions, but the error level is greater compared to that of the XFEM. A combination of both the techniques could work in 3D. The idea would be use strain smoothing to convert the volume integral to surface integral and then the SC mapping subsequently to integrate along the boundary of the interior and exterior subregions. Since each of these boundaries is composed of the union of polygons, the SC mapping (or any other method integrate numerically on polygons) can be used to evaluate the system matrices.

Cohesive cracks Note that a non-polynomial crack tip enrichment is commonly omitted when XFEM is used in combination with cohesive zone models and hence the SmXFEM is expected to perform at least as well as the Std. XFEM for cohesive cracks. By using a constant weight function and by applying the divergence theorem, the surface integration in 2D is transformed into line integration around the boundary. With SSM, no isoparametric mapping is required and the shape functions need to be computed along the edges of the smoothing cells in the physical space. This provides the flexibility of integrating on the line of discontinuity in the physical space without having to map it to parent element as normally done in the conventional XFEM. The cohesive cracks can be modelled with func-

tions of the form $r^\lambda, \lambda \geq 1$. The accuracy of the displacements in the vicinity of the crack tip can be improved by enriching with higher order terms in the expansion, despite the fact that there is no singularity. With strain smoothing the derivatives of such functions are no longer necessary.

Numerical integration in Element Free Galerkin Method (EFGM) The idea of SCCM can be used to locate the integration points in case of the EFGM which uses background cells for the purpose of numerical integration. Instead of using quadrilateral elements as background cells, a Voronoi tessellation can be done over the distributed nodes. Then each polygon can be mapped onto a unit disk to locate the integration points.

6.2 Publications

The following is the list of articles published in journals and presented at various national and international conferences.

Journal Publications

1. **S. Natarajan**, P. M. Baiz, S. Bordas, T. Rabczuk, P. Kerfriden. *Natural frequencies of cracked functionally graded material plates by the extended finite element method*, Composite Structures, *Article in press*, **2011**, doi:10.1016/j.compstruct.2011.04.007.

2. P.M. Baiz, **S. Natarajan**, S. P. A. Bordas, P. Kerfriden, T. Rabczuk, *Linear Buckling Analysis of Cracked Plates by SFEM and XFEM (SmXFEM)*, Journal of Mechanics of Materials and Structures, *Accepted for publication*, **2011**.

3. S. Bordas, **S. Natarajan**, P. Kerfriden, C. Augarde, D. R. Mahapatra, T. Rabczuk, S. D. Pont. *On the performance of strain smoothing for quadratic and enriched finite element approximations (XFEM/GFEM/PUFEM)*, International Journal for Numerical Methods in Engineering (Special issue: XFEM), 86(4–5), 637–666, **2011**, doi: 10.1002/nme.3156.

4. S. P. A. Bordas, T. Rabczuk, H. Nguyen-Xuan, V. P. Nguyen, **S. Natarajan**, T. Bog, D. M. Quan, V. H. Nguyen. *Strain smoothing in FEM and XFEM*, Computers & Structures, 88(23–24), 1419–1443, **2010**. doi: 10.1016/j.compstruc.2008.07.006

5. **S. Natarajan**, D. R. Mahapatra, S. Bordas. *Integrating strong and weak discontinuities without integration subcells and example applications in an XFEM/GFEM framework*, International Journal for Numerical Methods in Engineering, 83(3), 269–294, **2010**. doi: 10.1002/nme.2798

6. S. Bordas, **S. Natarajan**. *On the approximation in the smoothed finite element method (SFEM)*, International Journal for Numerical Methods in Engineering, 81(5), 660–670, **2010**. doi: 10.1002/nme.2713

7. **S. Natarajan**, S. Bordas, D. R. Mahapatra. *Numerical integration over arbitrary polygonal domains based on Schwarz-Christoffel conformal mapping*, International Journal for Numerical Methods in Engineering, 80(1), 103–134, **2009**. doi: 10.1002/nme.2589

Conference Proceedings

- S. Chakraborty, D. R. Mahapatra, **S. Natarajan**, S. Bordas. *Polygonal XFEM for modelling deformation of polycrystalline microstructures*, XFEM 2011, (ECCOMAS Thematic Conference) Cardiff, Jun 29– Jul 1, **2011**.

- **S. Natarajan**, P. Baiz, D. R. Mahapatra, T. Rabczuk, P. Kerfriden, S. Bordas. *Natural frequencies of cracked isotropic & specially orthotropic plates using the extended finite element method*, ACME 2011, Edinburgh, Apr 5 – 6, **2011**.

- **S. Natarajan**, P. Kerfriden, D. R. Mahapatra, S. Bordas. *Computation of effective stiffness properties for heterogeneous materials using XFEM*, ICC-CFT 2011, India, Jan 4–7, **2011**.

- **S. Natarajan**, H. Nguyen-Xuan, P. Kerfriden, D. R. Mahapatra, H. Askes, T. Rabczuk, S. Bordas. *Smoothed finite elements and partition of unity finite elements for nonlocal integral and nonlocal gradient elasticity*, WCCM/APCOM 2010, Australia, July 19–23, **2010**.

- **S. Natarajan**, S. Pont, S. Bordas. *Smoothed extended finite element method for coupled multi-physics fracture*, ASME International Mechanical Engineering Congress & Exposition, Lake Buena Vista, Florida, USA, 13–19 November **2009**.

- **S. Natarajan**, T. Rabczuk, S. Bordas. *Strain smoothing in extended finite element method*, International Conference on eXtended Finite Element Methods (XFEM2009), Aachen, Germany, 28–30 September **2009**.

- **S. Natarajan**, S. Bordas, T. Rabczuk. *The smoothed extended finite element method for strong discontinuities*, 23rd Biennial Conference on Numerical Analysis, Strathclyde, 23–26 June **2009**.

- **S. Natarajan**, S. Bordas, T. Rabczuk, Z. Guo. *On the Smoothed eXtended Finite Element Method for Continuum*, 17th UK Conference on Computational Mechanics (ACME-UK), Nottingham, 6–9 April **2009**.

- **S. Natarajan**, D. R. Mahapatra, S. Bordas, Z. Guo. *A novel numerical integration technique over arbitrary polygonal surfaces*, 17th UK Conference on Computational Mechanics (ACME-UK), Nottingham, 6–9 April **2009**.

- **S. Natarajan**, S. Bordas, D. R. Mahapatra. *On numerical integration of discontinuous approximations in partition of unity finite elements*, International Union of Theoretical and Applied Mechanics (IUTAM-MMS08), Bangalore, India, 10–13 December **2008**.

Appendices

A

Analytical Solutions

A-1 One-dimensional Bi-material problem

With no body forces, the exact displacement solution with $u_y = 0$ at $y = -1$ and $u_y = 1$ at $y = 1$ is given by:

$$u(y) = \begin{cases} (y+1)\,\alpha, & -1 \le y \le b, \\ 1 + \frac{E_1}{E_2}\,(y-1)\,\alpha, & b \le y \le 1 \end{cases}, \tag{A-1}$$

where,

$$\alpha = \frac{E_2}{E_2(b+1) - E_1(b-1)}. \tag{A-2}$$

A-2 Bi-material boundary value problem - elastic circular inhomogeneity

The governing equation in polar coordinates is

$$\frac{d}{dr}\left[\frac{1}{r}\frac{d}{dr}(ru_r)\right] = 0 \tag{A-3}$$

The exact displacement solution is written as

$$\begin{aligned} u_r(r) &= \begin{cases} \left[\left(1 - \frac{b^2}{a^2}\right)\beta + \frac{b^2}{a^2}\right] r, & 0 \le r \le a, \\ \left(r - \frac{b^2}{r}\right)\beta + \frac{b^2}{r}, & a \le r \le b, \end{cases} \\ u_\theta(r) &= 0. \end{aligned} \tag{A-4}$$

where

$$\beta = \frac{(\lambda_1 + \mu_1 + \mu_2)b^2}{(\lambda_2 + \mu_2)a^2 + (\lambda_1 + \mu_1)(b^2 - a^2) + \mu_2 b^2} \tag{A-5}$$

The radial (ε_{rr}) and hoop ($\varepsilon_{\theta\theta}$) strains are

$$\begin{aligned}
\varepsilon_{rr}(r) &= \begin{cases} \left(1 - \frac{b^2}{a^2}\right)\beta + \frac{b^2}{a^2}, & 0 \le r \le a, \\ \left(1 + \frac{b^2}{a^2}\right)\beta - \frac{b^2}{a^2}, & a \le r \le b, \end{cases} \\
\varepsilon_{\theta\theta}(r) &= \begin{cases} \left(1 - \frac{b^2}{a^2}\right)\beta + \frac{b^2}{a^2}r, & 0 \le r \le a, \\ \left(1 - \frac{b^2}{r^2}\right)\beta + \frac{b^2}{r^2}r, & a \le r \le b. \end{cases}
\end{aligned} \tag{A-6}$$

and the radial (σ_{rr}) and hoop ($\sigma_{\theta\theta}$) stresses are

$$\begin{aligned}
\sigma_{rr}(r) &= 2\mu\varepsilon_{rr} + \lambda(\varepsilon_{rr} + \varepsilon_{\theta\theta}), \\
\sigma_{\theta\theta}(r) &= 2\mu\varepsilon_{\theta\theta} + \lambda(\varepsilon_{rr} + \varepsilon_{\theta\theta}).
\end{aligned} \tag{A-7}$$

where the appropriate Lamé constants are to be used in the evaluation of the normal stresses.

A-3 Bending of a thick cantilever beam

The exact solution for displacements and stresses for the bending of thick cantilever beam is given by:

$$\begin{aligned}
u(x,y) &= \frac{Py}{6\overline{E}I}\left[(6L - 3x)x + (2 + \overline{\nu})(y^2 - \frac{D^2}{4})\right] \\
v(x,y) &= -\frac{P}{6\overline{E}I}\left[3\overline{\nu}y^2(L - x) + (4 + 5\overline{\nu})\frac{D^2 x}{4} + (3L - x)x^2\right]
\end{aligned} \tag{A-8}$$

where I, the moment of inertia (second moment of area) is given by: $I = \frac{D^3}{12}$. and $\overline{E}$ and $\overline{\nu}$ in Equation (A-8) are given by

$$\overline{E} = \begin{cases} E & \text{(plane stress)}, \\ \frac{E}{1-\nu^2} & \text{(plane strain)} \end{cases} \qquad \overline{\nu} = \begin{cases} \nu & \text{(plane stress)}, \\ \frac{\nu}{1-\nu} & \text{(plane strain)}. \end{cases}$$

The stresses corresponding to the displacements in Equation (A-8) are given by

$$\begin{aligned}\sigma_{xx}(x,y) &= \frac{P(L-x)y}{I};\\ \sigma_{yy}(x,y) &= 0;\\ \sigma_{xy}(x,y) &= -\frac{P}{2I}\left(\frac{D^2}{4}-y^2\right).\end{aligned} \tag{A-9}$$

A-4 Analytical solutions for infinite plate under tension

The closed form solution in terms of polar coordinates in a reference frame (r,θ) centered at the crack tip is:

$$\begin{aligned}\sigma_x(r,\theta) &= \frac{K_I}{\sqrt{r}}\cos\frac{\theta}{2}\left(1-\sin\frac{\theta}{2}\sin\frac{3\theta}{2}\right)\\ \sigma_y(r,\theta) &= \frac{K_I}{\sqrt{r}}\cos\frac{\theta}{2}\left(1+\sin\frac{\theta}{2}\sin\frac{3\theta}{2}\right)\\ \sigma_{xy}(r,\theta) &= \frac{K_I}{\sqrt{r}}\sin\frac{\theta}{2}\cos\frac{\theta}{2}\cos\frac{3\theta}{2}\end{aligned} \tag{A-10}$$

The closed form near-tip displacement field is:

$$\begin{aligned}u_x(r,\theta) &= \frac{2(1+\nu)}{\sqrt{2\pi}}\frac{K_I}{E}\sqrt{r}\cos\frac{\theta}{2}\left(2-2\nu-\cos^2\frac{\theta}{2}\right)\\ u_y(r,\theta) &= \frac{2(1+\nu)}{\sqrt{2\pi}}\frac{K_I}{E}\sqrt{r}\sin\frac{\theta}{2}\left(2-2\nu-\cos^2\frac{\theta}{2}\right)\end{aligned} \tag{A-11}$$

In the two previous expression $K_I = \sigma\sqrt{\pi a}$ denotes the stress intensity factor (SIF), ν is Poisson's ratio and E is Young's modulus.

B

Numerical integration with SCCM

In polygonal finite elements, the use of elements with more than four sides can provide greater flexibility and better accuracy. The polygonal elements can be used as a transition element and simplify meshing or to describe the microstructure of polycrystalline alloys in a rather straight forward manner. The use of polygonal element also necessitates the need to compute shape functions that satisfy all of the following properties: Non-negativeness, interpolation, partition of unity and linear completeness. Mathematically,

$$0 \leq N_I(\mathbf{x}) \leq 1, \;\; N_I(\mathbf{x}_J) = \delta_{IJ}, \;\; \sum_{I=1}^{n} N_I(\mathbf{x}) = 1, \;\; N_I(\eta)\mathbf{x}_I = \mathbf{x}(\eta). \tag{B-1}$$

where N_I is the shape function. In this section, two methods to construct shape functions on a polygonal finite element are discussed, viz., Laplace interpolants and Wachspress interpolants.

Definition: The Voronoi tessellation is a fundamental geometrical construct to get a polygonal mesh covering a given domain. Figure B-1 shows a Voronoi diagram of a point P. The Voronoi diagram is a sub-division of the domain into regions $V(p_i)$, such that any point in $V(p_I)$ is closer to node p_I than to any other node. In mathematical terms, the Voronoi polygon T_I is defined as

$$T_I = \{\mathbf{x} \in \mathbb{R}^2 \colon d(\mathbf{x}, \mathbf{x}_I) < d(\mathbf{x}, \mathbf{x}_J), \forall J \neq I, \} \tag{B-2}$$

where $d(\mathbf{x}_I, \mathbf{x}_J)$, the Euclidean matrix, is the distance between $\mathbf{x}_I$ and $\mathbf{x}_J$.

B-1 Laplace Interpolants

The Voronoi diagram and its dual the Delaunay triangulation, which are used in the construction of the natural neighbour interpolant, are useful geometric constructs that define an irregular set of points. The Laplace interpolant is also called natural neighbour inter-

polants and it also provides a natural weighting function for irregularly spaced nodes.

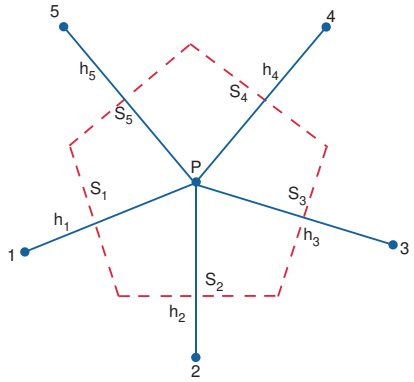

Figure B-1: Voronoi diagram of a point P.

In Figure B-1, the Voronoi cell for point P is shown. If the Voronoi cell for P and that of node P_i have a common Voronoi edge, then the node p_i is called a natural neighbour of the point P. Let t_{IJ} be the Voronoi edge that is common to V_I and V_J in Figure B-1 and $m(t_{IJ})$ denote the Lebesgue measure of t_{IJ}. If P_I and P_J do not have a common edge, then $m(t_{IJ}) = 0$. For the point P with n natural neighbours, the Laplace shape functions for node P_I can be written as:

$$\phi_I(\mathbf{x}) = \frac{\alpha_I(\mathbf{x})}{\sum_{j=1}^{n} \alpha_J(\mathbf{x})}, \quad \alpha_J(\mathbf{x}) = \frac{s_J(\mathbf{x})}{h_J(\mathbf{x})}, \quad \mathbf{x} \in \mathbb{R}^2 \tag{B-3}$$

where $\alpha_I(\mathbf{x})$ is the Laplace weight function, $s_I(\mathbf{x})$ is the length of the Voronoï edge associated with p and node p_I, and $h_I(\mathbf{x})$ is the Euclidean distance between p and p_I (Figure B-1). In a general d-dimensional setting, the computational of the Laplace basis function depends on the ratio of a Lebesgue measure of $\mathbb{R}^2$ divided by linear dimension.
The Laplace interpolant satisfies all properties as indicated in Equation (B-1) and the essential boundary conditions within a Galerkin procedure are treated as in the finite elements. On a bi-unit square, the Laplace, the Wachspress, and the finite element shape functions are identical. And on regular polygons, the Laplace and the Wachspress shape functions are the same.

B-2 Wachspress interpolants

Wachspress, by using the principles of perspective geometry, proposed rational basis functions on polygonal elements, in which the algebraic equations of the edges are used to ensure nodal interpolation and linearity on the boundaries. Wachspress proved that for an n-gon the shape functions are rational polynomials. In general, for an n-sided convex

polygon, a Wachspress shape function $N_I^{(n)}(x,y)$ is a rational polynomial of the following form:

$$N_I^n(x,y) = \frac{\mathcal{P}^{n-2}(x,y)}{\mathcal{P}^{n-3}(x,y)}$$
$$\mathcal{P}^{(m)}(x,y)\colon m - \text{degree polynomial in } x,y \tag{B-4}$$

Wachspress shape functions have the following essential features:

- Each function is positive in the convex domain;
- Each function is linear on each side of the convex n-gon;
- The set of functions exactly interpolates an arbitrary linear field.

In this section, Wachspress interpolants over a quadrilateral is presented. Consider the four-sided quadrilateral, as shown in Figure B-2. Let ℓ_1, ℓ_2, ℓ_3 and ℓ_4 be the equations of the lines corresponding to each of the four sides of the quadrilateral, $(A-B, B-C, C-D \& D-A)$, respectively, and be written in parametric form as

$$\begin{aligned}
\ell_1(x,y) &= a_1x + b_1y + c_1 = 0\\
\ell_2(x,y) &= a_2x + b_2y + c_2 = 0\\
\ell_3(x,y) &= a_3x + b_3y + c_3 = 0\\
\ell_4(x,y) &= a_4x + b_4y + c_4 = 0
\end{aligned} \tag{B-5}$$

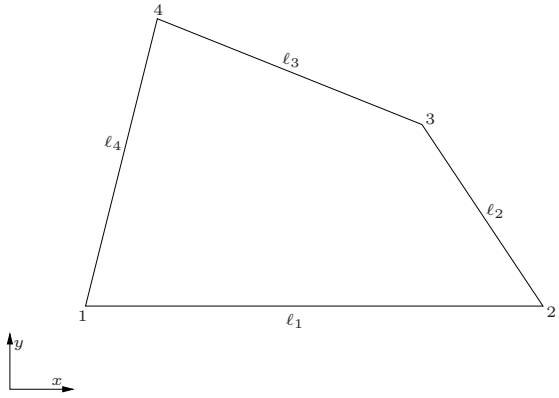

Figure B-2: A sample quadrilateral

where a_i, b_i and c_i for i =1,2,3,4 are real constants. The wedge functions corresponding to each node, w_i, are defined so that they vary linearly along the edges adjacent to each node

and vanish at the remaining nodes as:

$$\begin{aligned} w_1(x,y) &= \kappa_1 \ell_2 \ell_3 \\ w_2(x,y) &= \kappa_2 \ell_3 \ell_4 \\ w_3(x,y) &= \kappa_1 \ell_4 \ell_1 \\ w_4(x,y) &= \kappa_1 \ell_1 \ell_2 \end{aligned} \tag{B-6}$$

where the κ_i are constants. In order that the Wachspress interpolants N_i, satisfy te partition of unity requirement, it is defined as:

$$N_I(x,y) = \frac{w_I(x,y)}{\sum w_I(x,y)} \tag{B-7}$$

In a more general form, the wedge functions can be expressed as:

$$w_I = \prod_{J \neq I, I+1}^{J=n} \ell_J(x,y) \tag{B-8}$$

B-3 Numerical Example

An example in linear elasticity is taken to illustrate the effectiveness of the proposed numerical integration rule, which is referred to as SCCM. The results are compared to the analytical solution and the sub-triangulation method. In this study, the number of integration points per element is kept approximately the same between the sub-triangulation method and the proposed method. In case of the sub-triangulation method, an $n-$ gon is divided into triangles and 13 integration points per triangles are used. The total number of integration points is then computed by:

$$\text{Total number of integration points} = \text{Number of integration points per triangle} \times n \tag{B-9}$$

where n is the number of sides of an element.

B-3.1 Bending of thick cantilever beam

A two-dimensional cantilever beam subjected to a parabolic load at the free end is examined as shown in Figure B-3. The geometry is: length $L = 10$, height $D = 2$. The material properties are: Young's modulus $E = 3 \times 10^7$, Poisson's ratio ν=0.25 and the parabolic shear force $P = 150$. The exact solution to this problem is available as given in Appendix A.

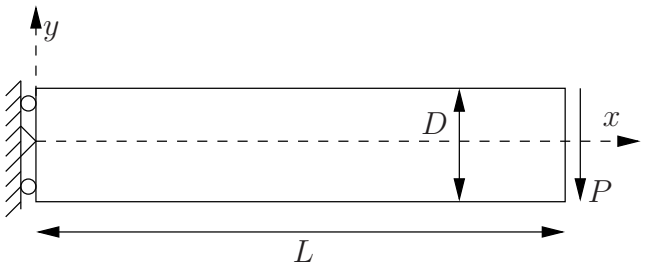

Figure B-3: Geometry and loading of a cantilever beam

In this problem, a structured polygonal mesh is generated. To get a structured polygonal mesh with hexagons, first a regular lattice of equilateral triangles is constructed and then the corresponding Voronoi diagram is generated to obtain the polygonal mesh. Figure B-4 illustrates a structured polygonal mesh. Figure B-5 shows the rate of convergence in the energy norm for the two numerical integration methods. It is seen that for the same number of integration points, the SCCM outperforms the conventional integration by subtriangulation. And with decreasing mesh size, both methods converge to the exact solution. An estimation of the convergence rate is also shown.

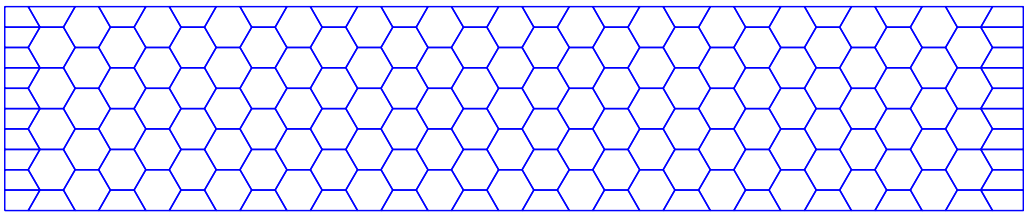

Figure B-4: Domain discretization of cantilever beam with structured polygonal mesh.

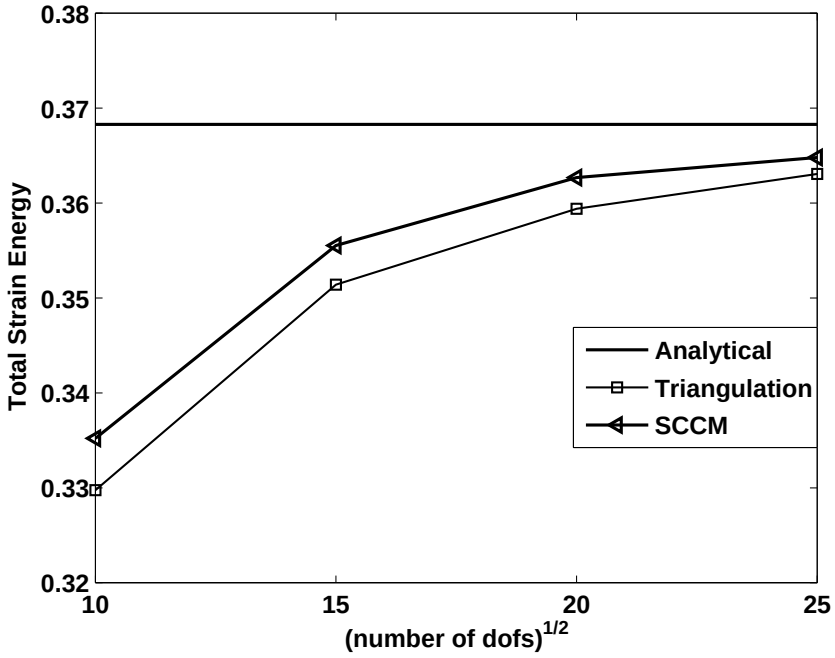

(a)

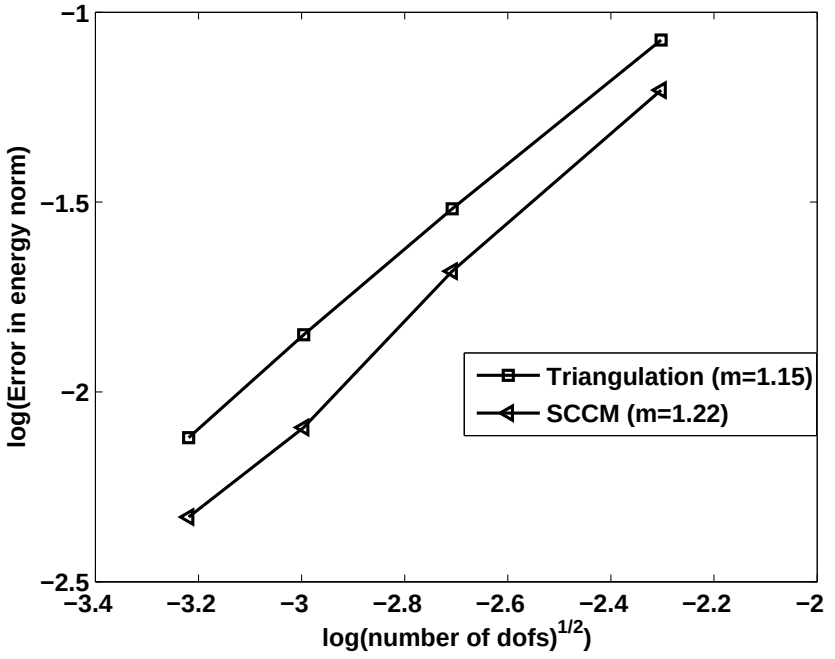

(b)

Figure B-5: The convergence of numerical strain energy to the exact strain energy and convergence rate in the energy norm for structured polygonal meshes: (a) Strain energy and (b) the convergence rate. The error is measured by the H_1 (energy) norm.

C

Strain smoothing for higher order elements

In this section, the strain smoothing is applied to higher order elements. The SFEM procedure for higher order elements is described in detail with a 1D example and is then extended to a two dimensional problem.

C-1 One dimensional problem

To illustrate the solution procedure by the SFEM for quadratic approximations, let us first consider a 1D bar shown in Figure C-1. The left edge of the bar is clamped and unit force is prescribed at the right end. The total length of the bar is $L(= L_1 + L_2)$=1. First the conventional FEM solution is given for completeness and then the SFEM solution is studied in detail. For the current study, consider a 1D three-noded element and with one degree of freedom per node.

FEM solution The assembled system of equations in case of the FEM is given by:

$$\frac{1}{3}\begin{bmatrix} 7 & -8 & 1 \\ -8 & 16 & -8 \\ 1 & -8 & 7 \end{bmatrix} \begin{Bmatrix} u_1 \\ u_2 \\ u_3 \end{Bmatrix} = \begin{Bmatrix} F_1 \\ 0 \\ F_3 \end{Bmatrix} \tag{C-1}$$

with boundary conditions, $u_1 = 0$ and $F_2 = 1$, the solution is given by $u = \{0, 1/2, 1\}$.

SFEM solution

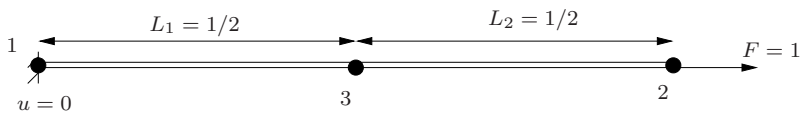

Figure C-1: One dimensional problem

One subcell In this case, the entire domain is treated with only one subcell. The internal node is embedded within the subcell. Because of this, the stiffness matrix has no knowledge of the internal node. The corresponding strain-displacement matrix is (see Equation (3.19)):

$$\tilde{\mathbf{B}} = \frac{1}{L}\left[\begin{array}{ccc} N_1 & N_2 & N_3 \end{array}\right]|_{x=0}^{x=L} \tag{C-2}$$

where in Equation (C-2) the shape functions are evaluated at the domain boundary. The strain displacement matrix for one subcell thus writes:

$$\tilde{\mathbf{B}} = \frac{1}{L}\left[\begin{array}{ccc} -1 & 1 & 0 \end{array}\right]. \tag{C-3}$$

It is clear from the above equation that the contribution from the interior node to the strain matrix is *'zero'*, because the shape function of the interior node is zero at the other two nodes. This leads to a singular stiffness matrix, $\tilde{\mathbf{K}}$.

Two subcells Now the bar is split into two subcells, with the subcell boundary conforming to the interior node. The strain displacement matrix for each of the subcells is given by:

$$\begin{aligned} \tilde{\mathbf{B}}_1 &= \frac{1}{L/2}\left[\begin{array}{ccc} -1 & 1 & 0 \end{array}\right], \quad \text{along } \mathrm{L}_1 \\ \tilde{\mathbf{B}}_2 &= \frac{1}{L/2}\left[\begin{array}{ccc} 0 & -1 & 1 \end{array}\right], \quad \text{along } \mathrm{L}_2 \end{aligned} \tag{C-4}$$

The assembled system of equations for SFEM is thus:

$$\left[\begin{array}{ccc} 2 & -2 & 0 \\ -2 & 4 & -2 \\ 0 & -2 & 2 \end{array}\right] \left\{\begin{array}{c} u_1 \\ u_2 \\ u_3 \end{array}\right\} = \left\{\begin{array}{c} F_1 \\ 0 \\ F_3 \end{array}\right\} \tag{C-5}$$

with boundary conditions, $u_1 = 0$ and $F_2 = 1$, the solution is given by $u = \{0, 1/2, 1\}$.

Remark: From the above discussion, it can be seen that there is a minimum number of subcells required in case of the SFEM. This is very similar to the number of Gauß points required to properly integrate the stiffness matrix in the FEM. For a three noded 1D element, the order of the polynomial is n = 2 and we would need m = 2 ($2m - 1 = n$) integration points for proper integration. Similarly, in case of the SFEM, a minimum of 2 subcells is required to avoid any spurious energy modes. It is interesting to note that the stiffness matrices from the two methods are not identical, but yield the same solution. This only means that $det|\mathbf{K} - \tilde{\mathbf{K}}| = 0$. It can also be verified that increasing the number of subcells, does not change the solution.

Conclusion For a three noded one dimensional element, the following can be concluded

- One subcell leads to a singular $\tilde{\mathbf{K}}$ matrix.
- Two subcells
  - Lead to a proper $\tilde{\mathbf{K}}$ matrix (i.e., avoid spurious zero energy modes). The solution is identical to the analytical solution,
  - The FEM stiffness matrix, $\mathbf{K}$ and the SFEM stiffness matrix, $\tilde{\mathbf{K}}$ are not the same, but yield identical solution.
- Using an even number of subcells (beyond 2), yields identical results to the 2 subcell version.
- With 3 subcells, the stiffness matrix is not singular, but produces erroneous results. This is because with odd number of subcell division, the subcell boundary will not conform to the interior node. In this case of odd number of subcells, the contribution from the interior nodes to the stiffness matrix is incorrect. But with an increase in the number of subcells, it approaches the analytical solution.

C-2 Two dimensional problems

From the previous discussion on the one dimensional element, we concluded that there is a minimum number of subcells required in the case of the SFEM to avoid spurious energy modes. Before proceeding with the two dimensional analysis, we will find the minimum number of subcells required for higher order two dimensional elements. This is done by computing the energy eigenmodes of the stiffness matrix. The element considered for this study is 8 noded quadrilateral element (labelled 'Q8'). The coordinates of the element chosen for this study are shown in Figure C-2. The Q8 element is divided into a number of subcells and for each subdivision, the element energy eigenmode is computed. Table C.1 shows the number of zero energy eigenmodes for Q8 element as a function of the number of subcells along the $x-$ and $y-$ directions. It can be seen that a minimum of 4 subcells is required to avoid spurious energy modes. The boundaries of the 4 subcells contains the mid-side nodes. This behavior is analogous to the 1D example previously studied.

Higher order patch test

The higher order patch test is performed on a Q8 element. In Figure C-3 a two-element patch of quadratic isoparameteric quadrilaterals is shown. For the FEM, a 3×3 Gaussian quadrature is used and for the SFEM, the number of subcells is varied. For each subcell

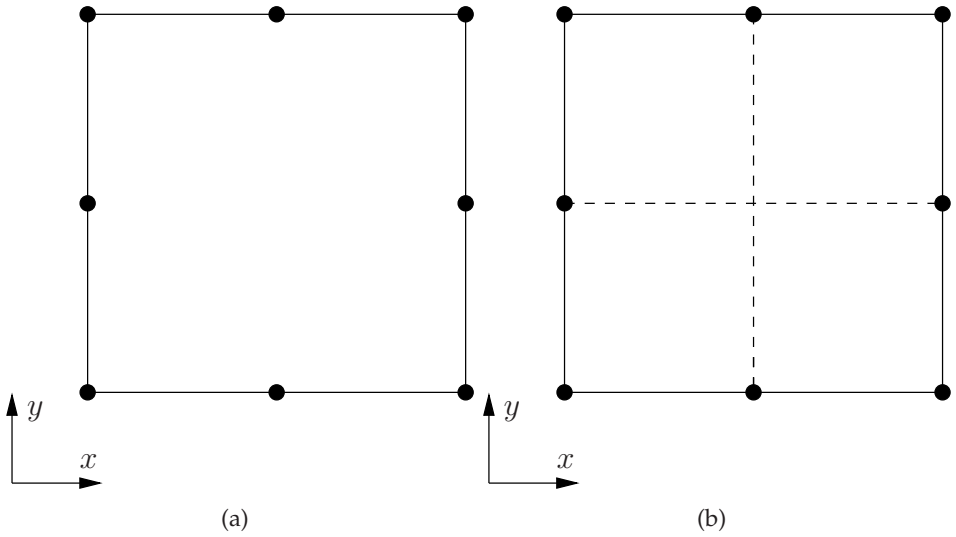

Figure C-2: (a) Q8 element and (b) subdivision of Q8 element by quadrilateral subcells. The dotted lines denote the subcell boundaries. Note that these boundaries contain the mid-side nodes. In this case, there are four subcells.

Table C.1: Q8 element energy eigenmodes for different number of subcells in each direction. The right number of vanishing eigenvalues for the elementary stiffness matrix should be 3 and it can be seen that a minimum of 4 subcells or a minimum of 2 in one direction and 4 in the other direction is required to avoid the spurious energy modes.

Number of subcells						
in $x-$	in $y-$					
	1	2	4	6	8	10
1	13	10	8	8	8	8
2	10	4^{-}	**3**	3	3	3
4	8	**3**	3	3	3	3
6	8	3	3	3	3	3
8	8	3	3	3	3	3
10	8	3	3	3	3	3

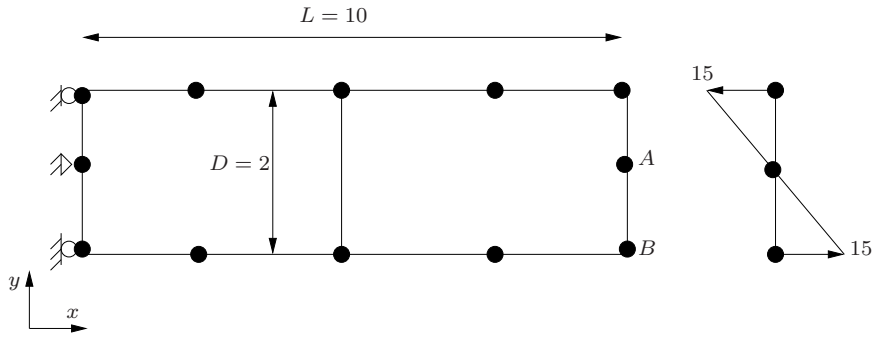

Figure C-3: Patch test for 8- noded isoparametric elements.

Table C.2: Higher order patch test. v_A is the displacement at point A in the $y-$ direction and u_B, v_B are the displacements at point B along the $x-$ and $y-$ direction, respectively.

Method	Quadrature rule	Subcells	v_A	u_B	v_B
Exact	-	-	0.75	0.15	0.75225
FEM	3×3	-	0.74999	0.14999	0.752249
SFEM	-	1	1.00000	0.20000	1.003000
	-	4	0.84375	0.16875	0.846282
	-	9	0.80000	0.16000	0.802400
	-	16	0.78125	0.15625	0.783593

variation, the solution at points A and B are monitored. From the results shown in Table C.2, it is seen that the SFEM does not pass the patch test.

Cantilever Beam problem

A two dimensional cantilever beam subjected to a parabolic load at the free end is examined as shown in Figure C-4. The geometry is: length $L = 8$, height $D = 4$ and thickness $t = 1$. The material properties are: Young's modulus $E = 3 \times 10^7$, and the parabolic shear force $P = 250$. The exact solution to this problem is available as given in Appendix A.
Under plane stress conditions and for a Poisson's ratio $\nu = 0.3$, the exact strain energy is 0.039833333. Figure C-5 shows the rate of convergence in the displacement norm and rate of convergence in the energy norm of elements built using the present method compared with those of the standard FEM Q8 element. It can be seen that the nice properties of the

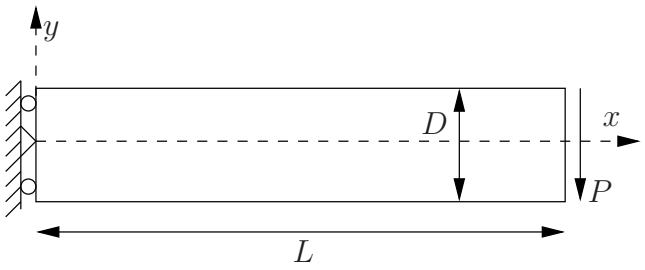

Figure C-4: A cantilever beam and boundary conditions.

strain smoothing, which were seen in the Q4 element are not seen in higher order elements. Although, with increase in the mesh density, the results converge to the analytical solution, the convergence rate is not optimal.

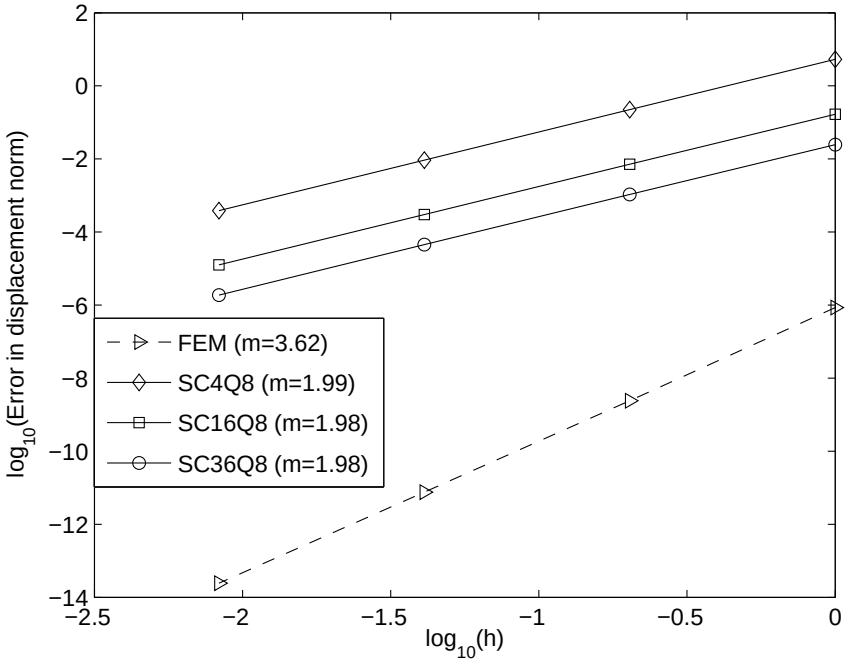

(a)

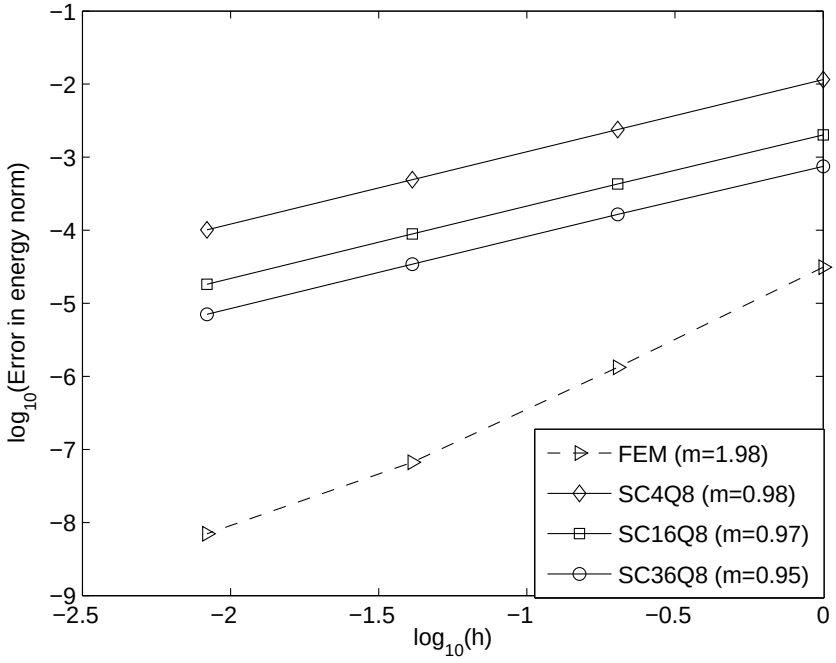

(b)

Figure C-5: Cantilever beam: (a) convergence rate in the displacement (L^2) norm and (b) the convergence rate in the energy $(\mathcal{H}_1)$ norm with Q8 mesh. SCkQ8 $(k = 4, 16, 36)$ denotes the number of subcells. m is the average slope.

D

Stress intensity factor by interaction integral

The energy release rate for general mixed-mode problems in two dimensions is written as:

$$G = \frac{1}{\tilde{E}}(K_I^2 + K_{II}^2) \tag{D-1}$$

where $\tilde{E}$ is defined as:

$$\tilde{E} = \begin{cases} \frac{E}{1-\nu^2} & \text{plane strain} \\ E & \text{plane stress} \end{cases} \tag{D-2}$$

Consider a crack in two dimensions. Let Γ be a contour encompassing the crack tip and $\mathbf{n}$ be the unit normal vector (see Figure 2.2). The contour integral J is defined as:

$$J = \lim_{\Gamma_o \to 0} \int_{\Gamma_o} \left[W \mathrm{d}x_2 - T_i \frac{\partial u}{\partial x_1} \mathrm{d}\Gamma \right] = \lim_{\Gamma_o \to 0} \int_{\Gamma_o} \left[W \mathrm{d}x_2 - \sigma_{ij} \frac{\partial u}{\partial x_1} n_j \mathrm{d}\Gamma \right] \tag{D-3}$$

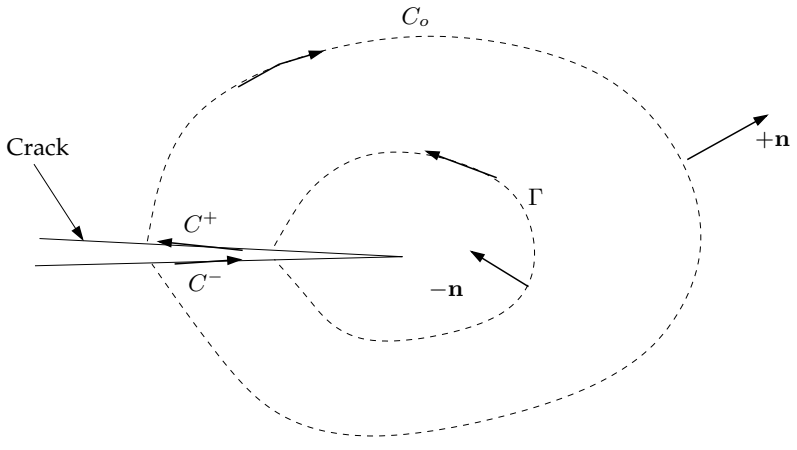

Figure D-1: Contours and domain for computation of mixed mode stress intensity factors.

where $\Gamma_o = \Gamma \cup C_o \cup C^+ \cup C^-$(see Figure D-1). Physically, the J integral can be interpreted as the energy flowing per unit crack advance, i.e., it is equivalent to the energy release rate.

Two states of the cracked body are considered, viz., the current (denoted as State 1) and the auxiliary state (referred to as State 2). The J integral given by Equation (D-3) is written as a superposition of these two states as:

$$J^{(1+2)} = \lim_{\Gamma_o \to 0} \int_{\Gamma_o} \left[\frac{1}{2}(\sigma_{ij}^{(1)} + \sigma_{ij}^{(2)}))(\varepsilon_{ij}^{(1)} + \varepsilon_{ij}^{(2)})\delta_{1j} - (\sigma_{ij}^{(1)} + \sigma_{ij}^{(2)}) \frac{\partial (u_i^{(1)} + u_i^{(2)})}{\partial x_1} \right] n_j \, \mathrm{d}\Gamma \quad \text{(D-4)}$$

By re-arranging the terms in Equation (D-4), we get:

$$J^{(1+2)} = J^{(1)} + J^{(2)} + I^{(1+2)} \quad \text{(D-5)}$$

where $I^{(1+2)}$ is called the interaction integral for the states 1 and 2 and is given by:

$$I^{(1+2)} = \lim_{\Gamma_o \to 0} \int_{\Gamma_o} \left[\frac{1}{2}(\sigma_{ij}^{(1)} \varepsilon_{ij}^{(2)} + \sigma_{ij}^{(2)} \varepsilon_{ij}^{(1)}) - \sigma_{ij}^{(1)} \frac{\partial u_i^{(2)}}{\partial x_1} - \sigma_{ij}^{(2)} \frac{\partial u_i^{(1)}}{\partial x_1} \right] n_j \, \mathrm{d}\Gamma \quad \text{(D-6)}$$

or,

$$I^{(1+2)} = \lim_{\Gamma \to 0} \left\{ \int_{\Gamma \cup C_o \cup C^+ \cup C^-} \left[W^{(1,2)} \delta_{1j} - \sigma_{ij}^{(1)} \frac{\partial u_i^{(2)}}{\partial x_1} - \sigma_{ij}^{(2)} \frac{\partial u_i^{(1)}}{\partial x_1} \right] q \, n_j \, \mathrm{d}s \right\} \quad \text{(D-7)}$$

For a combined state, Equation (D-1) can be re-written as:

$$J^{(1+2)} = J^{(1)} + J^{(2)} + \frac{2}{\tilde{E}}(K_I^{(1)} K_{II}^{(2)} + K_I^{(2)} K_{II}^{(1)}) \quad \text{(D-8)}$$

By comparing Equation (D-5) and Equation (D-8), we get:

$$I^{(1+2)} = \frac{2}{\tilde{E}}(K_I^{(1)} K_{II}^{(2)} + K_I^{(2)} K_{II}^{(1)}) \quad \text{(D-9)}$$

In order to facilitate the numerical implementation of the interaction integral, it is advantageous to recast the contour integrals into equivalent domain integrals. The equivalent domain form of the interaction integral is obtained by defining an appropriate test or weighting function and applying the divergence theorem. In this study, the weighting function is chosen to take a value of unity on an open set containing the crack tip and vanishes on an outer prescribed contour. By applying divergence theorem, to Equation (D-7), the interaction integral in domain form is given by:

$$I^{(1+2)} = \int_{\Omega} \left[-W^{(1,2)} \delta_{1j} + \sigma_{ij}^{(1)} \frac{\partial u_i^{(2)}}{\partial x_1} - \sigma_{ij}^{(2)} \frac{\partial u_i^{(1)}}{\partial x_1} \right] \frac{\partial q}{\partial x_j} \, \mathrm{d}\Omega \quad \text{(D-10)}$$

Remark: It is assumed that the crack faces are straight and traction free.

D-1 Interaction integral for non-homogeneous materials

The interaction integral for non-homogeneous materials and materials with discontinuities is:

$$I^{(1,2)} = \int_{\Omega} \left[\sigma_{ij}^{(1)} \frac{\partial u_i^{(2)}}{\partial x_1} + \sigma_{ij}^{(2)} \frac{\partial u_i^{(1)}}{\partial x_1} - W^{(1,2)} \delta_{1j} \right] \frac{\partial q}{\partial x_i} \, \mathrm{d}\Omega + \int_{\Omega} \sigma_{ij}^{(1)} \left[S_{ijkl}^{\text{tip}} - S_{ijkl}(X) \right] \sigma_{kl,1}^{(2)} \, q \, \mathrm{d}\Omega \tag{D-11}$$

To employ the interaction integral in the XFEM, Equation (D-11) is discretized as:

$$I = \sum_{n=1}^{N} \sum_{m=1}^{M} \left\{ (\sigma_{ij}^{(1)} \frac{\partial u_i^{(2)}}{\partial x_1} + \sigma_{ij}^{(2)} \frac{\partial u_i^{(1)}}{\partial x_1} - \sigma_{jk}^{(2)} \varepsilon_{jk} \delta_{1j}) \frac{\partial q}{\partial x_i} \right. \left. \sigma_{ij}^{(1)} \left[S_{ijkl}^{\text{tip}} - S_{ijkl}(X) \right] \sigma_{kl,1}^{(2)} \, q \right\} det|J| w_p \tag{D-12}$$

where N is the number of elements in the integral domain Ω; M is the number of integration points in one element; $det|J|$ is the determinant of Jacobian matrix and w_p corresponds to the weight at the integration point.

E

Level Set Method

The level set method (LSM) is a numerical technique proposed by Osher and Sethian for tracking moving interfaces. It is based upon the idea of representing the interface as a level set curve of a higher dimensional function $\phi(\mathbf{x}, t)$. In general, a moving interface $\Gamma \subset \mathbb{R}^2$ is formulated as the level set curve of a function $\phi(\mathbf{x}, t) \colon \mathbb{R}^2 \times \mathbb{R} \to \mathbb{R}$, where,

$$\Gamma(t) = \left\{ \mathbf{x} \in \mathbb{R}^2 \colon \phi(\mathbf{x}, t) = 0 \right\} \tag{E-1}$$

The resulting equation for the evolution of ϕ is given by:

$$\phi_t + F||\nabla\phi|| = 0, \qquad \phi(\mathbf{x}, t) = 0 \qquad \text{given} \tag{E-2}$$

where F is the velocity of the front. The initial condition on ϕ are typically defined as the signed distance to the interface as:

$$\phi(\mathbf{x}, t) = \pm \text{min}_{x \in \Gamma(t)} ||\mathbf{x} - \overline{\mathbf{x}}|| \tag{E-3}$$

The plus sign and minus sign are chosen on either side of the interface. In the LSM, the solution of Equation (E-2) is approximated on a grid or on a mesh by computational schemes.